Spring 1-1-2015

Hydroclimate Variability of the Indian Monsoon During Contemporary and Mid-Holocene Periods

Emily Gill
University of Colorado at Boulder, emily.gill@colorado.edu

Hydroclimate variability of the Indian monsoon during contemporary and mid-Holocene periods

by

E. C. Gill

B.S., Franklin & Marshall College, 2007

M.S., University of Colorado at Boulder, 2013

A thesis submitted to the

Faculty of the Graduate School of the

University of Colorado in partial fulfillment

of the requirements for the degree of

Doctor of Philosophy

Department of Civil, Environmental and Architectural Engineering

2015

This thesis entitled:
Hydroclimate variability of the Indian monsoon during contemporary and mid-Holocene periods
written by E. C. Gill
has been approved for the Department of Civil, Environmental and Architectural Engineering

_____
Dr. Rajagopalan Balaji

_____
Dr. Peter H. Molnar

_____
Dr. Thomas M. Marchitto

_____
Dr. Harihar Rajaram

_____
Dr. Joseph R. Kasprzyk

Date _____

The final copy of this thesis has been examined by the signatories, and we find that both the content and the form meet acceptable presentation standards of scholarly work in the above mentioned discipline.

Gill, E. C. (Ph.D., Civil Engineering)

Hydroclimate variability of the Indian monsoon during contemporary and mid-Holocene periods

Thesis directed by Dr. Rajagopalan Balaji

Although model projections suggest an intensified Indian summer monsoon under a warmer climate, the monsoon has remained below average in recent decades despite strong warming trends. An understanding of Indian summer monsoon variability in past climate might provide clues for the future. Paleoclimate proxies suggest that parts of India were wetter during the early- to mid-Holocene period ($\sim$ 10 to 6 thousand years ago, ka), a period that was warmer than present day due to increased summer insolation. Enhanced wetness has been attributed to land heating, a key ingredient of a strong summer monsoon. Recent paleoclimate proxy evidence, however, suggests that the tropical Pacific was in a cooler (La Niña) state, which guarantees a strong monsoon in present day. This thesis advances the hypothesis that the El Niño Southern Oscillation (ENSO) could explain the aridification of India since 10 ka. To test this hypothesis, modern-day spatial and temporal monsoon-ENSO teleconnections are used to reconstruct Holocene Indian monsoon hydroclimate variability. Specifically, this dissertation asks: (1) What is the present day signature of ENSO on the Indian summer monsoon?; (2) Could the wet mid-Holocene India be explained by teleconnections from a cooler Pacific?; and (3) How much wetter was it during the early- to mid-Holocene? Some key findings include: (1) present-day ENSO writes a distinct spatial signature over India whereby a 1°C cooling of the equatorial Pacific can contribute 30-100% greater monsoon precipitation; (2) maximum cold sea surface temperatures (SSTs) and zonal wind anomalies occurred at 10 ka across the equatorial Pacific, and maximum zonal SST differences at 10 and 6 ka, as revealed by a multi-proxy reduced dimension field reconstruction; (3) maximum winds and 40-60% greater precipitation over the core monsoon

region occurred at 10 ka, which have both decreased to present day; and (4) lakes in the northwestern region of India, which is currently desert, would require 40-65% greater precipitation than present day, based on the results of a hydrological water balance lake model. These findings provide the basis for research extensions that have the potential to improve seasonal monsoon forecasting efforts and to provide mechanistic insights into future monsoon variability.

Dedication

To *Mom & Dad* for teaching me to be open-minded.

—

To *Marty* for making everything more fun.

—

To *Balaji* for being generous, and inspiring creativity.

—

To *Peter* for being honest and supportive, and for maintaining a high bar.

Acknowledgements

This work would not have been possible without the support and guidance of many departments and individuals at the University of Colorado at Boulder. I first acknowledge my co-advisors Balaji Rajagopalan and Peter Molnar for imprinting on me the qualities of a good scientist and researcher. Together, you have guided me through an exploration of Indian monsoon dynamics by way of paleoclimate, and statistical modeling, while instilling in me the value of creative scientific inquiry and proper scientific writing. Your encouragement fostered my confidence and your infectious enthusiasm drove my progress. I feel fortunate and excited for the opportunity to continue along this road with you during my postdoctoral work.

I also express my sincere gratitude to the University of Colorado at Boulder, especially to the Department of Civil, Environmental, and Architectural Engineering (CEAE) for the opportunity to pursue my masters and doctoral degrees in Civil Engineering, and for funding my first two years through a department fellowship. Thank you to the Cooperative Institute for Research in Environmental Sciences (CIRES) for generously funding two projects through the Innovative Research Program, and my final semester with a Graduate Research Fellowship. I am very grateful to the Integrated Teaching and Learning Laboratory (ITLL), Janet Yowell, Malinda Zarske, and Jacqueline Sullivan for hiring me as an NSF GK-12 Teaching Fellow, which not only funded my education for two years, but also allowed me to acquire valuable teaching skills and lasting memories.

I am grateful to my committee members, Hari Rajaram, Joe Kasprzyk, and Tom Marchitto, for their thoughtful comments and suggestions, which greatly enhanced the quality

of my research. Thank you also to Tom Chase for mentoring me during my master's work and assisting me in publishing my first climate research article.

Thank you to my friends at CADSWES, a warm community of graduate students, for providing camaraderie and support. Thank you to S. Gadgil, M. Cane, Y. Kushnir, and Y. Enzel for valuable discussions that contributed to my work and stimulated new ideas.

Throughout this process the support of my family has been vital. I sincerely thank each of them: my parents, Maria and Tom, for teaching me to work hard, embrace change, and show compassion; my siblings, Brian and Beth, for being tough acts to follow; Grandma Gill, for providing me with an early strong female role model; Grandpa Gill for paving a path in water resource engineering; and Gram and Pop Palladino for being examples of unwavering perseverance and faith.

Last but not least, thank you to Marty, for his patience, positive attitude, assurance, humor, and love.

Contents

Chapter

Tables

Table

Figures

Figure

Chapter 1

Introduction

Abstract

Paleo-proxies that reconstruct temperature, precipitation, and winds across the monsoonal region suggest that the early- to mid-Holocene ($\sim$ 10 to 6 thousand years ago, ka) India was wetter than present day. The paleo evidence in support of a wetter India during this period includes, but is not limited to: (1) sediment records that suggest the existence of lakes in present-day northwestern desert of India; (2) marine isotope records that imply lower salinity at the mouths of India's major river systems (Ganges, Godavari, Indus Valley), and thus, greater precipitation over their respective basins; (3) cave speleothems in Oman and Yemen that reconstruct enhanced precipitation, and; (4) biological productivity records from the western Arabian Sea that suggest greater upwelling and stronger monsoon winds during this time.

The predominantly cited hypothesis suggests that greater insolation during summer months, due to the precessional cycle, warmed the Indian subcontinent, which strengthened the land-ocean temperature gradient and enhanced monsoon precipitation. This dissertation investigates the plausibility of an alternative hypothesis: teleconnections from an enhanced La Niña-like sea surface temperatures (SSTs) in the tropical Pacific helped maintain wetter conditions over India.

To test whether the Pacific could write a wetter signature on the Indian subcontinent during the early- to mid-Holocene, this collection of studies was designed to: (1) define the

present day signature of the El Niño Southern Oscillation (ENSO) on the Indian summer monsoon, (2) use modern day patterns of variability, along with paleo-proxy SST records, to reconstruct full fields of early- to mid-Holocene tropical Pacific SSTs and zonal winds, (3) use paleo-proxy SST records from across the Indo-Pacific region to reconstruct fields of summer winds over the monsoon region and Indian rainfall, and (4) build a hydrological lake model to quantitatively assess how much rain was necessary to fill lakes in the northwestern India during the early- to mid-Holocene time.

1.1 The Indian Summer Monsoon

Each year, the majority of India receives upward of 70% of its annual average precipitation from the Indian summer monsoon, which is most active from the months of June to September (Figure 1.1). Low thermal heat capacity of land, as compared to that of water, creates a large temperature difference between India and the surrounding ocean. Hot air rises and develops a low pressure zone over the Indian subcontinent that contrasts high pressure over the southern Indian Ocean. This sets up a system of surface-level moist winds blowing off the Indian Ocean. These winds, which constitute what is known as the Somali Jet (or monsoon jet), originate as southeasterlies in the southern Hemisphere, but upon crossing the equator, are deflected by the Coriolis effect and become south-westerlies that follow the African coastline northward to Oman and cross the Arabian Sea toward India. The productivity of the monsoon each year has been shown to be tied to the strength of these winds, which are typically modulated by two main mechanisms: (1) the intensity of land-warming during the pre-monsoon months; and (2) teleconnections from the tropical Pacific.

Temperatures over the Himalayan-Eurasian region during the spring have been shown to play an important role in the strength of the monsoon. Specifically, heating of the atmosphere over Tibet strengthens the land-ocean temperature gradient, allowing for stronger winds and greater convection over the Indian subcontinent (e.g. *Flohn*, 1957, 1968; *Yanai et al.*, 1992; *Yanai and Wu*, 2006). Although some studies have minimized the role of heating

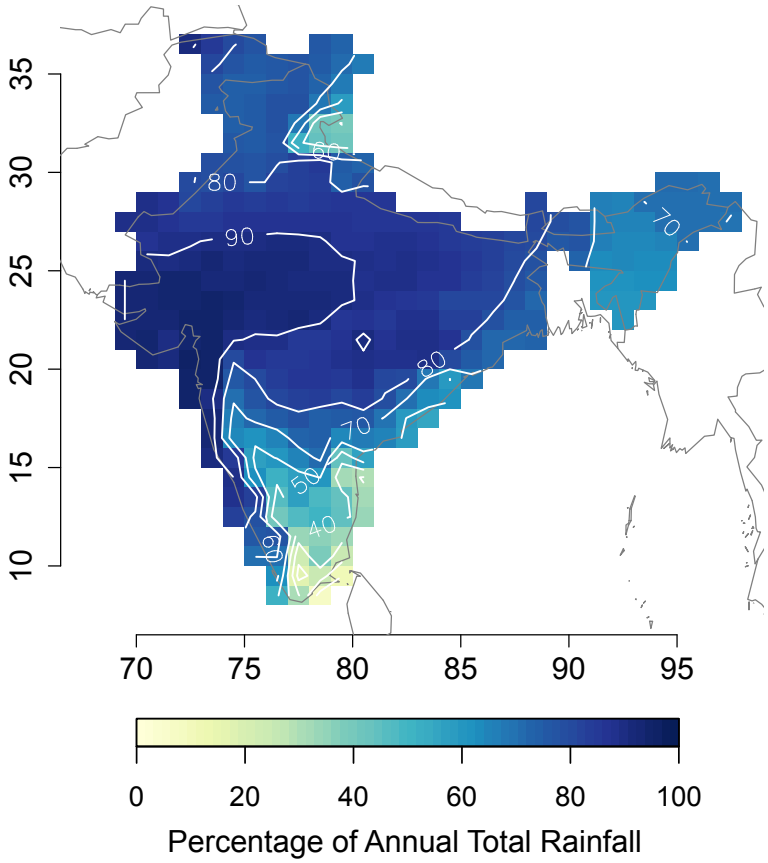

Figure 1.1: Percentage of total annual rainfall (averaged from 1901-2004 from *Rajeevan et al.* (2006)) that India receives between the months of June and September.

over Tibet (e.g. *Boos and Emanuel*, 2009; *Boos and Kuang*, 2010), *Rajagopalan and Molnar* (2013) show that heating does correlate with early and late monsoon rainfall, which constitutes as much as 30% of total monsoon rainfall.

An earlier study by *Walker* (1928) noted a reduction in strength of monsoon winds during anomalously high pressure over the western equatorial Pacific (El Niño conditions). Many studies since then have corroborated this dynamical link, or "teleconnection," between ENSO and the South Asian monsoon (e.g. *Krishna Kumar et al.*, 1995; *Parthasarathy and Pant*, 1985; *Shukla*, 1987; *Shukla and Paolino*, 1983; *Webster*, 1987; *Webster et al.*, 1998), in that a cooler eastern equatorial Pacific (La Niña conditions) favors a strong monsoon but a warmer Pacific (El Niño conditions) favors a weak monsoon. Under normal Pacific

SST conditions, the eastern equatorial Pacific off the coast of Peru is cooler than the western equatorial Pacific near the Maritime Continent. The Pacific portion of the Walker Circulation consists of low-level easterlies and upper-level westerlies that are connected by a zone of subsidence and high pressure over the cooler SSTs in the east, and a zone of convection and low pressure over the warmer SSTs in the west. This zone of ascent over the western Pacific leads to compensating descent over the western Indian Ocean as well. India lies on the margin of the western Pacific zone of convection and can be affected by shifts in this large circulation cell. During La Niña, the zone of convection shifts westward, as does the zone of descent over the Indian Ocean and this, favors a strong monsoon. During El Niño events, however, the Walker Circulation shifts eastward, which shifts the zone of descent over the Indian subcontinent. Subsiding air inhibits convection and weakens the monsoon.

Krishna Kumar et al. (2006) note an asymmetry in the monsoon-ENSO teleconnection: although La Niña conditions guarantee a strong monsoon, El Niño conditions do not always guarantee drought. This can be observed by a simple scatterplot (Figure 1.2) of June-September (JJAS) All-India Summer Monsoon Rainfall (AISMR), a country-wide average rainfall dataset (*Sontakke et al.*, 1993), versus anomalous sea surface temperatures (SSTs) in the NINO3.4 region (*Kaplan et al.*, 1998). Note that from 1901-2012, drought ocurred during La Niña (NINO3.4 $\leq$ -0.75) only once. During El Niño years (NINO3.4 $\geq$ +0.75), however, monsoon rainfall is usually below (AISMR $\leq$ -1) or at normal levels, but can also be above (AISMR $\geq$ +1). *Krishna Kumar et al.* (2006) attribute this asymmetry to the location of the locus of ascent in the equatorial Pacific. When El Niño-related warming is concentrated in the central Pacific, the zone of descent falls directly over India, which competes with normal monsoon convection and weakens the monsoon. If the warming, however, is concentrated in the eastern equatorial Pacific, the zone of ascent moves sufficiently eastward, as does the zone of descent over the monsoon region. In this case, the eastward shift of the zone of descent away from India allows normal convection over India and normal rainfall levels despite the existence of an El Niño.

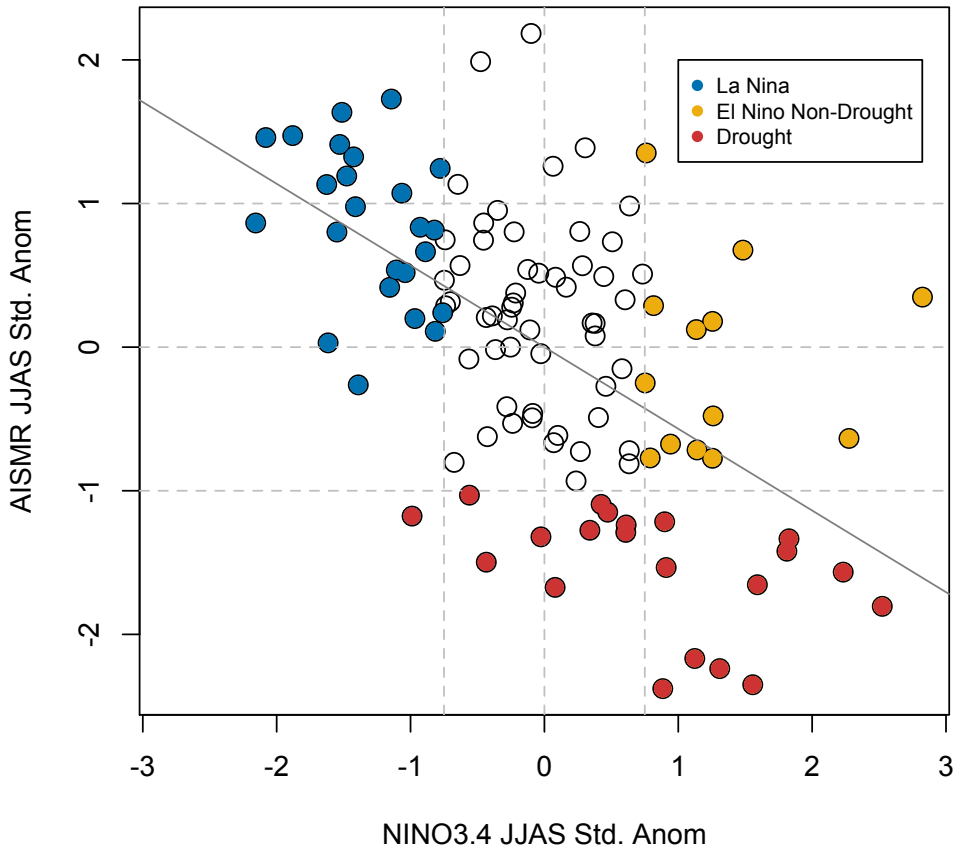

Figure 1.2: Plot of 1901-2012 standardized, All-India Summer Monsoon Rainfall (AISMR) anomalies and NINO3.4 SST anomalies for June to September (JJAS). Severe monsoon drought (JJAS AISMR $\leq$ -1), regardless of NINO3.4 index, is shown in red. Remaining La Niñas (NINO3.4 $\leq$ -0.75) and El Ninos (NINO3.4 $\geq$ +0.75) are shown in blue, and gold, respectively. AISMR and NINO3.4 anomalies are obtained from (*Sontakke et al.*, 1993) and (*Kaplan et al.*, 1998), respectively. This figure is adapted from Figure 1 of *Krishna Kumar et al.* (2006).

Under a warmer climate, model projections show increased monsoon rainfall for the upcoming century (e.g. *Hsu et al.*, 2013; *Islam et al.*, 2013; *Jourdain et al.*, 2013; *Sperber et al.*, 2013; *Zhou et al.*, 2009), but show difficulty in simulating the monsoon realistically. Additionally, simulations disagree on how ENSO will respond to a warming climate with some favoring a weakened zonal gradient and more El Niño-like SSTs (e.g. *Vecchi et al.*, 2006), but others favoring the opposite (.e.g *Cane et al.*, 1997; *Clement et al.*, 1996). Observations of surface temperature and monsoon rainfall over the late 20$^{\text{th}}$ century reveal that despite

strong warming trends, the Indian summer monsoon has weakened (*Krishna Kumar et al.*, 2011). Therefore, although it is generally agreed upon that both land-warming and ENSO would be affected by future climate warming, the way in which each would respond and interact with the monsoon is still debated.

1.2 Early- to Mid-Holocene India

To look at how the monsoon responded to warming in the past, this dissertation focuses on the early- to mid-Holocene period (∼10 to 6 thousand years ago, ka) during which the northern hemisphere was presumably warmer due to greater summer insolation as a result of the precessional cycle. Precession, one of the Milankovitch Cycles, is the slow change in the orientation of the Earth's axis with a 23,000 year periodicity. Today, in its slightly asymmetric elliptical orbit, Earth is closest to the sun ("at perihelion") during northern hemisphere winter and farthest from the sun ("at aphelion") during northern hemisphere summer. At 9 ka, however, northern hemisphere summer occured at perihelion, providing an additional 8% (∼40 W m^{-2}) greater summer insolation to latitudes around 30°N (*Berger and Loutre*, 1991), which aligns with the northern part of India.

Continental and marine climate proxies from the monsoonal region that span the past 10,000 years provide evidence that suggests aridification associated with a weakening of the Indian summer monsoon since the early- to mid-Holocene. These proxy records include pollen, lake level, precipitation, discharge, salinity, and biological productivity reconstructions that are scattered from Oman to the Bay of Bengal (Figure 1.3). Cave speleothems from the Hoti Cave (*Neff et al.*, 2001; *Fleitmann et al.*, 2007), Qunf Cave (*Fleitmann et al.*, 2003, 2007) and Defore Cave (*Fleitmann et al.*, 2007) in Oman imply greater precipitation during the early Holocene than present day. These align with the timing of records from the western Arabian Sea that measure upwelling through biological productivity and thus, imply wind strength (*Gupta et al.*, 2003; *Ivanochko et al.*, 2005). In conjunction with speleothems, these records suggest a stronger Somali jet during early- to mid-Holocene time, and thus, a

stronger Indian monsoon.

On the Indian subcontinent, many studies have identified dry lake beds in the northwestern desert region of India (see blue dots on 1.3) that have been dated back to the early- to mid-Holocene (*Achyuthan et al.*, 2007; *Bryson and Swain*, 1981; *Deotare et al.*, 2004; *Enzel et al.*, 1999; *Kajale and Deotare*, 1997; *Swain et al.*, 1983; *Singh et al.*, 1972, 1973, 1974, 1990; *Prasad et al.*, 1997; *Wasson et al.*, 1984). Additionally, marine records from the Arabian Sea (63KA and 3268G5 on 1.3) and the Bay of Bengal (16A and 126KL on 1.3) are strategically located at the mouths of India's largest rivers, and suggest greater river discharge during the

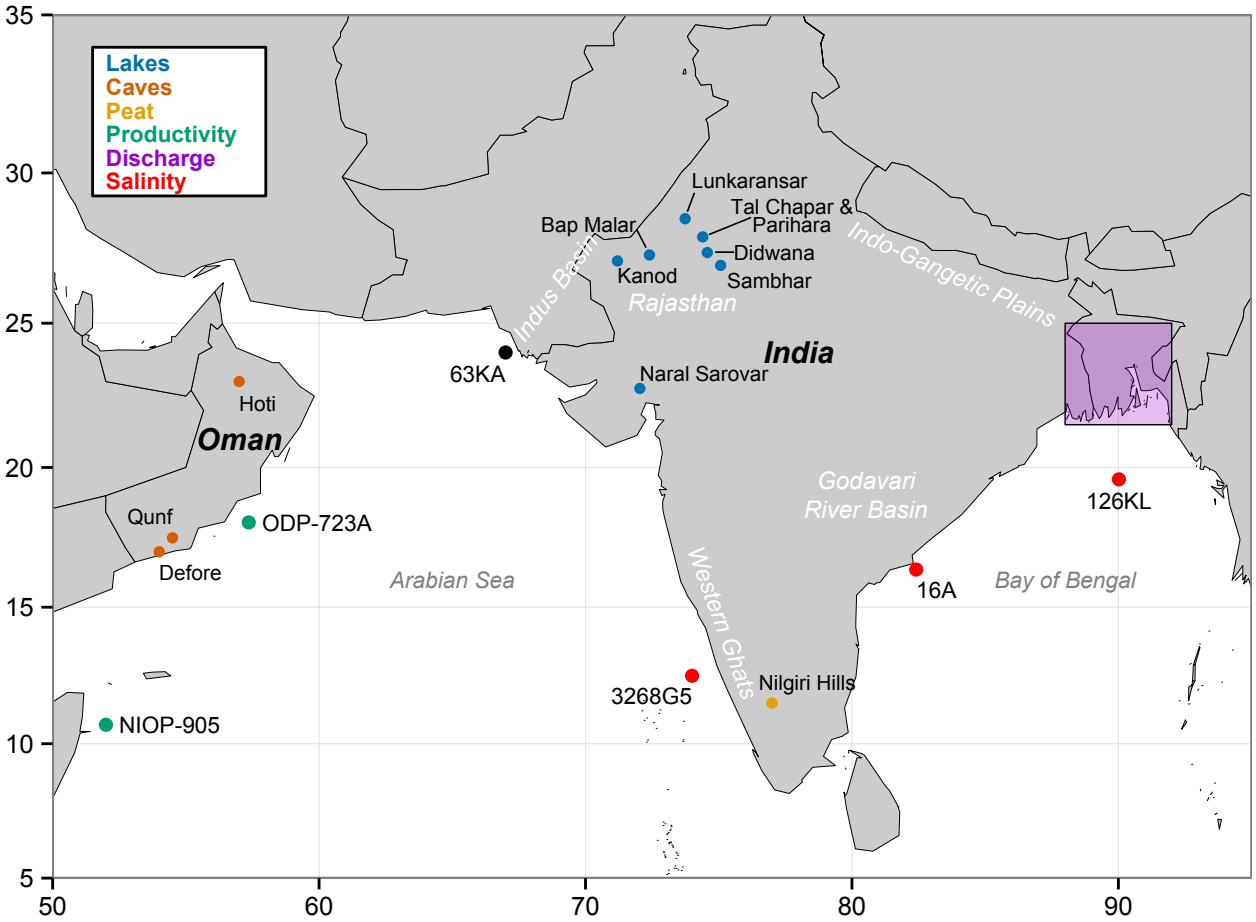

Figure 1.3: This map provides a partial summary of the locations of different types of proxy records that have been reconstructed through the past 10 ka, and suggest enhanced wetness over India during the early- to mid-Holocene and aridification during the late Holocene. This figure and these proxies are described further in Chapter 4.

early- to mid-Holocene (*Kudrass et al.*, 2001; *Ponton et al.*, 2012; *Staubwasser et al.*, 2003; *Sarkar et al.*, 2000). These records are discussed in further detail in Chapter 4.

1.3 Hypotheses of Holocene Monsoon Variability

The early- to mid-Holocene wetness has primarily been explained as being a consequence of a stronger land-ocean temperature gradient. The logic follows that due to increased summer insolation the continent was warmer during the pre-monsoon than it is during present day,. GCM simulations have displayed this mechnism (e.g. *Kutzbach*, 1981; *Kutzbach and Otto-Bliesner*, 1982; *Liu et al.*, 2000, 2003): greater heating of the Indian subcontinent creates a stronger land-ocean temperature and pressure gradient, which results in a stronger monsoon.

In the recent period, however, strong warming trends have been observed over India, but the Indian monsoon has remained remained below average (*Krishna Kumar et al.*, 2011), which suggests that other mechanisms are important.

This dissertation advances an alternative hypothesis to explain a wetter India during the early- to mid-Holocene. Recall that in present day, La Niñas almost guarantee a strong monsoon. Recent marine records from the equatorial Pacific that reconstruct past SSTs have suggested a shift from a more La Nina-like state during the early- to mid-Holocene to a more El Nino-like state during the late Holocene (e.g. *Conroy et al.*, 2008; *Koutavas et al.*, 2002, 2006; *Leduc et al.*, 2007, 2010; *Pahnke et al.*, 2007; *Stott et al.*, 2002, 2004). In addition, sediment records from Ecuador and Peru suggest a return of ENSO variability after the mid-Holocene (e.g. *Chazen et al.*, 2009; *Moy et al.*, 2002; *Riedinger et al.*, 2002; *Rein et al.*, 2005; *Rodbell et al.*, 1999; *Sandweiss et al.*, 1996, 2001). With the contemporary relationship between a cooler Pacific and a strong Indian monsoon, combined with the paleo-proxy evidence of a cooler Pacific during the mid-Holocene, this dissertation seeks to investigate whether teleconnections from the tropical Pacific could explain the increased wetness over India during the early- to mid-Holocene.

1.4 Motivating Research Questions

The overarching goal of this dissertation is use the present-day relationship between Pacific SSTs and the Indian summer monsoon, in order to reconstruct ENSO variability and monsoon hydro-climate fields during the previous 10 ka. Specifically, I ask:

(1) In present day, what spatial signature does ENSO write on the Indian summer monsoon, and how does this signature shift sub-seasonally? (Chapter 2)

(2) What were the dominant spatial patterns of SSTs and zonal winds across the equatorial Pacific throughout the past 10,000 years? (Chapter 3)

(3) Could the wetter early- to mid-Holocene over the Indian subcontinent be a result of teleconnections from a cooler equatorial Pacific? If so, how big of a signal could the tropical Pacific write on rainfall spatially over India? (Chapter 4)

(4) What magnitude of precipitation increase is necessary to sustain lakes in northwest India during the early- to mid-Holocene? (Chapter 5)

1.5 Dissertation Research Plan

In *Sub-Seasonal Variations in Spatial Signatures of ENSO on the Indian Summer Monsoon from 1901-2009* (Chapter 2), a high-resolution (1° by 1°) daily gridded dataset along with monthly SST anomalies from the NINO3.4 region (120°W - 170°W and 5°S-5°N) is used to investige the present-day role of Pacific SSTs on the Indian summer monsoon over the full peak season (June, July, August and September), as well as over three sub-seasons: early (June), middle (July and August), and late (September). In addition to highlighting the evolution of the ENSO-monsoon relationship throughout the monsoon season, this study also addresses asymmetries between the respective signatures of La Niña and El Niño on the Indian summer monsoon.

The next two chapters exploit paleo-SST proxy records from the Indo-Pacific region in reduced-dimension reconstruction methodologies that recreate annual Pacific SST, Indo-Pacific summer winds, and Indian summer monsoon rainfall fields over the past 10 ka. In *Multi-Proxy Reconstruction of the Equatorial Pacific SST and Zonal Wind Fields of the past 10,000 Years using Mg/Ca and Alkenone Records* (Chapter 3), I use sparsely distributed SST proxy records from the western and eastern equatorial Pacific to reconstruct the dominant patterns of variability in 1,000-year snapshots for the past 10 ka. Two slightly different reduced-dimension reconstruction methodologies are used: a Principal Component Analysis (PCA)-based method to reconstruct SSTs and a Canonical Correlation Analysis (CCA)-based method for reconstructing zonal winds. The significance of this study is two-fold, in that it allows us to: (1) identify the patterns common across the multi-proxy field to make sense of seemingly contradictory proxy records, and (2) make inferences about the central Pacific, which would otherwise be impossible as there are no existing proxy records covering the early- to mid-Holocene from that region.

Multi-Proxy Reconstruction of Indian Summer Monsoon Winds and Precipitation of the past 10,000 Years using Mg/Ca and Alkenone Records (Chapter 4), makes use of the same proxy SST records from Chapter 3 along with others from the Arabian Sea and Bay of Bengal, to obtain spatial coverage of the entire Indo-Pacific. Using a similar CCA-based reconstruction method, we reconstruct the fields of summer wind stress curl over the Arabian Sea, and Indian summer monsoon rainfall. We quantify the percentage increase in mean daily summer monsoon rainfall for various regions of India, and compare those to paleoclimatic evidence that extends across the subcontinent. This reconstruction allows us to test the hypothesis that cooling of the tropical Pacific could have been responsible for a wetter early- to mid-Holocene India.

An Assessment of the Mean Annual Precipitation Needed to Sustain Lake Sambhar in Rajasthan, India during Mid-Holocene Time (Chapter 5), shifts the focus to a single location in Rajasthan, a region of northwestern India that is desert in present day. Sedimentology

studies that date isotopes from dry lakebeds of this region suggest that most of these were full to some extent during early- to mid-Holocene. Pollen reconstructions also suggest a vastly different vegetation regime, citing the presence of plant species that require more water than the present day annual average of Rajasthan. Lake Sambhar is a closed-basin lake in this region that fills only slightly during the monsoon season, but remains dry for the rest of the year. This lake bed, however, provides a unique opportunity to hydrologically model how much excess precipitation is necessary to keep this lake full. In this chapter, I build a lake model built on the principles of a water-balance, that runs on a daily timescale and provides quantitative bounds on the amount of precipitation necessary to keep this lake full during the early- to mid-Holocene.

Lastly, Chapter 6 provides a summary of the key findings of this dissertation.

Chapter 2

Sub-Seasonal Variations in Spatial Signatures of ENSO on the Indian Summer Monsoon from 1901-2009

Abstract Correlations of 1° by 1° seasonal rainfall with Pacific sea-surface temperatures (SSTs) reveal spatially distinct teleconnections between El Niño-Southern Oscillation (ENSO) and Indian summer monsoon rainfall over the full monsoon season, as well as three sub-seasons. Over the full season (June-September), Pacific SSTs correlate with rainfall in western India more than that in eastern India. This spatial signature shifts as the monsoon progresses through early (June), middle or peak (July-August) and late (September) sub-seasons. Specifically, a 1°C cooling of the central equatorial Pacific (i.e. La Niña conditions) can result in: $\sim$ 70-100% increase in precipitation in north-central Indian and the Indo-Gangetic Plains during the early season, $\sim$ 30-80% increase in peak season precipitation in south-central India, and northwestern Rajasthan, and $\sim$ 60-100% increase in late season precipitation in northern, north-western, and central India. Furthermore, the spatial signatures between La Niña and El Niño are asymmetric in that for a particular location, the enhancement and suppression of rainfall associated with La Niña and El Niño conditions, respectively, are not equal. El Niño suppresses peak season rainfall in the south-central and northwestern Rajasthan regions more than La Niña enhances it, but, the opposite occurs during the late-season in northern, northwestern, and central India. Additionally, the correspondence of minima (maxima) in anomalies of velocity potential aloft with maxima (minima) at 925 mb and with positive (negative) surface pressure anomalies suggest that

anomalous subsidence (ascent) occurs in July, August, and September during El Niño (La Niña) times. In the early season, however, patterns of velocity potential composites suggest a region of descent (ascent) over the western equatorial Indian Ocean, along with a region of ascent (descent) over the Indian subcontinent that exists only during the early season, but not during the peak or late season. These patterns are consistent with the hypothesis that local Hadley cell circulation affects pressure, and thus, rainfall during the early season, but that a larger scale mechanism, such as eastward or westward shifts in the Walker circulation, may be more responsible for teleconnections seen throughout the remainder of the season. These findings indicate that focusing monsoon forecasting efforts on these regions and on sub-seasonal periods while incorporating ENSO asymmetries will yield useful and skillful regional forecasts, compared to the declining utility and skill of All-India summer monsoon rainfall (AISMR).

2.1 Background

The El Niño Southern Oscillation (ENSO), which manifests as recurring variations of sea-surface temperatures in the equatorial Pacific, is one of the main sources of regional climate variability around the world and plays a major role in predictions of monsoonal rainfall over India (e.g. *Shukla and Mooley*, 1987; *Webster et al.*, 1998). During normal conditions, the eastern equatorial Pacific is cool and the western equatorial Pacific is warm. During the cold phase of ENSO (La Niña) the western warm pool warms by a small amount, and the eastern cold tongue extends westward, resulting in an enhanced zonal temperature gradient across the equatorial Pacific. Due to this modest change in SSTs, La Niña is often considered an enhancement of normal conditions, which includes not only a strengthened Walker circulation but also stronger south Asian monsoonal rainfall. During the warm phase of ENSO (El Niño), anomalously warm water extends into the central Pacific, and into the eastern Pacific as well during major El Niño events. Moreover, during El Niño events the locus of rainfall and ascent through the troposphere moves eastward.

Since *Walker* (1924, 1928) first recognized the relationship between El Niño (La Niña) and weak (strong) Indian monsoon rainfall, a number of hypotheses responsible for this teleconnection have been proposed. During El Niño years, ascent in the eastern equatorial Pacific Ocean is enhanced and that over the western equatorial Pacific and Southeast Asia is reduced, which has been shown by numerical stimulations (*Keshavamurty*, 1982; *Palmer et al.*, 1992; *Shukla and Wallace*, 1983; *Soman and Slingo*, 1997). The entire Walker Circulation, with ascent over the Maritime Continent, and descent over the central Pacific and the western Indian Ocean, shifts eastward during El Niño, and slightly westward during La Niña. This has led to the widely cited hypothesis that during El Niño the descending branch of the Walker circulation over the western Indian Ocean shifts eastward to overlie the Indian subcontinent, which helps suppress monsoon rainfall during the warm ENSO phase (e.g. *Krishna Kumar et al.*, 1999, 2006; *Palmer et al.*, 1992).

Others have argued that the descending branch of the Walker circulation does not directly suppress monsoon rainfall during El Niño, but rather that the shifted Walker circulation enhances local Hadley cell descent over the Indian subcontinent and the Indian Ocean to its south (e.g. *Goswami*, 1998; *Ju and Slingo*, 1995; *Lau and Wu*, 2001; *Slingo and Annamalai*, 2000). *Goswami* (1998) note that under normal Pacific SST conditions, the descending branch of the Walker circulation sits over the Indian Ocean, which limits convection from the equator and allows the ITCZ to overlie land for the majority of the monsoon season. Anomalous warming of the eastern Pacific during El Niño shifts the ascending and descending branches of the Walker circulation so that warming occurs over the equatorial Indian Ocean. It is postulated that this enhances low-level convergence, and thus precipitation, over the equatorial warm waters of the Indian Ocean, and consequently, enhanced subsidence from the descending branch of the Hadley cell (and, thus, lower precipitation) occurs over the Indian subcontinent.

As an added nuance to this hypothesis, *Soman and Slingo* (1997) highlight the importance of the western equatorial Pacific. During La Niña events, modulation of the Walker

circulation is not the dominant mechanism responsible for a stronger monsoon; instead warm, western equatorial Pacific SST anomalies enhance the northward transition of a land-based ITCZ, which results in earlier monsoon onset and stronger rainfall. During El Niño events, modulation of the Walker circulation is the dominant mechanism for weaker monsoons. They add, however, that cooler, western equatorial Pacific SST anomalies delay the northward transition of the ITCZ over India, which, in addition to modulation of the Walker circulation, results in a generally weaker monsoon. In fact, *Soman and Slingo* (1997) note that, despite being an El Niño year, the 1994 Indian monsoon maintained high rainfall due to anomalous warming in the western equatorial Pacific.

Despite disagreement over the mechanism responsible, there exists a distinct asymmetry in the response of mean south Asian monsoon rainfall to equatorial Pacific sea surface temperatures (SSTs): although La Niña SSTs, which are atypically cool in the central Pacific, consistently imply a strong monsoon, El Niño SSTs, which are atypically warm in the central and east Pacific, do not assure a weak monsoon (*Krishna Kumar et al.*, 2006). As shown by the scatterplot (Figure 2.1a) of average monsoon-season (Jun-Sep) All-India Summer Monsoon Rainfall (AISMR) anomalies versus the widely used NINO3.4 index for ENSO (average SSTs in the 120°W-170°W and 5°N-5°S region), for a cooler NINO3.4 index (i.e. La Niña conditions), rainfall is consistently higher than normal, and variability is relatively small ($\sigma^2 = 0.45$). For a warm NINO3.4 index (i.e. El Niño conditions), however, rainfall is sometimes low, but sometimes normal or even above-normal, maintaining greater variability ($\sigma^2 = 1.04$) than during La Niña. *Ihara et al.* (2008c) attribute the asymmetry to the timing of the evolution of warm SSTs in the eastern Pacific. They found that when warming begins to evolve in the spring prior to the monsoon season, the western-central Pacific and Indian Oceans remain cold and AISMR is below-average, but if the warming begins in the winter prior to the monsoon season, the western and central Pacific are warmer than normal during the monsoon, and AISMR can be normal. In addition to the AISMR dataset, the asymmetry between La Niña and El Niño monsoon rainfall has been demonstrated over five

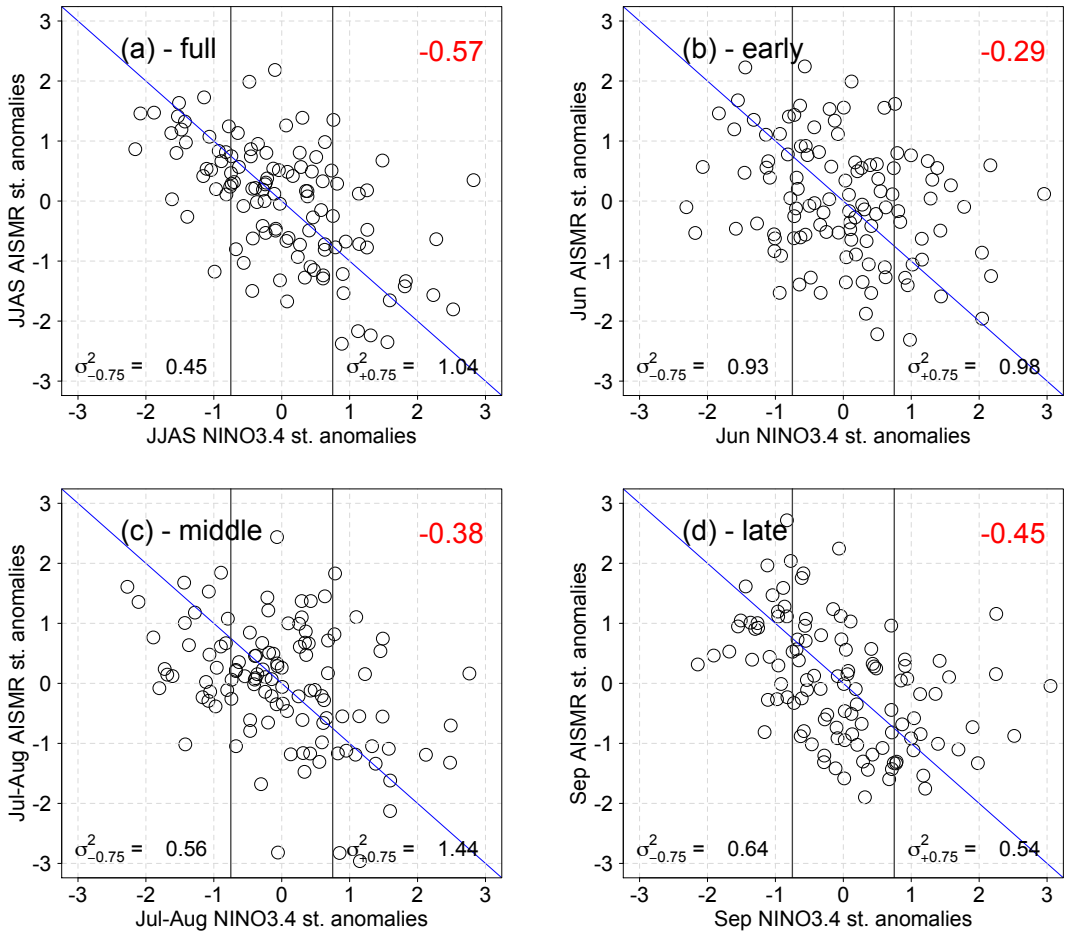

Figure 2.1: Scatterplots of NINO3.4 anomalies with AISMR standardized total rainfall anomalies for the (a) full, (b) early, (c) middle and (d) late seasons. The blue line plots the SMA regression trend through the points. The correlation between the two time series is marked in red in the upper right corner of each plot. NINO3.4 SST anomalies are provided from *Kaplan et al.* (1998). Standardized AISMR anomalies are created by subtracting the mean, μ, from the AISMR time series and dividing by the standard deviation, σ, for each of the four season definitions ($\mu_a = 8432$ mm, $\sigma_a = 810$ mm; $\mu_b = 1600$ mm, $\sigma_b = 354$ mm; $\mu_c = 5139$ mm, $\sigma_c = 531$ mm; $\mu_a = 1692$ mm, $\sigma_a = 363$ mm). The variance of rainfall associated with strong La Niñas (scaled NINO3.4 $\leq$ -0.75) and strong El Niños (scaled NINO3.4 $\geq$ 0.75) is displayed on the lower left and right sides, respectively, of the sub-plots.

homogeneous rainfall regions (e.g. northwest, west-central, central-northeast, northeast, and peninsular) of India for the full monsoon season (*Parthasarathy et al.*, 1994).

Krishna Kumar et al. (2006) found that monsoonal rainfall during El Niño has a strong dependence on the location of anomalous warming, whether it extends into the east, or is

confined to the central part of the Pacific. The latter is sometimes referred to as an "El Niño modoki" event (*Ashok et al.*, 2007; *Ashok and Yamagata*, 2009; *Weng et al.*, 2007; *Ratnam et al.*, 2010). Subsidence over India inhibits monsoonal rainfall most when El Niño warming is concentrated in the central equatorial Pacific (*Krishna Kumar et al.*, 2006), as has been shown to be the cause of the 2009 failure in the Indian summer monsoon (*Ratnam et al.*, 2010). Keeping these asymmetries in mind, we consider how both the warm and cold phases of ENSO manifest as spatially and sub-seasonally distinct rainfall patterns over India.

Analyses of the monsoon-ENSO teleconnection comparing rainfall across sub-divisional boundaries (*Singh*, 2001), and variously defined rainfall regions over India (*Cash et al.*, 2015; *Ihara et al.*, 2008a; *Kane*, 2000; *Krishnamurthy and Shukla*, 2000; *Parthasarathy et al.*, 1996; *Vecchi and Harrison*, 2004) and the Bay of Bengal (*Cash et al.*, 2015) have revealed that the strength of the relationship varies spatially across the monsoon region. Other studies have noted intra-seasonal variability by looking at the behavior of the monsoon-ENSO teleconnection month-to-month (*Kane*, 2000; *Ju and Slingo*, 1995; *Pattanaik*, 2012; *Singh*, 2001) and during active and break periods (*Annamalai and Slingo*, 2001; *Krishnamurthy and Shukla*, 2000, 2007). *Ju and Slingo* (1995) reported that the biggest difference between monsoonal strength of La Niña versus El Niño years is limited to the onset of the monsoon, but negligible during the remainder of the monsoon season. *Rajagopalan and Molnar* (2012, 2014), however, have emphasized the correlation between monsoon rainfall and ENSO during both early and late seasons.

Regional analyses of the monsoon-ENSO teleconnection have been limited to a few sub-divisional or homogeneous rainfall zones. To our knowledge, analyses of the anti-symmetry in the effects of the warm and cold phases of ENSO on monsoon rainfall have considered only the full monsoon season, not sub-seasons. We attempt a more spatially (1° x 1° resolution) and temporally (1901-2009) complete regional analysis of the monsoon-ENSO teleconnection that specifically addresses the signature of ENSO on monsoon rainfall as well as anti-symmetric behavior over the full and sub-seasons. Specifically, we ask the following questions:

(1) what is the spatial signature of monsoon-ENSO teleconnections over India and does it change as the monsoon season progresses through early (June), middle or peak (July-August), and late (September) sub-seasons?;

(2) how do the asymmetries that exist in La Niña versus El Niño monsoon variability manifest themselves spatially over India?; and

(3) by what mechinisms does ENSO affect monsoon rainfall?

2.2 Data

We used the Indian Institute of Tropical Meteorology All India Summer Monsoon Rainfall (AISMR) based on the monthly precipitation dataset that spans 1871-2012 and has been constructed by weighting station data to create a single representative series for the entire country (*Parthasarathy et al.*, 1994). To analyze spatial differences in Indian rainfall, we merged two Indian Meteorological Department's 1° by 1° daily rainfall data sets (1901-2004 and 1951-2009) to create a 109-year record of rainfall for each of 357 grid-cells over India (*Rajeevan et al.*, 2006). We then obtained daily average rates (mm d^{-1}) for each grid-cell during four monsoon seasons defined as: full (1 Jun to 30 Sep), early (1 Jun to 30 Jun), middle (1 Jul to 31 Aug), and late (1 Sep to 30 Sep).

Monthly average Pacific sea surface temperature (SST) anomalies were obtained for 1901-2009 from three NINO indices (*Kaplan et al.*, 1998): NINO4 (average SSTs in the western region of 150°W-160°E and 5°N-5°S), NINO3.4 (average SSTs in the central region of 120°W-170°W and 5°N-5°S) and NINO3 (average SSTs in the eastern region of 90°W-150°W and 5°N-5°S). SSTs from the NINO3.4 region are used in this analysis, but results using SSTs from the NINO4 and NINO3 are shown in Appendix A (Figures A.1 and A.2). Gridded SSTs (5° by 5°) for the region of 30°E - 80°W and 40°S - 40°N were obtained from *Kaplan et al.* (1998) as well.

Monthly gridded (2.5° x 2.5°) atmospheric variables were obtained from the NOAA

NCEP-NCAR CDAS-1 Reanalysis for the period of 1949-2012 (*Kalnay et al.*, 1996). These include yearly anomalies of 200 mb and 925 mb velocity potential (m^2 s^{-1} 10^{-6}), 850 mb geopotential height (gpm), 850 mb zonal and meridional winds (m s^{-1}), and total column precipitable water (kg m^{-2}).

2.3 Spatial signature of monsoon-ENSO teleconnection

We start with the traditional correlation between AISMR and the NINO3.4 index. Typically, AISMR is used in monsoon-ENSO diagnostics and forecasting efforts (*Krishna Kumar et al.*, 1995) due to its correlation over the entire period of record with Pacific SSTs during the full monsoon season. During the full season, AISMR correlations with NINO4, NINO3.4, and NINO3 are -0.46, -0.57, and -0.55, respectively. The correlation between NINO3.4 SSTs and AISMR is greatest for the entire season (-0.57), and notably weaker during the early (-0.29) and middle part (-0.38) of the season, increasing to -0.45 in the late season (Figure 2.1). Much of the seasonal monsoon-ENSO correlation is contributed by September rainfall. ENSO establishes itself firmly from September onwards, which explains the higher correlation. The AISMR, however, does not provide insights into the spatial signature of ENSO on rainfall, which is important for societal applications. Correlations with the NINO3 (-0.55, -0.30, -0.39, and -0.42 for full, early, middle and late seasons, respectively) and NINO4 (-0.46, -0.31, -0.22, and -0.47 for full, early, middle and late seasons, respectively) indices are similar. Given the similarities, but slightly larger full season correlations for NINO3.4 than the others, we present correlations and regressions only with the NINO3.4 index but include regression results for NINO4 and NINO3 in Appendix A.

We investigated the spatial signature of monsoon-ENSO teleconnection by utilizing gridded rainfall data over India. Figure 2.2 shows the gridded mean daily rainfall, along with the standard deviation and coefficient of variation (standard deviation divided by the mean). The majority of monsoon rainfall falls during the peak monsoon season with the coast and northeastern parts of India receiving the highest amount of rainfall. A given

location can receive anywhere between 20-60% of its total monsoon rainfall from the early and late season combined.

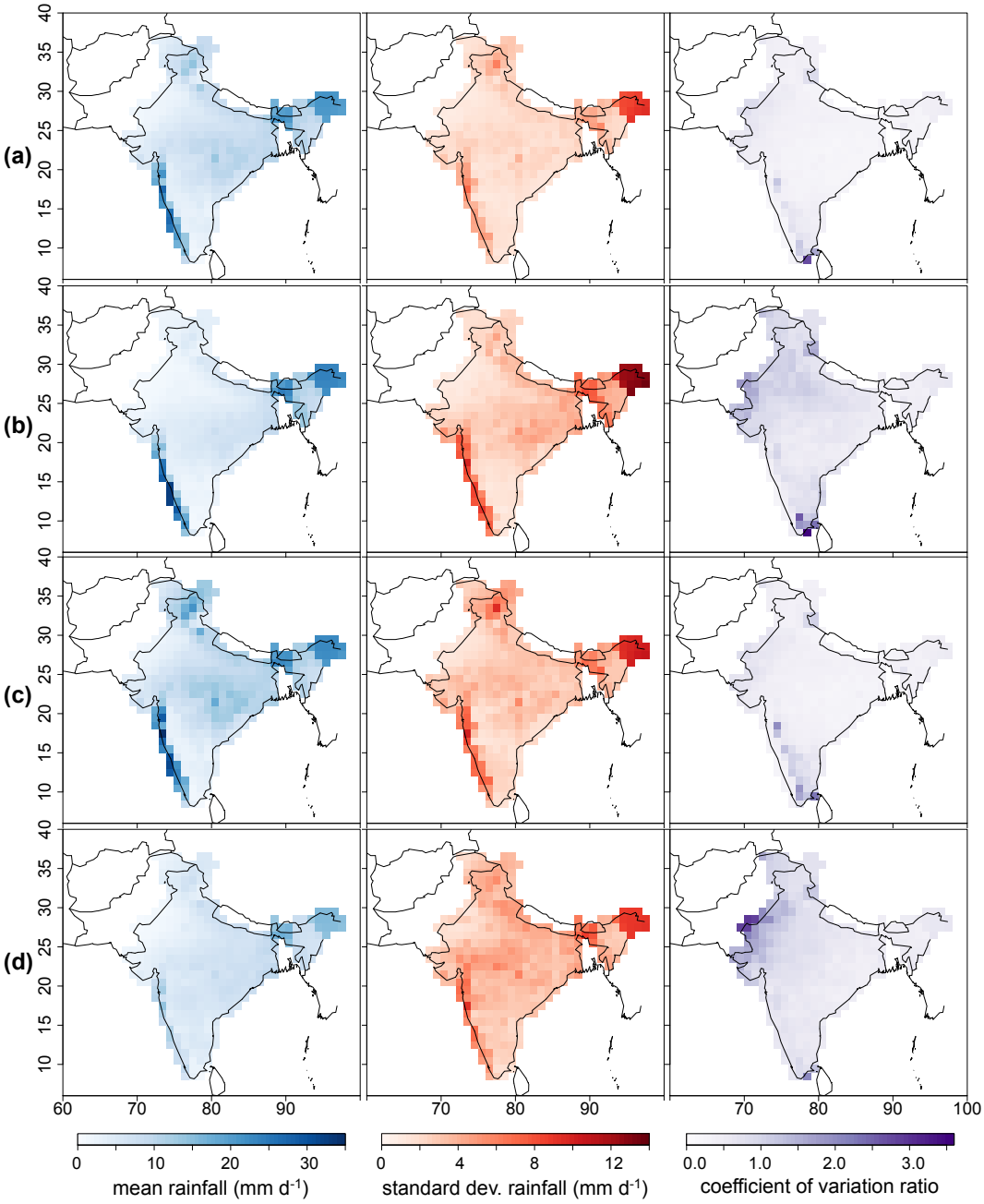

Figure 2.2: Mean (blue) and standard deviation (red) of *Rajeevan et al.* (2006) average daily rainfall (mm d^{-1} over the (a) full monsoon season and three defined sub-seasons (a - early, b - middle, and c - late). The third column provides the coefficient of variation (standard deviation divided by the mean).

For each grid-cell, a standard major axis (SMA) regression, also known as a reduced major axis regression or model 2 regression, was performed between the NINO index and average daily precipitation over the full season and three sub-seasons. An SMA regression (*Sprent and Dolby*, 1980) has the form,

$$y = b_0 + b_1 x \tag{2.1}$$

where (x_i, y_i) are a random sample from a bivariate distribution, b_1 is the slope, and b_0 is the y-intercept. In our case, x represents the SST anomaly (°C), and y the daily average rainfall (mm d^{-1}). The slope (mm d^{-1} °C^{-1}) is given by,

$$b_1 = \pm \frac{\sigma_y}{\sigma_x} \tag{2.2}$$

where σ_x and σ_y represent the standard deviations of the variables. The sign of the slope is determined by using the sign of the correlation coefficient. The y-intercept is given by,

$$b_0 = \bar{y} - b_1 \bar{x} \tag{2.3}$$

which follows that for least-squares regression, where $\bar{y}$ and $\bar{x}$ are the mean of y and x, respectively. An SMA regression accounts for uncertainty in both axes by minimizing the errors in both directions and is thereby preferable in scenarios when both variables are uncertain. The squared correlation coefficients R^2 and the analysis of variance, however, are similar to the standard least squares regression.

Figure 2.3 plots the slopes (mm d^{-1} °C^{-1}) and R^2 values of this relationship between average daily precipitation and the NINO3.4 across the full season and the three sub-seasons. Values are plotted only where the SMA regression is at least 95% significant. Obviously, rainfall over India is negatively correlated to central Pacific SSTs, in that a cooler central Pacific results in higher monsoon rainfall. Over the full monsoon season (Figure 2.3a), there are regions of India that are not correlated to Pacific SSTs, such as northeastern and south India. Furthermore, a 1°C decrease in NINO3.4 over the full season does not uniformly

increase precipitation over India. Instead, some regions of India prove more sensitive to Pacific SST anomalies, as indicated by the magnitudes of negative slopes.

Separating the season into sub-seasons reveals that the relationship between rainfall and Pacific SSTs is also not constant as the monsoon season progresses. The relationship between early season average daily rainfall and NINO3.4 SSTs (Figure 2.3b) is greatest in central India and the Indo-Gangetic Plains. Average daily rainfall during the middle season (Figure 2.3c), however, in Rajasthan (northwestern India) and the northern Himalaya, as well as the south-central India, maintain a significant correlation with Pacific SSTs. Rainfall in the coastal regions seems to be most related to ENSO during the early (Figure 2.3b) and late (Figure 2.3d) seasons. Although during early and peak monsoon seasons AISMR shows a relatively low correlation (Figure 2.1), the spatial analysis shows a teleconnection mosaic with distinct regions (e.g. south central, northwestern, and Indo-Gangetic Plains) that exhibit larger correlations with ENSO (Figure 2.3c-d). The results of the SMA regression analysis with NINO4 (Figure A.1) and NINO3 (Figure A.2) reveal similar patterns throughout the monsoon season and are provided in Appendix A.

These findings bear on forecasting efforts in two ways. First, using ENSO as a predictor in forecasting rainfall over a given region of India may be appropriate only during certain sub-seasons. For example, rainfall in Rajasthan during the full season (Figure 2.3a) is correlated to Pacific SSTs, but accounts for most of the correlated rainfall during the peak and late sub-seasons only. Second, many of the regions highlighted as having rainfall correlated to Pacific SSTs are agriculturally productive (e.g. Andhra Pradesh, Gujarat, Karnataka, Kerala, Madhya Pradesh, Maharashtra, Punjab, Rajasthan, Tamil Nadu, Telangana, Uttar Pradesh, and West Bengal, see Fig. 2.4 for a state map) and thereby rely on a strong monsoon each year for good crop yield. Using the SMA regression slopes, we calculate that a June-September average decrease of 1°C in the NINO3.4 index leads to a 20-60% increase in full season (June-September) average monsoon rainfall over many agricultural regions (Figure 2.4a). To refine this relationship, we show how a 1°C cooling of the NINO3.4 region

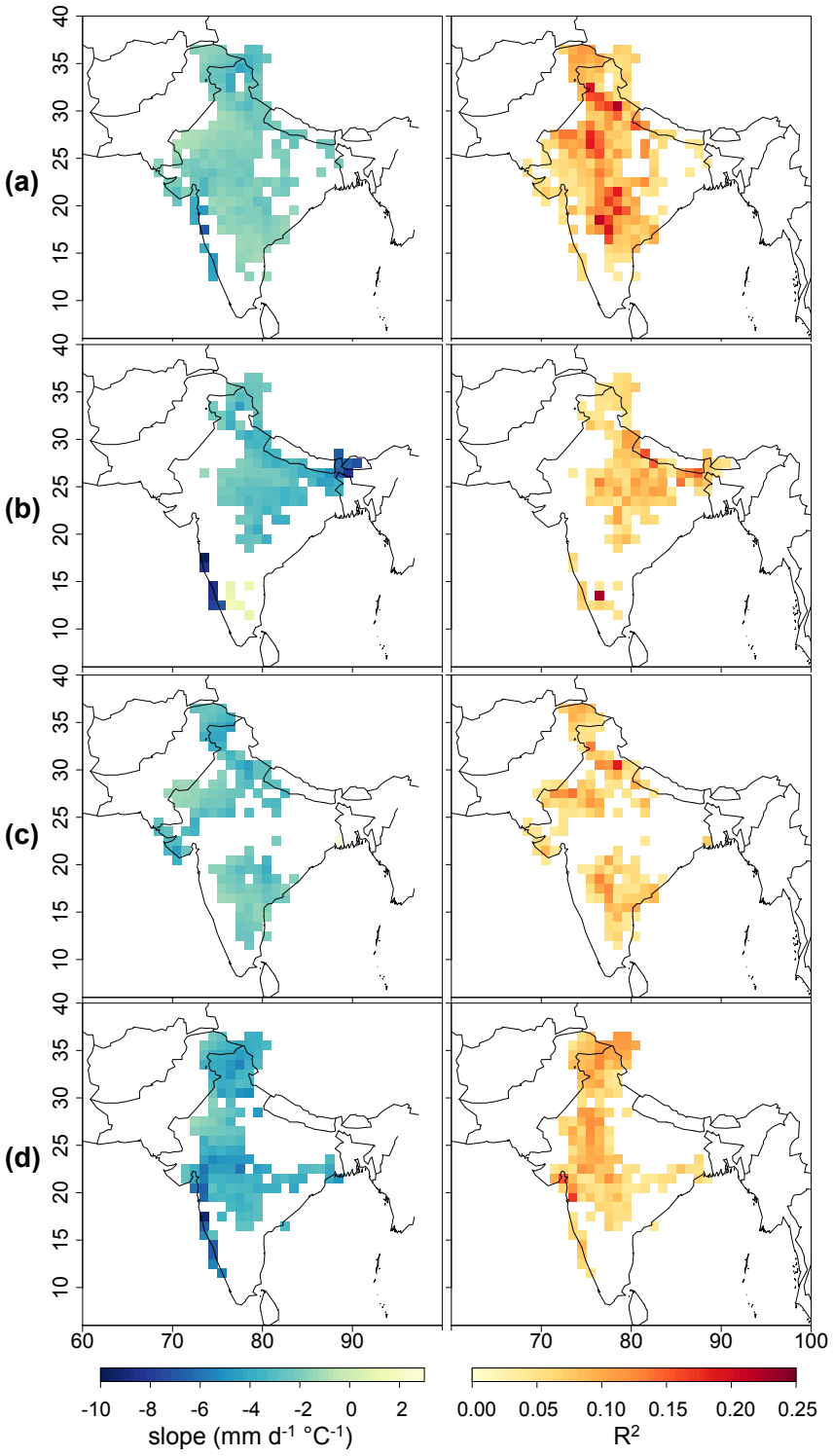

Figure 2.3: Slopes of SMA regression between average daily rainfall (*Rajeevan et al.*, 2006) and NINO3.4 SSTs from 1901-2009 (*Kaplan et al.*, 1998) for the full (a - June to September), early (b - June), middle (c - July and August), and late (d - September) seasons. The first and second columns show the slopes (mm d^{-1} $^{\circ}C^{-1}$) and R^2 values of the SMA regressions, respectively. Colored regions show values at least 95% significant.

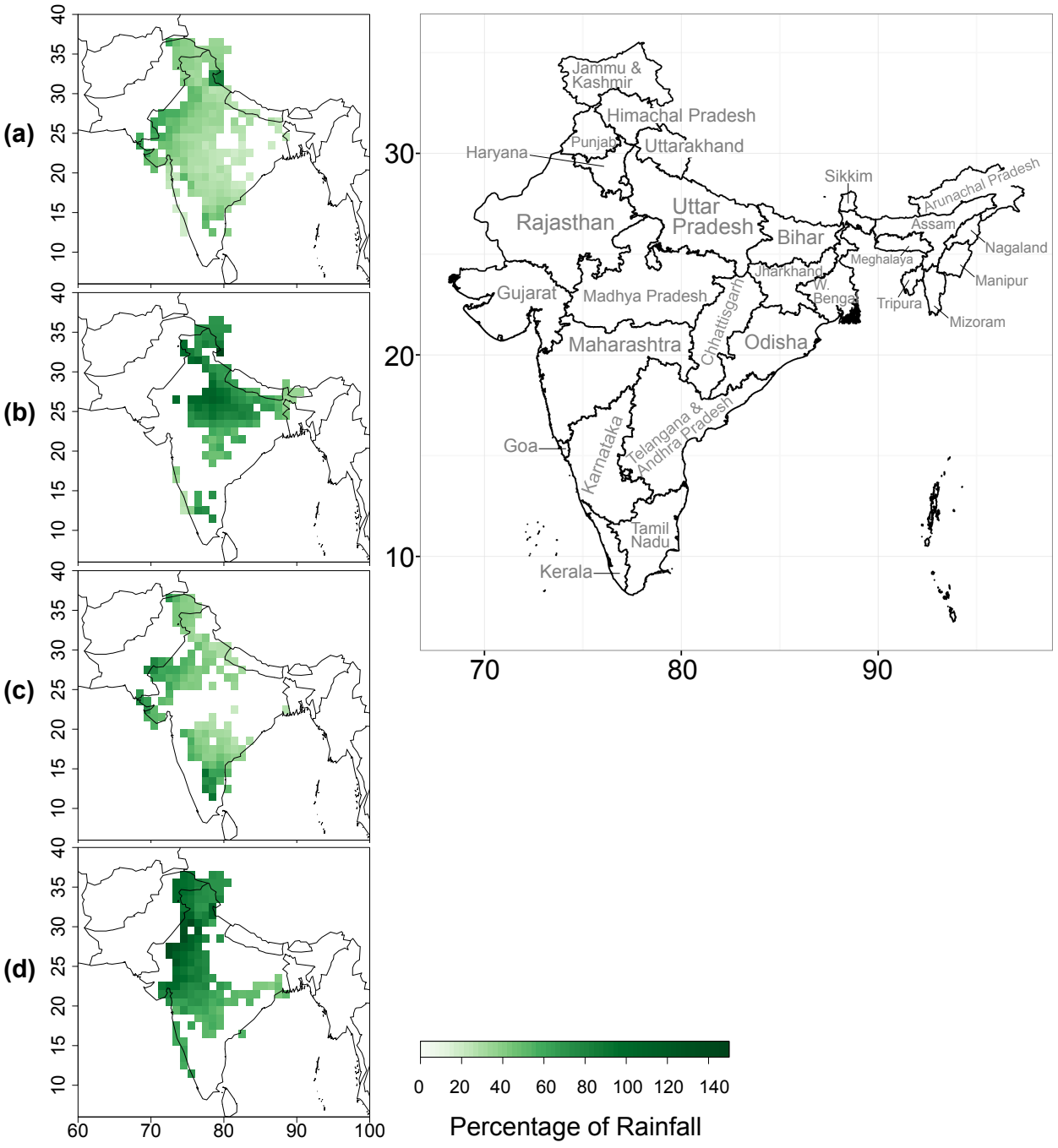

Figure 2.4: Percentage rainfall due to a 1°C cooling of the NINO3.4 index during the (a) full, (b) early, (c) middle and (d) late seasons. Colored regions show values at least 95% significant. Also included is a map of current states and territories of India to facilitate discussion of regions highlighted in sub-plots a-d.

would affect rainfall in the differing seasons. First, early season rainfall in the Indo-Gangetic Plains, which occupy the states of Punjab, Haryana, Uttarakhand, Uttar Pradesh, and Bihar, as well as parts of Madhya Pradesh and Chhattisgarh (Figure 2.4b) would increase by 70-100%. Second, peak season rainfall would increase by 30-80% throughout Rajasthan and the Godavari River basin, which includes parts of Maharashtra, Andhra Pradesh, and Karnataka (Figure 2.4c). Third, late season rainfall in central India as well as Punjab, Rajasthan, Madhya Pradesh, Maharashtra, and Telangana would increase by 60-100% (Figure 2.4d). These results suggest that forecasts, particularly for agricultural regions that depend on skillful prediction of the monsoon, could be more useful if they were issued sub-seasonally and considered smaller regions of India rather than the entire country or political districts.

2.4 Asymmetries between La Niña and El Niño teleconnections

Using the average gridded daily 1901-2009 precipitation data of *Rajeevan et al.* (2006) we produced composite rainfall maps of standardized anomalies for strong La Niña and strong El Niño years for the full monsoon season (Figure 2.5a) and the three sub-seasons (Figure 2.5b-d). Strong La Niña and El Niño years for each period are defined as those for which the standardized SST anomalies from the NINO3.4 index were $\leq$ -0.75 and $\geq$ +0.75, respectively, during the respective periods of the monsoon season (years used in each are provided in a Table 2.1). In this method, the subset of years differs for each sub-seasonal composite map. For example, La Niña conditions might characterize the early, but not late season. Because the monsoon responds dynamically to the evolving ENSO conditions and teleconnections are rapid, it is important to consider warming or cooling events during each sub-season separately, regardless of whether they persist for the entire season or not. As an example, consider ENSO conditions of 2014. A strong El Niño event was forecasted for the summer, which was expected to suppress the Indian monsoon. Consistent with these predictions, June NINO3.4 anomalies were + 0.8°C and monsoon rains were delayed and weak. In July and August, however, warming dissipated to +0.3°C and +0.2°C, respectively, and monsoon

rains returned to make up a substantial part of the deficit. The season as a whole ended with a rainfall deficit (-12.5%), which is slightly below the -10% threshold used by Indian Meteorological Department (IMD) to categorize as deficit monsoon year. Furthermore, the seasonal rainfall deficit was much lower than the initial forecast of drought, owing in large measure to the evolving monsoon-ENSO teleconnection within the season. Moreover, 2014 was not exceptional, for there have been several such years in recent history. It should also be noted that we do not explicitly consider "modoki" events. If we considered modoki versus non-modoki events, as well as sub-seasonal differences, we would be forced to split our subset of years into smaller samples. To avoid this, we count +0.75°C anomalies in the NINO3.4 region as strong El Niño seasons, regardless of whether it is modoki or not. We also do not consider the state of the Indian Ocean Dipole (IOD) in selection of La Niña or El Niño years (see Appendix A for an explanation).

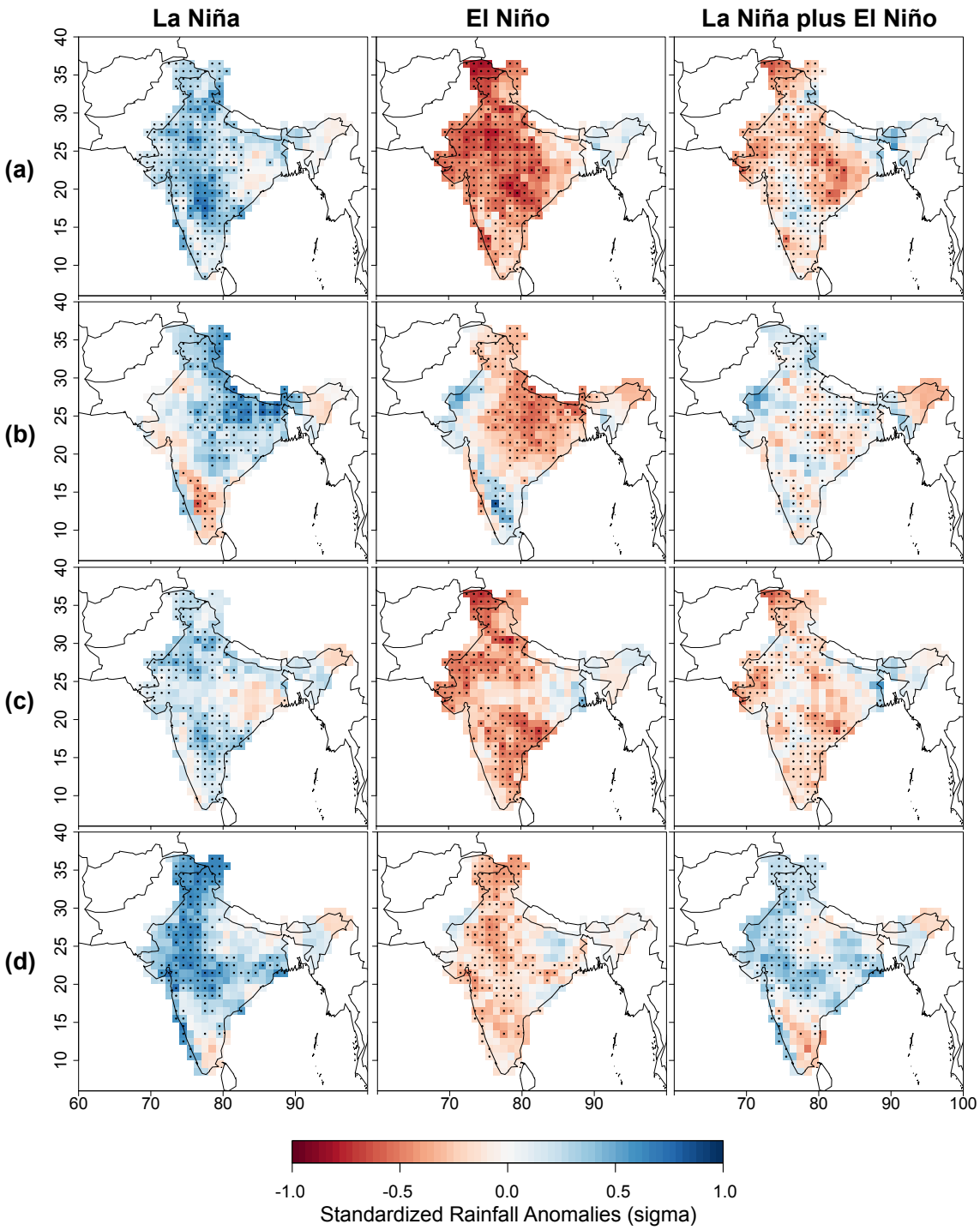

Figure 2.5: Composite maps of standardized anomalies of rainfall This figure uses *Rajeevan et al.* (2006) rainfall to plot the composite of standardized anomalies during strong La Niña (scaled NINO3.4 $\leq$ -0.75) and strong El Niño (scaled NINO3.4 $\geq$ 0.75) conditions for during the (a) full, (b) early, (c) middle and (d) late seasons. The third column provides the sum of the first two columns. Linear trends over the entire 109-year period have been removed from each grid cell. Stippling indicates regions where mean rainfall anomalies between La Niña and El Niño are significantly different by at least 95%. Table 2.1 provides the years used in the composites for La Niña and El Niño.

Table 2.1: Years classified as La Niña or El Niño according to NINO3.4 index for each season from 1901-2009.

Season Definition	**Mean (°C)**	**SD (°C)**	**La Niña Years**	**El Niño Years**
Full (Jun-Sep)	0.15	0.62	1908, 1910, 1916, 1924, 1933, 1938, 1942, 1945, 1949, 1950, 1954, 1955, 1956, 1959, 1964, 1970, 1971, 1973, 1974, 1975, 1978, 1981, 1988, 1989, 1998, 1999	1902, 1905, 1914, 1915, 1918, 1920, 1930, 1940, 1941, 1957, 1963, 1965, 1972, 1982, 1987, 1991, 1993, 1997, 2002, 2004, 2009
Early (Jun)	0.19	0.59	1908, 1909, 1910, 1916, 1933, 1938, 1949, 1950, 1952, 1955, 1956, 1964, 1971, 1973, 1974, 1975, 1978, 1984, 1985, 1988, 1989, 1999, 2000	1902, 1905, 1907, 1914, 1915, 1920, 1931, 1940, 1941, 1961, 1965, 1972, 1977, 1982, 1983, 1987, 1991, 1992, 1993, 1997, 2002, 2005, 2009
Middle (Jul-Aug)	0.14	0.63	1908, 1910, 1916, 1922, 1933, 1938, 1942, 1945, 1950, 1954, 1955, 1956, 1959, 1964, 1970, 1971, 1973, 1974, 1975, 1978, 1981, 1988, 1989, 1998, 1999	1902, 1905, 1914, 1915, 1918, 1920, 1923, 1926, 1930, 1940, 1941, 1957, 1963, 1965, 1972, 1982, 1987, 1991, 1997, 2002, 2004, 2009
Late (Sep)	0.12	0.73	1909, 1910, 1916, 1917, 1924, 1933, 1938, 1942, 1944, 1945, 1950, 1954, 1955, 1956, 1959, 1961, 1964, 1967, 1970, 1971, 1973, 1975, 1988, 1998, 1999, 2007	1902, 1905, 1914, 1918, 1923, 1930, 1941, 1951, 1953, 1963, 1965, 1969, 1972, 1976, 1982, 1986, 1987, 1991, 1994, 1997, 2002, 2004, 2006, 2009

A year classified as an "early season La Niña" is one in which the June NINO3.4 SST anomaly was $\leq$ -0.75. A "peak season El Niño" is one in which the July-Aug average NINO3.4 SST anomaly was $\geq$ +0.75. This accounts for years when La Niña or El Niño conditions did not persist for the full monsoon season.

As expected, strong La Niña (El Niño) conditions typically result in positive (negative) rainfall anomalies. In general, the spatial distribution of rainfall anomalies between the cold and warm phases of ENSO are opposite in their signs, in that regions of India that see positive rainfall anomalies during La Niña tend to see negative anomalies during El Niño. Asymmetries in the monsoon-ENSO teleconnection, however, are apparent in the magnitudes of positive and negative anomalies between La Niña and El Niño (Figure 2.5, left and middle column), respectively. To illustrate this asymmetry, we sum anomalies associated with La Niña composites and anomalies associated with El Niño composites (Figure 2.5, right column). During the full season (Figure 2.5a), the negative rainfall anomalies in the summation composite reveal that El Niño suppresses rainfall more than La Niña enhances it, which also characterizes northwest and south-central India during the peak season (Figure 2.5c). The opposite, however, holds during the late season (Figure 2.5d): La Niña enhances rainfall more than El Niño suppresses it.

Composites SST anomalies of strong La Niña years and strong El Niño years for each sub-season reveal that the patterns in SSTs compared across the two modes are generally symmetric in the eastern equatorial Pacific and to some extent in the central Pacific, with cooling (warming) of the eastern equatorial Pacific during La Niña (El Niño) events. This is associated with warming (cooling) of the west Pacific and cooling (warming) in the Indian Ocean (Figure 2.6), but the patterns are not symmetric. Furthermore, warming during El Niño seasons, exceeds one standard deviation in some parts of the eastern equatorial Pacific, which is greater in magnitude than the cooling associated with La Niña.

During the full monsoon season and all three sub-seasons, low (high) pressure anomalies during La Niña (El Niño) suggest convergence and ascent (divergence and subsidence) across much, but not all of India, which are consistent with more (less) precipitation. This is demonstrated by the similarity of the difference in geopotential height anomalies (Figure 2.7, third column) with the difference in rainfall anomalies (Figure 2.7, fourth column) between La Niña and El Niño. During the early season, the biggest difference in pressure between the

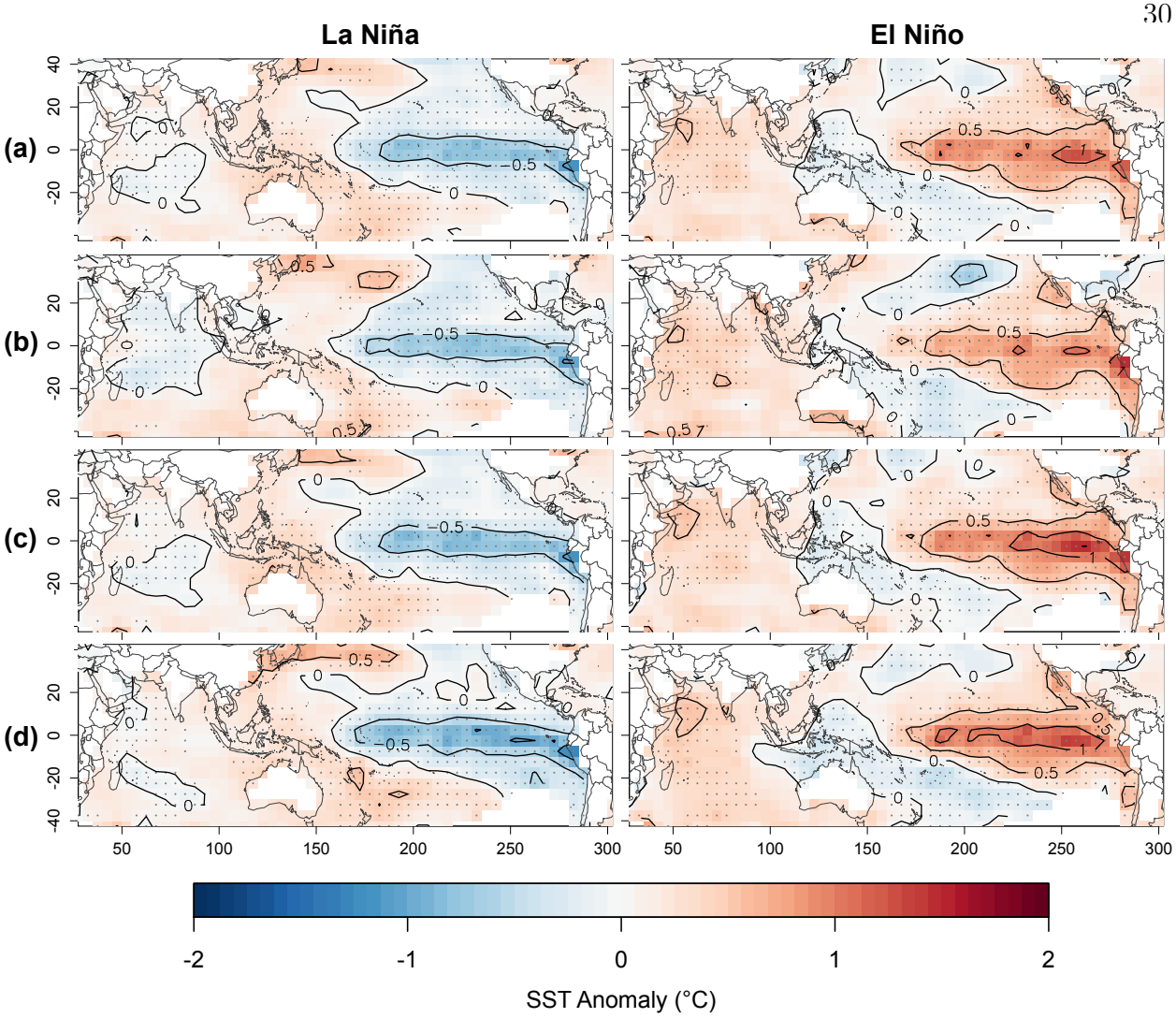

Figure 2.6: Composites maps of SST anomalies (*Kaplan et al.*, 1998) in the Indo-Pacific region for strong La Niña years (left column) and strong El Niño years (right column) for the (a) full, (b) early, (c) middle and (d) late seasons. Stippling indicates regions where mean SST anomalies between La Niña and El Niño are significantly different by at least 95%. Table 2.1 provides the years used in the composites for La Niña and El Niño.

two ENSO modes occurs in north-central India and the Indo-Gangetic Plains (Figure 2.7b, third column), which are the same regions that see the biggest difference in rainfall (Figure 2.7b, fourth column). During the middle (peak) season, significant differences in pressure are limited to south-central India and along its west coast (Figure 2.7c, third column), and they align with parts of India that have the biggest difference in rainfall (Figure 2.7c, fourth

column). The late season has the largest pressure anomalies of the three sub-seasons, with large low (Figure 2.7d, first column) and high (Figure 2.7d, second column) pressure systems concentrated in the west-central part of India, but significant differences between La Niña and El Niño spanning the entire country (Figure 2.7d, third column). We suspect that pressure anomalies are greatest during September, because ENSO is firmly developed at that time compared to early and peak season.

Composite analyses for the total atmospheric water vapor available in a column of air (Figure 2.8) and 850 mb wind anomalies reveal positive (negative) precipitable water anomalies during La Niña (El Niño). This pattern is consistent with the pressure anomaly composites in Figure 2.7, in that we would expect greater precipitable water over regions of low pressure where convergence and ascent of moist air should occur. During early-season La Niñas, high pressure off the southern tip of India is geostrophically balanced in part by southwesterly winds from over the Indian Ocean onto the Indian subcontinent, which deliver moisture to north-central India and the Indo-Gangetic Plains. The opposite pattern occurs during El Niños. During middle-season La Niñas, winds from the Bay of Bengal are strongest which presumably helps to deliver rain to northwest Rajasthan (*Joseph*, 2012). In the late season, cyclonic and anti-cyclonic wind patterns for La Niña and El Niño, respectively, are consistent with the large low- and high-pressure systems that form over west-central India.

To understand large-scale climate features that accompany this SST distribution and the associated rainfall signature, we composite 200 mb and 925 mb velocity potential anomalies (Figures 2.9 and 2.10, respectively) as a surrogate for regional convergence and divergence both aloft and at the surface during strong La Niña and strong El Niño seasons. Because ageostrophic winds vary with the horizontal gradient of velocity potential, to a first approximation positive (negative) velocity potential represents convergence (divergence) and presumably descent (ascent). Perhaps not surprisingly, positive (negative) anomalies at 200 mb overlie regions with negative (positive) anomalies at 925 mb. At 200 mb, across all four seasons, cooler SSTs in the central and eastern Pacific during La Niña are accompanied by

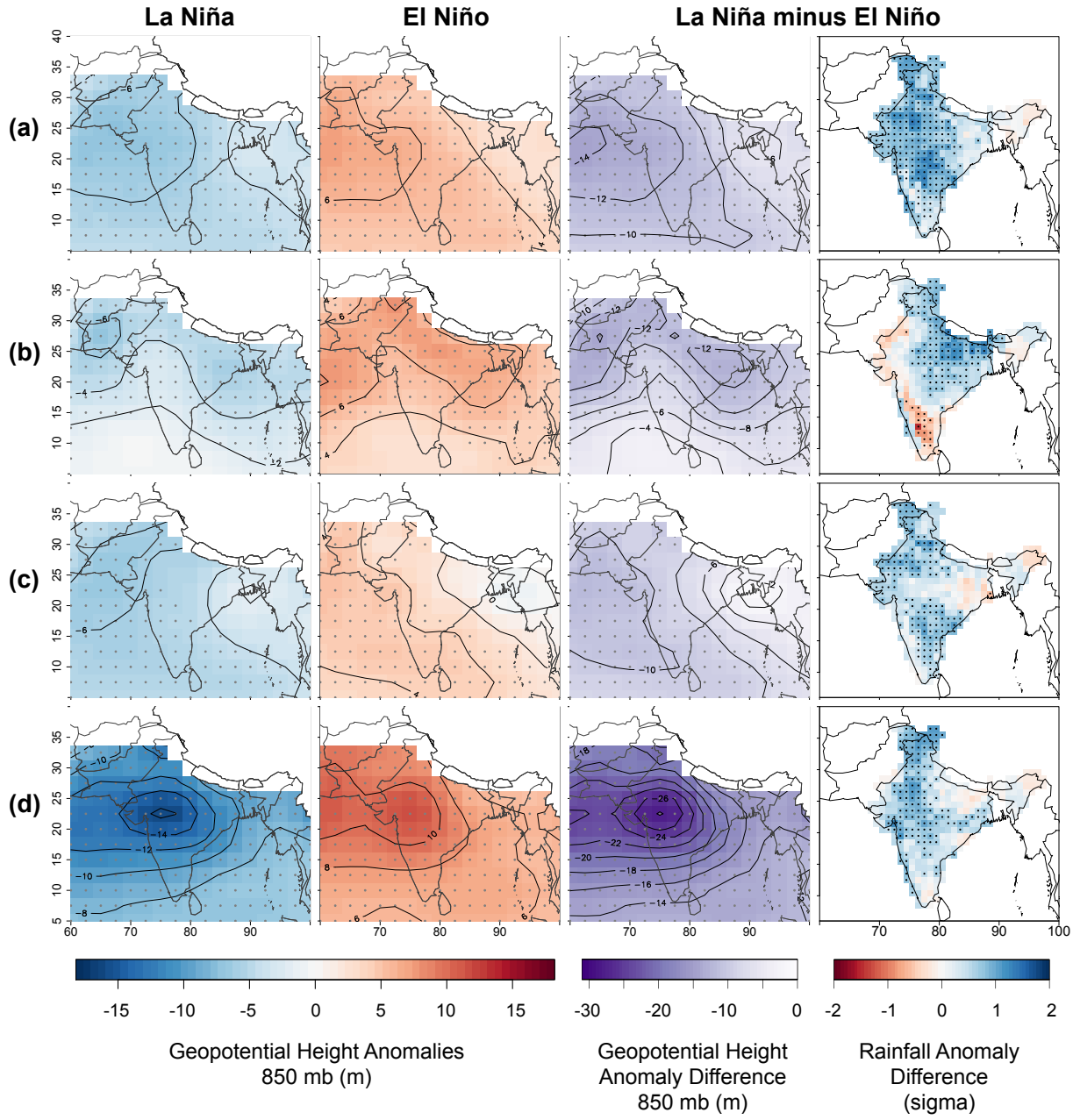

Figure 2.7: Composite maps of 850 mb geopotential height anomalies and 850 mb wind anomalies from the NCEP-NCAR Reanalysis (*Kalnay et al.*, 1996) for strong La Niña years (first column), strong El Niño years (second column) and the difference between the two (third column) for the (a) full, (b) early, (c) middle and (d) late seasons. Contours are plotted at an interval of two meters. The fourth column provides the difference in mean rainfall anomalies between La Niña and El Niño years for the four seasons. Stippling indicates regions where mean rainfall anomalies between La Niña and El Niño are significantly different by at least 95%. Table 2.1 provides the years used in the composites for La Niña and El Niño. Areas that lie above the 850 mb level have been omitted from shading.

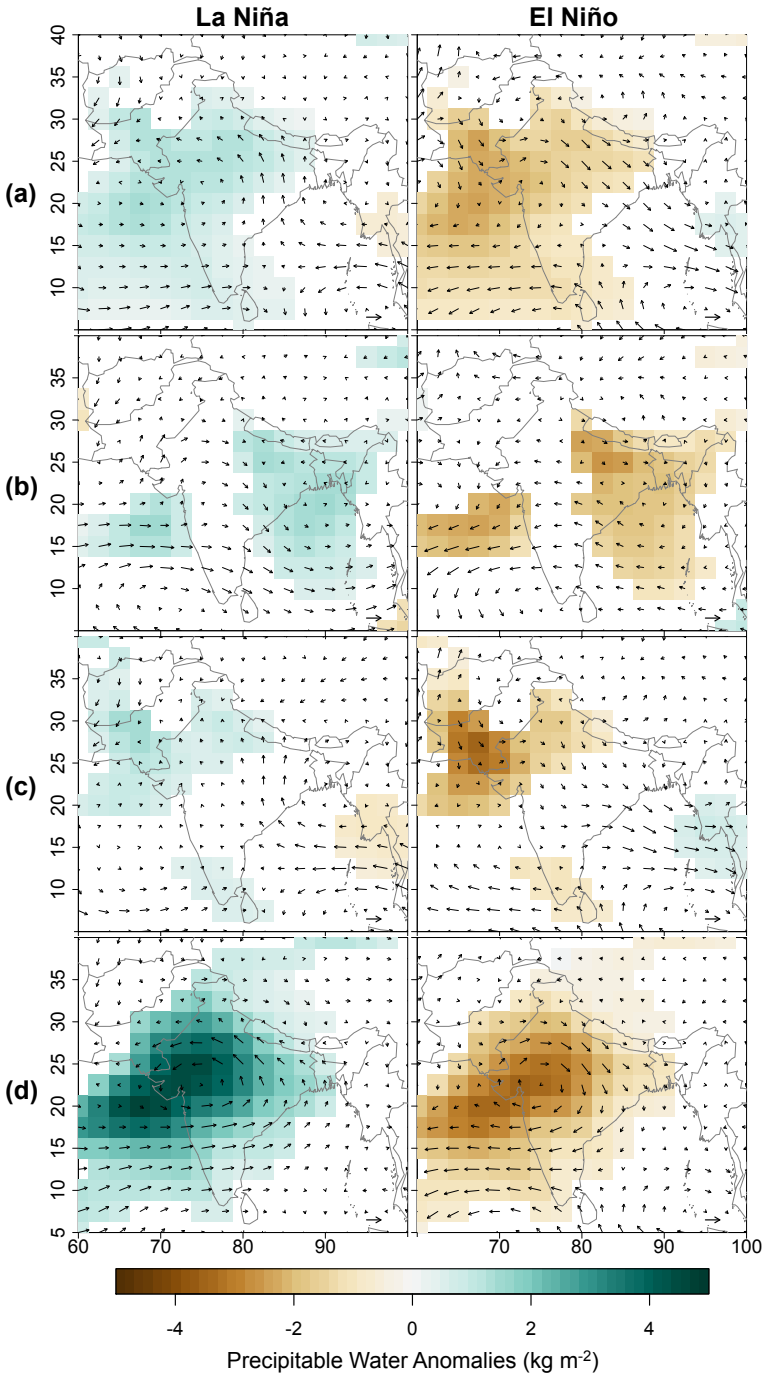

Figure 2.8: Composites of precipitable water anomalies and 850 mb wind anomaly from the NCEP-NCAR Reanalysis (*Kalnay et al.*, 1996) for strong La Niña years (left column) and strong El Niño years (right column) for the full (a - June to September), early (b - June), middle (c - July and August), and late (d - September). Shading is provided where the mean precipitable water anomalies between La Niña and El Niño were significantly different by at least 95%. Bold arrow at bottom-right of each sub-plot scales to 1 m s^{-1}. Table 2.1 provides the years used in the composites for La Niña and El Niño.

negative velocity potential anomalies aloft over the Indian Ocean region, and positive anomalies over the eastern equatorial Pacific, which strengthen as the monsoon season progresses. The opposite characterizes El Niño seasons. Note, however, that during El Niño seasons, maximum velocity potential anomalies aloft the tropical Pacific occur during the middle season instead of the late season. The opposite signs of velocity potential anomalies aloft and near the surface concur with the simple interpretation that such pairs reflect anomalies in ascent or descent through the troposphere.

As we would expect under the shifted Walker Circulation hypothesis (*Shukla and Wallace*, 1983; *Palmer et al.*, 1992), a zone of ascent (descent) overlies the south-Asian and Indian region during all four La Niña (El Niño) seasons. Note, however, the zone of positive (negative) velocity potential anomalies over the western equatorial Indian Ocean during early season of La Niña (El Niño) that does not exist in any of the other seasons. This is consistent with the hypothesis that during the early season, a shifted Walker Circulation affects the local Hadley cell (*Goswami*, 1998; *Ju and Slingo*, 1995; *Lau and Wu*, 2001; *Slingo and Annamalai*, 2000), such that during the early season of El Niño, the ascending branch of the Hadley cell is located at the equator, as suggested by regions of divergence at 200 mb (Figure 2.9b, right) and convergence at 925 mb (Figure 2.10b, right). This anomalous ascent on the equator results in anomalous subsidence over the Indian subcontinent. By contrast, during the early season of La Niña, negative velocity potential anomalies overlie the Indian subcontinent while the descending branch over the western equatorial Indian Ocean is strengthened, as shown by regions of convergence at 200 mb (Figure 2.9b, right) and divergence at 925 mb (Figure 2.10b, right). Patterns consistent with local Hadley cell modulation disappear throughout the remainder of the season, suggesting a larger-scale mechanism, such as a strengthened and shifted Walker circulation, is responsible for the rainfall signature during the middle and late seasons.

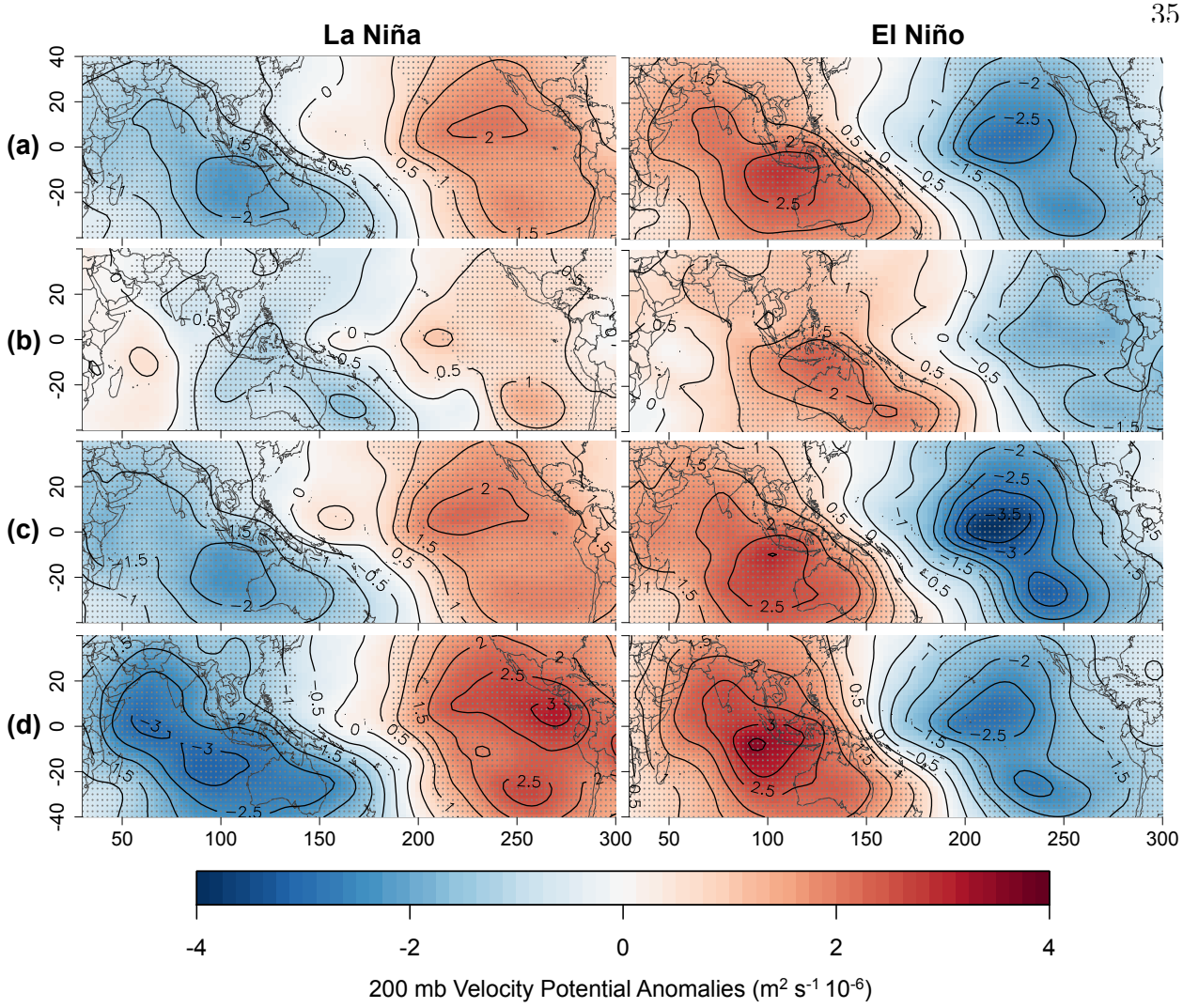

Figure 2.9: Composites maps of 200 mb velocity potential (m^2 s^{-1} 10^{-6}) anomalies from NCEP-NCAR Reanalysis (*Kalnay et al.*, 1996) for strong La Niña years (left column) and strong El Niño years (right column) for the (a) full, (b) early, (c) middle and (d) late seasons. Stippling indicates regions where mean rainfall between La Niña and El Niño are significantly different by at least 95%. Table 2.1 provides the years used in the composites for La Niña and El Niño.

2.5 Discussion

The monsoon-ENSO teleconnection varies throughout the summer season over India (Figure 2.3a). This finding, while consistent with previous studies that have looked at regional differences (*Cash et al.*, 2015; *Kane*, 2000; *Krishnamurthy and Shukla*, 2000;

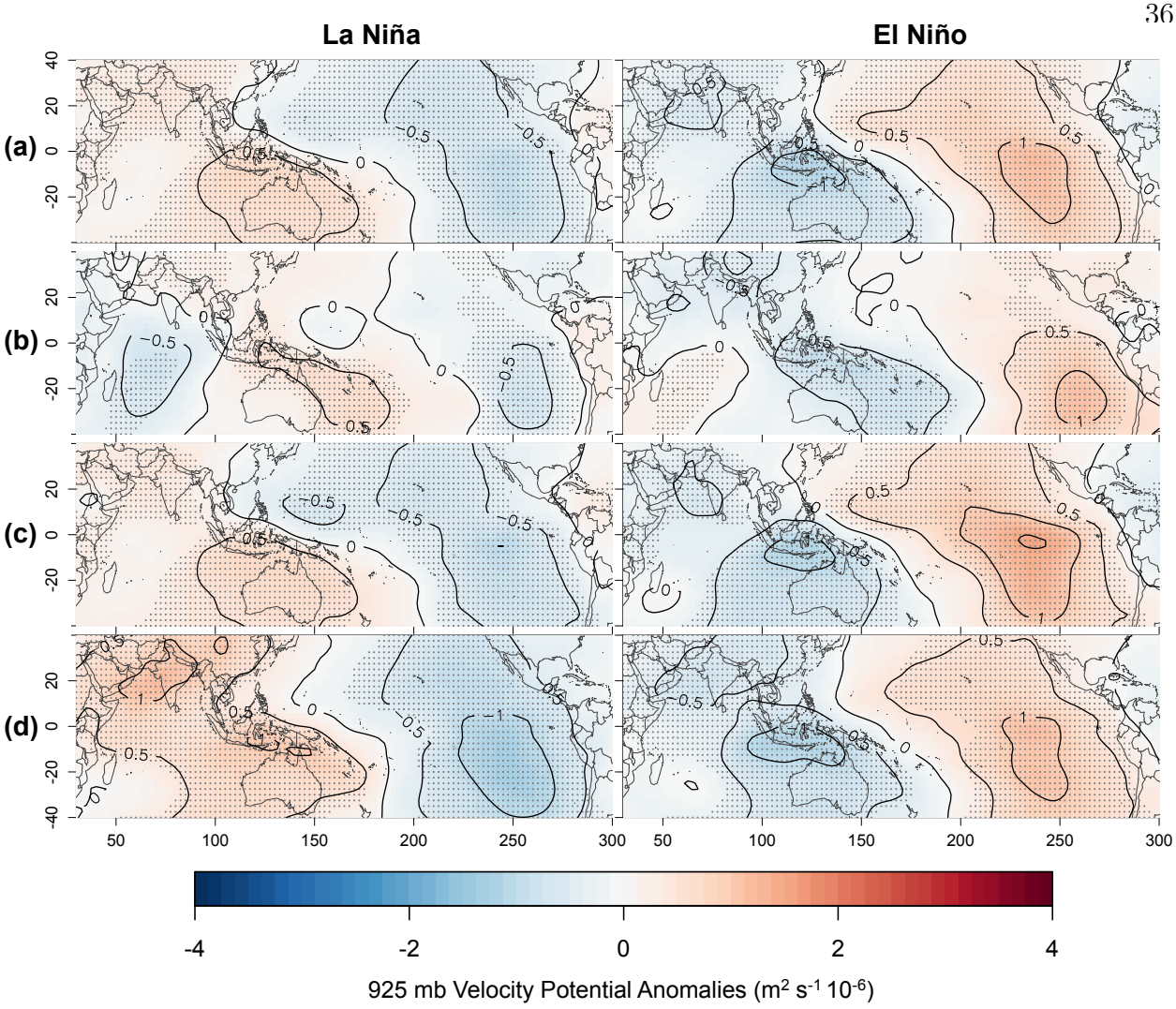

Figure 2.10: Same as Figure 2.9 but for 925 mb velocity potential (m^2 s^{-1} 10^{-6}) anomalies.

Parthasarathy et al., 1996; *Singh*, 2001), provides insights into the spatial signature of the monsoon-ENSO teleconnection on a finer spatial scale and over a longer time period than done before. We find that as the season progresses through early (June), peak (July-August) and late (September) sub-seasons, ENSO's spatial signature shifts (Figure 2.3b-d). Consequently, the correlations of different region's rainfall to Pacific SSTs evolve differently throughout the monsoon season. Rainfall over northwestern India is sensitive to NINO3.4 SSTs during the peak and late season, but not the early season. Rainfall over most of the

Indo-Gangetic Plains and west-central India is sensitive to SSTs only during the early and late seasons, respectively. Parts of northern India remain sensitive throughout the entire season. These differences emphasize the importance of examining the monsoon on a sub-seasonal timescale, which has been acknowledged in other recent studies (*Singh et al.*, 2014; *Pattanaik*, 2012; *Rajagopalan and Molnar*, 2014).

The spatial and temporal differences in rainfall over India also highlight the inherent asymmetry in the monsoon-ENSO teleconnection: La Niña and El Niño rainfall composites are not equal and opposite across all of India (Figure 2.5). Although this asymmetry has been cited before in regards to AISMR data during the entire monsoon season (*Krishna Kumar et al.*, 2006), we show that the asymmetry varies spatially across India, and that it evolves through the monsoon season. For example, El Niño conditions suppress rainfall more during the peak season than La Niña enhances it, but La Niña seems to enhance rainfall more during the late season than El Niño suppresses it. We infer that during the peak monsoon season, when conditions are favorable for rainfall, La Niña must be very strong in order to enhance rainfall. On the other hand, even a modest El Niño, which counters the climatological conditions, can effect a conspicuous reduction in rainfall. These sub-seasonal differences suggest a regionally important nuance in the use of ENSO forecasts applied to monsoon rainfall.

Composites of velocity potential at 200 and 925 mb show an anomaly over the western Indian Ocean, south of India consistent with local Hadley cell modulation in the early season that ceases to exist during the middle and late season (*Goswami*, 1998; *Lau and Wu*, 2001; *Slingo and Annamalai*, 2000). *Ju and Slingo* (1995), in particular, recognized that this role of a local Hadley cell occurs only in the early season. We presume that as SST anomalies intensify in the central and eastern Pacific towards the end of the monsoon season, the strengthening anomalous Walker circulation writes a stronger signature on the monsoon rainfall than the local Hadley circulation does.

The following suggestions emerge from this research that might improve monsoon fore-

cast skills of socio-economic benefit: (i) AISMR forecast is of limited utility especially in light of declining ENSO teleconnections (e.g. *Krishna Kumar et al.*, 1999); (ii) sub-seasonal forecast of spatial regions with strong ENSO teleconnections appears to be promising avenue for increasing forecast skill; and (iii) forecasting strategies should be different for El Niño and La Niña events and should incorporate the distinct circulation features associated with them, including Indian Ocean temperatures.

Chapter 3

Multi-Proxy Reconstruction of Equatorial Pacific SST and Zonal Wind Fields of the past 10,000 years using Mg/Ca and Alkenone Records

Abstract

A multi-proxy, reduced-dimension methodology blends magnesium-calcium (Mg/Ca) and alkenone ($U_{37}^{k'}$) paleo sea surface temperature (SST) records from the eastern and western equatorial Pacific, to recreate snapshots of full field SSTs and zonal winds from 10 to 2 ka BP in two-thousand year increments. In the multi-proxy reconstruction, the coldest SST anomalies of $\sim$ -1°C occur at 10 ka in the eastern equatorial Pacific with concurrent easterly maximum wind anomalies of $\sim$ 8 m s^{-1} throughout the central Pacific. The largest zonal temperature anomaly differences (average east Pacific SST minus average west Pacific SST) are -0.36°C and -0.33°C, which occur at 6 and 10 ka, respectively. The eastern equatorial Pacific warms and central Pacific easterly winds weaken gradually from 10 to 2 ka, but western Pacific SSTs fluctuate throughout the period. Although both Mg/Ca and $U_{37}^{k'}$ act as SST proxies, comparisons of the single proxy SST field reconstructions (Mg/Ca-only versus $U_{37}^{k'}$-only) reveal differences in the timing and duration of maximum cooling across the equatorial Pacific. Due to this, the multi-proxy approach is beneficial in revealing the common patterns of variability between the two different SST proxies.

3.1 Background

Paleoclimatic proxy records spanning the early- to mid-Holocene ($\sim$ 10-6 thousand years ago, ka) suggest that the equatorial Pacific was in an "enhanced La Niña-like state" during this time, consistent with reduced El Niño - Southern Oscillation (ENSO) variability due to a cooler eastern (e.g. *Koutavas et al.*, 2006) and perhaps a slightly warmer western (e.g. *Stott et al.*, 2004) Pacific. Not all paleo records show reduced ENSO variability *Cobb et al.* (2013), and those that do tend to disagree on timing and duration. Clastic sediment records from lakes in the Andes (*Moy et al.*, 2002; *Rodbell et al.*, 1999) and marine records (*Koutavas et al.*, 2006; *Tudhope et al.*, 2001) show reduced ENSO variability around 6 ka, which agrees with GCM simulations (*Liu et al.*, 2000; *Otto-Bliesner et al.*, 2003; *Timmermann et al.*, 2007; *Zheng et al.*, 2008) and has been theorized to be tied to orbital forcing (*Clement et al.*, 1999; *Luan et al.*, 2012; *Zheng et al.*, 2008). From pollen, *Shulmeister and Lees* (1995) inferred a drying of Australia at $\sim$ 4 ka, which they attributed to an onset of modern-like ENSO conditions. Other more recent marine records (*Carré et al.*, 2014; *McGregor et al.*, 2013) have challenged the timing of these results and suggest that ENSO variability was at its lowest around 4-5 ka.

Paleoclimatic proxy data are intrinsically point measurements, and therefore associating one paleoclimate time series with a process that reaches over a huge area takes a risk. Moreover, because of dissolution of carbonate tests and low sedimentation rates at great depth, useful cores for SSTs proxy records (Tables 3.1 and 3.2, Figures 3.1 and 3.2) are commonly limited to regions of relatively shallow depth, near coasts, from aseismic ridges, or over young oceanic crust. As a result, the absence of long-term records from the central Pacific makes it difficult to draw conclusions about large-scale spatial patterns of ENSO-relevant SST fields over paleoclimatic timescales. The records that exist along the ocean margins are often irregularly sampled (spatially and temporally), and different proxies from the same core can sometimes yield contradictory inferences. With these limitations in mind, we use

all available SST information at various points from the east and west Pacific in order to reconstruct the full field of tropical Pacific SSTs and zonal winds (10°S to 10°N and 100°E to 60°W) over the past 10 ka.

Table 3.1: A list of the Mg/Ca-based proxy records from the western and eastern equatorial Pacific used in the SST and zonal wind reconstruction

Record #	**Core**	**Lat**	**Lon**	**Calibration**	**Reference**
Western Equatorial Pacific (Figure 3.1, left)					
1	MD98 - 2176	-5.00	133.45	*Nürnberg et al.* (1996)	*Stott et al.* (2004)
2	MD98 - 2181	6.30	125.83	*Nürnberg et al.* (1996)	*Stott et al.* (2004)
3	MD98 - 2162	-4.69	117.90	*Hastings et al.* (2001)	*Visser et al.* (2003)
4	MD01 - 2390	6.64	113.41	*Dekens et al.* (2002)	*Steinke et al.* (2008)
5	MD97 - 2141	8.80	121.30	*Rosenthal and Lohmann* (2002)	*Rosenthal et al.* (2003)
6	MD97 - 2138 *	1.25	146.14	*de Garidel-Thoron et al.* (2005)	*de Garidel-Thoron et al.* (2007)
7	ODP - 806b	0.32	159.35	*Lea and Martin* (1996)	*Lea et al.* (2000)
8	MD98 - 2165	-9.65	118.34	*Dekens et al.* (2002)	*Levi et al.* (2007)
9	MD98 - 2170	-10.59	125.39	*Nürnberg et al.* (1996)	*Stott et al.* (2004)
10	MD06 - 3067	6.51	126.50	*Anand et al.* (2003)	*Bolliet et al.* (2011)
Eastern Equatorial Pacific (Figure 3.1, right)					
11	ODP - 1242	7.86	-83.61	*Anand et al.* (2003)	*Benway et al.* (2006)
12	TR163 - 22	0.52	-92.40	*Dekens et al.* (2002)	*Lea et al.* (2006)
13	ODP - 1240	0.02	-86.45	*Dekens et al.* (2002)	*Pena et al.* (2008)
14	V21 - 30 *	-1.22	-89.68	*Dekens et al.* (2002)	*Koutavas et al.* (2006)
15	V19 - 28 *	-2.51	-84.65	*Dekens et al.* (2002)	*Koutavas et al.* (2006)

* Asteriks denote records that have both Mg/Ca and $U^{k'}_{37}$ SST records.

Table 3.2: A list of the $U_{37}^{k'}$-based proxy records from the western and eastern equatorial Pacific used in the SST and zonal wind reconstruction.

Record #	**Core**	**Lat**	**Lon**	**Calibration**	**Reference**
Western Equatorial Pacific (Figure 3.2, left)					
16	SO139 - 74KL	-6.54	103.83	*Conte et al.* (2006)	*Lückge et al.* (2009)
17	GIK 17964	6.16	112.21	*Müller et al.* (1998)	*Pelejero et al.* (1999)
18	GIK 18252-3	9.23	109.38	*Pelejero and Grimalt* (1997)	*Kienast et al.* (2001)
19	GIK 18287-3	5.65	110.65	*Pelejero and Grimalt* (1997)	*Kienast et al.* (2001)
20	MD97 - 2151	8.72	109.87	*Pelejero and Grimalt* (1997)	*Zhao et al.* (2006)
21	MD97 - 2138 *	1.25	146.14	*Prahl et al.* (1988)	*de Garidel-Thoron et al.* (2007)
Eastern Equatorial Pacific (Figure 3.2, right)					
22	MD02 - 2529	8.21	-84.12	*Sonzogni et al.* (1997)	*Leduc et al.* (2007)
23	KNR176 - JPC32	4.85	-77.96	*Prahl et al.* (1988)	*Pahnke et al.* (2007)
24	V19 - 27	-0.47	-82.67	*Prahl et al.* (1988)	*Koutavas and Sachs* (2008)
25	ME0005A - 24JC	1.50	-89.68	*Prahl et al.* (1988)	*Kienast et al.* (2006)
26	V21 - 30 *	-1.22	-89.68	*Prahl et al.* (1988)	*Koutavas and Sachs* (2008)
27	V19 - 30	-3.38	-83.52	*Prahl et al.* (1988)	*Koutavas and Sachs* (2008)
28	RC11 - 238	-1.52	-85.82	*Prahl et al.* (1988)	*Koutavas and Sachs* (2008)
29	V19 - 28 *	-2.51	-84.65	*Prahl et al.* (1988)	*Koutavas and Sachs* (2008)

* Asteriks denote records that have both Mg/Ca and $U_{37}^{k'}$ SST records.

Previous studies have used paleo-proxy data with various statistical approaches to reconstruct full fields (e.g. *Cook et al.*, 1999; *Kaplan et al.*, 1998; *Luterbacher et al.*, 2004; *Mann et al.*, 1998, 2008; *Tingley and Huybers*, 2010) or time-series (e.g. *Kaufman et al.*, 2009; *Lee et al.*, 2008; *Li et al.*, 2010; *Mann et al.*, 2008; *Moberg et al.*, 2005) of climate variables. We use reduced-dimension reconstruction approaches, in which contemporary patterns of variability are related to a sparse sampling of points to resolve full fields or time-series of climate variables. Reduced-dimension approaches have been used to reconstruct surface temperature (e.g. *Luterbacher et al.*, 2004; *Mann et al.*, 1998; *Rutherford et al.*, 2005), pressure (e.g. *Luterbacher et al.*, 2002), and drought (e.g. *Cook et al.*, 1999; *Zhang et al.*, 2004). *Evans et al.* (2002) provide an example of a reduced-dimension SST field reconstruction using $\delta^{18}O$ proxy records from coral.

3.2 Data

Contemporary (1854-2013) gridded (2° by 2°) monthly SSTs were obtained from the NOAA NCDC Extended Reconstruction Sea Surface Temperature (ERSST) version 3b dataset (*Smith et al.*, 2008). Contemporary (1949-2013) gridded (2.5° by 2.5°) monthly zonal winds were obtained from NOAA NCEP-NCAR CDAS-1 Global Reanalysis (*Kalnay et al.*, 1996). Monthly anomalies were calculated for each dataset using 1981-2010 climatology. Monthly anomalies for SSTs and winds were then converted into annual averages by averaging from May to the following April in order to capture the annual ENSO cycle.

Two common proxies for paleothermometry in the Pacific exploit magnesium-calcium (Mg/Ca) ratios from foraminifera shells and alkenones ($U_{37}^{k'}$) from coccolithophores to infer SSTs. Numerous Mg/Ca and $U_{37}^{k'}$ proxy records have been reported for the east and west Pacific (see *Leduc et al.* (2010) for a review). At high temperatures, more Mg is incorporated in the shells of foraminifera, and a ratio of Mg/Ca can be used to infer SSTs back through time (e.g. *Lea et al.*, 1999; *Nürnberg et al.*, 1996). Alkenones are a trans-fat altered by cocclithophores, or algae, under various temperatures: lower temperatures lead

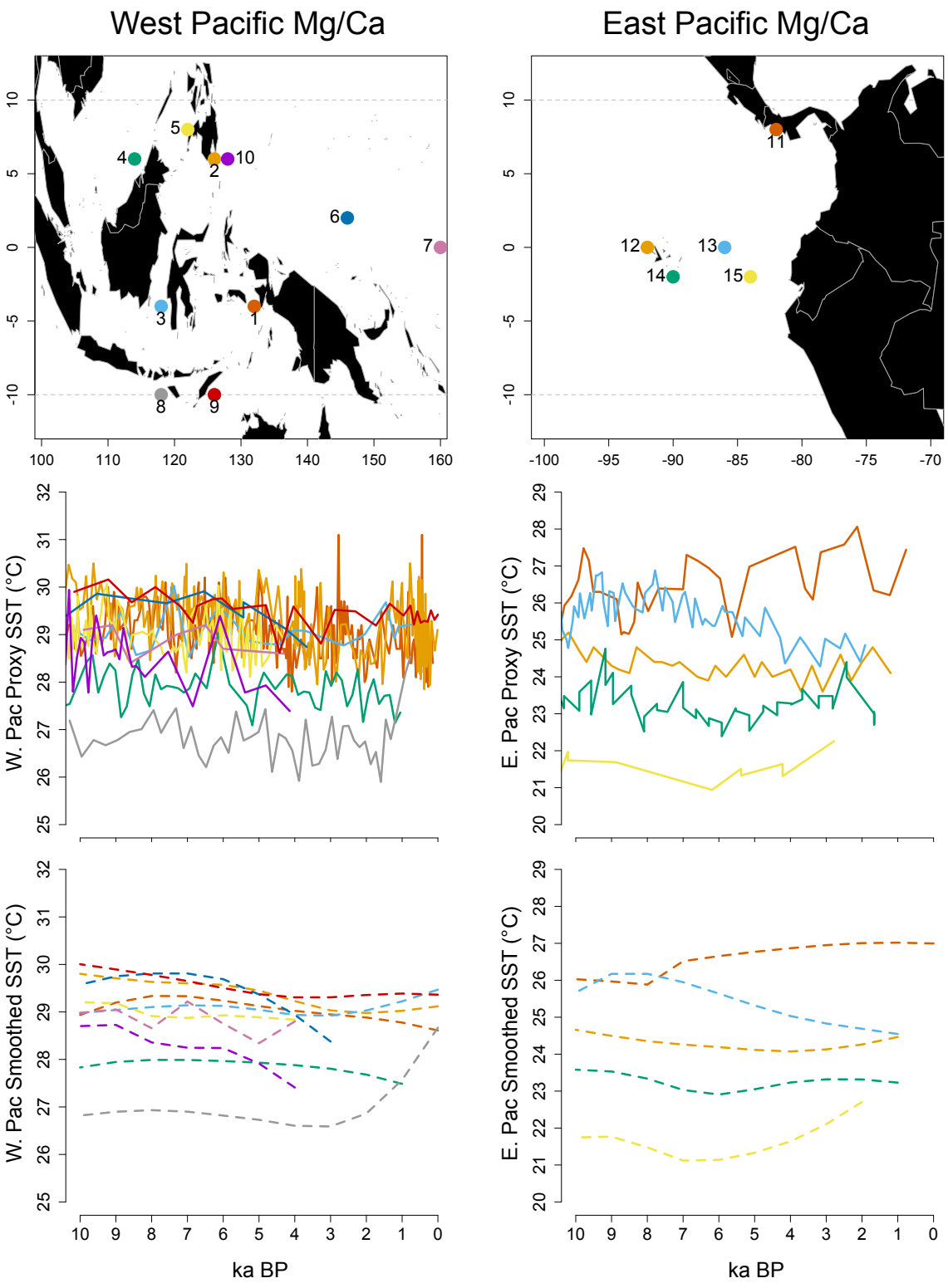

Figure 3.1: Maps of western and eastern Pacific Mg/Ca based SST records. The second row provides raw SST estimations as calibrated by original authors listed in Table 3.1. The third row provides the records smoothed by a second order local polynomial method with a local neighborhood of 70% nearest data points.

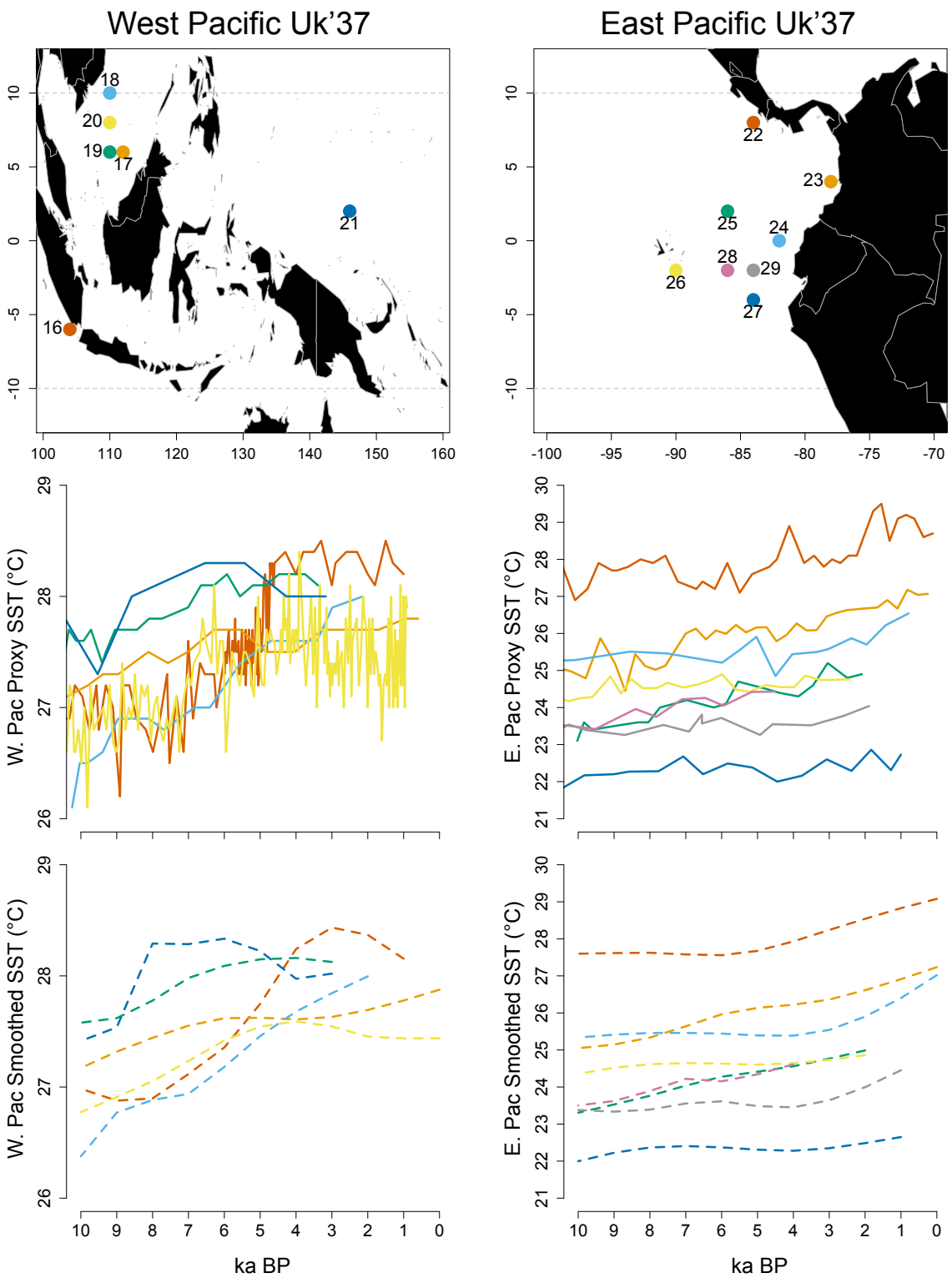

Figure 3.2: Maps of western and eastern Pacific $U_{37}^{k'}$ based SST records. The second row provides raw SST estimations as calibrated by original authors listed in Table 3.2. The third row provides the records smoothed by a second order local polynomial method with a local neighborhood of 70% nearest data points.

to an increase in the degree of unsaturation. The ratio of di- to tri-unsaturated alkenones is used to create an Unsaturation Index named $U_{37}^{k'}$ (e.g. *Brassell et al.*, 1986; *Herbert*, 2003). The remains of foraminifera and coccolithophores sink to the bottom of the ocean and are preserved in the sediment record. Mg/Ca (Table 3.1 and Figure 3.1) and $U_{37}^{k'}$ (Table 3.2 and Figure 3.2) SST records (Tables 1 and 2) were obtained from the archives of NCDC (http://www.ncdc.noaa.gov/data-access/paleoclimatology-data/datasets) and Pangaea (http://www.pangaea.de/).

Most proxy records listed in Tables 3.1 and 3.2 reach back to 10 ka, but some records stop prior to 0 ka. All the records were generated at various resolutions of at least one SST value per 1,000 years. In order to reconstruct 2, 4, 6, 8, and 10 ka snapshots of the equatorial pacific SST and wind fields, each paleoceanographic record was smoothed (Figures 3.1 and 3.2) using a local polynomial method with a second order polynomial and a local neighborhood consisting of 70% of the nearest data points (e.g. *Loader et al.*, 1996). These records were then converted to SST anomalies using the climatological mean temperature from ERSST at the grid-cell closest to the location of the proxy record.

3.3 Methodology

Our work is rooted in similar methodologies and assumptions to the work of (*Mann et al.*, 1998) who used a multi-proxy reduced-dimension approach to combine instrumental records with proxies from tree rings, ice cores, and corals to reconstruct global annual temperature patterns over the past six centuries. We use a principal component analysis (PCA) approach (Figure 3.3) to reconstruct SSTs and a canonical correlation analysis (CCA) approach to reconstruct winds.

3.3.1 Principal Component Analysis (PCA) Reconstruction for Pacific SST

In PCA, multivariate space-time data is decomposed into orthogonal space-time components via eigen-decomposition of the covariance matrix. These components, also referred

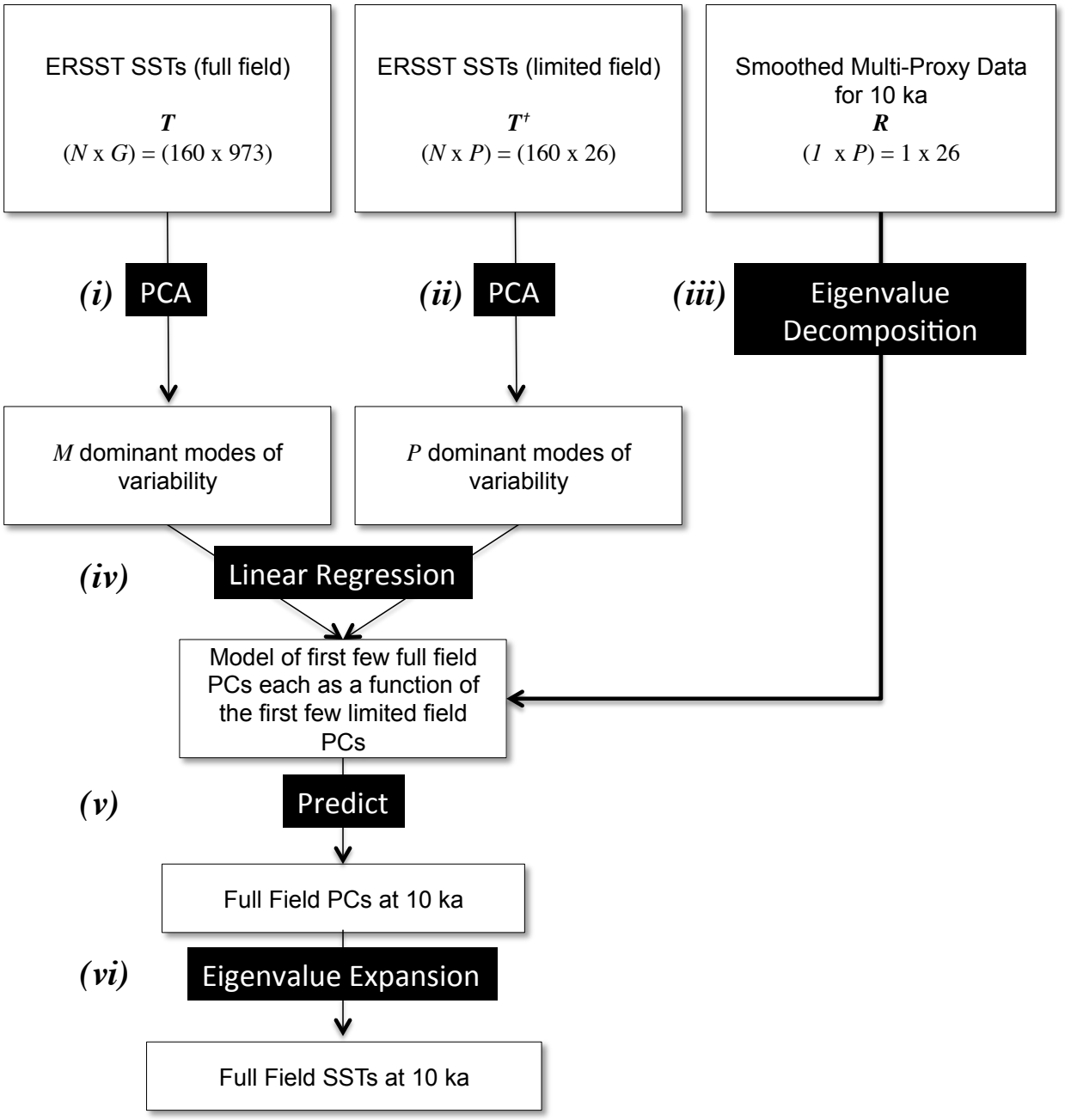

Figure 3.3: Flow chart of principal component analysis approach used for the multi-proxy SST reconstruction. The steps are given for producing SSTs representative of 10 ka. Steps $(iii - vi)$ are repeated for 8, 6, 4, and 2 ka.

to as patterns or modes, are ordered based on the percentage of total variance that each resolves. For most climatological datasets, the first few modes capture the majority of the variance of the original data - thus, reducing the dimension of the data. Using bold-faced uppercase variables to denote matrices, with brackets used only when specifying the dimensions of the matrix, and lower-case bold-faced variables as vectors, the formulation for a PCA is as follows:

$$[\boldsymbol{X}]_{NxG} = [\boldsymbol{Y}]_{NxG}[\boldsymbol{U}]_{GxG} \tag{3.1}$$

$$[\boldsymbol{Y}]_{NxG} = [\boldsymbol{X}]_{NxG}[\boldsymbol{U}]^T_{GxG} \tag{3.2}$$

where $\boldsymbol{X}$ is the matrix of the original data, $\boldsymbol{Y}$ is a matrix of principal components (PCs), and $\boldsymbol{U}$ is a matrix of eigenvectors, N is the length of data at each location (i.e. the number of times sampled), and G is the number of grid-points. $\boldsymbol{U}$ is considered a transformation matrix, as it transforms the correlated data $\boldsymbol{X}$ into the orthogonal Principal Component (PC) space of $\boldsymbol{Y}$, or transforms the PCs back into the data-space. In theory, the eigenvectors are obtained sequentially by solving a constrained optimization problem. The first eigenvector, $\boldsymbol{u}_1$, is found such that $\epsilon_1 = E[\boldsymbol{X} - \boldsymbol{X}\boldsymbol{u}_1]^2$ is minimized and subjected to the orthonormality constraint of $\boldsymbol{u}_1\boldsymbol{u}_1^T = 1$. The subsequent eigenvectors are obtained to minimize the residual mean squared errors. Thus the variance of all the PCs sum to the variance of the original data. *Von Storch and Zwiers* (2001) give details of PCA and other multivariate analysis techniques. In practice, eigenvectors are obtained simultaneously by decomposing the covariance matrix into left-singular vectors or eigenvalues ($\boldsymbol{U}$), right singular vectors ($\boldsymbol{V}$) and a diagonal matrix of singular values (λ). The application steps of this method to our reconstruction is described below and shown as a flowchart (Figure 3.3).

3.3.1.1 Step (i)

Let $\boldsymbol{T}$ be an NxG matrix of contemporary average annual (May-Apr) SST anomalies composed of 160 years of data (1854-2014) at each of 973 grid-points spanning the equatorial Pacific from 10°S to 10°N and 100°E to 60°W (300°E). A PCA is performed on $\boldsymbol{T}$, such that:

$$[\boldsymbol{T}]_{NxG} = [\boldsymbol{Y}]_{NxG}[\boldsymbol{U}]_{GxG} \tag{3.3}$$

$$\boldsymbol{T} = \sum_{i=1}^{G} \lambda_i \boldsymbol{y}_i \boldsymbol{u}_i \tag{3.4}$$

whereby $\boldsymbol{T}$ is decomposed into G orthogonal eigenvectors, $\boldsymbol{U}$. For each i^{th} eigenvector or mode, we find an G-vector empirical orthogonal function (EOF) represented by $\boldsymbol{u}_i$ and an N-vector principal component (PC) represented by $\boldsymbol{y}_i$, which respectively describe the spatial and temporal variability of that particular eigenvector. In addition, λ_i is a scalar that provides the fraction of total variance of the original data that is resolved by the i^{th} mode. The first four EOFs (Figure 3.4a) and PCs (Figure 3.4b) explain almost 90% of the total variance of the full field SST data ($\lambda_1 = 0.688$, $\lambda_2 = 0.111$, $\lambda_3 = 0.071$, $\lambda_4 = 0.025$).

3.3.1.2 Step (ii)

Let $\boldsymbol{T}^\dagger$ be a matrix of contemporary SST anomalies at the locations for which we have proxy records (referred to as the "limited field" hereafter), which makes it order NxP, where P is 26. A PCA is performed on $\boldsymbol{T}^\dagger$, which similarly results in P orthogonal eigenvectors $\boldsymbol{U}^\dagger$, each with an P-vector $\boldsymbol{u}_i^\dagger$, N-vector $\boldsymbol{y}_i^\dagger$, and a scalar $\lambda_i^\dagger$.

$$[\boldsymbol{T}^\dagger]_{NxP} = [\boldsymbol{Y}^\dagger]_{NxP}[\boldsymbol{U}^\dagger]_{MxP} \tag{3.5}$$

$$\boldsymbol{T}^\dagger = \sum_{i=1}^{P} \lambda_i^\dagger \boldsymbol{y}_i^\dagger \boldsymbol{u}_i^\dagger \tag{3.6}$$

The first four modes (Figure 3.5) explain almost 95% of the total variance of the limited field SST data ($\lambda_1^\dagger = 0.782$, $\lambda_2^\dagger = 0.126$, $\lambda_3^\dagger = 0.022$, $\lambda_4^\dagger = 0.017$)

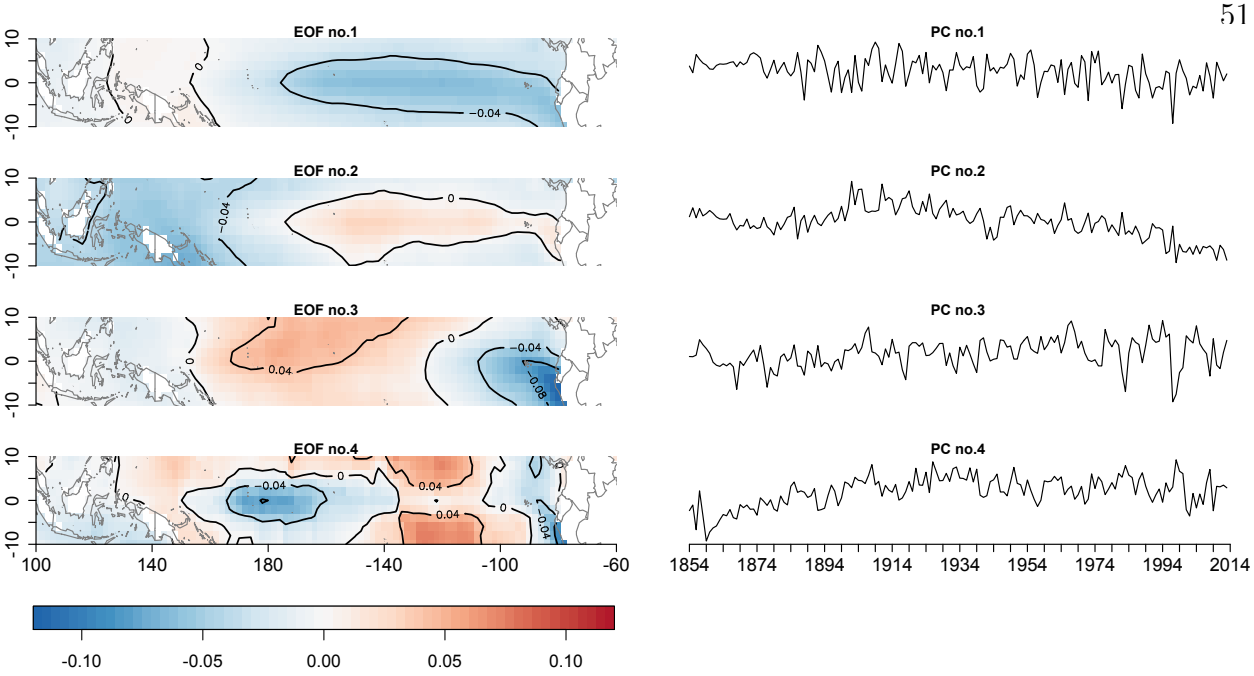

Figure 3.4: This figure provides the EOFs and PCs of the four leading modes of the PCA performed on the full field of equatorial Pacific annually averaged (May to April) SSTs obtained from the 1854-2013 2° x 2° ERSST dataset (*Smith et al.*, 2008). The first four eigenvectors account for 68.8%, 11.1%, 7.1%, and 2.5%, respectively, of the total variability in the full field SST data.

3.3.1.3 Step (iii)

We performed the following steps for each of six reconstruction periods: 2, 4, 6, 8, and 10 ka. It should be noted that although there are 29 independent proxy records, there are three locations at which the sediment core was analyzed for both Mg/Ca and $U_{37}^{k'}$. For those three cases in the multi-proxy reconstruction, the Mg/Ca records were kept, and the $U_{37}^{k'}$ records were ignored to maintain equal representation from each proxy in each part of the Pacific. When removing the Mg/Ca records and keeping the $U_{37}^{k'}$, however, differences in the results were negligible. Using the smoothed proxy records, all 26 values for, say, 10 ka are contained in matrix $\boldsymbol{R}$ of order 1 by P, where $P = 26$. $\boldsymbol{R}$ undergoes eigenvalue decomposition by multiplying it with the eigenvalue transformation matrix $\boldsymbol{U}^{\dagger}$ obtained from the limited

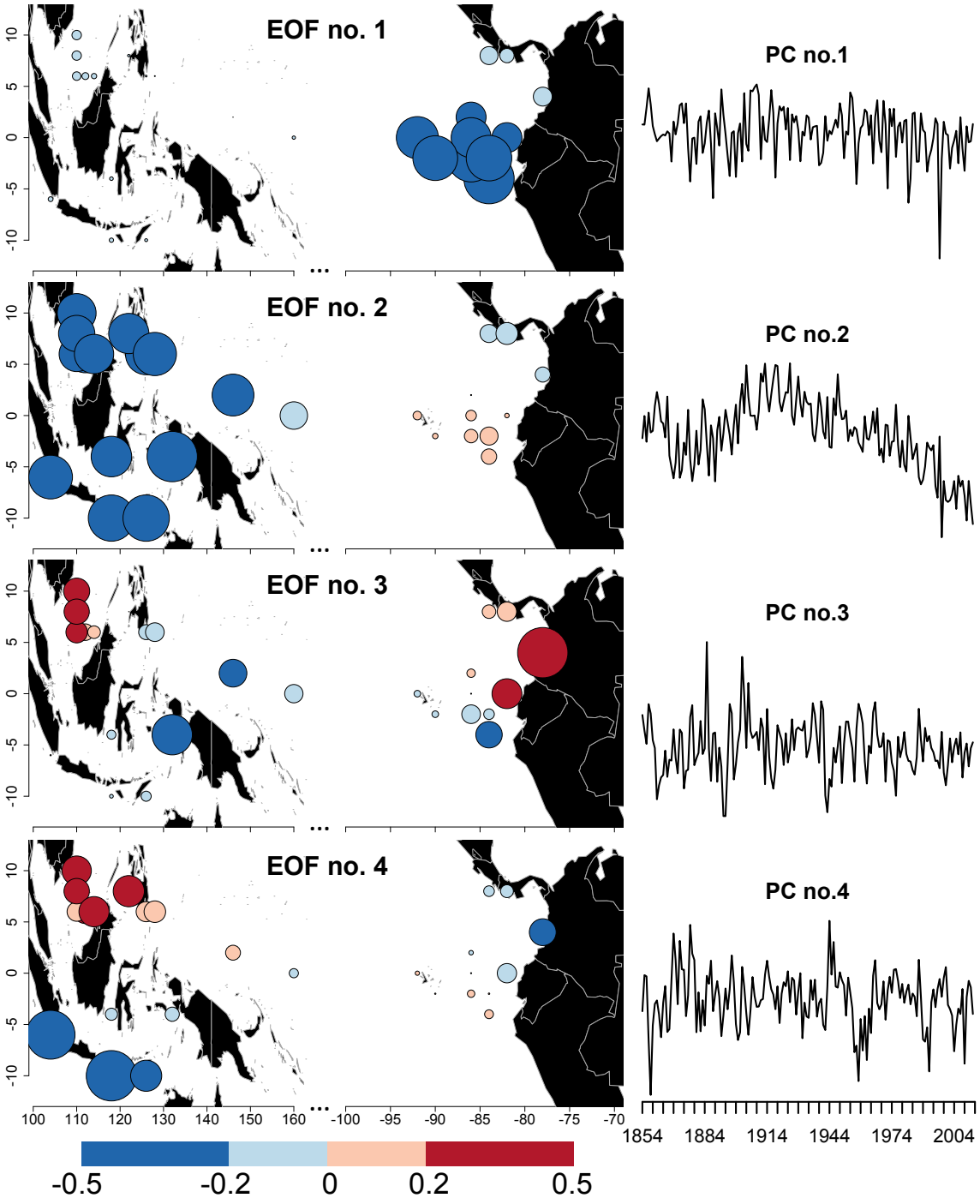

Figure 3.5: This figure is the same as Figure 3.4, but for the limited field of equatorial Pacific annually averaged (May to April) SSTs obtained from the 1854-2013 2° x 2° ERSST dataset (*Smith et al.*, 2008). The first four eigenvectors account for 78.2%, 12.6%, 2.2%, and 1.7%, respectively, of the total variability in the limited field SST data. The radius of each circle is scaled to the magnitude of the eigenvalue.

field PCA in Step (*ii*):

$$[\boldsymbol{Y}^R]_{1xP} = [\boldsymbol{R}]_{1xP}[\boldsymbol{U}^\dagger]^T_{PxP} \tag{3.7}$$

where $\boldsymbol{Y}^R$ represents the PCs of the proxy SST values for 10 ka.

3.3.1.4 Step (iv)

For the reconstruction model, we use a few of the PCs of the limited field as predictors to model each of the first few full-field PCs. The decision to keep a certain number of PCs and predictors is somewhat arbitrary, but depends on the distribution of variance resolved across the modes. Although keeping more modes may increase the total resolved variance, inclusion of too many PCs can introduce noise into the calculated fields. Given the eigenvalue spectrum (EVS) of the full-field and limited-field λ-values (Figure 3.6), we were faced with a few reasonable options in deciding how many limited-field predictor PCs to use and how many full-field PCSs to reconstruct. First, we could limit the reconstruction to only the dominant mode, or first PC (represented by the green points on Fig. 3.6). In this case, we would model the first PC of the full field as a function of the first PC of the limited field. As a second option, we could choose some percentage of resolved variance as a threshold. If we choose PCs that resolve 10% or more of the variance, we would model the first two PCs of the full field (green dot and orange dot in Fig. 3.6a) each as functions of the first two PCs of the limited field (green dot and purple dot in Fig. 3.6b). If we chose 5% as a threshold, the number of predictors would remain the same, but we would now model the first three PCs of the full field (green, orange, and purple dots in Fig. 3.6a). A final option would be to use the "knee" in the eigenvalue spectra as thresholds. The "knee" (purple points in Figure 3.6) of each EVS is located at the PC just before each noise floor (grey points in Figure 3.6). Coincidentally, it turns out that using either 5% or the "knee" as a threshold achieves the same combination of PCs (first three) and predictor PCs (first two). Reconstructions of SSTs for each of these three scenarios were considered. Using only the first PC of each

did not reconstruct modern day SSTs well enough because it omitted other important non-noise modes. Although the second (10% threshold) and third (5% threshold, or "knee") scenarios reconstructed both modern day and Holocene SSTs similarly, we chose to use the latter to include the most possible PCs. Under this combination, the first three full-field PCs capture 87% of the full-field variance, and the first two limited-field PCs capture 91% of the limited-field variance.

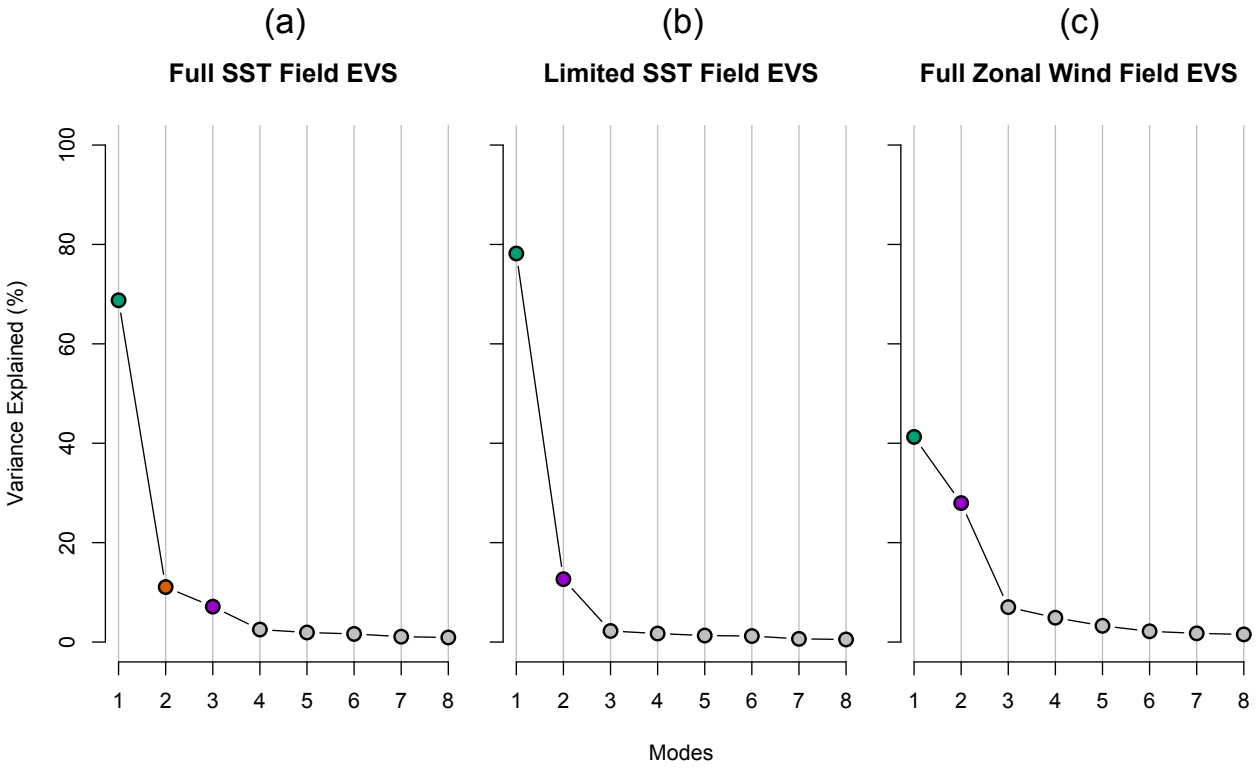

Figure 3.6: Eigenvalue spectrums (EVS) for the (a) full SST field (1854-2013), (b) limited SST field (1854-2013), and (c) full zonal wind field (1949-2013). The limited SST field consists of contemporary SSTs only at locations for which there exists either Mg/Ca or alkenone SST records. The green points represent the variance explained by the first mode of each field. The purple dots represent the variance explained at the âĂIJknee,âĂİ which is the point just before the noise floor (represented by the grey dots). The orange dot on the full field EVS represents the mode that would be included in the model if the threshold for variance resolved was at least 10%. Description of how these are used to determine the number of retained PCs and predictors used in the model is provided in the text under Section 3.3.1.4.

With this reasoning in mind, we model the first three PCs of the full field each as a linear function of the first two PCs of the limited field:

$$\boldsymbol{y}_1 = f(\boldsymbol{y}_1^\dagger, \boldsymbol{y}_2^\dagger)\boldsymbol{y}_2 = f(\boldsymbol{y}_1^\dagger, \boldsymbol{y}_2^\dagger)\boldsymbol{y}_3 = f(\boldsymbol{y}_1^\dagger, \boldsymbol{y}_2^\dagger) \tag{3.8}$$

The best linear regression model for each is identified via step-wise model selection based on Bayesian Information Criterion.

3.3.1.5 Step (v)

We use the PCs of the proxy data $\boldsymbol{Y}^R$ to reconstruct the first three PCs representative of 10 ka ($\hat{\boldsymbol{y}}_1$, $\hat{\boldsymbol{y}}_2$, $\hat{\boldsymbol{y}}_3$), and similarly for other times. The remaining G minus 3 reconstructed PCs ($\hat{\boldsymbol{y}}_{4...G}$) are the means of the PCs from the full field ($\boldsymbol{y}_{4...G}$).

3.3.1.6 Step (vi)

Finally, we transform the reconstructed PCs into a field of reconstructed SST anomalies via eigenvalue expansion, by multiplying by the original eigenvalue matrix from Step (i):

$$[\hat{\boldsymbol{T}}]_{1xG} = [\hat{\boldsymbol{Y}}]_{1xG}[\boldsymbol{U}]_{GxG} \tag{3.9}$$

Since $\hat{\boldsymbol{T}}$ is estimated using only the first few PCs, the reconstructed SSTs represent only the dominant signal. Steps ($ii - vi$) are repeated for 8, 6, 4, and 2 ka.

Standard errors from the regressions in Step (iv) are used to generate 500 ensembles of the first three PCs. Five hundred ensembles for each of the remaining PCs were created by bootstrapping values from the original PCs at each grid point. The standard deviation of these ensembles provides an estimate of uncertainty. As these errors were similar across the five reconstruction periods, we present the standard errors only from 2 ka in Figure 3.7. Standard errors are generally between 0.1-0.2°C throughout the central Pacific, with some errors reaching 0.3°C immediately along the coast of South America. Present-day variance is concentrated in the "cold tongue" of the eastern and east-central Pacific. In most places,

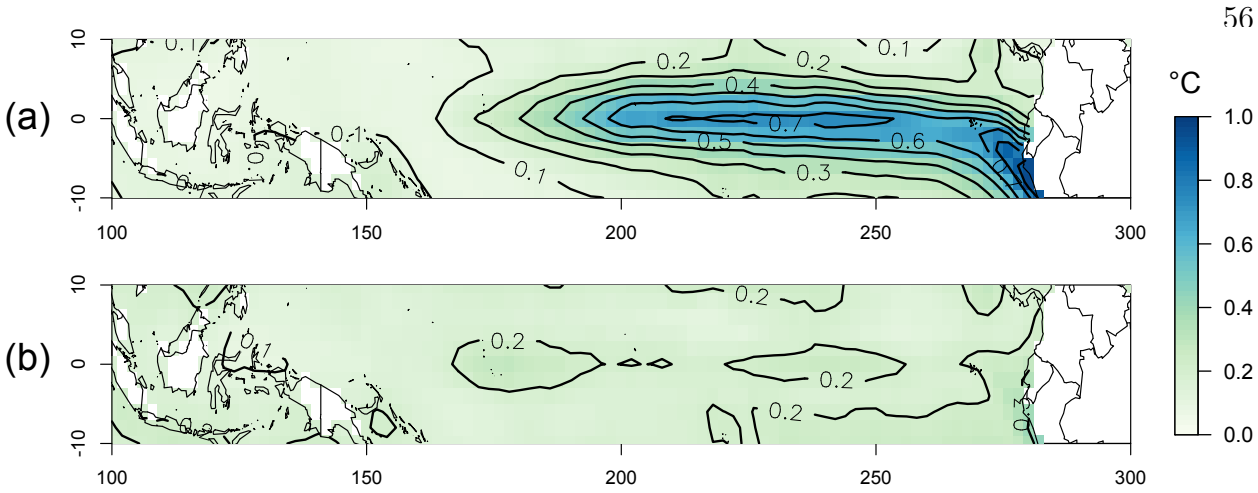

Figure 3.7: (a) Variance of 1854-2013 observed SSTs and (b) standard error SST map for 2 ka. The standard error map was produced by using the standard errors from the model regression and generating 500 ensembles of the first three PCs. The remaining PCs were bootstrapped from the original PCs to complete ensembles for each grid-point. This map is similar to those for other time periods reconstructed.

the standard errors are only a small fraction (<10%), of the present-day variance (Figure 3.7).

3.3.2 Canonical Correlation Analysis (CCA) Reconstruction of Pacific Zonal Winds

The CCA-reconstruction method is quite similar to the PCA-based method depicted in Figure 3.3 and described in Section 3.1. CCA, however, is preferred over standard PCA in a scenario such as this where the patterns of one variable, e.g. SSTs, are being used as predictors of patterns for a related variable, e.g. winds. This method is widely used for multi-site forecasting of precipitation (e.g. *Barnston*, 1994; *Barnston and Smith*, 1996), temperature (e.g. *Barnett and Preisendorfer*, 1987; *Barnston*, 1994; *Barnston and Smith*, 1996; *Mo*, 2003), streamflow (e.g. *Salas et al.*, 2010), and SSTs (e.g. *Barnston and Ropelewski*, 1992). See *Bretherton et al.* (1992), *Von Storch and Zwiers* (2001), and *Cherry* (1996) for details on CCA. Here, we use SST patterns to reconstruct zonal winds across the equatorial

Pacific. We choose to reconstruct zonal winds because in this region zonal winds are much larger than meridional winds.

For the most part, the CCA method follows the PCA method described in Figure 3.3 through Steps ($i - iii$), and then differs from Step (iv) onward. For Steps (i) and (ii), $\boldsymbol{T}$ becomes a matrix of 1949-2013 zonal wind anomalies, which we will call $\boldsymbol{Z}$, and $\boldsymbol{T}^{\dagger}$ remains a matrix of SST anomalies for the limited field. Since we only have 65 years of zonal wind data, N is now 65. As before, a PCA on both of these fields results in:

$$[\boldsymbol{Z}]_{NxG} = [\boldsymbol{Y}]_{NxG}[\boldsymbol{U}]_{GxG} \tag{3.10}$$

$$[\boldsymbol{T}^{\dagger}]_{NxP} = [\boldsymbol{Y}^{\dagger}]_{NxP}[\boldsymbol{U}^{\dagger}]_{PxP} \tag{3.11}$$

where $\boldsymbol{Y}$ and $\boldsymbol{U}$ are the full field PCs and eigenvectors of the zonal winds (Figures 3.6c and 3.8), and $\boldsymbol{Y}^{\dagger}$ and $\boldsymbol{U}^{\dagger}$ are still the limited field PCs and eigenvectors (Figures 3.5 and 3.6b). Step (iii) is the same: the proxy data $\boldsymbol{R}$ are decomposed into PCs, $\boldsymbol{Y}^{R}$, by multiplying by the limited field eigenvalues, $\boldsymbol{U}^{\dagger}$.

At this point, N_{PC} from $\boldsymbol{Y}$ and $\boldsymbol{Y}^{\dagger}$ are retained. Note that the numbers of full-field and limited-field PCs retained must be equal. It is also worth noting that since a canonical correlation resolves the joint correlation between two PCs, it is acceptable to retain more PCs than one typically does during a standard PCA reconstruction. In fact, for zonal winds, keeping the first six PCs ($N_{PC} = 6$), which involves keeping PCs below the "knee" in Figure 3.6c, strengthened the model statistics (Section 3.3.3.) and allowed us to account for 85% of the full-field variance. A canonical correlation is performed between the two to resolve the joint correlation between the two sets of PCs:

$$[\boldsymbol{Y}]_{NxN_{PC}} = [\boldsymbol{S}]_{NxN_{PC}}[\boldsymbol{A}]_{N_{PC}xN_{PC}} \tag{3.12}$$

$$[\boldsymbol{Y}^{\dagger}]_{NxN_{PC}} = [\boldsymbol{S}^{\dagger}]_{NxN_{PC}}[\boldsymbol{B}]_{N_{PC}xN_{PC}} \tag{3.13}$$

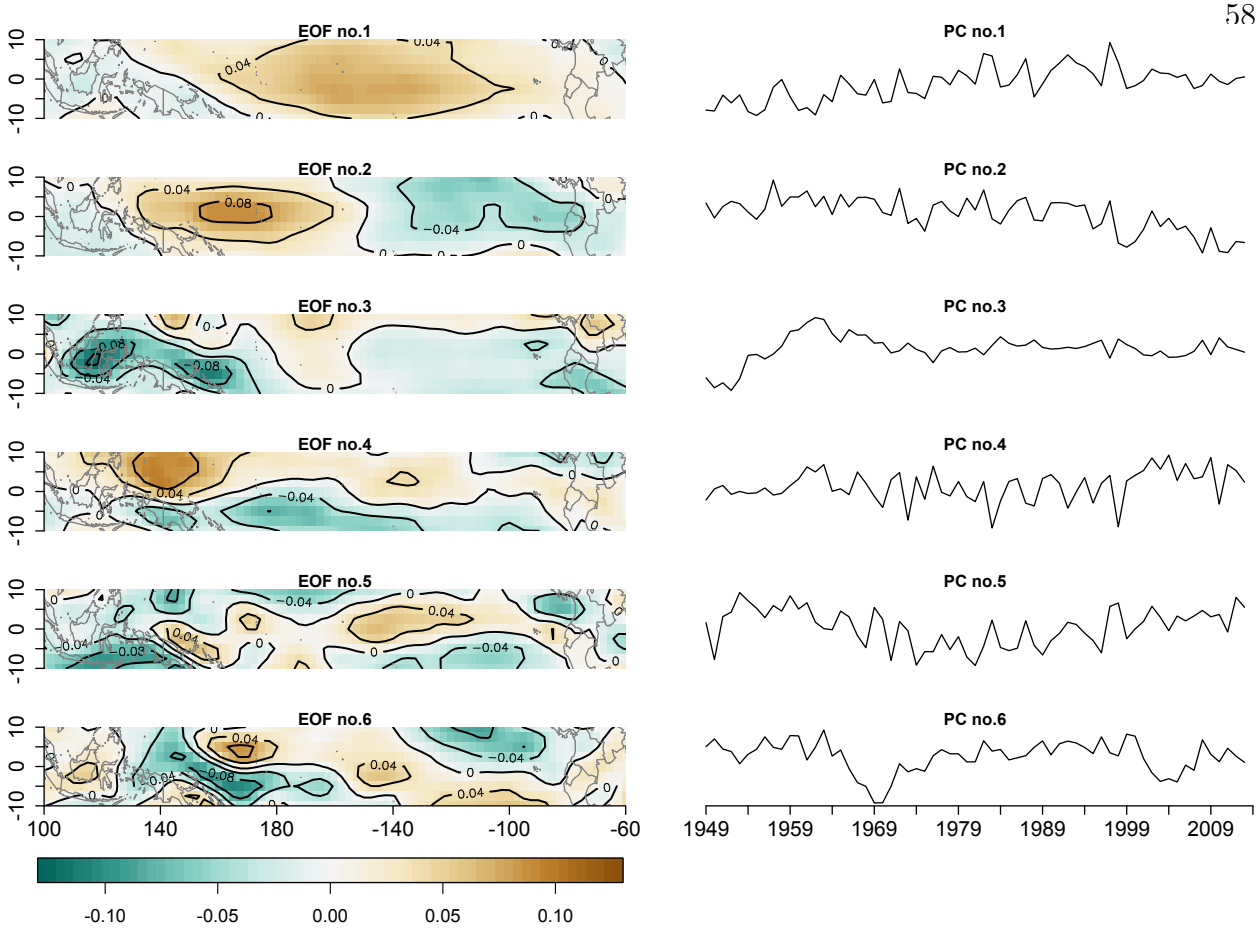

Figure 3.8: EOFs and PCs of the six leading modes of the PCA performed on the full field of equatorial Pacific annually averaged (May to April) zonal winds obtained from the 1949-2013 2.5° x 2.5° NCEP-NCAR Reanalysis (*Kalnay et al.*, 1996). The first four eigenvectors account for 41.3%, 28.0%, 7.0%, and 4.9%, respectively, of the total variability in the full field zonal wind data.

where $\boldsymbol{A}$ and $\boldsymbol{B}$ are now the canonical transformation functions, $\boldsymbol{S}$ and $\boldsymbol{S}^{\dagger}$ are N_{PC} pairs of canonical components (CCs), each of which explains more of the joint variance than the next, and all of which are uncorrelated to each other. The CC of the full-field are regressed against the corresponding CC of the limited field, such that:

$$s_j = \hat{a}_j + \hat{\beta}_j s_j^{\dagger} \tag{3.14}$$

where j is 1 through N_{PC}, and $\hat{\boldsymbol{\beta}}$ is the solution to the least squares optimization. The first N_{PC} reconstructed PCs of the full wind field $\hat{\boldsymbol{Y}}$ are obtained through expansion by

multiplication of first N_{PC} proxy PCs with the full-field canonical transformation matrix $\boldsymbol{A}$ and the $\hat{\boldsymbol{\beta}}$ solution to the regression:

$$[\hat{\boldsymbol{Y}}]_{1xN_{PC}} = [\boldsymbol{Y}^R]_{1xN_{PC}}[\boldsymbol{A}]_{N_{PC}xN_{PC}}[\hat{\boldsymbol{\beta}}]_{N_{PC}xN_{PC}} \tag{3.15}$$

We calculate the remaining $G - N_{PC}$ PCs ($\hat{y}_{7...M}$) by taking the means of the PCs from the full field. Finally, we obtain the reconstructed zonal winds $\hat{\boldsymbol{Z}}$ by eigenvalue expansion:

$$[\hat{\boldsymbol{Z}}]_{1xG} = [\hat{\boldsymbol{Y}}]_{1xG}[\boldsymbol{U}]_{GxG} \tag{3.16}$$

We repeated this process for each of the six time periods (10, 8, 6, 4, and 2 ka).

Implicit in this approach are a few assumptions. First, we assume that the calibration equations used by the authors of each proxy record represent the "best" calibration for that particular record. There are a number of calibration equations that can be used to transform Mg/Ca or $U_{37}^{k'}$ to SST. The "best" equation is typically chosen by considering proxy type, location, dissolution effects (in the case of Mg/Ca), and sampling method. We do not convert all records using the same calibration equation because we assume that the authors of each proxy record have chosen the calibration equation that is most appropriate for their particular record. Second, we assume that spatial patterns of the proxy network are linearly related to spatial patterns in the contemporary period. Third, we assume that the main patterns of variability that exist in the contemporary dataset have not changed over the past 10 ka. *Molnar and Cane* (2002, 2007) show that ENSO teleconnection patterns of present-day seems to have existed as far back as the early Pliocene ($\sim$ 5 Ma), suggesting that the major patterns of variability have not changed significantly over the relatively short period of time considered in this analysis.

3.3.3 Calibration and Validation

To assess the reliability of the procedure above to reproduce contemporary SSTs and zonal winds from the limited field contemporary SST data, we use the 'resolved variance'

statistic β, given by:

$$\beta = 1 - \frac{\sum (y - \hat{y})^2}{\sum y^2} \tag{3.17}$$

where y is the contemporary data and $\hat{y}$ is the reconstructed data for the full period of each dataset (1854-2013 for SST, 1949-2013 for winds). We compute this statistic at each grid-point over the reconstruction domain (Figure 3.9, top). For a perfect fit, one would expect β = 1, and for two random series, one would expect β = -1. Across most of the reconstruction region, β is greater than 0.6 for both SSTs and zonal winds. The lowest β-values are found over the central Pacific for SSTs and over the landmasses in the west and east Pacific for zonal winds.

We also correlated the observed and reconstructed data at each grid-point, and plot maps of the squared correlation coefficient, R^2 (Figure 3.9, bottom). For SSTs, the east and west Pacific show the highest correlations, which we should expect, as those areas provide the SST data for the reconstruction. The western "cold tongue" region of the east-central Pacific, where there are no data, shows correlations greater than or equal to 0.5. The lowest correlation region for SSTs is the west-central Pacific with values of 0.2-0.3. For zonal winds, the R^2 values are largest in the central Pacific, which is perhaps not surprising, as the central Pacific winds depend on SSTs at either end of the Pacific. As with the β-test, the worst performance for winds is seen over continental landmasses east and west of the Pacific.

For additional calibration, we compare the actual and reconstructed SST and zonal wind fields for the anomalous ENSO years of 1988-1989 (strong La Niña with standardized SST anomalies of -1.5°C in the NINO3 index region of 150°W - 90°W and 5°S - 5°N) and 1997-1998 (strong El Niño with standardized NINO3 index SST anomalies of +2.8°C). For 1988-1989, the model captures anomalies slightly cooler than -1°C, which are not as cold and do not extend as far westward as the actual anomalies seen during this particular La Niña year (Figure 3.10, top). The reconstructed zonal wind pattern for this year follows a similar shape to that of actual zonal winds, with strongly negative anomalies (strengthened

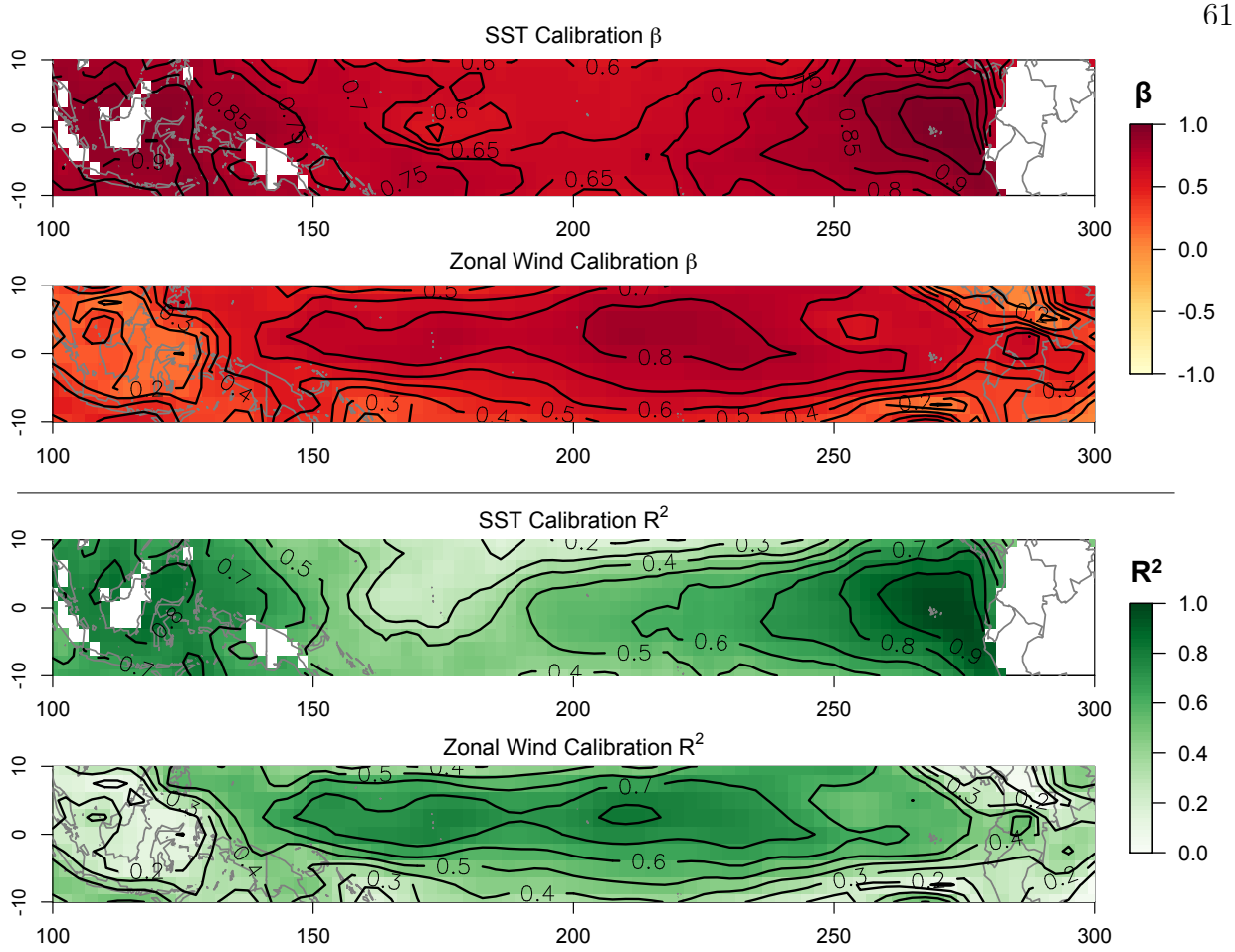

Figure 3.9: Model calibration statistics for the PCA-based SST model and the CCA-based zonal wind model showing the skill of the models in reconstructing each contemporary dataset (1854-2013 for SSTs and 1949-2013 for zonal winds). The β-statistic represents the resolved variance captured by the reconstructed contemporary data. The R^2 provides the correlation between the observed contemporary data and the reconstructed contemporary data.

easterlies) across the central Pacific and into the western Pacific north of the equator, with positive anomalies over the Indonesian archipelago (Figure 3.11, top). The reconstruction captures the two regions of highest negative anomalies (-3.5 m s^{-1} for the central Pacific and -2.5 m s^{-1} for the western Pacific), but switches the magnitudes in the reconstruction. The negative anomalies in winds over the far eastern Pacific off the coast of South America are not captured by the reconstruction, which is consistent with the relatively low β- and R^2-values seen in that region (Figure 3.9).

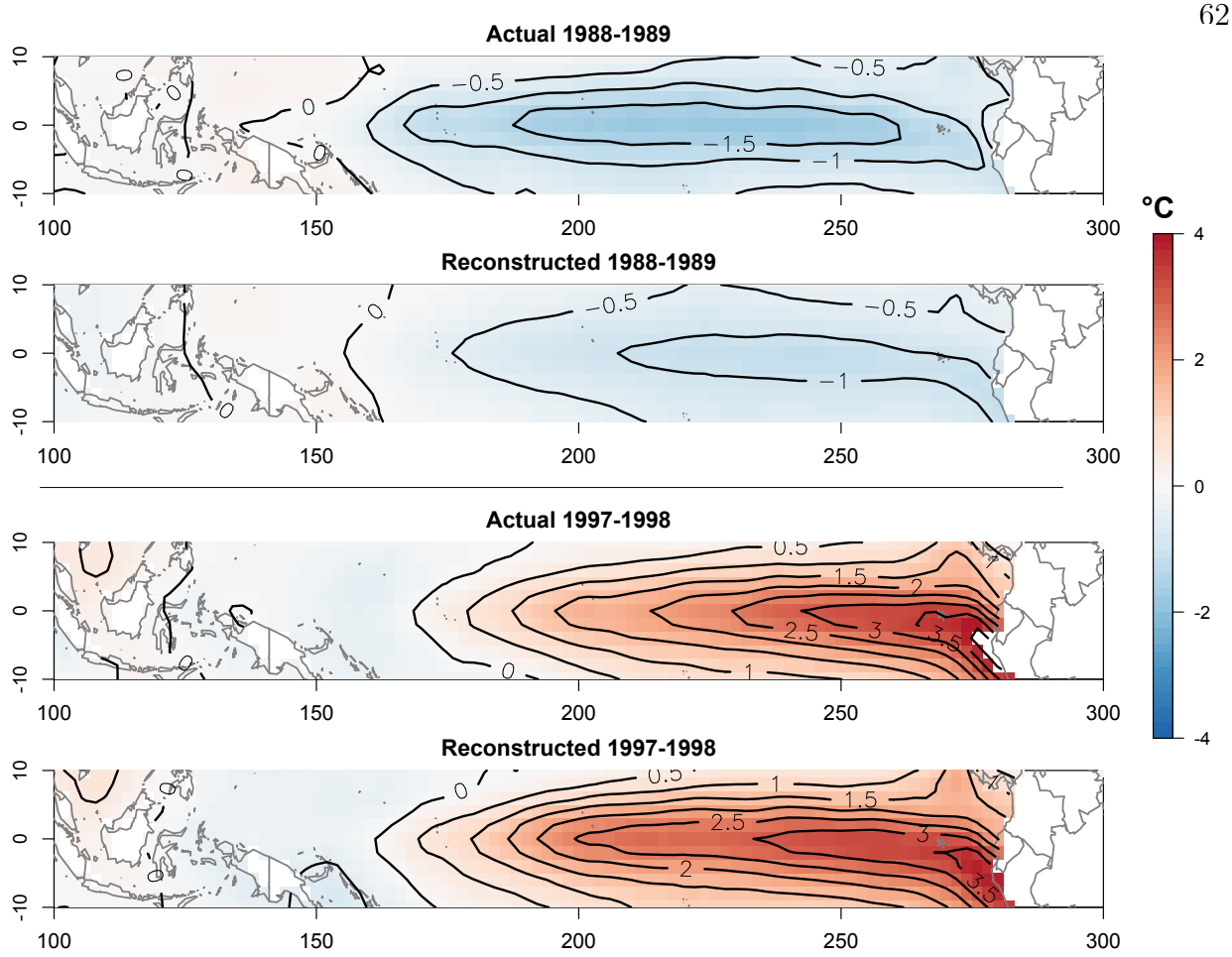

Figure 3.10: Actual and reconstructed SST anomalies (°C) for 1988-1989 (a strong La Niña year) and 1997-1998 (a strong El Niño year).

The magnitude and spatial pattern of anomalous SSTs is reconstructed better for the strong El Niño year of 1997-1998 (Figure 3.10, bottom) than for 1988-1989. Consistent with actual warming, the reconstructed "warm tongue" extends just west of the dateline, the greatest magnitude of warming, which is off the coast of Peru in the far eastern Pacific, reaches approximately +3.5°C, and the distribution of temperatures within the reconstructed "warm tongue" closely resemble those of the observed SSTs. It is likely that the failure of the limited-field model to capture La Niña and El Niño SST anomalies across the entire Pacific is due to the restricted locations of the proxy records. The cold La Niña anomaly of 1988-1989 is centered in the east-central Pacific, where there are no proxy records. The maximum warm

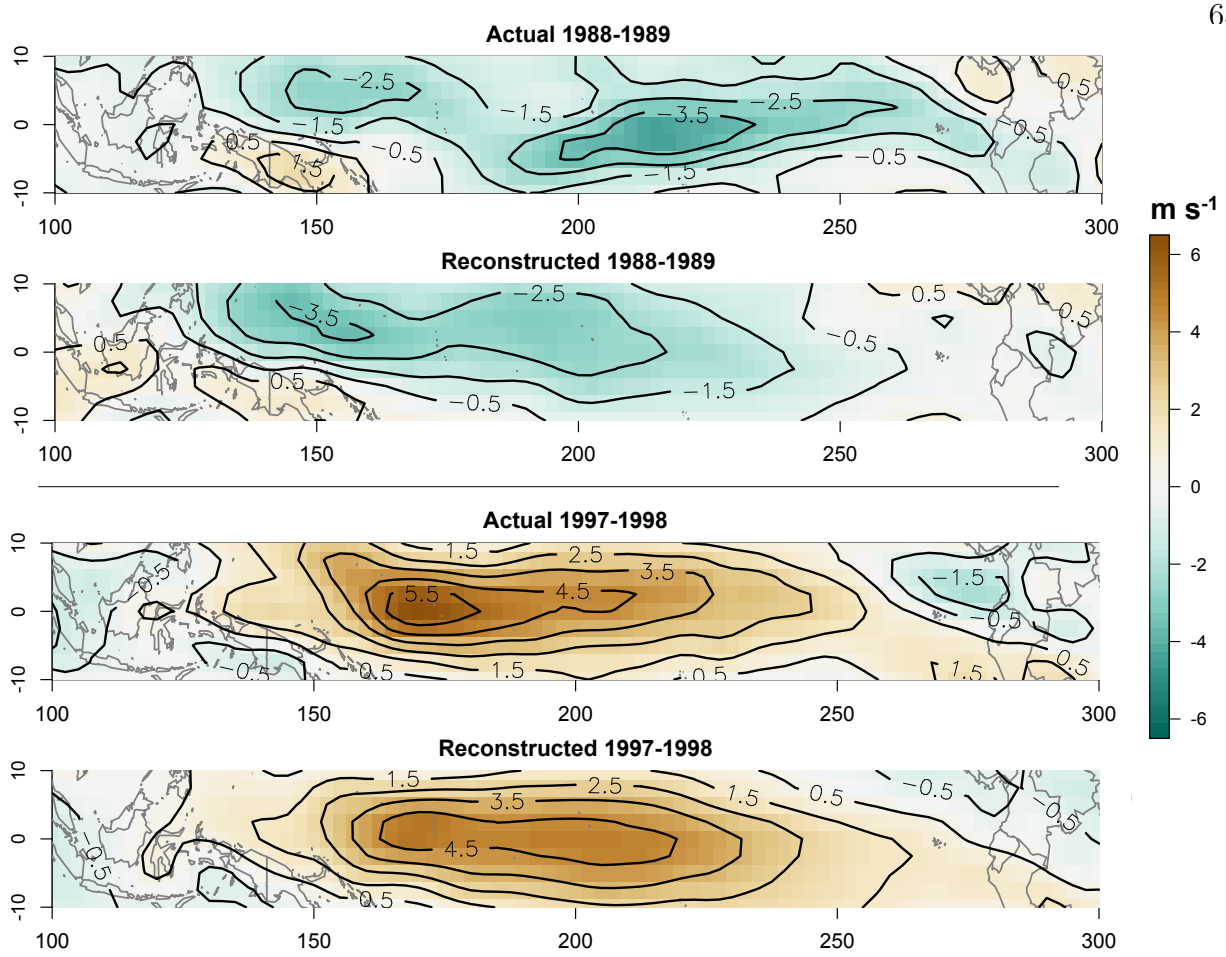

Figure 3.11: Actual and reconstructed zonal wind anomalies (m s^{-1}) for 1988-1989 (a strong La Niña year) and 1997-1998 (a strong El Niño year).

anomaly of the 1997-1998 El Niño, however, is located in the far eastern Pacific, which the paleoceanographic data sample well. Reconstructed winds for the El Niño year are arguably better than those for the La Niña year as well. The spatial patterns resemble one another, but the magnitude of the maximum reconstructed easterlies is underestimated by about 1 m s^{-1}.

For model verification, we train the PCA and CCA models using only the most recent data (1980-2013) and withhold the data from earlier periods (1854-1979 for SST, 1949-1979 for winds). Then, we reconstruct the fields from the earlier epoch using each respective model. As expected, the distribution of β and R^2 statistics (Figure 3.12) show smaller val-

ues than the calibration statistics for the complete data sets (Figure 3.9), but the regions that were reconstructed best during the calibration experiments (Figure 3.9) match those reconstructed best in the verification test (Figure 3.12). For SSTs, the training model reconstructs the earlier period everywhere except the west-central Pacific and areas near 10°S and 10°N in the central Pacific. For zonal winds, the central Pacific is the only region that is reconstructed using the training model. These patterns are consistent across both the β and R^2 statistics.

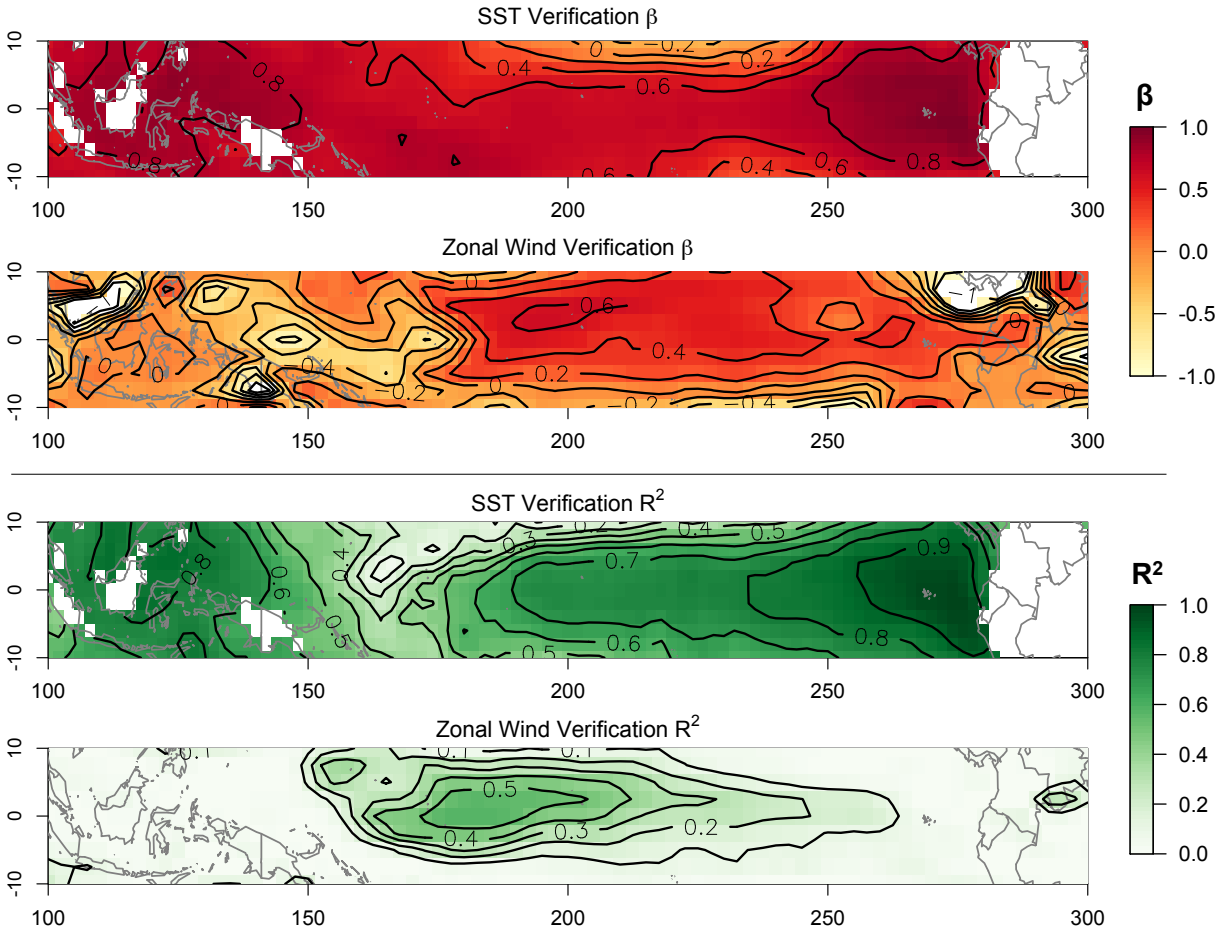

Figure 3.12: Model verification performed by training the model on 1980-2013 data, and using that model to validate SSTs and zonal winds from the period prior (1854-1979 for SSTs and 1949-1979 for zonal winds). The β- and R^2-statistics are used once again to quantify model skill.

3.4 Multi-proxy Reconstruction of Pacific Holocene Annual SST and Zonal Wind Field

We reconstruct full-field SSTs and zonal winds for 10, 8, 6, 4, and 2 ka using the multi-proxy approach described above (Figure 3.13, top). We choose not to reconstruct 0 ka since many of the proxy records do not extend to 0 ka and extrapolation of late Holocene SST trends introduces bias, especially in the east. Instead, we provide the mean present-day state (1854-2013 for SSTs and 1949-2013 for zonal winds) as reconstructed using the limited-field data (Figure 3.13). The multi-proxy SST reconstructions show the far-eastern Pacific to have been a maximum of -1°C cooler than today at 10 ka, along with a cooler (-0.8°C) "cold tongue" extending to about 140°W at 10 ka. The western Pacific was -0.6°C cooler for the same time period. From 10 to 6 ka, conditions changed little, both in magnitude and location, with the exception of a slight warming in the west and west-central Pacific. By 4 to 2 ka, the majority of the region had warmed by 0.4-0.6°C since 10 ka. The present-day reconstructions show small cool anomalies of 0.4°C throughout the Pacific. Recall that anomalies in Figure 3.13 are relative to the 1981-2010 climatology of each variable.

The multi-proxy reconstruction of winds (Figure 3.13, bottom) reveals maximum easterlies (large negative zonal winds) at 10 ka, which is also the period of lowest SSTs in the eastern Pacific, consistent with increased easterlies seen during present-day La Niña events. Consistently throughout the reconstructions, the zone of strongest easterlies is centered around 140°W. Easterlies are strongest at 10 ka, as much as 8 m s^{-1} stronger than present. Between 8 and 2 ka, the difference between past and present winds decreases and the location of the maximum difference moves eastward. Present-day reconstructions of zonal winds show the weakest easterlies of the Holocene (only -1 m s^{-1}) concentrated in the east-central Pacific.

The zonal difference in SSTs from west to east is also of interest, as some (e.g. *Koutavas et al.*, 2006) have argued that an "enhanced zonal gradient" characterized the early- to mid-

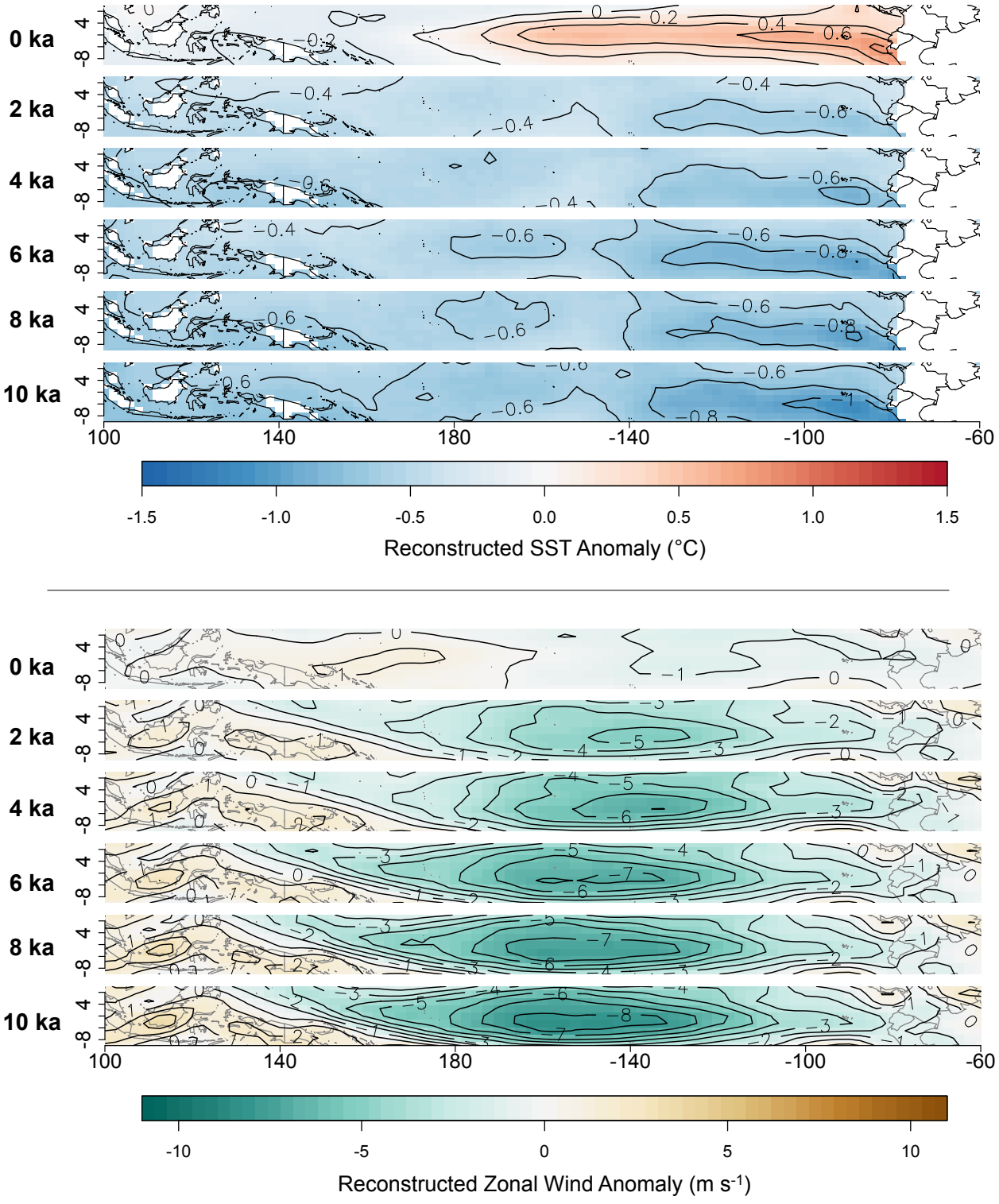

Figure 3.13: Multi-proxy reconstructed SSTs and zonal winds for 10, 8, 6, 4 and 2 ka. The top panel provides a reconstruction of present-day SSTs (1854-2013) and zonal winds (1949-2013) using the limited-field data.

Holocene Pacific. To quantify such gradients, Table 3.3 provides various indices throughout the Pacific (WPAC, NINO4, NINO3.4, NINO3, and NINO1+2) as well as difference indices (TNI and WTNI). The domain used in calculating each index is depicted in Figure 3.14 and provided in the notes of Table 3.3. The TNI index quantifies the zonal SST difference by subtracting NINO4 from NINO1+2. NINO4, however, is farther east than all of the western proxy records. For this reason, we also report a difference index called the WTNI, which is calculated by subtracting the WPAC (120°E - 180°E and 4°S to 4°N) from NINO1+2. Although the period of maximum eastern Pacific cooling was 10 ka, both 6 and 10 ka appear to have had the largest zonal difference in SSTs with -0.36 ± 0.29°C and -0.33 ± 0.30°C, respectively (Table 3.3a). The next largest zonal difference occurs at 8 ka (-0.25°C ± 0.29°C). From 4 to 2 ka, the zonal difference was only -15°C ± 0.28°C.

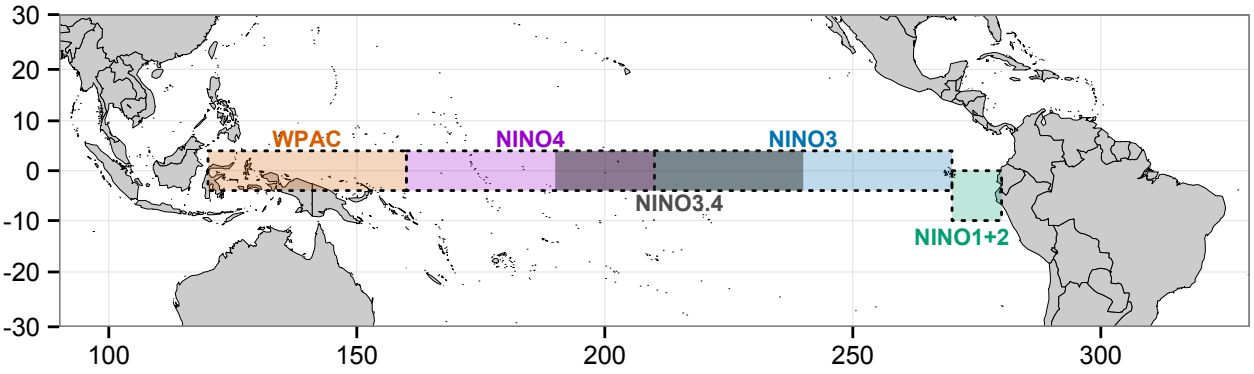

Figure 3.14: Regions used for the various ENSO indices reported in Table 3.3.

Table 3.3: Reconstructed SST anomalies for various NINO indices.

ka BP	Single Indices					Trans-Pacific Indices	
	WPAC	**NINO4**	**NINO3.4**	**NINO3**	**NINO 1+2**	**TNI**	**WTNI**
a. Multi-proxy Reconstruction							
10	-0.64 ± 0.13	-0.65 ± 0.18	-0.72 ± 0.17	-0.81 ± 0.17	-0.97 ± 0.27	-0.33 ± 0.33	-0.33 ± 0.30
8	-0.59 ± 0.13	-0.58 ± 0.18	-0.63 ± 0.18	-0.71 ± 0.17	-0.84 ± 0.26	-0.26 ± 0.32	-0.25 ± 0.29
6	-0.48 ± 0.13	-0.57 ± 0.18	-0.67 ± 0.18	-0.74 ± 0.17	-0.84 ± 0.26	-0.27 ± 0.32	-0.36 ± 0.29
4	-0.56 ± 0.12	-0.52 ± 0.18	-0.54 ± 0.17	-0.60 ± 0.17	-0.71 ± 0.26	-0.18 ± 0.31	-0.15 ± 0.28
2	-0.44 ± 0.13	-0.46 ± 0.18	-0.50 ± 0.18	-0.54 ± 0.17	-0.60 ± 0.27	-0.14 ± 0.33	-0.16 ± 0.30
b. Mg/Ca-only Reconstruction							
10	-0.12 ± 0.12	-0.41 ± 0.18	-0.58 ± 0.17	-0.61 ± 0.17	-0.57 ± 0.26	-0.16 ± 0.32	-0.44 ± 0.29
8	-0.14 ± 0.12	-0.45 ± 0.17	-0.65 ± 0.17	-0.69 ± 0.17	-0.67 ± 0.26	-0.22 ± 0.31	-0.52 ± 0.29
6	-0.16 ± 0.13	-0.57 ± 0.18	-0.84 ± 0.17	-0.91 ± 0.17	-0.93 ± 0.27	-0.37 ± 0.32	-0.77 ± 0.30
4	-0.46 ± 0.12	-0.59 ± 0.18	-0.73 ± 0.17	-0.81 ± 0.17	-0.91 ± 0.25	-0.31 ± 0.31	-0.45 ± 0.28
2	-0.34 ± 0.13	-0.47 ± 0.19	-0.57 ± 0.18	-0.62 ± 0.18	-0.65 ± 0.27	-0.18 ± 0.33	-0.31 ± 0.30
b. $U^{k'}_{37}$*-only Reconstruction*							
10	-1.52 ± 0.15	-1.07 ± 0.22	-0.91 ± 0.24	-1.05 ± 0.23	-1.42 ± 0.31	-0.36 ± 0.38	+0.09 ± 0.35
8	-1.28 ± 0.14	-0.85 ± 0.20	-0.67 ± 0.22	-0.77 ± 0.22	-1.04 ± 0.29	-0.19 ± 0.35	+0.24 ± 0.32
6	-1.04 ± 0.14	-0.67 ± 0.20	-0.48 ± 0.20	-0.55 ± 0.20	-0.73 ± 0.28	-0.07 ± 0.33	+0.32 ± 0.29
4	-0.82 ± 0.13	-0.52 ± 0.19	-0.36 ± 0.18	-0.39 ± 0.18	-0.51 ± 0.26	+0.02 ± 0.33	+0.32 ± 0.29
2	-0.58 ± 0.13	-0.41 ± 0.19	-0.24 ± 0.18	-0.20 ± 0.18	-0.14 ± 0.27	+0.27 ± 0.33	+0.45 ± 0.30

Single indices are calculated by averaging the mean SST anomaly over the following regions: WPAC (120°E to 160°E, 4°S to 4°N), NINO4 (160°E to 190°E, 4°S to 4°N), NINO3.4 (190°E to 240°E, 4°S to 4°N), NINO3 (210°E to 270°E, 4°S to 4°N), NINO1+2 (270°E to 280°E, 10°S to 0°). Note that typically, NINO4, NINO3.4, and NINO3 are averaged over 5°S to 5°N, but the ERSST dataset used in this study is gridded only for every 2°, and we therefore average over 4°S to 4°N.TNI is calculated as NINO1+2 minus NINO4. WTNI is calculated as NINO1+2 minus WPAC.

A comparison of reconstructed SST values with proxy SST anomalies from the western (Figure 3.15) and eastern (Figure 3.16) Pacific reveals better matches at some locations than others, which we quantify with the residual sum of squares (RSS) in the top right of each scatterplot. Recall that the first two modes of the limited field were used as predictors of SSTs. Eigenvalues from the first and second modes under each scatterplot help explain why some proxy records are replicated better than others. These eigenvalues correspond to those plotted in the first two maps of Figure 3.5. Although not always the case, high RSS values, and hence poor fits, can often be attributed to low EOF values assigned to those locations, which suggests that these data contributed little to the reconstructed SST fields.

For the first mode (Figure 3.5, EOF no. 1), the signal is dominated by the east Pacific, with eigenvalues of much greater magnitude than those from the west Pacific (note the low EOF1 values on all of the west Pacific scatterplots of Figure 3.15). Of all the locations in the east Pacific, the three most northern records (proxy no. 11, 22, and 23) have the lowest EOF1 values, and of these, records 11 and 23 have high RSS values. Proxy no. 22, despite a low EOF1 value, is reconstructed quite well (RSS = 1.49°C^2). The two records with the lowest RSS values (RSS = 0.9°C^2), proxy no. 27 and 14, have two of the highest EOF1 values.

The second mode EOF no. 2 (Figure 3.5) is dominated by records from the western Pacific (note the low EOF2 values on the east Pacific scatterplots of Figure 3.16). It is important to remember, however, that the second mode explains only 12.6% of the limited-field variance (as compared to 78.2% by the first mode). Nevertheless, only 3 out of 15 reconstructions for the west Pacific show RSS values greater than 10°C^2, which suggests that reconstructions match proxy records better in the west than in the east, for which RSS >10°C^2 for 5 of 11 reconstructions.

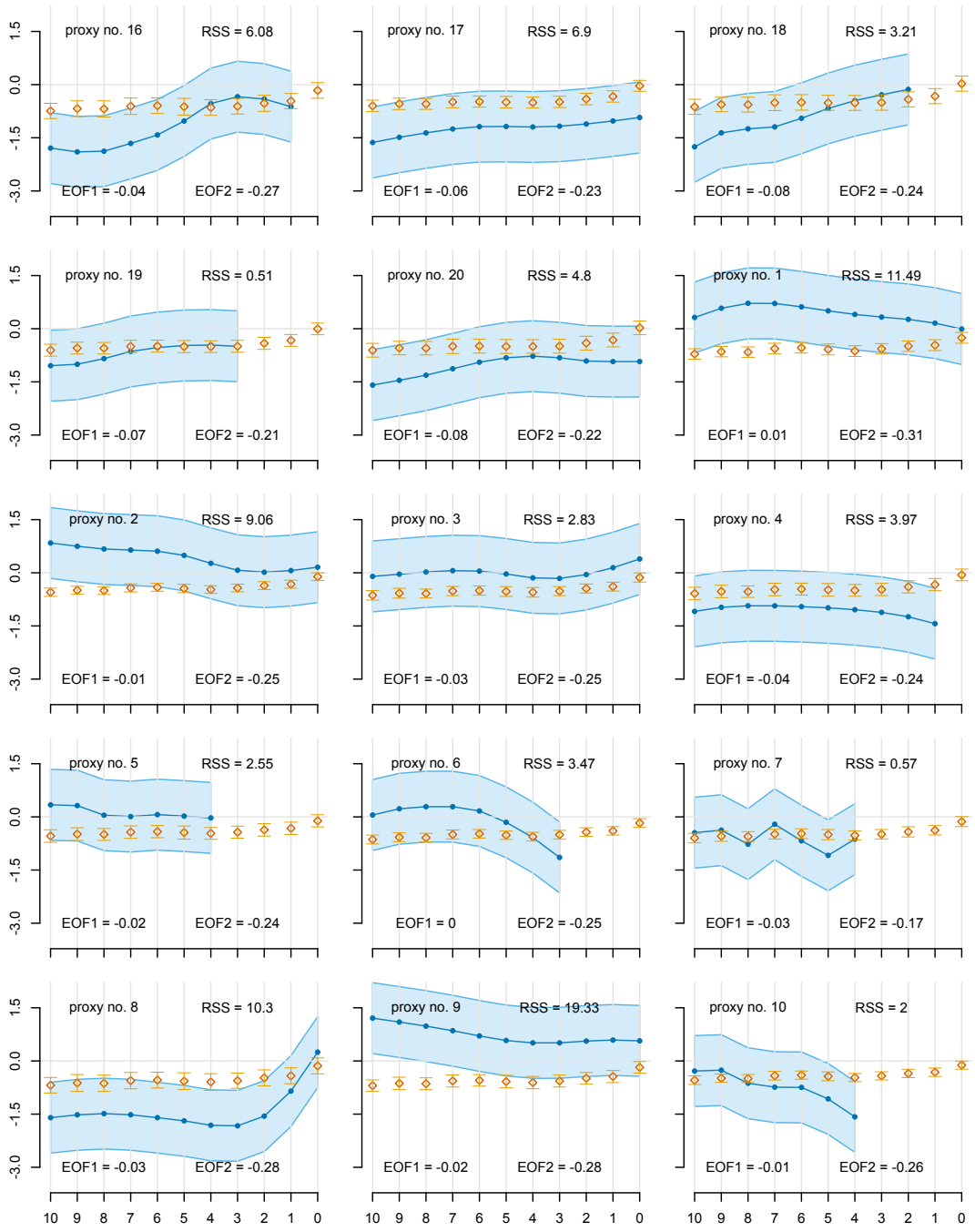

Figure 3.15: Scatterplots of each original proxy record from the western Pacific (blue) along with the reconstructed SST values for the grid-point nearest each record (orange). A nominal error value of ±1°C is shaded in light blue around each proxy record. Standard errors from the reconstruction model are plotted as orange whiskers. Proxy numbers in the upper left correspond to the numbers in Tables 1 and 2 and Figures 3.1 and 3.2. The residual sum of squares is provided to quantify how closely the reconstructed SSTs match the proxy SSTs. Recall that the first two PCs of the limited field were used as predictors for the PCA-based reconstruction model. The first two eigenvalues are written on the lower part of each scatterplot.

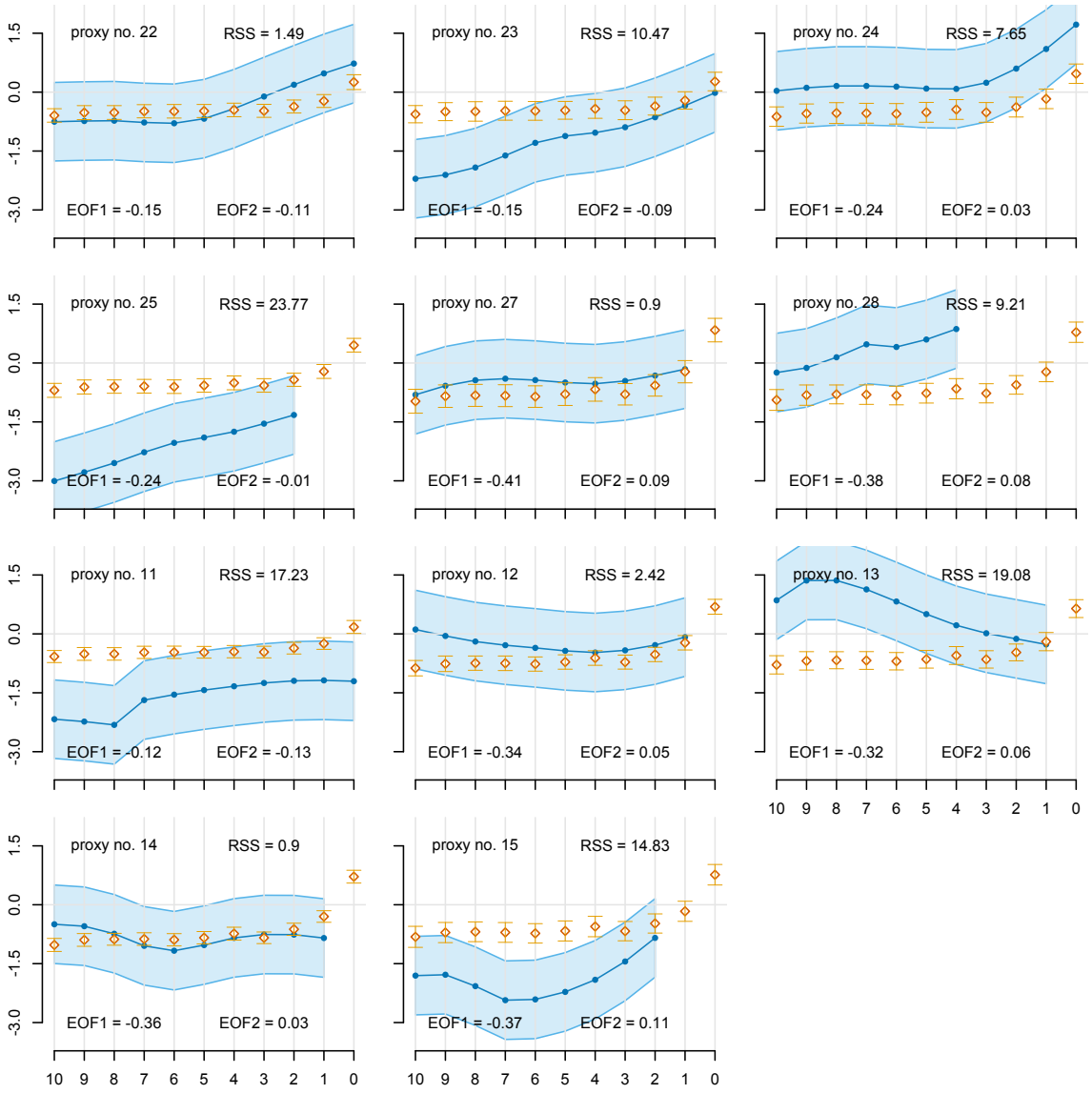

Figure 3.16: Same as Figure 3.15 but for eastern Pacific records.

3.5 Sensitivity to Proxy Type

Although Mg/Ca and $U_{37}^{k'}$ both provide reconstructions of SSTs, they differ in methodology and calibration. Furthermore, they are produced by two different groups of organisms that may each reflect biases related to season of production, depth habitat, water column stratification, and preservation (*Leduc et al.*, 2010). It is clear from Figures 3.1 and 3.2 that for a given location, records based on different proxies are not always consistent. These inconsistencies exist within proxy type as well. In a case for which there are many records, a reduced-dimension reconstruction approach is particularly beneficial, assuming that biases across the various proxy reconstructions cancel out. By combining all records, this method extracts common features across the proxies and allows for a robust reconstruction of the most dominant patterns of variability. Additionally, including all the proxy records together allows for wider coverage in both space and time, than if one were to reconstruct using only one proxy type. For these reasons, we recommend the multi-proxy approach. We recognize, however, that comparing a reconstruction based only on Mg/Ca with one based only on $U_{37}^{k'}$ provides a test of the sensitivity of proxy type to the multi-proxy reconstruction. All 15 records listed in Table 3.1 were used in the Mg/Ca-only reconstruction (Figure 3.17, top), and all 14 records listed in Table 3.2 were used in the $U_{37}^{k'}$-only reconstruction (Figure 3.17, bottom).

SST reconstructions based on either Mg/Ca or $U_{37}^{k'}$ show negative anomalies throughout 10-2 ka, and weak negative anomalies for the present-day 1854-2013 period. They differ, however, in magnitude and timing of cold anomalies. First, for Mg/Ca, the coldest eastern equatorial SST anomalies occur in a well-defined "cold tongue" pattern at 6 ka, which is also the period of largest zonal difference in SSTs of -0.77°C ± 0.30°C (Table 3.3b). For $U_{37}^{k'}$, however, maximum eastern equatorial cooling occurs at 10 ka. The zonal difference during this time is slightly positive, though, since larger negative anomalies are seen in the western Pacific (Table 3.3c).

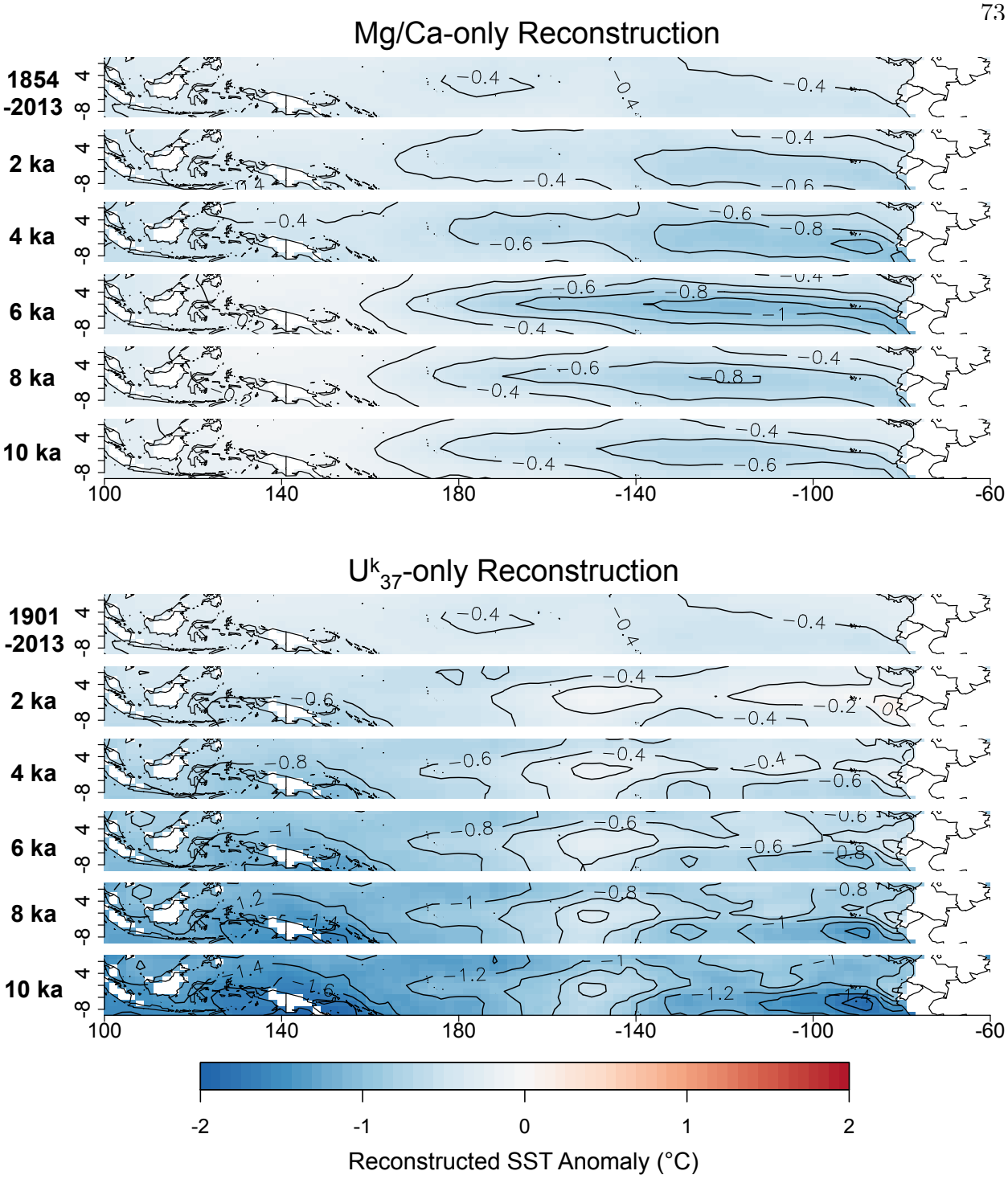

Figure 3.17: Single proxy reconstructions of 10, 8, 6, 4, and 2 ka SSTs using only Mg/Ca proxies (top) and $U_{37}^{k'}$ proxies (bottom). The top panel of each provides a reconstruction of present-day (1854-2013) SSTs using the limited-field data.

Second, the evolution of SSTs in the west Pacific is strikingly different: In the Mg/Ca reconstruction, the western Pacific cold anomalies are always smaller than those of the eastern Pacific, but in the $U_{37}^{k'}$ reconstruction, west Pacific cold anomalies are almost always as large as and sometimes larger than those of the eastern Pacific. This characteristic in the $U_{37}^{k'}$ reconstruction is inconsistent with a typical La Niña-like SST configuration, where the western Pacific is warmer than the eastern Pacific, and is also inconsistent with model results for the early- to mid-Holocene (*Liu et al.*, 2000; *Otto-Bliesner et al.*, 2003; *Zheng et al.*, 2008).

Lastly, only the $U_{37}^{k'}$ reconstruction shows warmer eastern equatorial SSTs during 2 ka than present-day. This would be consistent with marine records *Koutavas et al.* (2006); *Tudhope et al.* (2001) and sediment records *Moy et al.* (2002); *Rodbell et al.* (1999) that have suggested an abrupt return of ENSO variability (i.e. more El Niño's and thus, warmer eastern equatorial SSTs) at around 2 ka.

3.6 Discussion

We apply PCA-based and CCA-based reduced-dimension reconstructions of the full field of SSTs and ENSO variability during the past 10 ka. Using a limited spatial field of 26 locations provides enough data to resolve the major patterns of variability for the entire Pacific SSTs and most of the central Pacific zonal winds.

For the multi-proxy reconstruction, the period with the coolest eastern equatorial Pacific (-1°C) and strongest easterly winds (-8 m s^{-1}) across the central Pacific occurred at 10 ka, with similar patterns, but gradually decreasing magnitudes persisting until 6 ka. By 4 to 2 ka, the Pacific remained in a state cooler than present, but with SST anomalies around -6 to -4°C.

Assuming decreased ENSO variability is consistent with an enhanced La Niña-like state, the timing of maximum cooling in these findings is consistent with the timing reconstructed by both *Rodbell et al.* (1999) and *Moy et al.* (2002), who used records of sedimentation in lakes in Ecuador to infer ENSO variability over the past 15 and 12 ka, respectively,

and who showed an increasing occurrence of ENSO following 7 ka along with a low frequency of ENSO events prior to that. Additionally, in a comparison of east and west Pacific proxy SST reconstructions, *Koutavas et al.* (2006) claimed that the period of an enhanced zonal gradient across the Pacific, and thus, an enhanced La Niña-like state, existed from 11 ka until 5 ka. *Clement et al.* (2000), who used an orbitally forced model to reconstruct ENSO variability during the past 12 ka, found that the amplitude of ENSO events increased from 10 ka to present, but that both the amplitude and frequency increased during the latter half of that period. Our reconstructions are consistent with this if one assumes that increased ENSO amplitude and frequency would result in warmer anomalies during the mid- to late-Holocene.

Koutavas et al. (2006) emphasized the role of the zonal difference between the east and west Pacific that helped create persisting La Niña conditions, and inferred that although the enhanced zonal SST difference lasted from 11-5 ka, it was strongest at 6 ka. This calls attention to the importance of considering not only periods of greatest cooling, but also the periods when the SST difference between eastern and western Pacific was greatest. As noted in Table 3.3a, the zonal difference in the multi-proxy reconstructions was largest at 6 and 10 ka. This timing coincides well with the timing suggested in the multi-proxy reconstructions: (1) the largest zonal difference, and presumably lowest ENSO variability, occurs at 10 and 6 ka, (2) between 10 and 6 ka, the zonal difference decreases slightly, but remains "La Niña-like," and (3) the late Holocene (4 to 2 ka) show only small negative zonal differences.

The PCA and CCA based methods offer several advantages: they are conceptually simple, and have a well-developed theoretical foundation and rich history of application to climate field reconstructions. They are, however, limiting in other ways: the reconstructions are based on only linear projections, quantification of uncertainty in the reconstructions can be unwieldy and, it is not straightforward to incorporate uncertainty information of the proxy data. Emerging Bayesian Hierarchical Modeling framework offers attractive alternatives to addressing these limitations, especially in estimating uncertainties in a robust manner by

including data and model uncertainties.

Chapter 4

Multi-Proxy Reconstruction of Indian Summer Monsoon Winds and Precipitation of the past 10,000 Years using Mg/Ca and Alkenone Records

Abstract

Using a multi-proxy reduced dimension methodology we reconstruct full fields of summer monsoon wind stress curl and rainfall anomalies over the Indian monsoon region since the early-Holocene using SST proxies (Mg/Ca and alkenones) from forty locations scattered across the Arabian Sea, the Bay of Bengal, and the east and west equatorial Pacific. Summer wind stress curl reconstructions reveal that the greatest magnitudes of positive wind stress curl ∼30% greater than present day off the coastlines of Oman and Yemen occurred at 10 ka, suggesting enhanced ocean upwelling and a strong monsoon jet during this time. Strong positive anomalies in these regions continued but weakened slightly from 8 to 6 ka. By 2 to 4 ka, wind stress curl anomalies in the monsoon jet region weakened to 10-20% greater than present day. This pattern is consistent with previous studies that use the fraction of *Globigirina bulloides* to reconstruct upwelling strength in the western Arabian Sea over the past 10 ka. Spatial rainfall reconstructions reveal the greatest difference in precipitation at 10 ka over the core monsoon region (20-60% greater than present day), and the greatest deficit in rainfall in North East India and on the eastern side of the Western Ghats (10-30% less than present day). Rainfall over the core monsoon region was about 30% greater than present day from 8 to 6 ka, but decreased to not much more than 20% from 4 to 2 ka. These findings advance the hypothesis that teleconnections from the equatorial Pacific could ex-

plain greater early- to mid-Holocene wetness over India as recorded by various paleoclimate proxies.

4.1 Background

Paleoclimatic evidence from climate proxy data suggests that India has aridified over the past 10 thousand years (ka). The predominantly cited explanation rests on the idea that greater summer insolation in early Holocene time, due to the precessional cycle, caused greater heating of the Indian subcontinent, which increased the land-ocean temperature gradient which created a stronger early than late Holocene monsoon (e.g. *Kutzbach*, 1981; *Kutzbach and Otto-Bliesner*, 1982; *Liu et al.*, 2000, 2003). This idea relies on the basic understanding of monsoon dynamics. The monsoon begins each year in mid-May due to the intense spring heating of the Indian subcontinent and possibly the Tibetan Plateau, which creates a temperature, and thus, surface pressure gradient between the land and the surrounding ocean that forces the monsoon jet (e.g. *Li and Yanai*, 1996; *Wu et al.*, 2007), at least during the early (mid-May to mid-June) and late (Sep to mid-Oct) seasons (*Rajagopalan and Molnar*, 2013). In principle, over the course of the entire monsoon season, the degree of the local land warming can modulate the strength not only of the jet strength but also of monsoon rainfall. Therefore, a sensible hypothesis follows that enhanced land warming during the early- to mid-Holocene contributed to greater wetness over India. Since the mid-1990s, however, surface temperatures over India have risen dramatically while monsoon rainfall has remained below average (*Krishna Kumar et al.*, 2011), which suggests that other processes also affect monsoon strength, whether measured by rainfall or wind speeds.

Teleconnections from the equatorial Pacific - El Niño Southern Oscillation (ENSO) - also modulate the strength of the monsoon on inter-annual time scales. During La Niña (El Niño), when central and eastern tropical Pacific SSTs are anomalously cool (warm), monsoon rainfall commonly is strong (weak). There is an asymmetry in this relationship (See Chapter 2 and *Krishna Kumar et al.* (2006)) in that La Niña conditions almost always are associated

with a strong monsoon year, but El Niño conditions have historically resulted in either normal or weak monsoon years. *Krishna Kumar et al.* (2006) attribute this asymmetry to the location of El Niño-related warming in the Pacific and explain that central Pacific warming favors drought more than eastern Pacific warming.

Proxy records from the east and west Pacific that reconstruct SSTs throughout the past 10 ka suggest a shift from a more La Niña-like state during the early- to mid-Holocene to a more El Niño-like state during the late-Holocene (e.g. *Conroy et al.*, 2008; *Koutavas et al.*, 2002, 2006; *Leduc et al.*, 2007, 2010; *Pahnke et al.*, 2007; *Stott et al.*, 2002, 2004). Additionally, primary productivity records from the Banda Sea (*Beaufort et al.*, 2010) as well as sediment records from Ecuador and Peru (e.g. *Chazen et al.*, 2009; *Moy et al.*, 2002; *Riedinger et al.*, 2002; *Rein et al.*, 2005; *Rodbell et al.*, 1999; *Sandweiss et al.*, 1996, 2001) all suggest an increase in ENSO variability after the mid-Holocene. Climate model simulations for Holocene time also suggest a cooler equatorial Pacific and rare El Niõ events until around 6 ka (e.g. *Clement et al.*, 1999, 2000; *Emile-Geay et al.*, 2007).

Assuming the contemporary relationship between ENSO and the monsoon persisted through the past 10 ka, and given the reliability of La Niña in producing strong monsoons, we advance a second hypothesis that is independent from the land-warming hypothesis: equatorial Pacific cooling (i.e. La Niña-like state) during the early- to mid-Holocene contributed to greater rainfall over India. Following similar logic, the return of ENSO variability during the late Holocene could have contributed to aridification in late-Holocene. As these two hypotheses (land-warming and ENSO) are not mutually exclusive, we aim not to disprove the land-warming hypothesis, but to test the plausibility of the ENSO hypothesis.

To do so, we exploit SST proxy data from the eastern and western equatorial Pacific (Tables 3.1 and 3.2, Figures 3.1 and 3.2), as well as the Indian Ocean (Table 4.1, Figure 4.1). In Chapter 3, we used a reduced-dimension multi-proxy reconstruction approach to combine magnesium/calcium (Mg/Ca) and alkenone ($U^{k'}_{37}$) SST records from the east and west Pacific to reconstruct full fields of tropical Pacific SSTs and zonal winds. We found

that the coldest eastern equatorial Pacific SST anomalies occurred during the early Holocene (10 ka), but the largest reconstructed zonal SST differences between east and west Pacific occurred during 10 and 6 ka. The smallest zonal differences were seen from 4 to 2 ka. This timeline is consistent with an enhanced La Niña-like state during the early- to mid-Holocene, but not during the late Holocene.

Table 4.1: A list of the Mg/Ca- and $U^{k'}_{37}$-based proxy records from the Indian Ocean used in the summer monsoon wind and rainfall reconstructions.

Record #	**Core**	**Lat**	**Lon**	**Calibration**	**Reference**
Mg/Ca-based SST records					
30	SK 237 - GC04	11.0	75.0	*Dekens et al.* (2002)	*Saraswat et al.* (2013)
31	GeoB 10029 - 4	-1.5	100.1	*Anand et al.* (2003)	*Mohtadi et al.* (2010)
32	GeoB 10038 - 4	-5.9	103.3	*Anand et al.* (2003)	*Mohtadi et al.* (2010)
33	SK 157 - GC04	2.4	78.0	*Dekens et al.* (2002)	*Saraswat et al.* (2005)
34	AA S9/21	14.5	72.7	*Bemis et al.* (1998)	*Govil and Naidu* (2010)
$U^{k'}_{37}$-based SST records					
35	MD77 - 194	10.3	75.1	*Prahl et al.* (1988)	*Sonzogni et al.* (1998)
36	SO90 - 39KG	24.8	65.9	*Sonzogni et al.* (1997)	*von Rad et al.* (1999); *Doose-Rolinski et al.* (2001)
37	MD85 - 668	0.02	46.0	*Prahl et al.* (1988)	*Bard et al.* (1997)
38	SO90 - 93KL	23.6	64.2	*Müller et al.* (1998)	*Schulz et al.* (2002)
39	SO90 - 136KL	23.1	66.5	*Müller et al.* (1998)	*Schulte and Müller* (2001)
40	SO93 - 126KL	20.0	90.0	*Sonzogni et al.* (1997)	*Kudrass et al.* (2001)
41	TY93 - 905	11.1	52.0	*Prahl et al.* (1988)	*Kim et al.* (2004)
42	TY93 - 929/P	13.7	53.3	*Prahl et al.* (1988)	*Rostek et al.* (1997)
43	SO139 - 74KL	-6.5	103.8	*Conte et al.* (2006)	*Lückge et al.* (2009)

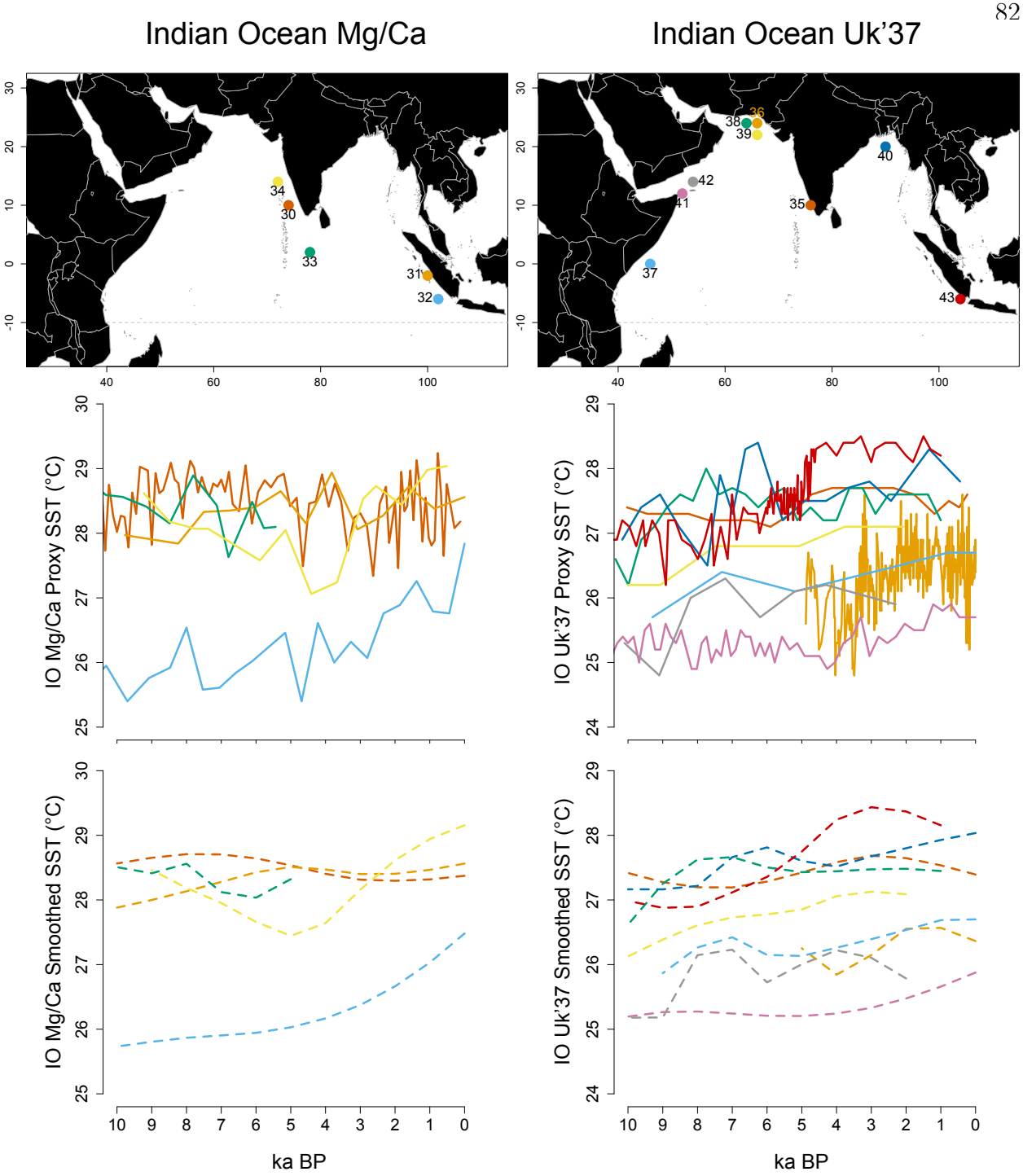

Figure 4.1: Maps of Indian Ocean Mg/Ca- and $U^{k'}_{37}$-based SST records. The second row provides raw SST estimations as calibrated by original authors listed in Table 4.1. The third row provides the records smoothed by a second order local polynomial method with a local neighborhood of 70% nearest data points.

Motivated by this hypothesis and the scattered proxy records across the Indian monsoon region in Figure 1.3 (explained in further detail in Section 4.2), we ask: Could the aridification of India since 10 ka be attributed, at least in part, to teleconnections from the Pacific? We use the same reduced-dimension multi-proxy reconstruction approach to reconstruct full fields of summer wind stress curl over the Arabian Sea and Indian summer monsoon rainfall anomalies for the past 10 ka using only SST proxy records from the Indo-Pacific region along with contemporary patterns of variability.

4.2 Paleoclimatic Evidence of a Wetter India

Evidence suggesting a stronger early- to mid-Holocene ($\sim$ 10-6 ka BP) Indian summer monsoon exists as both continental and marine proxy records that extend across the monsoonal region from southern Oman across the Bay of Bengal (Figure 1.3). Greater precipitation during the early- to mid-Holocene than late-Holocene (post 4 ka) has been inferred (*Bryson and Swain*, 1981; *Swain et al.*, 1983) from pollen reconstructions (*Singh et al.*, 1972, 1973, 1974, 1990) and lake-bed sedimentology records (*Achyuthan et al.*, 2007; *Deotare et al.*, 2004; *Enzel et al.*, 1999; *Kajale and Deotare*, 1997; *Prasad et al.*, 1997; *Wasson et al.*, 1984) from northwestern India. Although the lakes Bap Malar, Didwana, Kanod, Lunkaransar, Nal Sarovar, Sambhar, Tal Chapar, and Parihara (Figure 1.3, blue) did not dry up simultaneously, each shows maximum wetness occurring sometime during the early- to mid-Holocene, followed by a period of aridification during the late Holocene. Interestingly, a carbon isotope record obtained from peat located in Nilgiri Hills region of south India (Figure 1.3, yellow) shows an arid phase during the mid-Holocene followed by a wetter phase in the recent period (*Sukumar et al.*, 1993). Though opposite to those cited above for the region to the north, his finding is actually consistent with the lake records, as this region, positioned in the rain shadow of the Western Ghats, is typically out of phase with the rest of the sub-continent in present-day rainfall (*Gill et al.*, 2015).

Marine isotope records from boreholes located just south of the mouths of major Indian

river systems that empty into the Arabian Sea and Bay of Bengal have also been exploited to reconstruct isotope or sediment records that reflect discharge during the past 10 ka. In the Arabian Sea, *Staubwasser et al.* (2003) used δ^{18}O from the mouth of the Indus River (Figure 1.3, 63KA) from the last 6 ka to infer a drastic reduction in discharge at 4.2 ka, which is concurrent with the termination of the ancient Harappan civilization that inhabited the Indus Valley. Farther south, numerous rivers drain from the Western Ghats into the eastern Arabian Sea. Oxygen isotopes from a sediment core just off the coast (Figure 1.3, red 3268G5) has been used to reconstruct Holocene evaporation minus precipitation, and *Sarkar et al.* (2000) inferred relatively high precipitation from 10 to 6 ka, followed by an arid episode from 3.5 to 2 ka. For the Bay of Bengal, *Ponton et al.* (2012) used a borehole (NGHP-16A) located at about 16°N (Figure 1.3, red 16A) to reconstruct Godavari River basin vegetation changes as well as salinity changes in the Bay. They report a period of aridity beginning at 4 ka and unprecedented high salinity from 3 ka to present-day, implying lower precipitation and lower river discharge during the late Holocene compared to either the early- or mid-Holocene. Farther north *Kudrass et al.* (2001) use alkenone temperature data (*Sonzogni et al.*, 1998) and δ^{18}O data (*Rostek et al.*, 1993) from SO93-126KL (Figure 1.3, red 126KL) to reconstruct salinity at the mouth of the Ganges River in the northern Bay of Bengal. They find that salinity decreased during the early Holocene, reaching a minimum at 6 ka, and subsequently increased until present-day. In the same region, *Goodbred and Kuehl* (2000) analyzed over 50 borehole records scattered across the coastal region of Bangladesh (Figure 1.3, purple box) to reconstruct sediment discharge from the Ganges and found high sediment discharge from 11 to 7 ka. This, combined with the findings of *Kudrass et al.* (2001), suggests that river discharge from the Ganges, which is reflective of precipitation over the Indo-Gangetic Plains, was high during the early- and mid-Holocene.

Monsoon variability and strength has also been reconstructed using continental and marine records from Oman and the western Arabian Sea, where biological productivity and isotope proxies are used to infer ocean upwelling, wind strength, and precipitation for the past

10 ka. Speleothem records in Oman from the Hoti Cave (*Neff et al.*, 2001; *Fleitmann et al.*, 2007), Qunf Cave (*Fleitmann et al.*, 2003, 2007) and Defore Cave (*Fleitmann et al.*, 2007) suggest a more intense rainfall during early Holocene but decreasing monsoon strength during the mid- to late-Holocene (Figure 1.3, orange). When the monsoon jet sweeps across the coastlines of Somalia and Oman, it induces upwelling, which enhances biological productivity. *G. bulloides* is a planktic foraminifer that thrives in this cold nutrient-rich upwelling water during the monsoon and acts as a proxy for wind strength (e.g. *Curry et al.*, 1992; *Prell and Curry*, 1981). A high-resolution record provided by *Gupta et al.* (2003) from core site ODP-723A reveals a monotonic decrease in *G. bulloides* between 10 ka and 2 ka, which is inferred to imply decreasing strength of winds during the summer monsoon. Another productivity record (using Ba/Al ratios from *N.dutertrei*) off the Somali coast (NIOP-905) also implies decreased upwelling from 10 ka to present (*Ivanochko et al.*, 2005).

4.3 Modern Data

Contemporary (1901-2013) gridded (2° by 2°) monthly SSTs were obtained from the NOAA NCDC Extended Reconstruction Sea Surface Temperature (ERSST) version 3b dataset (*Smith et al.*, 2008). Contemporary monthly gridded (1.875° by 1.875°) wind stress curl (10^{-8} kg m^{-2} s^{-2}) was calculated using NOAA NCEP-NCAR CDAS-1 zonal and meridional momentum flux data for the period 1949-2013 (*Kalnay et al.*, 1996) and masked to include only the surface wind stress curl over Arabian Sea gridcells. Monthly anomalies were calculated for each dataset using the 1981-2010 climatology. Monthly SST anomalies were then converted to annual averages by averaging from May to the following April in order to capture the annual ENSO cycle. Summer wind stress curl anomalies were calculated by averaging June, July, August and September anomalies. Daily gridded (1° by 1°) rainfall was obtained from the India Meteorological Department (*Rajeevan et al.*, 2006). Seasonal average daily rainfall (mm d^{-1}) time series were created for each grid point by averaging the daily totals from 1 Jun to 30 Sep over the 1901-2004 period.

Two common paleo-proxy records are used: magnesium/calcium ratios in planktonic foraminifera (Mg/Ca) and an index of unsaturation in alkenones ($U_{37}^{k'}$) that formed at shallow depths. See Chapter 3 for more information on the use of these proxies in this reconstruction framework. *Lea et al.* (1999) and *Nürnberg et al.* (1996) summarize Mg/Ca paleothermometry, and *Brassell et al.* (1986) and *Herbert* (2003) describe $U_{37}^{k'}$ paleothermometry.

There are 43 total SST proxy records (20 Mg/Ca and 23 $U_{37}^{k'}$), but for 3 sites both types of proxy records have been obtained. In those instances, we use the Mg/Ca records instead of the $U_{37}^{k'}$, as we did in Chapter 3. All 43 proxy records are listed in Tables 3.1, 3.2, and 4.1. As shown in Figures 3.1, 3.2, and 4.1, these records are sampled at various temporal resolutions. We, therefore, smooth the raw SST records using a local polynomial method with a second order polynomial and a local neighborhood consisting of 70% of the nearest data points (e.g. *Loader et al.*, 1996). These records were then converted to SST anomalies using the climatological mean temperature from ERSST at the grid-cell closest to the location of the proxy record. All paleo-SST records were obtained from the archives of NCDC (http://www.ncdc.noaa.gov/data-access/paleoclimatology-data/datasets) and Pangaea (http://www.pangaea.de/).

4.4 Methodology

During summer season, SSTs over northern Indian Ocean (Arabian Sea and Bay of Bengal) are modulated by the monsoon (*Krishnamurthy and Kirtman*, 2003), wherein strong winds enable cooler SSTs from coastal upwelling and evaporative cooling. Therefore, reconstructing the winds obviates the need for SST reconstructions. Indian Ocean SSTs exhibit a well documented (e.g. *Allan et al.*, 1995; *Terray and Dominiak*, 2005; *Ihara et al.*, 2008b; *Roxy et al.*, 2014) recent warming trend largely attributed to anthropogenic sources. This anthropogenic SST signal, which might have been imparted to the wind stress curl, must be removed so that only the internal variability is reconstructed. To this end, first, a principal component analysis (PCA) of 1949-2013 ERSST Indian Ocean SSTs was performed and as

expected the first orthogonal mode accounts for nearly 70% of the total variability in the data (Figure 4.2b), and is characterized by a strong warming trend (Figure 4.2a). Each of the remaining modes, however, explains only a small fraction of the remaining variance (Figure 4.2b). Then we regressed summer wind stress curl at each of the 262 grid points over the Arabian Sea against the first Principal Component (PC). The residuals from the regression represent the de-trended wind stress curl time series at each grid point.

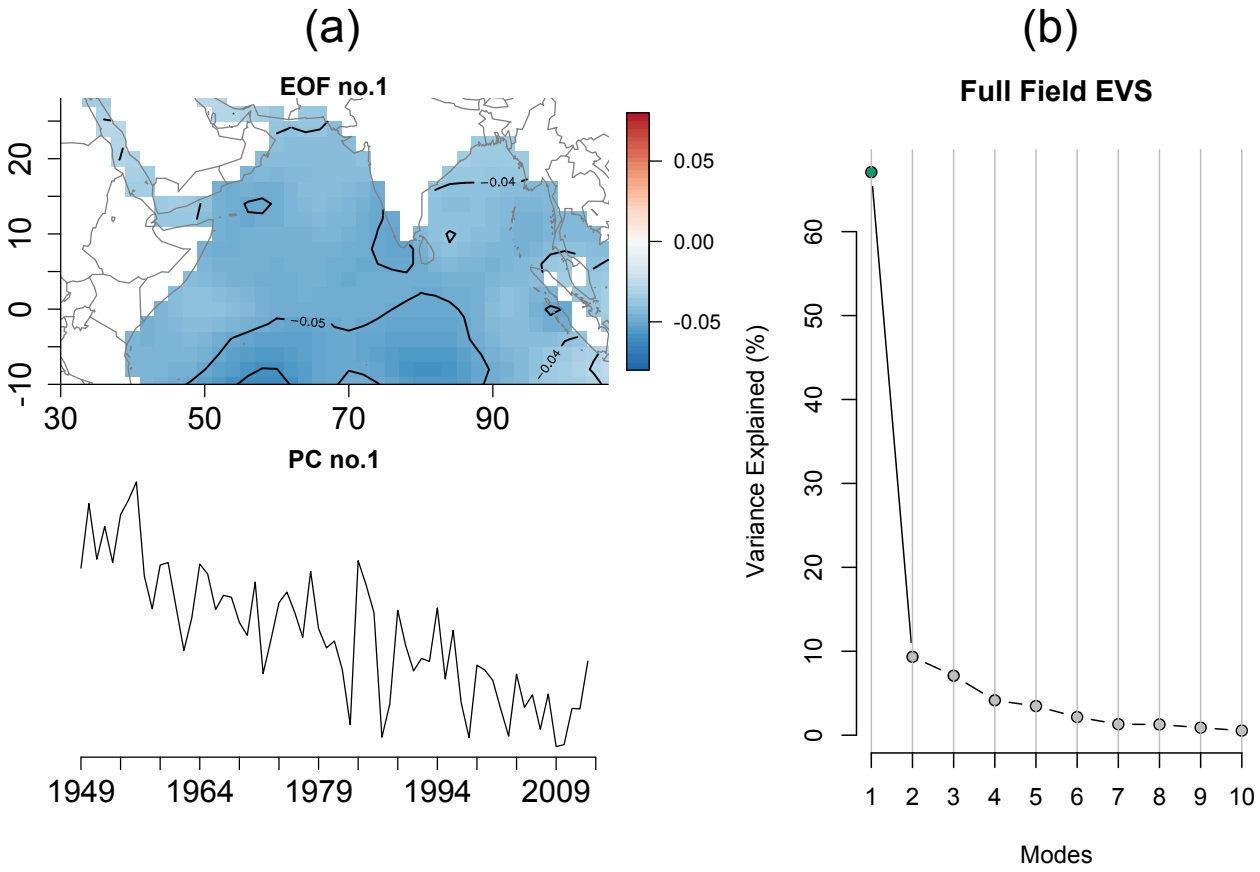

Figure 4.2: First orthogonal mode of summer (June-Sep) Indian Ocean SSTs from 1949-2013 (*Smith et al.*, 2008). As shown by the spatial EOF (a, top) and the PC (a, bottom), the most dominant mode is a strong contemporary trend. The influence of this trend was removed from summer contemporary wind data prior to paleo-reconstructions. This mode accounts for nearly 70% of the total variance of the data, which can be seen on the eigenvalue spectrum (right, b), which explains the resolved variance of each of the first ten modes. The 2^{nd} and 3^{rd} modes explain 9% and 7% of the total variance, respectively. The 4^{th} mode, and all modes after, each explain less than 5% of the total variance.

Interannual variability of monsoonal winds and consequently the Indian summer rainfall are influenced by the Walker Circulation, which is directly affected by equatorial Pacific SSTs (e.g. *Krishna Kumar et al.*, 1995; *Parthasarathy and Pant*, 1985; *Shukla and Mooley*, 1987; *Shukla and Paolino*, 1983; *Webster*, 1987; *Webster et al.*, 1998) and to a lesser extent Indian Ocean SSTs. Therefore, to reconstruct variations in monsoon strength, we use SST proxy records from the Indian Ocean and equatorial Pacific to reconstruct anomalies in Arabian Sea summer wind stress curl, as well as in monsoon rainfall over India. The reconstruction methodology consists of two key steps on the contemporary fields - (i) using PCA to isolate a small number of leading modes of variability in the contemporary limited SST field (i.e. SSTs at the locations of the proxy data) and the contemporary full u- and v-wind fields of the Indian Ocean, and (ii) using Canonical Correlation Analysis (CCA) to obtain the best relationship that relates the modes of wind fields to that of SST. Then we use these relationships along with the proxy data to reconstruct the modes of variability of wind stress curl and consequently the spatial field. The same approach is employed for reconstructing rainfall over the Indian subcontinent. The flowchart of this approach is shown in Figure 4.3 and described in detail in Chapter 3 where we used this to reconstruct SSTs and zonal winds over equatorial Pacific during the past 10,000 years. We describe steps of the methodology briefly below and for details we refer the reader to Chapter 3.

4.4.1 Reconstruction of Summer Monsoon Wind Fields

The contemporary, de-trended, full-field summer wind stress curl obtained as described above is organized into a matrix of dimension NxG, where N (= 65, 1949-2013) is the number of years and G (=262) is the number of grid points.

Step (i). A Principal Component Analysis (PCA) is performed on the wind stress curl field. The first four PCs of the wind stress curl field account for 22.1%, 10.6%, 9.7%, and 8.9%, respectively, of the total variance of the field (Figure 4.4a). The spatial and temporal patterns of these modes are shown as empirical orthogonal functions (EOFs) and PCs for

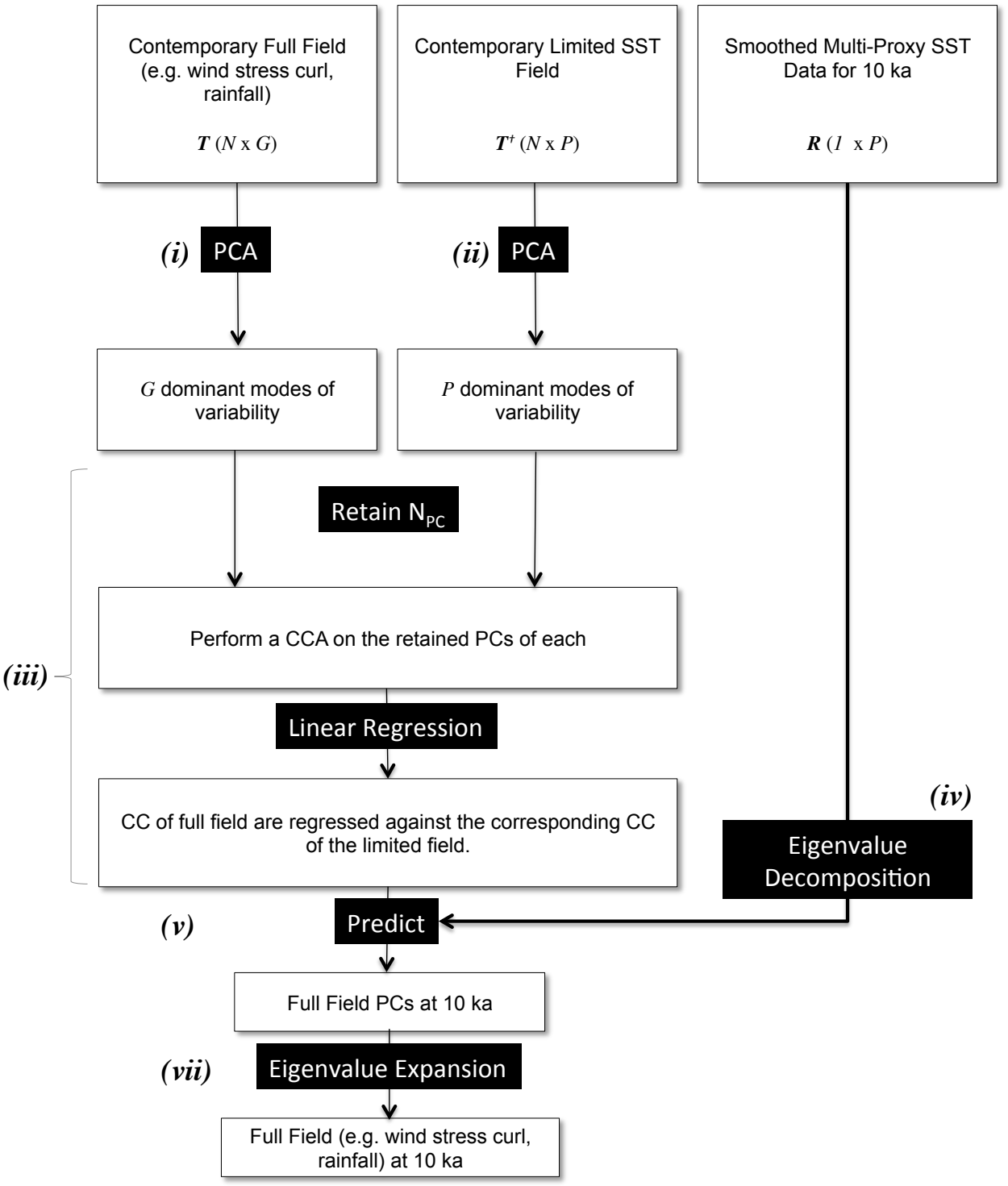

Figure 4.3: Flow chart of canonical correlation analysis (CCA) approach used for the multi-proxy summer wind stress curl and rainfall reconstruction. The steps are given for producing SSTs representative of 10 ka. Steps $(iii - vi)$ are repeated for 8, 6, 4, and 2 ka.

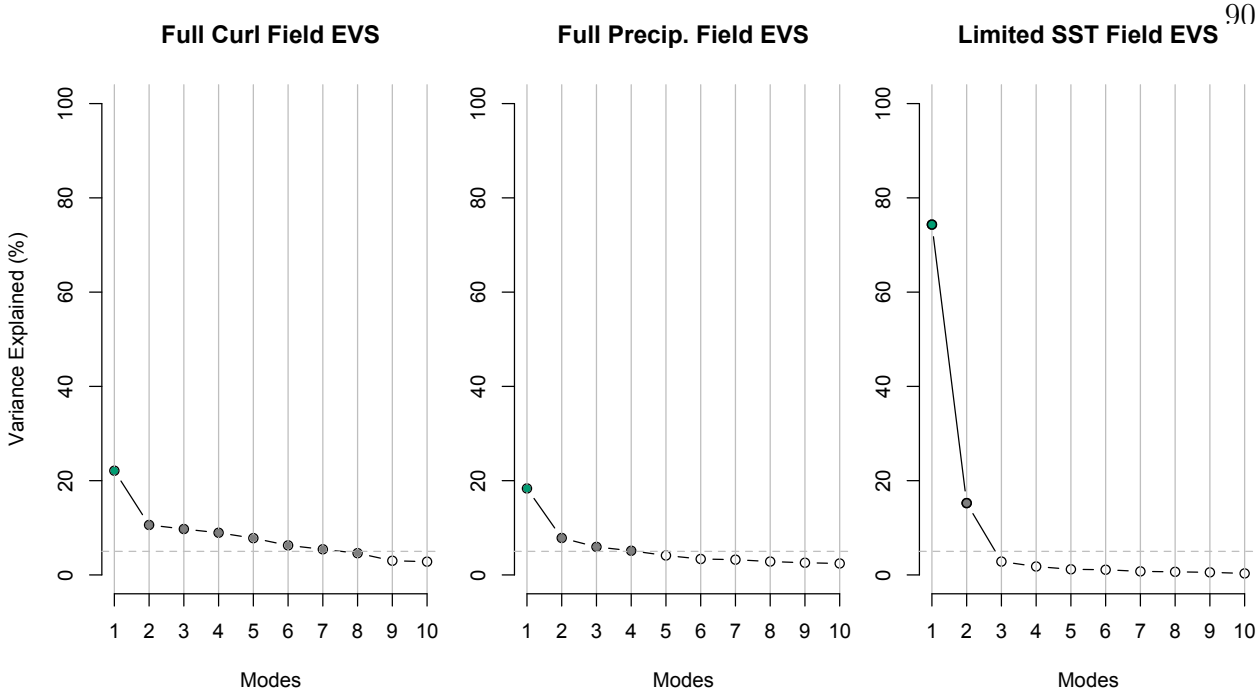

Figure 4.4: Eigenvalue spectrums (EVS) for the (a) full field of Arabian Sea summer wind stress curl (1949-2013) (*Kalnay et al.*, 1996), (b) full field of Indian summer monsoon rainfall (1901-2004) (*Rajeevan et al.*, 2006), and (c) limited Indo-Pacific SST field (1949-2013) (*Smith et al.*, 2008). The green points represent the variance explained by the first mode of each field. The grey dots represent all subsequent modes that each explain at least 5% of the total variance of the respective datasets. This 5% threshold was considered in deciding how many PCs to retain for each CCA reconstruction.

Arabian Sea wind stress curl (Figure 4.5). The first PC of the wind stress curl shows strong eigenvalues in the monsoonal jet region over the Arabian Sea.

Step (ii). Let the contemporary limited-field SST data at the locations of paleo-proxy data, which extend across the Indo-Pacific region (Figures 3.1, 3.2, and 4.1), be organized as a matrix of dimension NxP. Where N is the length of the contemporary time period as before (1949-2013 therefore $N = 65$) and P $(= 40)$ is the number of paleo-proxy records . A PCA on this limited field reveals that the first four modes of the limited Indo-Pacific SST field account for 74.3%, 15.2%, 2.8%, and 1.8% of the limited field variance (Figure 4.4). As seen in Figure 4.6 the first EOF is heavily weighted by changes in the eastern Pacific.

Step (iii). We retain a small number of PCs (N_{PC}) from the contemporary full field

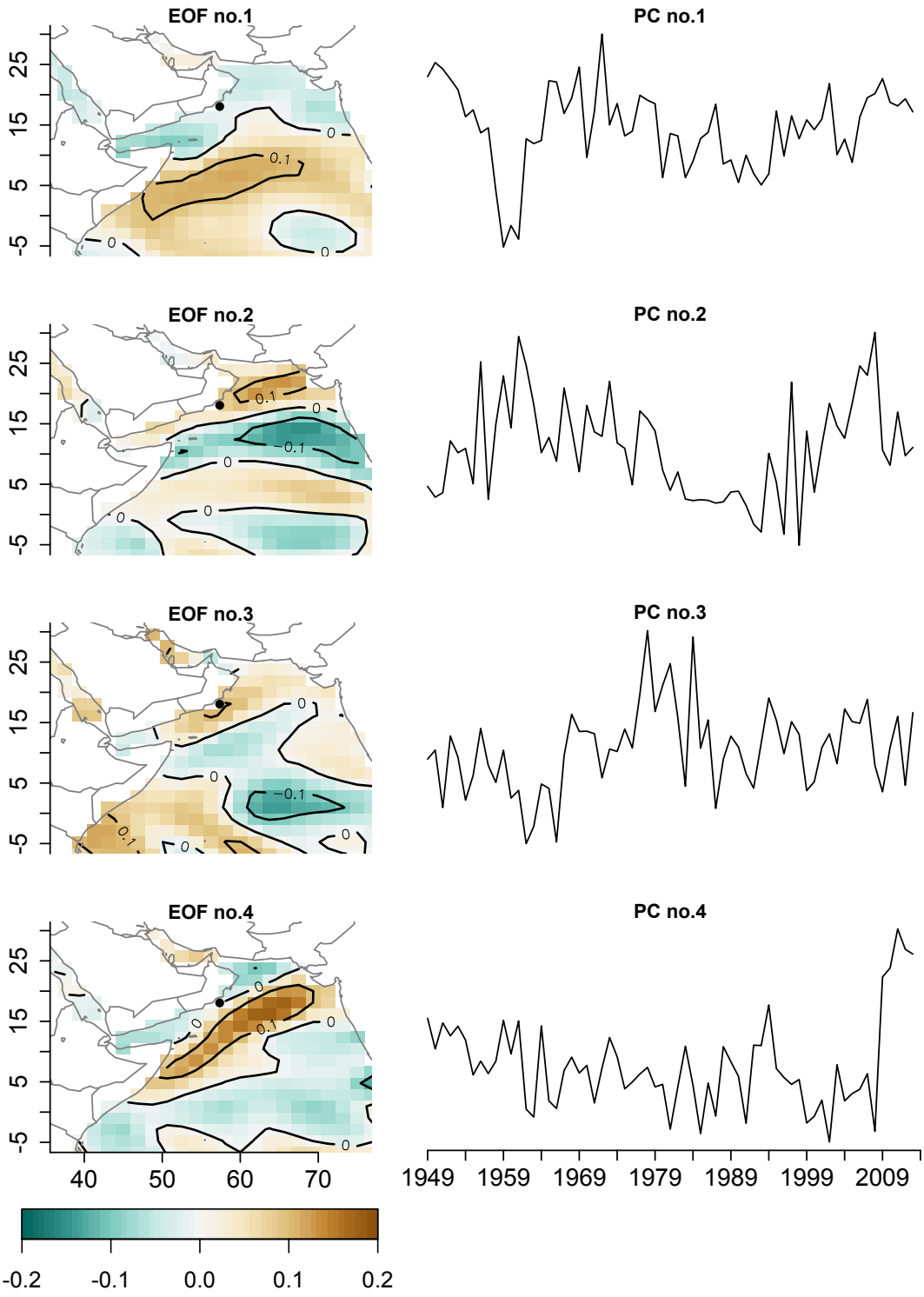

Figure 4.5: First four orthogonal EOFs and PCs of Arabian Sea summer wind stress curl over the monsoon region from 1949-2013 (*Kalnay et al.*, 1996). The first four modes of wind stress curl explain 22.1%, 10.6%, 9.7%, and 8.9%, respectively, of the full field variance. The black point off the coast of Oman indicates the location of the *Gupta et al.* (2003) *G. bulloides* record.

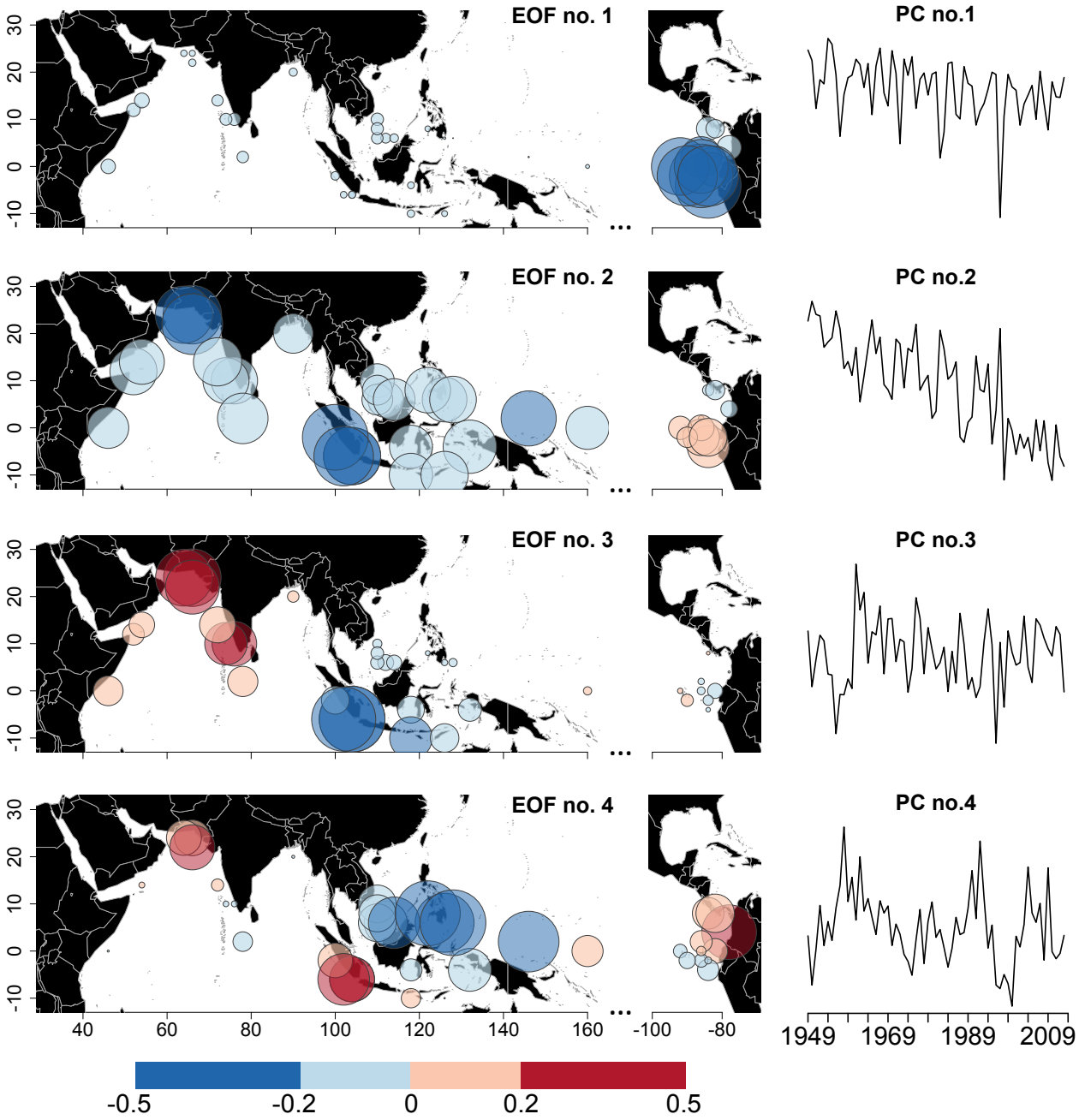

Figure 4.6: First four EOFs of the limited SST field using data from *Smith et al.* (2008). The first four modes of the limited Indo-Pacific SST field account for 74.3%, 15.2%, 2.8%, and 1.8% of the limited field variance.

PCA (Step i) and the limited field PCA (Step ii). To determine the optimal number of PCs to retain, we compared the calibration statistics across a number of scenarios that involved retaining PCs that explained no less than 5% of the variance. Using this, for summer wind stress curl, $N_{PC} = 8$ (75.5% of the full field variance) was selected. A Canonical Correlation Analysis (CCA) was performed on the eight retained PCs of wind stress curl with the first eight PCs of the limited SST field. This results in eight pairs of canonical components (CCs), each of which explains more of the joint variance than the next. In each pair, CCs are highly correlated. For example, CC_1 of wind stress curl is correlated to CC_1 the limited SST field with an R^2 value of 0.81. Each CC of the full wind stress curl field is then linearly regressed with the corresponding CC of the limited SST field.

Step (iv). For a given paleo time-period (e.g. 10 ka), the smoothed proxy data are contained in a 1 xP matrix (where P is the number of proxy records that have values for the given reconstruction period). Using the eigenvalue transformation matrix from the PCA in Step (ii), these proxy data are transformed into PC-space.

Step (v). From Steps ii and iii, N_{PC} canonical components were obtained. The estimated components are back transformed to yield N_{PC} reconstructed PCs. For the remaining PCs, mean values from the contemporary period in Step i are used. This results in a vector of PCs of wind stress curl of length G (=262), corresponding to 10 ka.

Step (vii). Finally, we obtain the reconstructed wind stress curl anomalies by back transforming the PC vector obtained from Step (v). Steps iii-v are repeated for 8, 6, 4 and 2 ka. To avoid introducing bias, we choose not to reconstruct 0 ka, since several of the proxy records do not extend to 0 ka. Instead, we show the average present-day (1949-2013) wind stress curl, reconstructed as anomalies relative to the 1981-2010 climatology (Figure 4.7).

4.4.2 Reconstruction of Summer Monsoon Rainfall Fields

For rainfall, the reconstruction process follows that for wind stress curl. There is no trend in the rainfall data that requires removal prior to the CCA-reconstruction. The

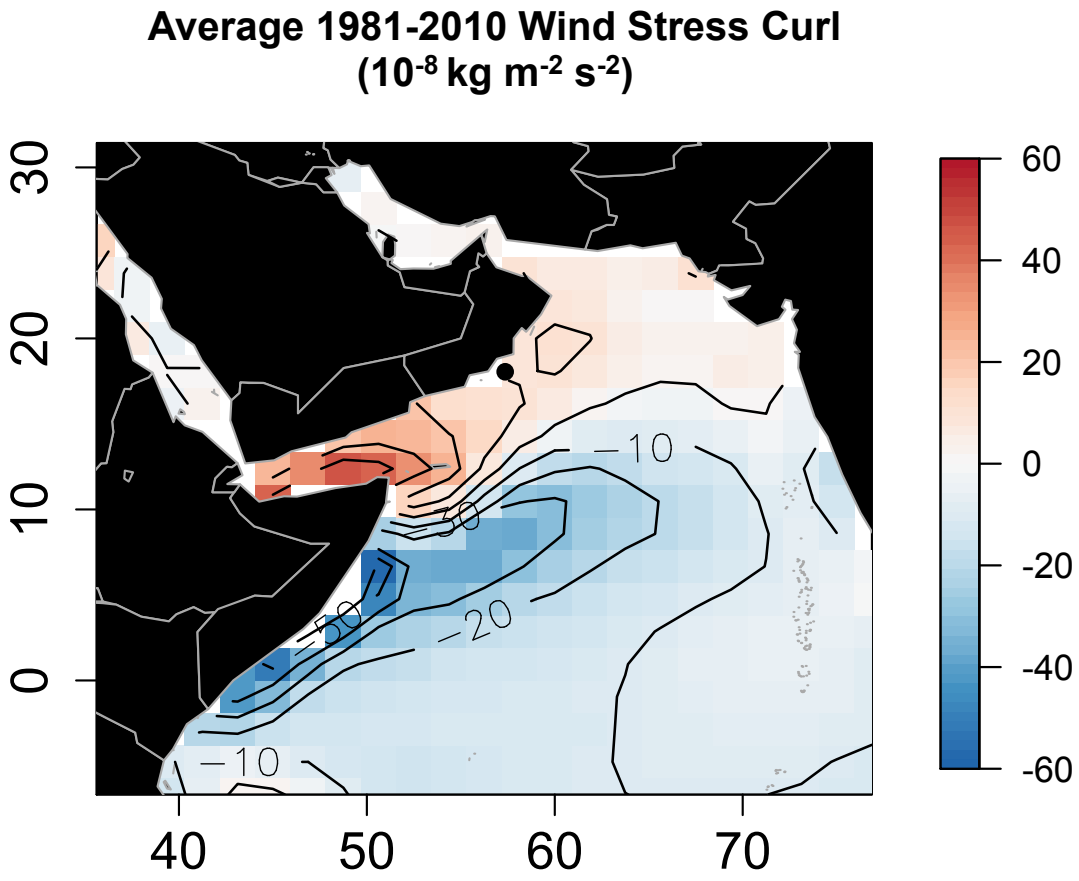

Figure 4.7: The 1981-2010 summer wind stress curl climatology (10^{-8} kg m^{-2} s^{-2}) over the Arabian Sea.

seasonal average daily rainfall data is scaled (using means and standard deviations of each grid cell) and a PCA is performed. The first four modes explain 18.3%, 7.8%, 5.9%, and 5.1% of the total-field variance (Figure 4.8). The only difference in this methodology from that of the wind reconstruction is that $N = 104$ (for 1901-2004 data), $G = 357$ (grid cells over India), and we choose to retain the first four PCs ($N_{PC} = 4$) for the CCA, which jointly explain 37% of the variance.

It should be underscored that this reconstruction focuses on capturing the variance present in the leading retained modes (i.e. the dominant 'signal'). For rainfall, this is only $\sim$ 37% for rainfall, which is notably less than the 80 - 90% of variance captured in the equatorial Pacific SST reconstructions of Chapter 3. This is understandable given the highly

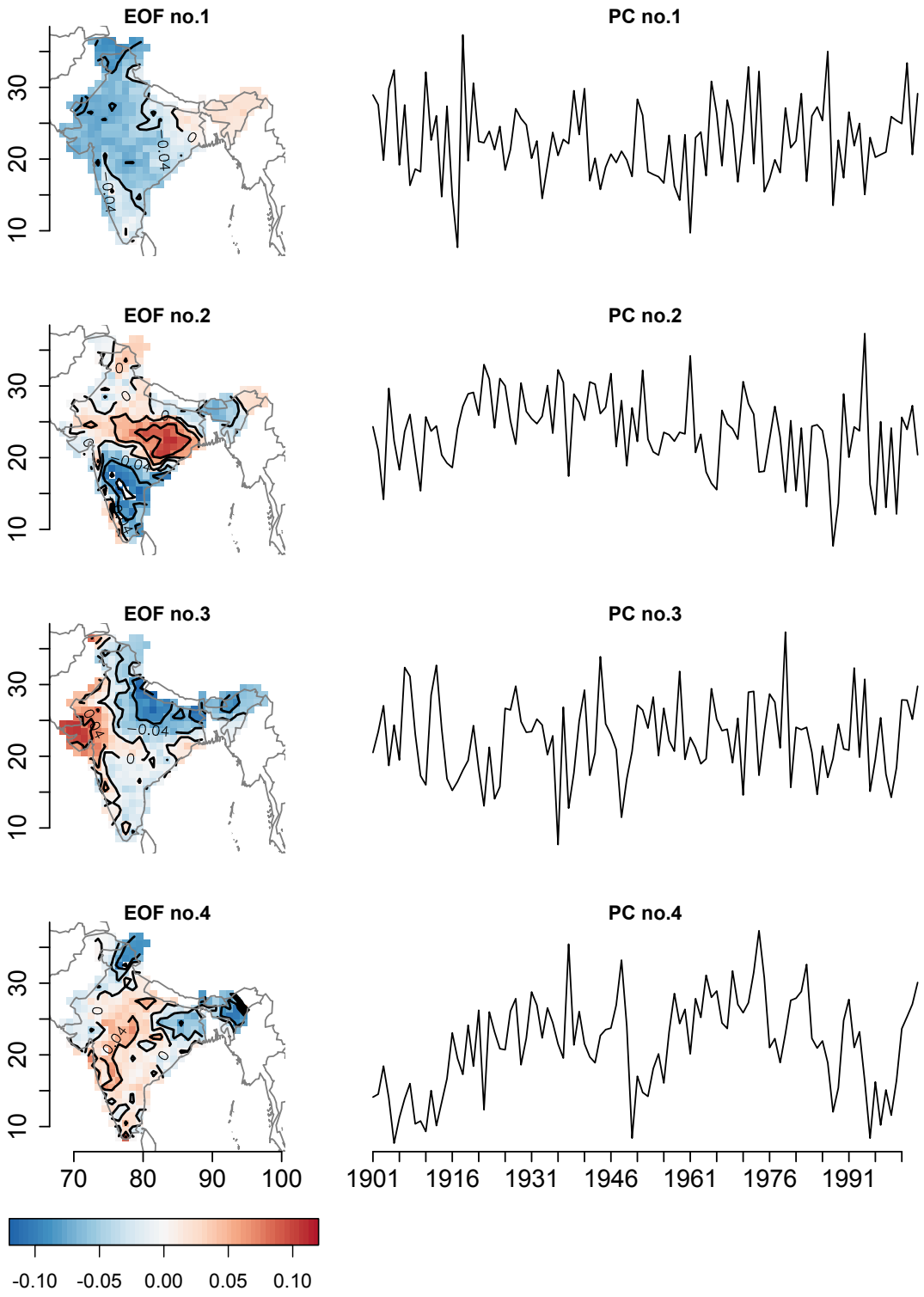

Figure 4.8: Eigenvalue spectrum (left), first four EOFs (middle), and first four PCs (right) from a PCA on 1901-2004 *Rajeevan et al.* (2006) rain data. The first four modes of Indian summer monsoon rainfall account for 18.3%, 7.8%, 5.9%, and 5.1% of the full field variance.

variable nature of rainfall.

4.4.3 Model Calibration and Verification

As mentioned above, the reconstructions recover the dominant signal in the wind stress curl and rainfall fields, which account for a relatively small percentage of the total variance. Thus, comparing the reconstructions to the full original data field will result in modest to poor skills. To be consistent, we compute the calibration and validation measures on the signal component of the original field. The signal components are obtained by projecting the PCs on to the retained eigenvectors. For example, let $\boldsymbol{X}$ be the original data matrix of size NxG, $\boldsymbol{PC}$ be the matrix of all the principal components also of size NxG and, $\boldsymbol{E_R}$ be the reduced eigenvector matrix of size GxG with the first N_{PC} columns containing the eigenvectors of the first N_{PC} modes and zero for the rest. The signal component of the original data ($\boldsymbol{X_R}$) is obtained by $\boldsymbol{X_R} = [\boldsymbol{PC}]\boldsymbol{E_R}$.

Model calibration is performed on the signal components at each grid point using the 'resolved variance' statistic, β, given by:

$$\beta = 1 - \frac{\sum (y - \hat{y})^2}{\sum y^2} \tag{4.1}$$

where y is the contemporary signal data obtained in $\boldsymbol{X_R}$ above, and $\hat{y}$ is the reconstructed signal data for the full period. We also compared the squared correlation, R^2, between y and $\hat{y}$ at each grid point. These two statistics assess the reliability of the procedure in reproducing the contemporary signal data (See Chapter 3 for more details). The β-statistic serves as a measure of the resolved variance: for a perfect fit, one would expect β=1, and for two random series, one would expect β=-1.

For wind stress curl (Figure 4.9 top left), most of the monsoon region is fairly well reconstructed with β >0.25, with the weaker areas scattered throughout the Arabian Sea. This is, perhaps, better observed in the R^2 plot, in regions where R^2 >0.25 (Figure 4.9, top right). For rainfall (Figure 4.9, bottom), all calibration β values are highly positive (>0.75)

and R^2 >0.8 (Figure 4.9 bottom left), indicating that the model resolves the variability of the rainfall signal (first four PCs) well.

As additional calibration, we pick two example years: (1) 1988-1989 - a strong La Niña year, and (2) 1997-1998 - a strong El Niño year. These two years also happen to be strong

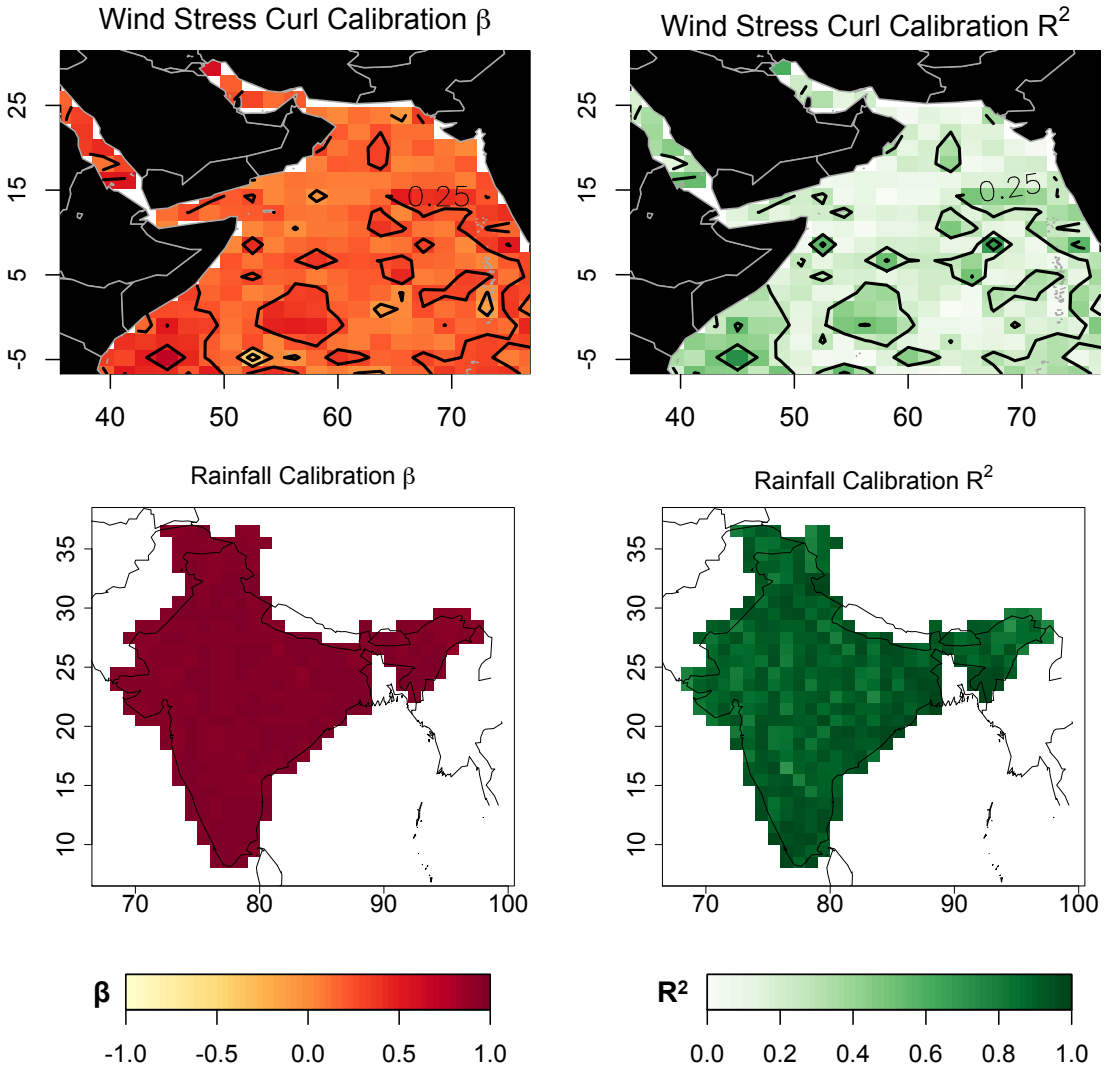

Figure 4.9: Model calibration statistics for wind stress curl (top; using the first 8 PCs), and rain (bottom; using the first 4 PCs) for the CCA-based reconstruction models. The β-statistic (left) represents the resolved variance captured by the reconstructed contemporary data (1949-2013 for wind stress curl, 1901-2004 for rain). The R^2 (right) provides the correlation between the observed contemporary data and the reconstructed contemporary data. These statistics are calculated on the PC signal only, which is further clarified in the text.

and weak monsoon years, respectively, according to the All-India Summer Monsoon Rainfall (AISMR) dataset (*Sontakke et al.*, 1993). In either reconstruction, the general patterns of winds are captured in the key regions, if, as expected the strengths are underestimated. For example, in the La Niña summer of 1988 (Figure 4.10, top left), positive wind stress curl anomalies, indicative of ocean upwelling, extended from the Yemen and northern Somali coastlines across the Arabian Sea and along the western border of India. This zone of positive wind stress curl anomalies was neighbored to the north and south by negative wind stress curl anomalies, indicative of ocean downwelling zones. The reconstruction captures the correct signs and similar spatial extents of these anomalies, but with positive magnitudes underestimated in the upwelling zone. In terms of rainfall, the summer of 1988 was interesting: although AISMR, a country-wide average monsoon rainfall index, reports an above average monsoon season, there was deficit rainfall in the north central region (Figure 4.10, top right). Typically, during La Niña, one would expect excess rainfall across the core monsoon region, which makes this particular year unusual. Despite this, the reconstructed rainfall anomaly field shows a similar pattern to that of observed anomalies, capturing the dry anomalies just west of Bangladesh. Again, magnitudes are muted.

For the El Niño summer of 1997, a band of strongly negative (-4 x 10^{-8} kg m^{-2} s^{-2}) wind stress curl anomalies extends from the Yemen and northern Somali coastlines across the Arabian Sea to the southern half of the Indian border (Figure 4.10, bottom left). This negative (downwelling) zone is neighbored to the north by a positive (upwelling) zone that extends from Oman to the northern half of the Indian border and to the south by a second positive zone that encompasses the western half of the equatorial Arabian Sea. This pattern is mostly captured, with the exception of the northern positive (upwelling) zone which is omitted from the reconstruction. Magnitudes of the negative wind stress curl zone are underestimated. The rainfall reconstruction captures the main signal of deficit rainfall, but with negative rainfall anomalies across India that are more homogeneous than observed anomalies (Figure 4.10, bottom right).

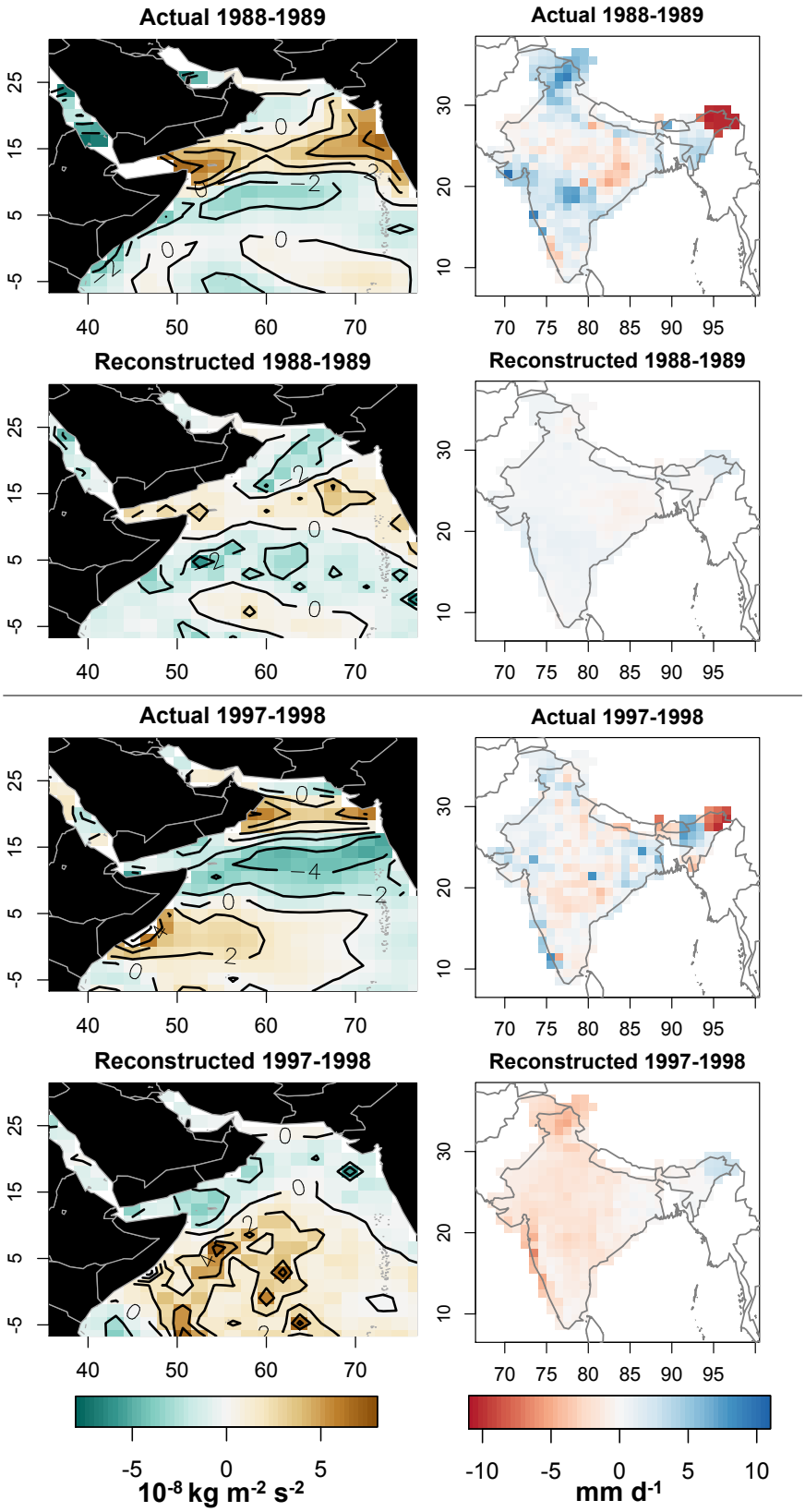

Figure 4.10: Actual and reconstructed wind stress curl (10^{-8} kg m^{-2} s^{-2}) and rain anomalies (mm d^{-1}) for 1988-1989 (a strong La Niña year and strong monsoon year) and 1997-1998 (a strong El Niño year and weak monsoon year).

For independent verification we fitted the modes on using 1980-2013 for wind stress curl and 1980-2004 for rainfall and then predicted the signal for the earlier period (1949-1979 for wind stress curl and 1901-1979 for rainfall). The verification maps for the two fields are similar to resemble the calibration maps (Figure 4.11) but with lower magnitudes of β and R^2. For wind stress curl (Figure 4.11 top panels) the verification skills are poor (β <0) over the Arabian Sea. The rainfall , however, shows skill with β >0.75, R^2 >0.75 across the country (Figure 4.11, bottom panels).

4.5 Multi-Proxy Reconstruction of Holocene Summer Wind Stress Curl and Rainfall Fields

Figure 4.12 shows the reconstructions for wind stress curl anomalies for 10 ,8, 6, 4, and 2 ka. At 10 ka (Figure 4.12, bottom right), strongest positive wind stress curl anomalies of $\sim$ 2 x 10^{-8} kg m^{-2} s^{-2} are shown off the coast of Oman and central Somalia, extending across the northern Arabian Sea. Also shown is the reconstructed average anomaly for 1949-2013, which shows small anomalies as expected. A zone of negative ($\sim$ -2 x 10^{-8} kg m^{-2} s^{-2}) wind stress curl (downwelling) appears at the tip of the northern Somali coastline, and along the southern half of the Indian coastline. This general pattern remains similar throughout the Holocene, but gradually decreases in magnitude from 8 to 6 ka. By 4 to 2 ka, both positive and negative anomalies are minimal, barely exceeding 1 x 10^{-8} kg m^{-2} s^{-2}.

In agreement with the wind stress curl reconstructions, the greatest difference in rainfall from present day occurred at 10 ka (Figure 4.13). The 10 ka reconstruction suggests that compared to present day: (a) most of Rajasthan and northern India received 40% greater precipitation, with some areas parts up to 60% greater precipitation, (b) the regions of the Ganges and Godavari River Basins (Figure 1.3) received about 20% greater precipitation, and (c) the rain shadow region of the Western Ghats, along with North East India, received less rainfall ($\sim$ 25%). (Note that *Sukumar et al.* (1993) had inferred relative arid conditions in this region when Rajasthan was wet.) Throughout 10 to 6 ka, this pattern changes little. By

4 ka, percentage differences in rainfall over Rajasthan and Northern India had decreased to 30% greater than present-day, but the central Ganges and Godavari regions remain at about 20% greater precipitation than present day. At 2 ka, precipitation across the core monsoon region does not exceed 10-20% greater than present day. The reconstructed rainfall for the 1901-2004 contemporary period shows small negative anomalies across most of India.

Although the strength of a CCA method is in isolating dominant signals in a system,

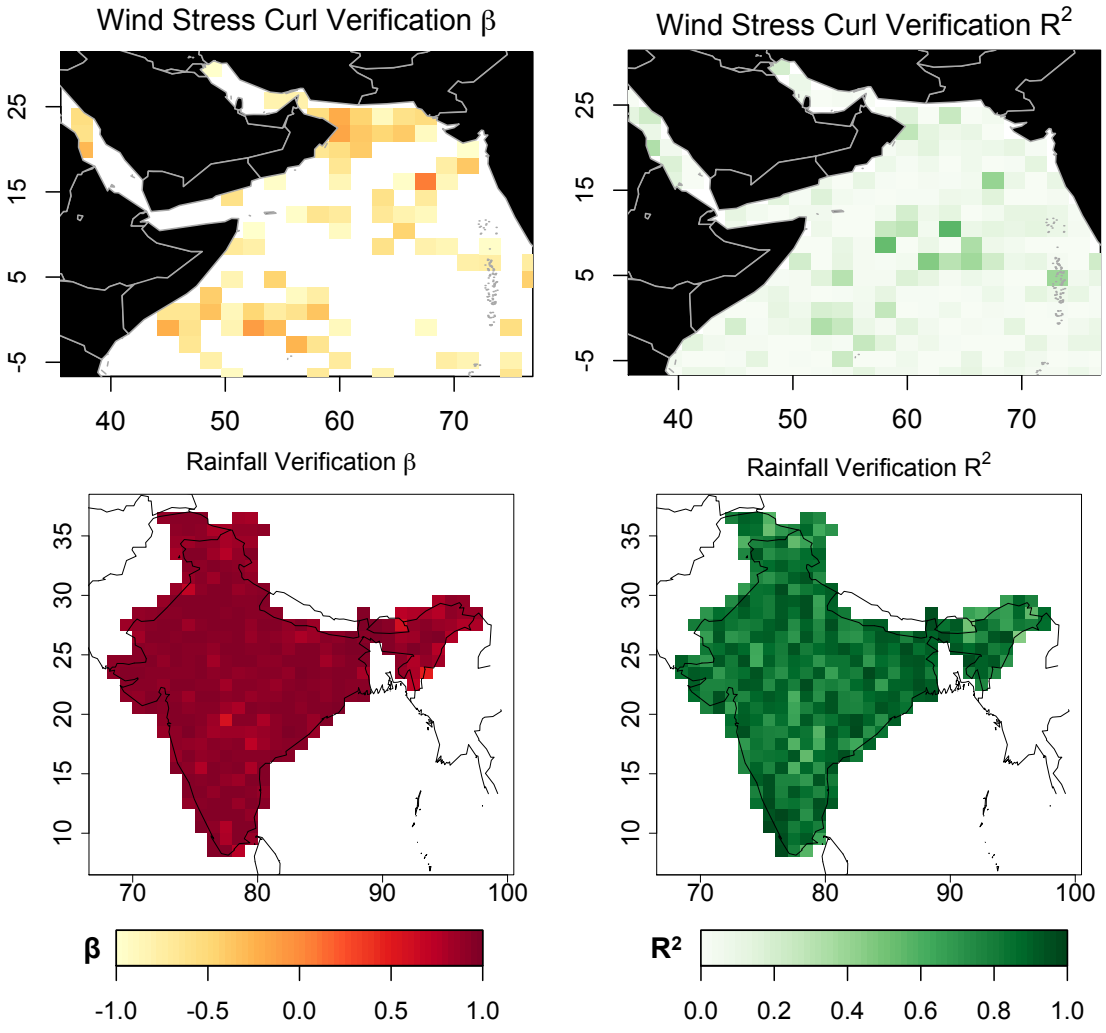

Figure 4.11: Model verification performed by training the model on the most recent period (1980-2013 for wind stress curl, 1980-2004 for rainfall), and using that model to validate the period prior (1949-1979 for winds and 1901-1979 for rain). The β- and R^2-statistics are used once again to quantify model skill and the statistics are calculated in the PC signal only.

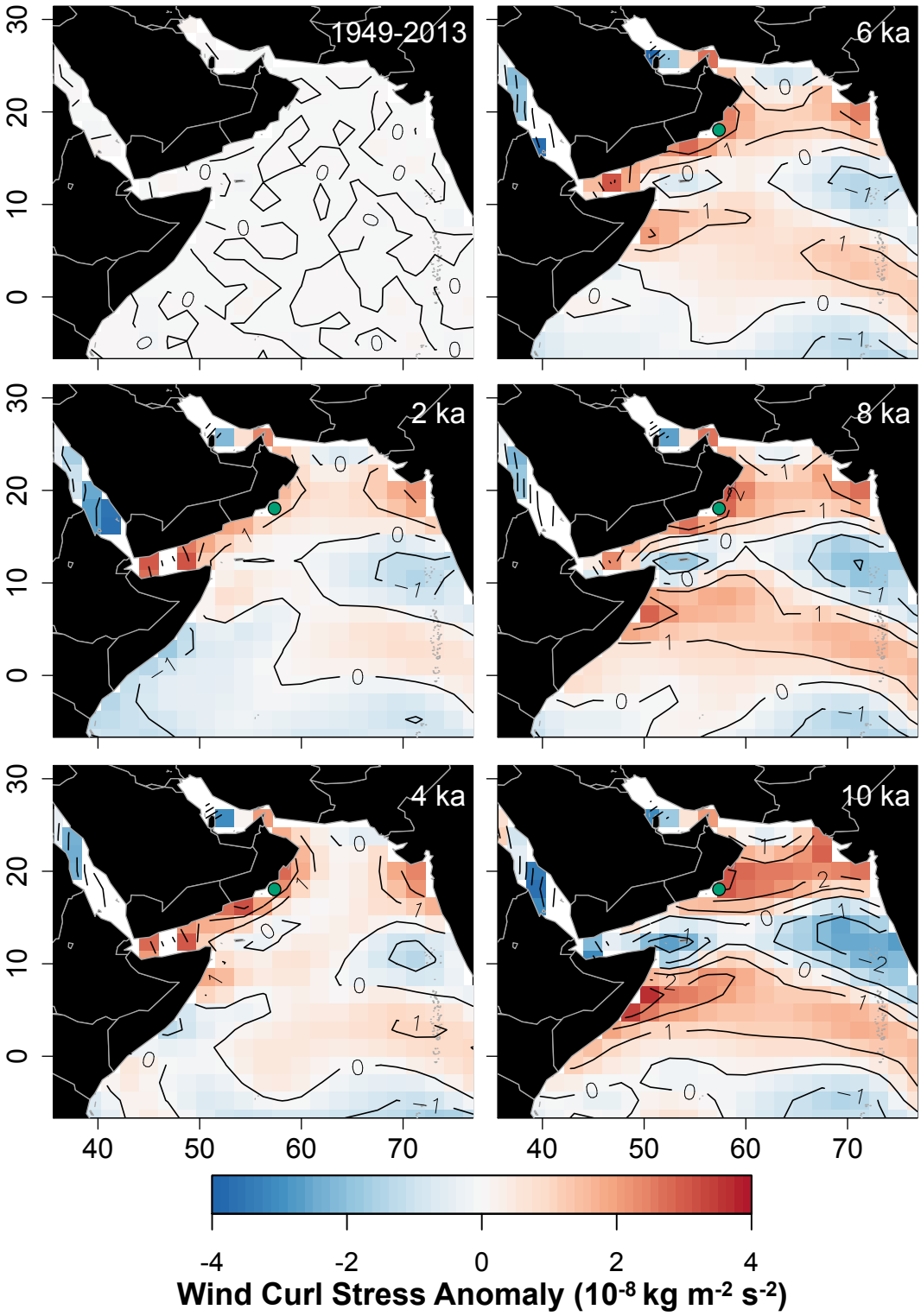

Figure 4.12: Multi-proxy reconstructed summer wind stress curl anomalies for 10, 8, 6, 4, and 2 ka over the Arabian Sea region. The 1949-2013 panel of provides a reconstruction of present-day wind stress curl anomalies using the limited-field data. The green point off the coast of Oman in the northwestern Arabian Sea indicates the location of the *G. bulloides* productivity/upwelling reconstruction provided by *Gupta et al.* (2003).

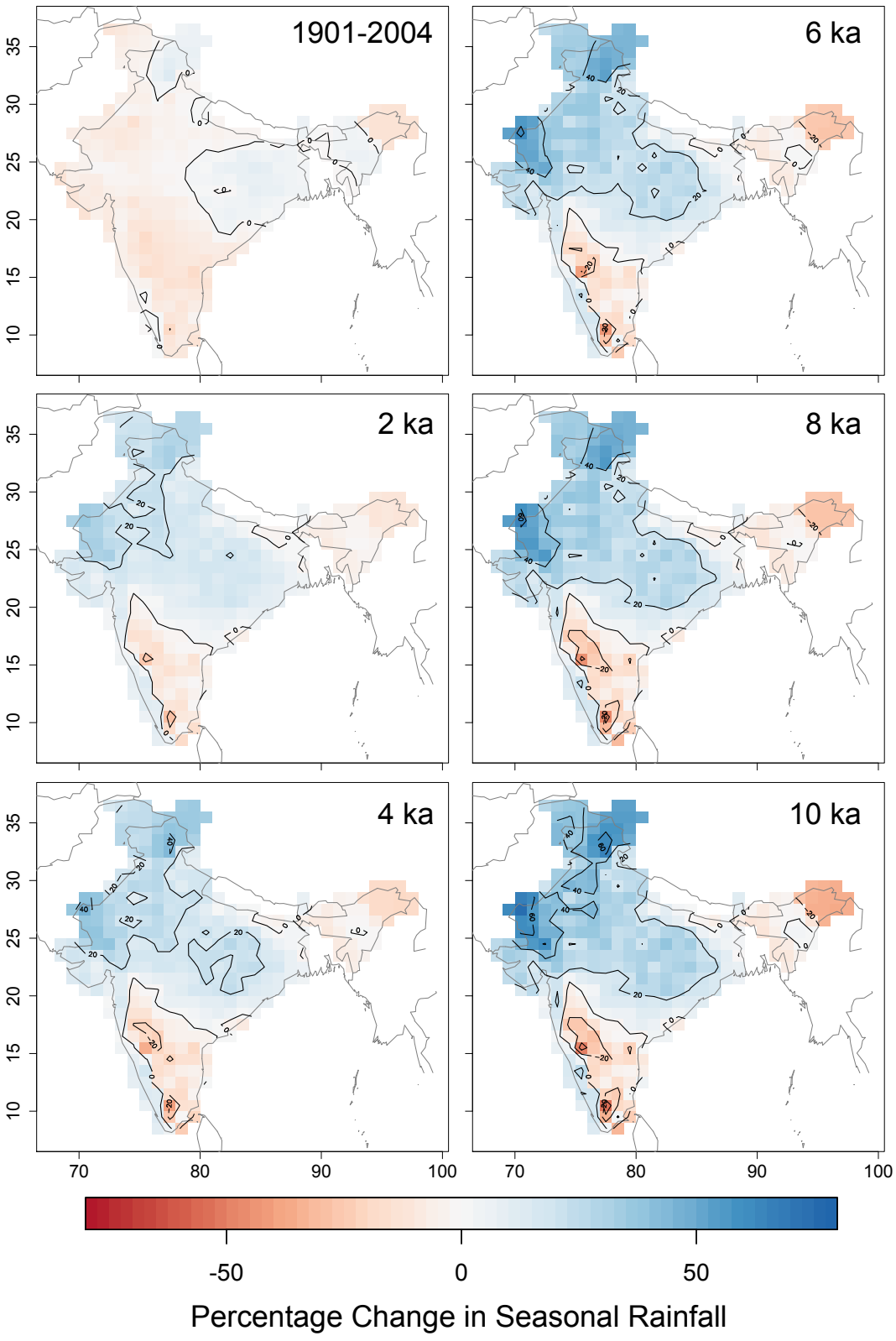

Figure 4.13: Multi-proxy reconstructed rainfall over India for 10, 8, 6, 4, and 2 ka. These are presented as percentage departures from the present day mean summer (June-Sep) daily rainfall. Once again, the 1949-2013 panel of provides a reconstruction of present-day rainfall percentage change anomalies using the limited-field data.

its biggest weakness is in dealing with uncertainties. Unfortunately, uncertainties in the reconstruction of PCs, eigenvalues, and eigenvectors are not robustly treated and difficult to obtain without drowning out the dominant signal in noise. We quantify uncertainty on the PCs of the dominant signal by calculating the standard error between the signal of the observed period and the signal of the reconstruction (Figure 4.14). Standard errors in both wind stress curl and rainfall are small (within 2% of present day values), which indicates that the reconstruction of the signal is robust. We emphasize, however, that this represents only the uncertainty on the dominant signal, not the total uncertainty in the entire field.

4.6 Comparisons of Reconstructions to Proxy Records

Recall from Figure 1.3 that a reconstruction of *G. bulloides* has been used to infer enhanced upwelling of the coast of Oman (site OPD-732A) during early Holocene, which has been used to suggest a weakening of the monsoon winds since 10 ka (*Gupta et al.*, 2003). The interpretation follows the logic that when the monsoon jet is strong, positive wind stress curl across the western Arabian Sea coastlines induces upwelling and a flux of cold nutrient-rich water to the surface. This nutrient-rich water allows surface dwelling organisms, such as *G. bulloides* to bloom. Reconstructed summer wind stress curl anomalies at the ODP-732A site (Figure 4.15, blue) to the *Gupta et al.* (2003) *G. bulloides* data (Figure 4.15, black), compare well in the timing and trends of suggested upwelling. The *G. bulloides* record peaks at 8 ka, but is high from 10 to 8 ka. The reconstructed wind stress curl is consistently high throughout 10 to 8 ka, and decreases only slightly throughout that period. Following 8 ka, the *G. bulloides* record monotonically decreases to 2 ka. Although the reconstructed wind stress curl does not decrease at a constant rate, anomalies lessen from 8 to 6 ka, and from 4 ka to present day, with a minimum at present day.

The proxy data that suggest enhanced early- to mid-Holocene rainfall over the Indian subcontinent tend to cluster in defined regions of India (Figure 1.3). For example, most of the lake evidence is contained to the northwestern region of Rajasthan, which is also near

the 63KA proxy record recording discharge from the Indus River Basin (*Staubwasser et al.*, 2003). Another region is the Godavari River Basin, which extends across central India from the Western Ghats to its mouth at 16A (Figure 1.3) . As shown in the spatial reconstructions, the Indo-Gangetic Plains located along the northeastern border of India saw approximately 20% more rainfall during the early Holocene. With this information in mind, we define six regions over India, for which we aim to reconstruct mean daily monsoon rainfall time series: Northern India, Rajasthan, Western Ghats, Indo-Gangetic Plains, NE India, and Godavari

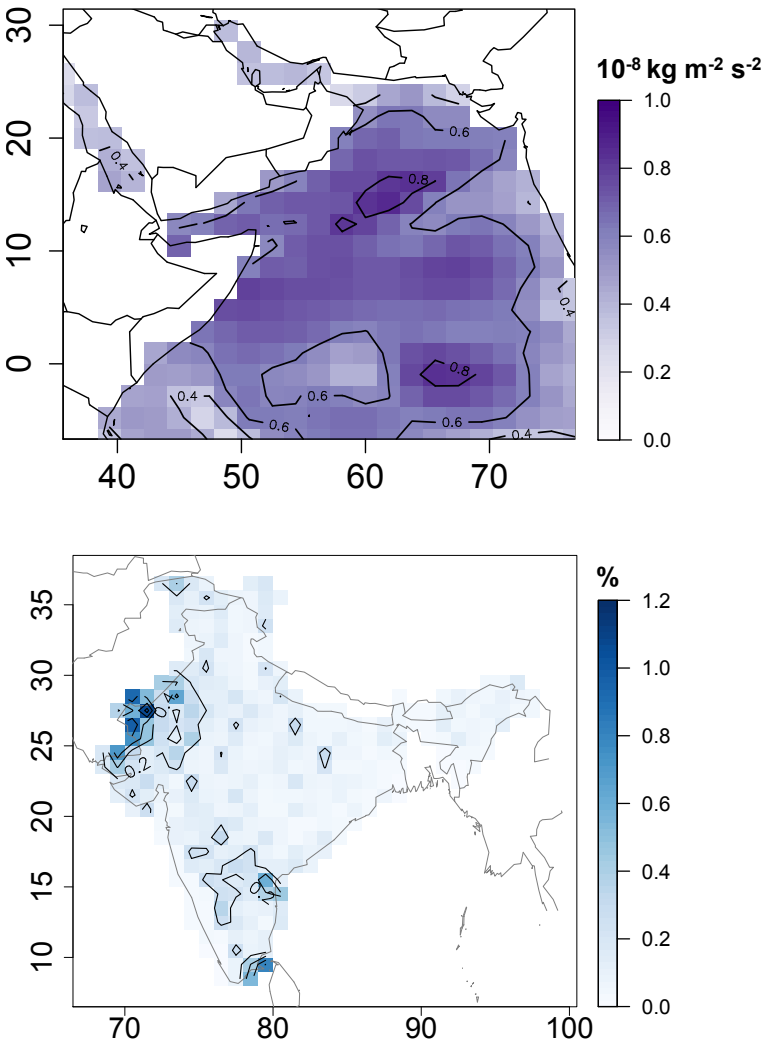

Figure 4.14: Standard error calculated from the actual 1949-2013 wind stress curl and 1901-2004 rain anomalies and those reconstructed by the limited proxy field.

(Figure 4.16).

For each region, mean 1901-2004 daily summer rainfall time series are averaged over the regions defined in Figure 18. We then regressed these time series as functions of the first four limited-field PCs from *Step (ii)* (Figure 10). These functional relationships, along with the paleo PCs from Step iii, are used to predict rainfall for each 1000-year period from 10 to 1 ka (Figure 4.16). Standard errors from the regression model fit provide errors on the rainfall reconstructions.

Among interesting features, first, most of the records reveal greater precipitation than in the present day during the early- and mid-Holocene, as reflected in the spatial CCA reconstruction (Figure 4.16). The one record that shows the opposite trend is Northeast India, which is consistent with the spatial reconstruction, but also consistent with contemporary patterns. North East India is known (e.g. *Guhathakurta and Rajeevan*, 2008) to be out of

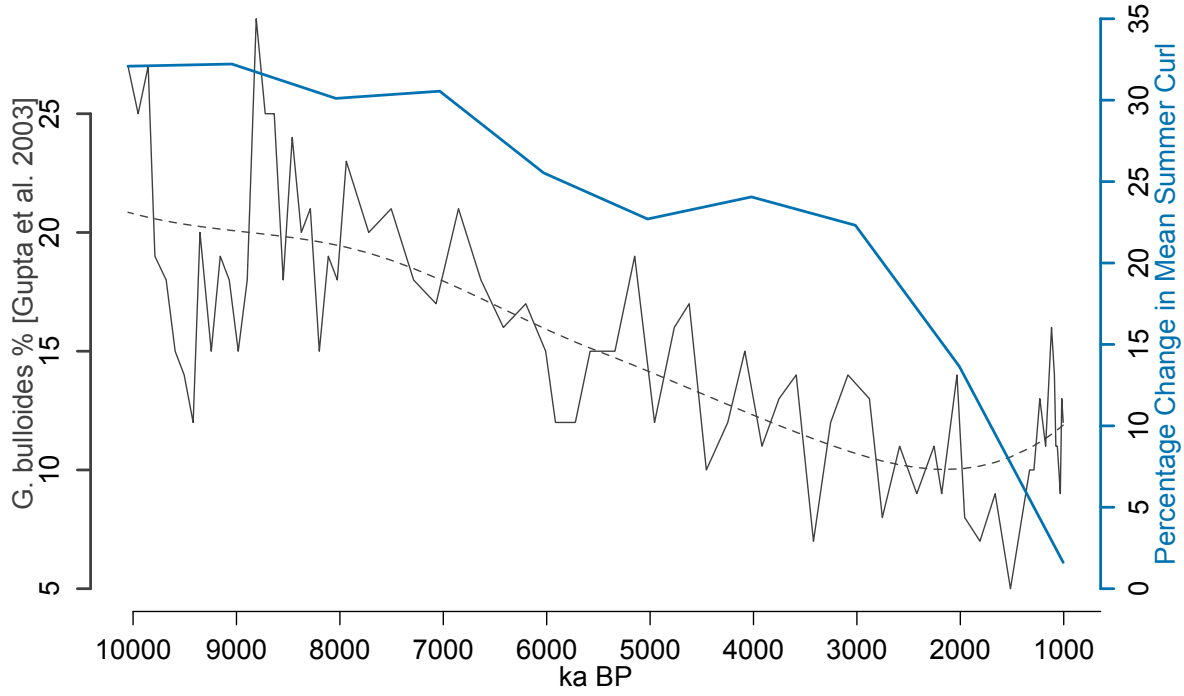

Figure 4.15: Comparison of the *G.bulloides* reconstruction of (*Gupta et al.*, 2003) (black) to reconstructed percentage change in wind stress curl (blue) from 10 to 1 ka. A local polynomial is used to smooth the *G. bulloides* data and is provided by the dotted line.

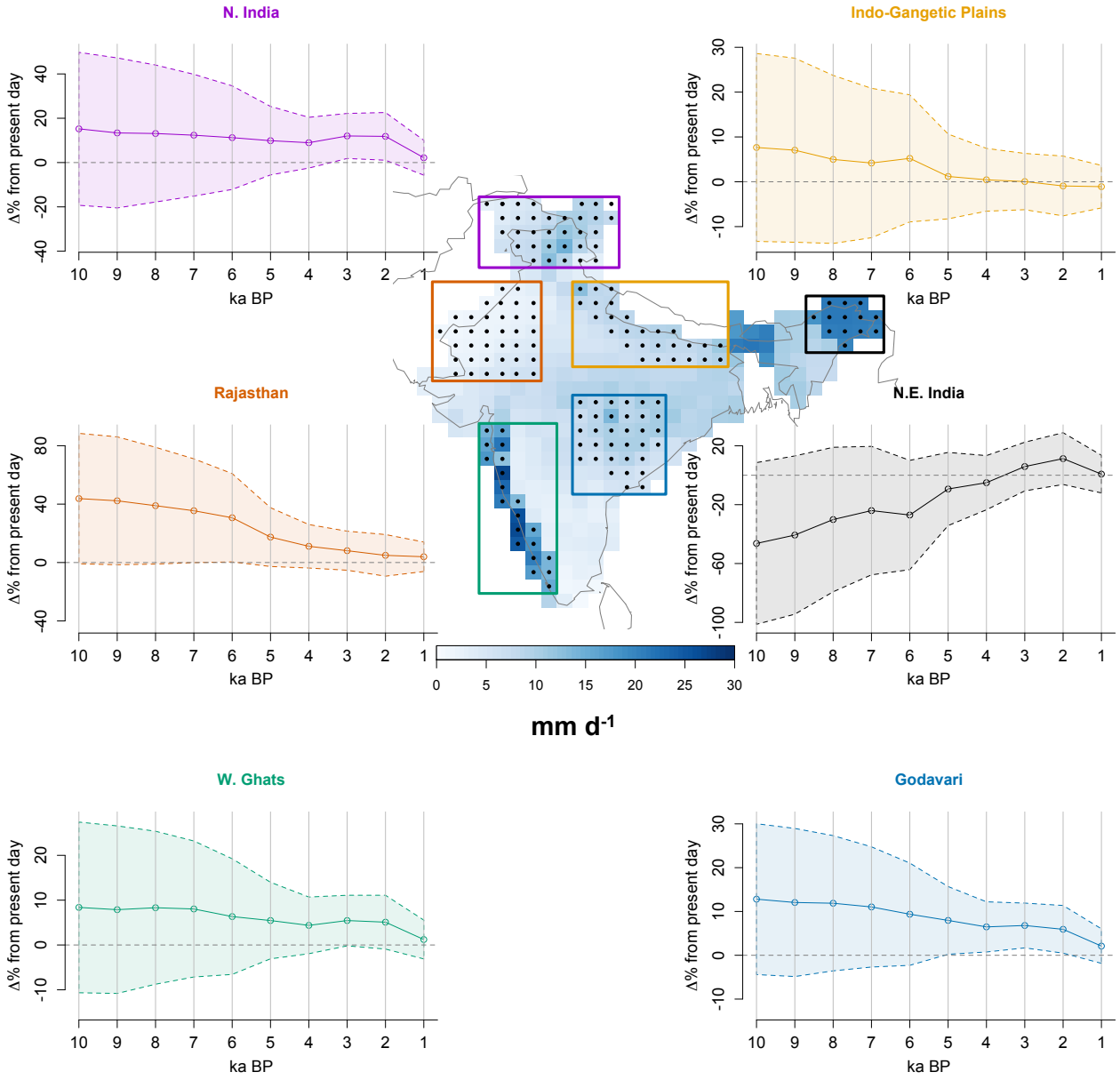

Figure 4.16: Reconstructed mean daily rainfall (mm d^{-1}) for the monsoon season for six regions: (a) Northern India, (b) Rajasthan, (c) Western Ghats (green), (d) Indo-Gangetic Plains, (e) North East India, and (f) Godavari River Basin. The stippled regions inside the larger boundaries are the grid cells used for each respective reconstruction. *Rajeevan et al.* (2006) mean daily rainfall from 1901-2004 is shaded on the map. Rainfall is reconstructed by mean daily monsoon rainfall from each stippled region as a function of the limited field SST proxies.

phase with the rest of the core monsoon region in terms of interannual variability (see the first EOF of rainfall in Figure 4.8), in that its relationship with ENSO (higher rainfall during El Niño years) is opposite to that of the core monsoon region (lower rainfall during El Niño years). Additionally, during the late Holocene when most records in the core monsoon region suggest aridification, the precipitation time series for North East India is near present day, if not slightly above, which would be consistent with a return of ENSO variability. Second, the seemingly monotonic decrease in rainfall since 10 ka suggested by the spatial reconstruction (Figure 4.13) looks less monotonic in the time series reconstructions. For instance, the Indo-Gangetic Plains time series shows greater precipitation than present day only during 10 to 6 ka, but not after. This is consistent with proxy records representative of runoff from the Ganges River basin: (1) *Kudrass et al.* (2001) cite a minimum in salinity from the early- to mid-Holocene that gradually increases to present day, and (2) *Goodbred and Kuehl* (2000) cite greatest sediment discharge between 11 and 7 ka. For the Godavari River Basin, the period of wetness extends to 3 ka, which is consistent with *Ponton et al.* (2012) who cite increased salinity past 3 ka. The period of wetness for Rajasthan extended from 10 to 4 ka, but seems more prominent in the earlier half of that time period.

A hydrological lake model Chapter 5 revealed that average annual precipitation 40-65% greater than present day was necessary to sustain Lake Sambhar in Rajasthan India (Figure 1.3). Reconstructions for Rajasthan of both spatial pattern (Figure 4.13) and the appropriate Holocene time series (Figure 4.16) suggest that, although uncertainty is large, it is possible that ENSO teleconnections during an early- to mid-Holocene La Niña-like state contributed enough summer rainfall to Rajasthan to explain the enhanced wetness recorded by lake proxy records.

The uncertainties on the each time series rainfall reconstruction is large, in part, because the PC models must predict rainfall outside that of the observed range. In most cases, the large uncertainties make these trends marginally significant. At the least, these reconstructions suggest that it is within the realm of possibility for equatorial Pacific SSTs to

externally force increased wetness over India.

4.7 Discussion

A total of forty proxy SST records (Mg/Ca and $U_{37}^{k'}$ that span the west Pacific, east Pacific, Arabian Sea, and Bay of Bengal are used in a reduced dimension methodology to reconstruct the full field dominant signal of Indian summer monsoon wind stress curl and rainfall at 10, 8, 6, 4 and 2 ka. The reconstructions reveal greatest wind stress curl and rainfall anomalies, as compared to present day, at 10 ka. These anomalies weaken and lessen throughout the mid- and late- Holocene.

These reconstructions are consistent with a marine proxy record off the coast of Oman (*Gupta et al.*, 2003) that suggests enhanced upwelling during the early Holocene as compared to late Holocene. Additionally, average rainfall time series for the past 10 ka for six regions throughout India (Northern India, Rajasthan, Western Ghats, Indo-Gangetic Plains, North-east India, and the Godavari Basin) are reconstructed using the PCs from the multi-proxy limited field. The rainfall reconstructions are consistent with many marine and continental proxy records that suggest enhanced rainfall during the early- to mid-Holocene as compared to late Holocene. Although most rainfall time series reconstructions suggest greatest precipitation at 10 ka, they reveal slight differences in the timing of each region that can be applied to various proxy records for precipitation and monsoon strength that have been reconstructed across the Indian subcontinent 1.3.

The significance of these findings lies in the fact that only the patterns of wind stress curl and rainfall tied to Indo-Pacific SSTs are reconstructed. Therefore, although these findings suggest nothing of the effects of land warming, they imply that it is possible for Pacific teleconnections to have written a signal on the Indian monsoon wetness that has been suggested for the early- to mid-Holocene. Additionally, it is possible that a return of ENSO variability in the late Holocene could be responsible for the aridification over India at that time.

The significance of these findings lies in the fact that only the patterns of wind stress curl and rainfall tied to Indo-Pacific SSTs are reconstructed. Therefore, while these findings suggest nothing of the effects of land warming, they imply that it is possible for Pacific teleconnections to have written a signal on the Indian monsoon wetness that has been suggested for the early- to mid-Holocene. Additionally, it is possible that a return of ENSO variability in the late-Holocene could be responsible for the aridification over India at that time.

Chapter 5

An Assessment of the Mean Annual Precipitation Needed to Sustain Lake Sambhar in Rajasthan, India during Mid-Holocene Time

Abstract

An application of a simple hydrological model to likely climatic conditions of Lake Sambhar provides tighter bounds on the range of increased precipitation seen during the early- to mid-Holocene than those inferred from paleoclimatic proxies. To examine past lake levels, we developed a simple lake model, based on hydrological principles of a watershed balance between precipitation, evaporation, and runoff from the watershed to calculate daily depth and volume. Calculations reveal that early- to mid-Holocene rainfall was most likely in a range of 40-65% greater than present levels, resulting in lake depths of $\sim$ 6 to 8 m. This estimate incorporates all major sources of uncertainty into the lake model, but it is likely that the value of mid-Holocene precipitation lies in the lower part of the 40-65% range. Additionally, a 40-65% greater precipitation could have led to greater interannual variability in lake levels, which may account for the lack of clear shorelines. We find, however, that it is unlikely Lake Sambhar filled to its maximum depth of 21 m above the present-day lake bed during this period due both to the much greater precipitation than today required to maintain a lake of such depth (greater than double present-day precipitation) and to the lack of current evidence (no shorelines and little vegetation). We also find that differences between mid-Holocene and present-day winter insolation alone have virtually no effect on average annual lake depths.

5.1 Background

Although the ability to predict the response of the South Asian monsoon to global warming is of great interest to both the scientific field and society as a whole, there is much disagreement as to whether the monsoon will intensify (strengthen) or stabilize (weaken) in response to a warmer climate. Arguments for a future strengthening of the monsoon rest on the theory that higher temperatures enhance the moisture-holding capacity of the atmosphere and thus, on the presumption that with increased atmospheric moisture, more rain will fall. The 1990 IPCC Scientific Assessment reported the results of several studies using General Circulation Models (GCMs) of climate that simulated an intensification of the monsoon in response to increased anthropogenic forcing. Since then, numerous other GCM studies have predicted a similar intensification of the monsoon in response to warming (e.g., *Meehl and Washington*, 1993; *Lal et al.*, 1995; *Kitoh et al.*, 1997; *Bhaskaran and Mitchell*, 1998; *Hu et al.*, 2000; *Hsu et al.*, 2013). Alternatively, other studies have suggested a future stabilization of the monsoon due to warming sea surface temperatures resulting in both a decreased land-ocean pressure gradient and a weakened Walker circulation (e.g., *Yang and Lau*, 1998; *Xu et al.*, 2012). In general, historical datasets of precipitation over India during the past century show no overall trend in increased monsoon strength over the country as a whole (*Krishnan et al.*, 2013). In fact, both APHRODITE (*Yatagai et al.*, 2012) and India Meteorological Department (IMD) gridded daily rainfall (*Rajeevan et al.*, 2006) for the period of 1951-2007 show a decrease in the rainfall rate for the summer monsoonal period in the north and central regions of India (see Fig. 1 of *Krishnan et al.*, 2013). Although some studies have found no discernible trend within the last century (*Krishna Kumar et al.*, 2011), others have suggested a change in overall variability of extreme monsoon events despite the absence of a long-term mean trend (*Menon et al.*, 2013). It remains to be determined how the South Asian monsoon will respond to a warmer climate.

Taking an alternative approach, we call attention to times of warmer climates dur-

ing Earth's history, namely the early- to mid-Holocene (∼10,000 - 5,000 years ago). It is understood that the warmer conditions that characterize reconstructions of paleo-climate during this period resulted from the precession of Earth's orbit, with greater insolation during summer months of that period than today. Specifically, average summer (June, July and August) insolation at 25° N, the latitude of the site in our study, gradually decreased from ∼ 483 W m^{-2} at 9 thousand years ago (ka) to ∼451 W m^{-2} during Present Day (*Berger*, 1992). Although the mid-Holocene is not a strict analogue for future conditions, *Bartlein et al.* (2011) claims, "the mid-Holocene offers the possibility of studying a period with warmer conditions and longer growing seasons in many regions, comparable in some respect to climates expected as a result of increasing radiative forcing in the future."

The existence of salt lake deposits in the northwestern region of India was first reported during the 1950s (*Aggarwal*, 1951; *Deb*, 1952; *Godbole*, 1952; *Aggarwal*, 1957). With the scientific advances of the last half-century, we have gained more insight concerning the history of these lakes. Isotopic analysis of oxygen and hydrogen from in and around these lakes shows that the water is of meteoric origin with the salt content originating from weathering of rocks (Ramesh et al. 1993). Pollen reconstructions reveal warmer and wetter conditions during 9 - 6 ka throughout the deserts of Rajasthan (*Singh et al.*, 1974; *Bryson and Swain*, 1981), Bap Malar, and Kanod (*Deotare et al.*, 2004; *Kajale and Deotare*, 1997) as compared to present-day conditions (see Figure 5.1). *Wasson et al.* (1984) reconstructed history of salinity and water-level changes at Lake Didwana by using sediment texture and mineralogy of evaporites and precipitates, and they found that lake level varied widely during early-Holocene with the deepest conditions around 6 ka. Water level dropped around 4 ka and then dried quickly. Studies of the lithostratigraphy and mineralogy of Lunkaransar (*Enzel et al.*, 1999) and Sambhar (*Sinha et al.*, 2004) found similar timing of Holocene wet and dry periods. They inferred that winter precipitation increased around 6 ka when the lake filled to its maximum depth.

Other studies using various proxies of monsoon strength have suggested a general

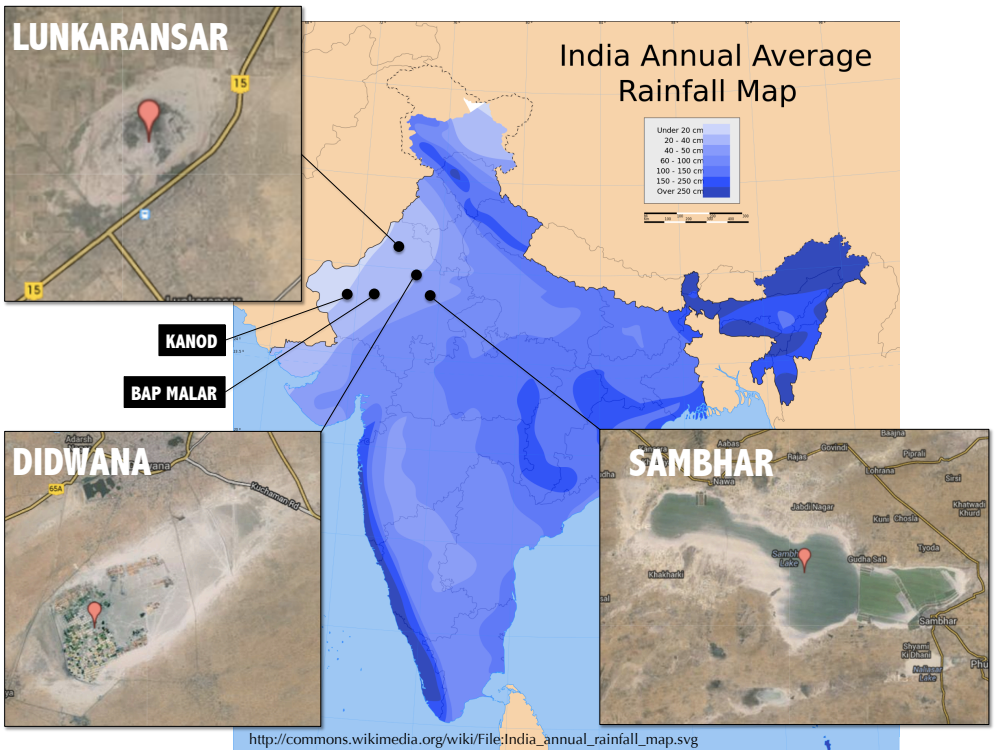

Figure 5.1: Ancient lakebeds of Lakes Lunkaransar, Didwana and Sambhar, located in the Rajasthan desert region, used in this study to reconstruct lake levels through the early Holocene. The map of rainfall over India was obtained from the Survey of India.

increase in monsoon intensity during this same time period as compared to the Present. Reconstruction of the prevalence of *Globigerina bulloides*, a planktic foraminifer that blooms along the western Arabian Sea during times of intense upwelling, suggests that monsoon winds were strong during the early- to mid-Holocene and have gradually become weaker (*Gupta et al.*, 2003). High-resolution oxygen isotope (δ^{18}O) profiles of stalagmites from Oman (*Neff et al.*, 2001; *Fleitmann et al.*, 2003) and Yemen (*Fleitmann et al.*, 2007) serve

as proxies for monsoon rainfall and reflect a wetter early Holocene with gradual decreases in precipitation after 8 ka to the Present.

Finally, *Krishna Kumar et al.* (2006) provide a recent example of the robust relationship between La Niña-like Pacific sea-surface temperature (SST) conditions and a strong monsoon. Consistent with this relationship, Pacific SST reconstructions of the western warm pool and eastern cold tongue show the largest zonal SST gradient during this 9-6 ka period (*Koutavas et al.*, 2002, 2006; *Stott et al.*, 2004). Some have inferred from this that the Pacific was in an enhanced La Niña-like state during this period (*Clement et al.*, 1999, 2000; *Marchitto et al.*, 2010), which contributed to stronger rainfall and wetter conditions over India (*Koutavas et al.*, 2002; *Conroy et al.*, 2008).

A recent study, which used the National Center for Atmospheric Research (NCAR) Community Climate System Model 3.0 (CCSM3) GCM, along with a simple water-balance model to simulate lake-level changes in monsoonal Asia, reported high lake levels during the early- to mid-Holocene caused by a combination of low lake evaporation and high precipitation (*Li and Morrill*, 2010). Another GCM study contrasting precession extremes (*Battisti et al.*, 2014) showed higher rainfall in times analogous to the early Holocene, but because of increased cloud cover, they also found lower summer temperatures and, presumably, lower evaporation.

Although there seems little doubt that the Rajasthan region in the early- to mid-Holocene was wetter than today, we ask the question, how much wetter was it? To investigate the sensitivity of these lakes to changes in insolation and precipitation, we develop a hydrological model to simulate lake level fluctuations in Lake Sambhar of Rajasthan, India, back through the early Holocene (since 10 ka).

5.2 Methodology and lake model

5.2.1 Study area and data

Lake Sambhar, the main lake investigated in this study, is a closed basin lake located in Rajasthan, India (Figure 5.1). Sambhar, a tourist location centered at 26° 56' 25" N, 75° 05' 07" E, is filled year-round with seasonally fluctuating lake levels and with a watershed area of ∼5400 km^2. The playa is fed by two major streams (Mendha and Rupangarh), which are part of a larger dense drainage network reflecting abundant water supply during wetter phases (*Sinha et al.*, 2004). Two other nearby closed basin lakes were used in calibration of the hydrological model: (1) Lake Lunkaransar, a perennially dry lakebed centered at 28° 30' 10" N, 73° 44' 35" E with a watershed area of ∼102 km^2 and (2) Lake Didwana, a seasonal lakebed centered at 27° 22' 20" N, 74° 34' 12" E with a watershed area of ∼288 km^2. The average annual rainfall during the period 1969-2005 taken from *Rajeevan et al.* (2006) for Lakes Sambhar, Didwana, and Lunkaransar, respectively, is 532 ± 137 mm yr^{-1}, 450 ± 148 mm yr^{-1}, and 345 ± 139 mm yr^{-1}. During the 1969-2005 period, Lake Sambhar experienced a mean daily temperature of 25.5 ± 0.5°C, while its average coldest (hottest) month was January (May and June) with temperatures around 15 ± 0.8°C (33 ± 1.2°C) (*Srivastava et al.*, 2009). The temperature regimes for Lakes Didwana and Lunkaransar follow that of Lake Sambhar's closely.

We rely on the deduction of *Singh et al.* (1974), who state that "the dry bed of the lake lies at about 360 m a.s.l. but the lake sediments, consisting mainly of silt and clay, extend some 6.1 m above the general surface in raised beaches formed on the slopes of the promontory jutting into the basin in the extreme northwest." This, albeit tentative, finding provides the best geologic evidence for the maximum depth of Lake Sambhar. Although this lake sediment has not been dated back to the mid-Holocene, pollen reconstructions (*Bryson and Swain*, 1981; *Singh et al.*, 1974; *Swain et al.*, 1983) from the area limit the "lifetime" of these lakes to the mid-Holocene epoch; the absence of pollen suggests lakes were dry prior to

$\sim$10 ka and following $\sim$5 ka. Further evidence of shorelines would significantly enhance the value of a study like ours. For instance, if an unambiguous shoreline were found at a certain depth and dated back to the mid-Holocene period, the lake model that we exploit could be easily used to estimate the precipitation necessary to produce such depths. Furthermore, a more detailed recent history of lake depths at Lakes Lunkaransar, Didwana, and Sambhar would also enhance this study. We infer the present conditions of these three lakes from satellite imagery and anecdotal information.

Watershed areas and lake hypsometry were determined using 30-arc second digital elevation maps of the regions and the Hydrology toolset in ESRI's ArcMap 10.1. For the hypsometry, we obtained relationships for volume versus depth and depth versus surface area, which are used for each lake (Figure 5.2). The hypsometric relationships in Figure 5.2 are representative of present-day relationships between depth, volume, and surface area. *Singh et al.* (1972) find through stratigraphic analysis of the far eastern section of Lake Sambhar, that at most 2 m of sediment (1.5-1.6 m since 4665 $\pm$ 110 BP and 1.85-1.95 m since 6235 $\pm$ 135 BP) have been deposited since the mid-Holocene period. Additionally, 2 m and 1.5 m of sediment have been deposited in Lakes Didwana and Lunkaransar, respectively (*Singh et al.*, 1972)). When running the lake model for present-day conditions, we use the contemporary hypsometric relationships. When modeling mid-Holocene conditions (as in Section 5.4), however, we must account for potentially deeper lake bottoms during that time by shifting the hypsometry of each lake deeper by the amounts cited above.

5.2.2 Hydrological water budget

Previous studies have modeled shifts in average lake level and its variance using a generalized water budget model (e.g., *Shanahan et al.*, 2007), which is similar to the model we use here. The volume (V) of water in any lake can be expressed as the balance between hydrological input volumes of precipitation (P_V) and of watershed runoff into the lake (R_V) and hydrological output volumes of evaporation from the lake (E_V) and of discharge from

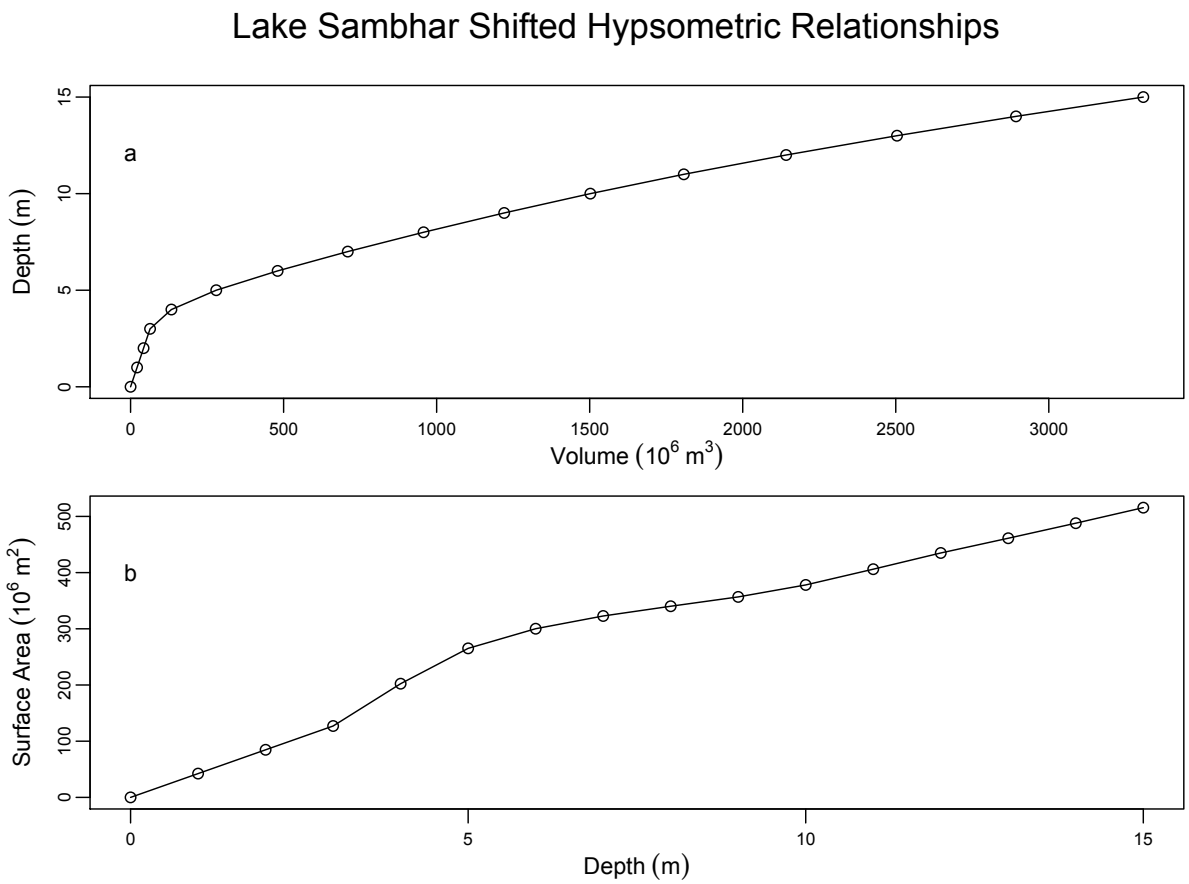

Figure 5.2: Hypsometric relationships, depth vs. volume (a) and surface area vs. depth (b) for Lake Sambhar derived using 30-arc-second DEMs, Google Earth and ESRI ArcMap.

the lake (D_V). Lakes Sambhar, Didwana, and Lunkaransar lie in closed-basins, and therefore have no discharge. With this, our water budget equation becomes

$$\Delta V = P_V + R_V - E_V \tag{5.1}$$

where ΔV is the change in lake volume between each time-step. Our water budget does not consider snowmelt since: (1) temperatures at Sambhar throughout the year are too warm for snow, and (2) the watershed that feeds Sambhar does not extend into high ground that would be snow covered during modern or previously warmer periods, such as the mid-Holocene. The model is run using a daily time-step, set by temporal resolution in our precipitation and temperature datasets.

5.2.3 Runoff

The U.S. Department of Agriculture Soil Conservation Service (SCS), now known as the Natural Resource Conservation Service, developed a method of estimating runoff using cumulative precipitation over a watershed (*Mockus and Hjelmfelt*, 2004). The beauty of this method is that it directly estimates runoff based on daily totals of precipitation, eliminating the need for sub-daily storm precipitation rate details. This method has been shown to model runoff well in various watersheds of India (*Gajbhiye et al.*, 2014; *Mishra et al.*, 2006) and has previously been used in Rajasthan, India by *Durbude et al.* (2001). Using this method, one calculates a curve number, a dimensionless number between 0 and 100, with 100 used for a completely impervious surface such as impermeable pavement. The curve number is a function of land use, soil type, antecedent soil moisture, and other factors affecting runoff and retention in a watershed (*Mays*, 2011). For a heterogeneous watershed, one can determine the composite (weighted) curve number,

$$CN_{comp} = aCN_a + bCN_b + ... + nCN_n \tag{5.2}$$

where $a, b, ..., n$ are fractions of total area for each curve number, such that $a + b + ... + n = 1$, and $CN_a, CN_b, ..., CN_n$ are the respective curve numbers for each fraction of the watershed. In the case of a homogeneous watershed, computation of a composite curve number is unnecessary.

5.2.3.1 Land use and soil type

In SCS four main soil group types are considered (*Mockus and Hjelmfelt*, 2004; *Mays*, 2011): (A) deep sand, deep loess, aggregated silts; (B) shallow loess, sandy loam; (C) clay loams, shallow sandy loams, soils low in organic content, and soils usually high in clay; (D) soils that swell significantly when they contain wet, heavy plastic clays, and certain saline soils. Land use percentages for each region were taken from The Government of India's Department of Agriculture (DOA) Contingency Plans *Department of Agriculture*

(2014) for Jaipur, Nagaur, and Bikaner districts - the districts of Lake Sambhar, Didwana, and Lunkaransar, respectively. Using these reports, all three watersheds were given a soil type defined as 50% soil Type A and 50% soil Type B, as well as a composite land cover that is a combination of cultivated small grain contoured agriculture, desert shrubland, barren/pasture land, and forest. The percentages of land-use applied and resulting composite curve numbers (via Equation 5.2) for each of the three watersheds are found in Table 5.1.

Table 5.1: Land-use percentages in each watershed used in calculating the resulting composite curve numbers using the SCS rainfall-runoff method.

	Lunkaransar (%)	**Didwana (%)**	**Sambhar (%)**
Cultivated	5	11	23
Desert/Shrubland	90	84	63
Pasture/Barren	2	4	7
Forest	3	1	7
Composite CN	**58**	**59**	**59**

Note that composite curve numbers were calculated using 50% soil type A (sand), 50% soil type B (loam), Land-Use in Good Condition, and AMCII moisture conditions. Curve numbers are subsequently converted to either AMCI or AMCIII using information on the cumulative rainfall over the previous 5-day period.

5.2.3.2 Antecedent moisture condition (AMC)

Antecedent soil moisture, in addition to land use and soil type, plays a role in defining three curve numbers specific to any given region. In the SCS method, AMC condition (I, II, or III), is determined by calculating the cumulative rainfall for the previous five days. More specifically, AMCII is the average moisture condition depending on whether it is the dormant (0.5 to 1.1 inches) or growing (1.4 to 2.1 inches) season. AMCI and AMCIII are the low (for the dormant season: $<$0.5 inches, or for the growing season: $<$1.4 inches) and the high (dormant season: $>$1.1 inches, or growing season: $>$2.1 inches) moisture conditions, respectively. This classification is particularly important for the monsoon season when Rajasthan not only is persistently wet, but also likely to be in AMCIII, and therefore

should produce a higher amount of runoff than during the non-monsoonal time of year, when Rajasthan is dry and likely in AMCI. Curve numbers are provided in AMCII for a multitude of land surface conditions on SCS. Conversion to the two other AMC conditions can be done using the following empirically derived formulae (*Mockus and Hjelmfelt*, 2004):

$$CN(I) = \frac{4.2CN(II)}{10 - 0.0058CN(II)} \tag{5.3}$$

$$CN(III) = \frac{23CN(II)}{10 + 0.13CN(II)} \tag{5.4}$$

For each of the three watersheds, the composite curve numbers from Equation 5.2 are either left as CN(II) appropriate for AMCII conditions, or converted to CN(I) or CN(III) based on the cumulated daily precipitation from the previous five days provided by the datasets of *Rajeevan et al.* (2006) and the thresholds for each AMC condition outlined above. The defined AMC thresholds in Equations 5.3 and 5.4 do not vary with location. However, since precipitation does vary with region, so does the percentage of time a CN spends in either AMC I, II, or III. Also, CNs vary with region due to differences in land use and soil type.

Although the assignments of curve number might seem to require many arbitrary decisions, we emphasize that this approach has a long history in hydrology.

5.2.3.3 Calculating runoff

Following determination of a curve number that represents the entire watershed, one can calculate the potential maximum retention of the watershed, S (mm), which is estimated by the following relationship developed from empirical studies (*Mockus and Hjelmfelt*, 2004):

$$S = \frac{1000}{CN} - 10 \tag{5.5}$$

As curve numbers can typically range between 30 and 90, S commonly lies between 1 mm and 23 mm. Furthermore, there is some amount of water that is initially abstracted, I_a, (through

processes such as interception by vegetation), which has been determined commonly to be $I_a = 0.2S$ from a study of many small experimental watersheds (*Mockus and Hjelmfelt*, 2004). If the daily precipitation total is less than the initial abstraction ($P \leq I_a$), there will be no runoff. If $P \geq I_a$, then the effective runoff, R, for that day can be calculated to be a fraction of $P - I_a$, where the fraction depends on S:

$$R = \frac{(P - I_a)^2}{P - I_a + S} = \frac{(P - 0.2S)^2}{P + 0.8S} \tag{5.6}$$

For example, using the composite curve number calculated for Lake Sambhar (CN=59) during AMCII, the potential maximum retention would be 6.9 mm (via Equation 5.5) and the initial abstraction would be 1.4 mm. Assuming a cumulative five-day daily precipitation total of 4 mm during AMCII, the SCS curve number method would estimate a cumulative daily runoff amount of 0.7 mm (via Equation 5.6). Assume, instead, that the previous five days had been particularly wet and pushed the model into AMCIII, then CN=76.8 (via Equation 5.4), S=3.0 mm, I_a =0.6 mm, and runoff would therefore increase from 0.7 mm during AMCII to 1.8-mm due to saturated ground conditions. Likewise, if the previous five-day cumulative rainfall was low enough to push the model to AMCI, then CN=37.7 (via Equation 5.3), S=16.5 mm, I_a=3.3 mm, and runoff would decrease from 0.7 mm during AMCII to 0.03 mm. This method was applied on a daily timescale to estimate a volume of runoff that directly fed each of the three lakes.

5.2.4 Radiation

Radiation is necessary to calculate losses to evaporation from the lake itself. We know that seasonal variation in the top-of-the-atmosphere insolation at 10 ka was different from that of today, with higher insolation in the summer and lower insolation in the winter. Therefore, presumably, the balance between precipitation and evaporation, which works to sustain lakes, could have been different. Furthermore, if the monsoon activity was different, cloud cover, and therefore atmospheric transmissivity, likely differed as well.

Net radiation is given by $R_N = SW_N - LW_N$, where SW_N is the net shortwave radiation onto the lake and LW_N is the net longwave radiation back to space. To determine net shortwave radiation, one must consider not only the incoming solar insolation, but also the transmissivity of the atmosphere. Transmissivity, t_r, is calculated by,

$$t_r = a + (1 - cc)b \tag{5.7}$$

where a and b are empirical constants and cc is cloud cover. Ideally, empirical constants would be derived by comparing on local ground measurements with values of a and b. In the absence of locally calibrated values, *Shuttleworth* (2012) recommends assuming a and b to be 0.25 and 0.75, referring to 25% and 75% losses of energy on clear-sky and overcast days, respectively. Without reliable daily cloud cover data for this area for the entire 1969-2005 period, we used the relationship between observed cloud cover over Sanganer Airport (weather station #33936 from NOAA National Climatic Data Center) in Jaipur, India during the monsoonal season of 2004 and the corresponding daily precipitation rate during the same period (mean rainfall rate = 35 mm d^{-1}, sd = 8.3 mm d^{-1}). Trace precipitation amounts (less than 0.25 mm d^{-1}) were recorded at 0% cloud cover. Cloud cover was recorded as 100% on days when precipitation was equal to or exceeded three standard deviations greater than the mean ($\sim$60 mm d^{-1}). A local logistic regression (*Loader*, 1999, e.g.) was fitted to model the relationship between daily cloud cover percentage and daily rainfall values between these thresholds (Figure 5.3). When simulating sequences of 2000-year periods, cloud cover was estimated daily from this relationship using the randomly sampled daily precipitation values.

Actual net solar radiation, S_d, is equal to,

$$S_d = t_r \cdot S_{TOA} \tag{5.8}$$

where S_{TOA} is the top-of-the-atmosphere insolation.

Finally, net shortwave radiation can be calculated using,

$$SW_N = (1 - \alpha) \cdot S_d \tag{5.9}$$

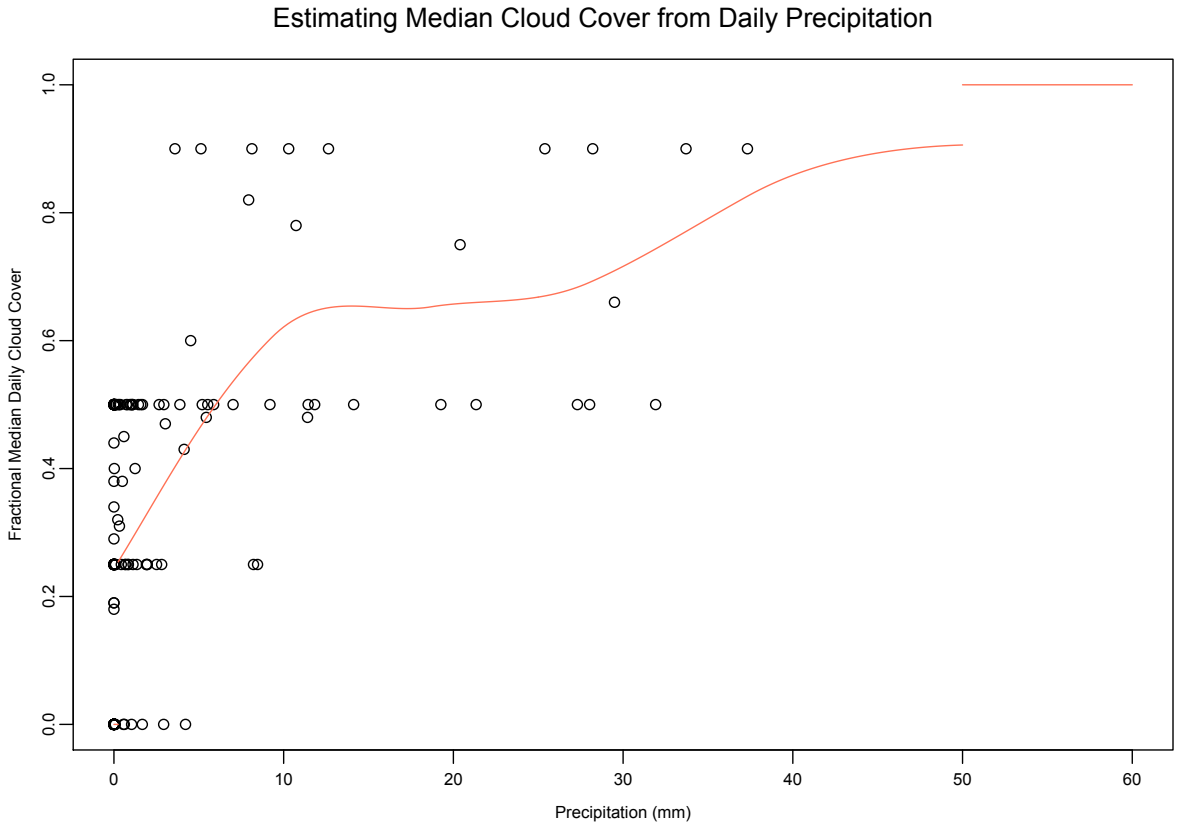

Figure 5.3: Median fractional daily cloud cover from NOAA NCDC versus daily precipitation from *Rajeevan et al.* (2006), with a local logistic regression (red line). Trace values of precipitation (less than 0.25mm per day) were assigned a median fractional cloud cover of 0%, and values greater than 50 mm per day were assigned a median fractional cloud cover of 100%. An F-test for significance showed that the logistic regression model fit the data significantly better (p-value = 2.1 x 10-6) than the global logistic model. Efron's R^2 was calculated as 0.36.

where α is the surface albedo. Completely bare desert has an approximate albedo of 0.4. Introduction of vegetation creates higher absorption, reducing albedo values toward 0.2 for complete vegetation cover. In our case, we consider a desert environment with minimal vegetation (*Maidment et al.*, 1992). Variations in albedo between 0.2 and 0.3 resulted in negligible changes in lake level, and therefore we used an albedo value of 0.3.

The empirically based Berliand formula *Berliand and Berliand* (1952), which uses the theoretical dependence of net long-wave radiation upon the temperature and the specific

humidity of the air, has been shown to accurately estimate net long-wave radiation, LW_N (*Maidment et al.*, 1992; *Budyko*, 1974) as,

$$LW_N = \epsilon\sigma T^4(0.39 - 0.058\sqrt{e_{sat}})(1 - 0.54 \cdot t_r^2) \tag{5.10}$$

where ϵ is the emissivity of water (0.96) , σ is the Stefan-Boltzmann constant ($5.67 \times 10^{-8} Wm^{-2}K^{-4}$), T (K) is the temperature of the water surface (assumed to be equal to the surface air temperature) and e_{sat} is the saturation vapor pressure (kPa) given by,

$$e_{sat} = 0.611exp\left(\frac{17.3 \cdot T}{237.3}\right) \tag{5.11}$$

where the temperature is given in °C.

5.2.5 Evaporative losses

Through the SCS method, runoff is directly estimated based on subsurface soil and surface land characteristics, eliminating the need to estimate evaporative losses from the watershed itself. However, evaporative loss from the lake must be considered in calculating lake depth. With the methods described here we assume that: (1) due to the shallow depth of Lake Sambhar, lake stratification does not affect evaporative losses, and (2) due to the warm temperatures of the Lake Sambhar region throughout the year, lake ice does not affect evaporative losses. A common method for evaluating evaporation is the Penman combination approach (*Penman*, 1948) given by,

$$E = \frac{R_n}{\lambda_v}\frac{\Delta}{\Delta + \gamma} + E_a\frac{\gamma}{\Delta + \gamma} \tag{5.12}$$

where $\Delta = \frac{de_{sat}}{dT}$, λ_v is the latent heat of vaporization, R_n is the net radiation, E_a is the evaporation due to wind and the vapor pressure gradient, and γ is the psychrometric constant, which is equal to $\frac{c_p P_r}{0.622\lambda_v}$, where c_p is the specific heat and P_r is atmospheric pressure. Calculating evaporation due to wind (E_a) requires wind and humidity data. For our purposes, we lack both reliable daily wind speed and specific or relative humidity values for the Rajasthan

region, and we have no easy way to estimate these for the early Holocene. To bypass this, we use the Priestley-Taylor method (*Priestley and Taylor*, 1972), which has been shown to accurately model evaporation in situations lacking humidity information (*Shanahan et al.*, 2007). This approach recognizes that the first term in Equation 5.12 dominates the total evaporation rate. Evaporation can therefore be estimated by,

$$E = \omega \frac{R_n}{\lambda_v} \frac{\Delta}{\Delta + \gamma} \tag{5.13}$$

where ω is the Priestley-Taylor constant. Although ω =1.26 is a typical value for the Priestley-Taylor constant, we used 1.74, which is the value recommended (*Maidment et al.*, 1992; *Shuttleworth*, 2012) for arid regions, such as Rajasthan. Our estimated present-day annual total Priestley Taylor evaporation ($\sim$2130 mm yr^{-1}) compares well with present-day annual total pan evaporation measurements ($\sim$2340 mm yr^{-1}) near Lake Samhbar provided by the Government of India (*Central Water Commission*, 2006).

5.3 Comparison of lake model with present-day conditions

At present, Lake Sambhar fluctuates between 0 and 3 meters while responding to the seasonal cycle but remains dry most of the year (*Sinha et al.*, 2004; *Sangha*, 2008). Furthermore, using present-day lake hypsometry (Figure 5.2) and a typical average runoff coefficient of 0.075 for sandy soils (*Maidment et al.*, 1992) such as the Lake Sambhar watershed, one can calculate that neglecting precipitation into and evaporation from the lake itself, an annual total of at least 590 mm of rain over the watershed is necessary to fill the lake to a 3 m depth (equivalent to $\sim$240 x 106 m3 volume of water via Figure 5.2). Using the contemporary record of precipitation from (*Rajeevan et al.*, 2006), we calculate that this amount of annual rainfall occurred once in the 37-year period. Therefore, we assume that lake model depths fluctuate above 3 m approximately 3% of the time. Figure 5.4 shows the effect of CN on Lake Sambhar depth using contemporary precipitation for the 37-year period. For CN=59 (Table 5.1; Figure 5.4) modeled Lake Sambhar depths exceed 3 m 3.5% of the time

(469 days out of 37 years) with maximum and minimum average annual depths of 2.11 m and 0.15 m and an overall average depth of 1.16 m. There is inherent error involved in selecting one single curve number for a watershed that is both heterogeneous in terms of land-use and soil content. On the upper end, a curve number greater than or equal to 64 for Lake Sambhar would result in average annual depths that exceeds 3 m at least 10% of the time, which seems too often given the 37 year history for which there are records. On the lower end, a curve number less than or equal to 55 is representative of a watershed entirely composed of sand. A curve number below 55 would inaccurately model the Lake Sambhar watershed since some percentage of the soil is loam, which has a higher runoff yield than sand. Moreover, a curve number of 55 results in lake depths exceeding 3 m only 1% of the time. Therefore, in combining all of the information we have on the present-day state of Lake Sambhar, we consider possible curve number to range from 55 to 64. We emphasize that although evaporation was neglected from this calculation, which was used to determine reasonable bounds for possible curve numbers in the absence of observational lake-level data, evaporation is not neglected in the lake model itself. Evaporation is calculated in the lake model using net radiation on a daily basis as described in Section 5.2.5.

In an application of the model to the Lake Sambhar watershed, using the parameters discussed above, the lake responds to the seasonal cycle of monsoonal rainfall (Figure 5.5). Figure 5.5 provides precipitation record for the period of 1969-2005 as well as the resulting modeled Lake Sambhar depths using observed precipitation, temperature, and insolation. *IndiaToday* (1999) cited that periods of persistent rainfall during the early 1980s resulted in a deeper Lake Sambhar, which is successfully captured in contemporary runs of our model (Figure 5.5).

5.4 Effects of insolation and precipitation

To investigate the feasibility of various increases in precipitation suggested by paleo-climate studies, and consequent increases in lake depth, we ran a sensitivity study by calculat-

ing the response of average annual Sambhar lake depth for various increases in precipitation and changes in insolation. Recall that insolation plays a direct role in evaporation rates from the lake. It should also be noted that changes in temperature could affect evaporation rates as well. In our model, a 1°C increase (decrease) in temperature, results in an approximate 0.03 mm d^{-1} ($\sim$11 mm yr^{-1}) increase (decrease) in evaporation (assuming a mean cloud cover of 10% and mean annual insolation 32.6 MJ m^{-2} d^{-1}). Additionally, we do not know the exact magnitude by which temperatures shifted from the mid-Holocene to present day.

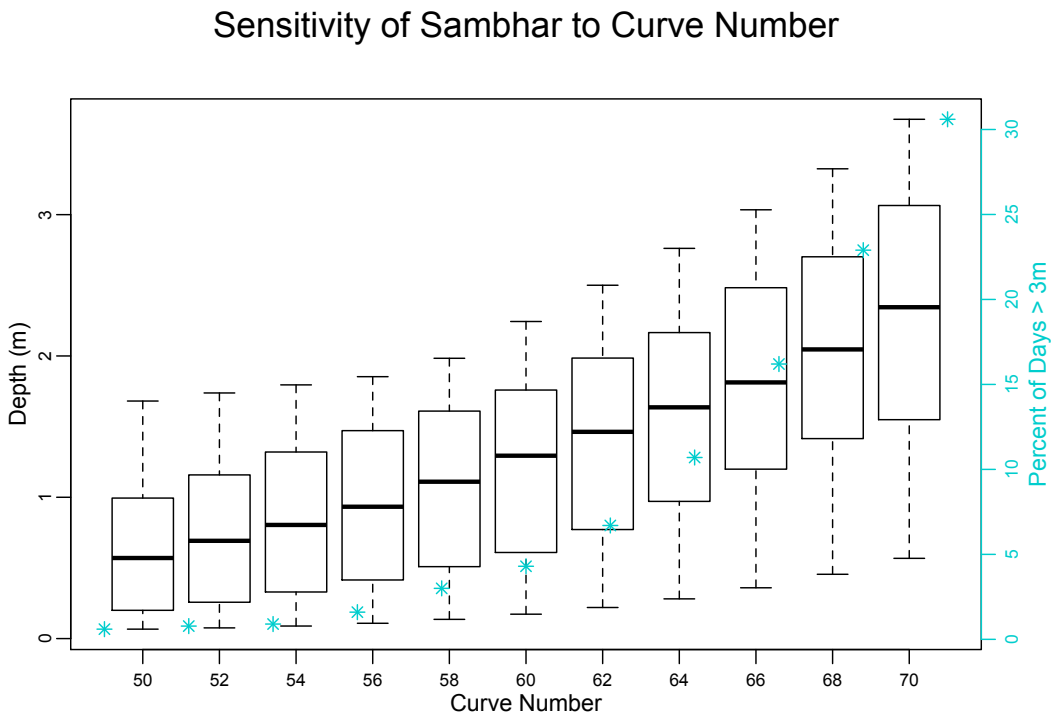

Figure 5.4: This figure boxplots the annual depths (m) from Lake Sambhar modeled using contemporary precipitation and insolation, while varying the curve number from 50 to 70. The boxplots show the median (thick center line), first quartile (bottom of box), third quartile (top of box), minimum (bottom whisker) and maximum (top whisker) annual lake depths. The secondary axis plots blue asterisk to represent the percentage of time Lake Sambhar spends at depths greater than 3 meters, which is the maximum depth most cited for present-day Lake Sambhar conditions (*Sinha et al.*, 2004; *Sangha*, 2008).

Therefore, we chose to run the model with present day temperatures to avoid introducing another free parameter into the model.

Berger's Orbital Insolation Database (*Berger*, 1992) contains insolation values in 1 kyr increments by 10° latitude bands per month for the past 100 thousand-years. For this study, we calculated an average 20-30°N monthly insolation for 10-9 ka, 7-6 ka, 4-3 ka and 0 ka to represent early Holocene, mid-Holocene, late Holocene, and Present Day, respectively. To create 2000-year long daily sequences with which to run the model, we randomly selected

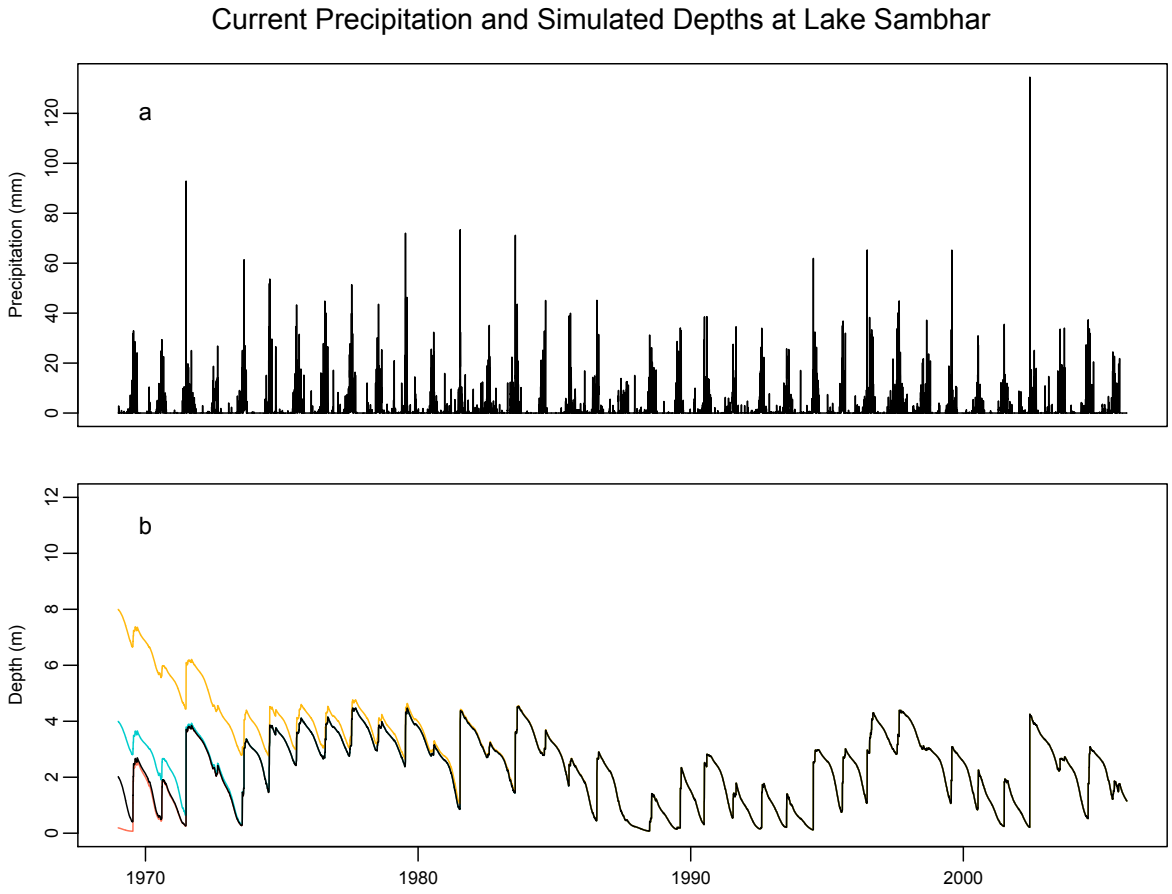

Figure 5.5: Daily observed precipitation (mm) from 1969-2005 (top) and calculated Lake Sambhar depth (m) using current precipitation, temperature and insolation records (bottom). The various colors correspond to different initial depths of the lake, red = 0 m (empty), black = 2 m, blue = 4 m, and yellow = 8 m, and are included to show that initial condition does not play a significant role in the long-term behavior of Sambhar lake depth.

years of precipitation and temperature from those measured over the past 60 years (*Rajeevan et al.*, 2006). Differences in insolation alone had an almost unrecognizable effect, less than a few percent, on the annual average calculated depth of each lake for each precipitation level (Table 5.2). However, insolation changes throughout the Holocene may have played a subtle role in the likelihood that Lake Sambhar entered different states (discussed further in Section 5.6).

Table 5.2: Average annual lake depths resulting from both Early Holocene (8 - 9 ka), Mid Holocene (5 - 6 ka), Late Holocene (2 - 3 ka) and present-day insolation from *Berger* (1992) across various precipitation levels (present-day levels to a doubling).

	Early Holocene	**Mid Holocene**	**Late Holocene**	**Present Day**
Current	1.15	1.19	1.12	1.14
25% increase	2.52	2.54	2.52	2.44
50% increase	5.58	5.50	5.66	5.66
75% increase	12.00	12.13	12.05	12.08
100% increase	17.94	17.85	18.28	18.10

Since insolation alone had a negligible effect on annual average calculated depths, we continue the analysis using present-day insolation values. For the remaining model runs aimed at simulating paleo lake conditions, we use the shifted hypsometry for each respective lake, as discussed in the methodology. In shifting the hypsometry, we assume that 2 m of sediment accumulated in Lakes Sambhar and Didwana and 1.5 m of sediment accumulated in Lake Lunkaransar since the mid-Holocene. Besides insolation and hypsometry, the other likely significant change throughout the Holocene was the mean annual precipitation rate. For this, we ran the model for 2000-year sequences at current insolation for a range of precipitation increases in steps of 10% up to 100% increase for all three lakes (Figure 5.6). The average annual depths displayed in Figure 5.6a are for the composite curve numbers provided in Table 5.1. Under a constant curve number, as precipitation increases, the watershed spends a higher percentage of time in AMCIII and therefore has higher runoff (Table 5.3). Furthermore, we find that summer evaporation decreases due to higher cloud cover,

which is consistent with findings by *Li and Morrill* (2010) for areas in Rajasthan, India. Reduced summer evaporation helps sustain higher lake levels due in large part to greater precipitation.

Figure 5.6b considers the error introduced not only by variability in precipitation, but

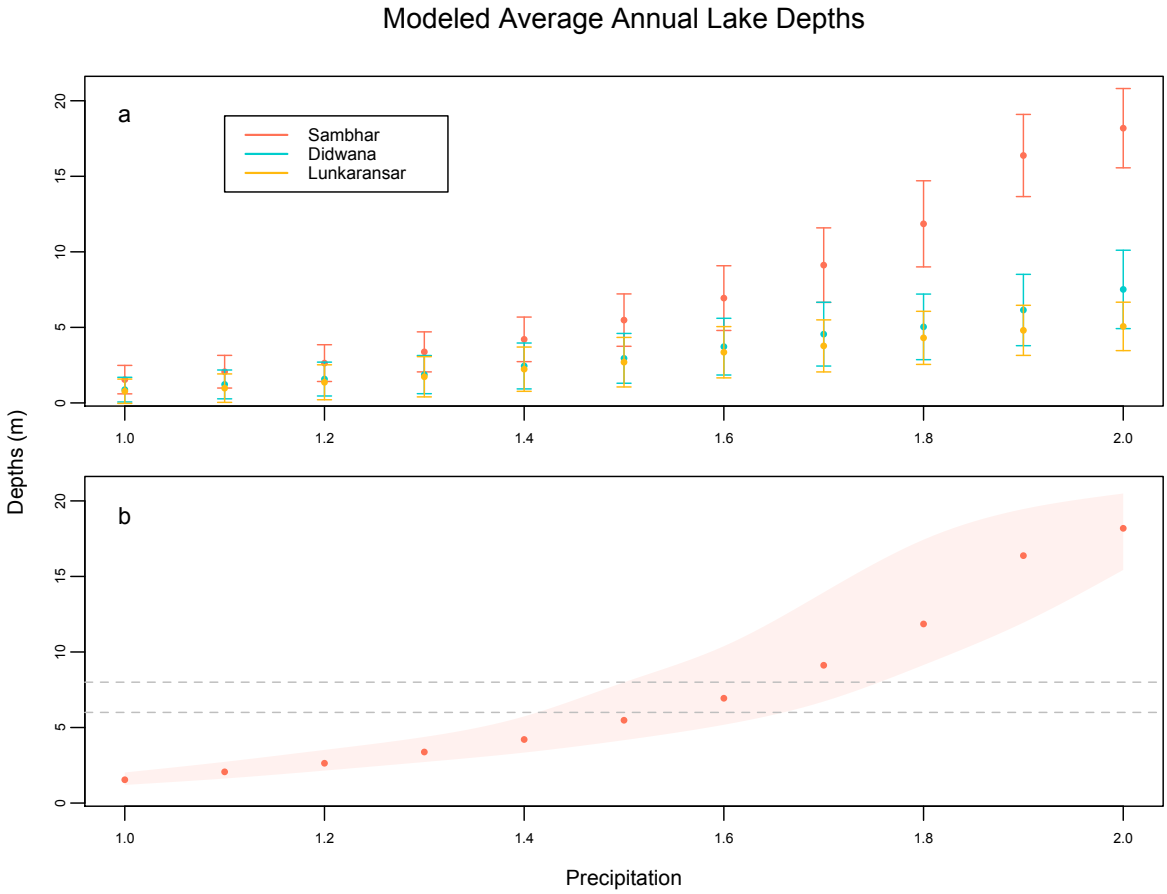

Figure 5.6: Calculated average annual lake depths for ratios of different annual amounts of precipitation to that of present (1.0) up to a doubling (2.0) of current precipitation showing both error from (a) variability in precipitation and (b) curve number shift through time. For Figure 5.6b, the points are the average annual depth for Lake Sambhar using CN=59, while the shaded region is the uncertainty due to a range of possible curve numbers ranging from 55 to 64, intended to represent possible curve numbers from early Holocene to present-day. The dashed lines represent uncertainty in sedimentation since the mid-Holocene. *Singh et al.* (1974) cited a shoreline at 6 m above the present-day lake bottom, which, assuming no sedimentation, is marked by the lower dashed line. The upper dashed line marks the depth of this shoreline assuming that 2 m of sedimentation has accumulated since the mid-Holocene.

Table 5.3: Effect of increasing current precipitation on the percentage of time Lake Sambhar spends in each antecedent moisture condition: low (AMC I), medium (AMC II), or high (AMC III).

	AMC I (%)	**AMC II (%)**	**AMC III (%)**
Current	92	4	4
25% increase	90	4	6
50% increase	88	5	7
75% increase	86	5	9
100% increase	85	5	10

also the error in the curve number and possible curve number shifts back through time. If precipitation were greater during the early- to mid-Holocene, vegetation would also have been greater, and although greater vegetation presumably does not affect overall soil type, it might alter soil texture (i.e. the increased precipitation could shift the percentages from equal sand and loam to higher loam than sand). The shaded region on Figure 5.6b encompasses calculated lake depths for a plausible range of curve numbers (55 to 64) that allow for a shift in soil texture. Figure 5.6b also includes uncertainty bands to account for a range of sedimentation between 0-2 m since the mid-Holocene. The upper dashed line at 8 m provides a range of precipitation necessary assuming that sedimentation has raised the floor of the lake everywhere by 2 m. The lower dashed line at 6 m provides a range of precipitation necessary for a lake bottom the same as present-day (i.e. no sedimentation since the mid-Holocene).

The inference by *Singh et al.* (1974) that the surface of the lake was 6 m above the present-day lakebed is the best available geologic evidence of Lake Sambhar's mid-Holocene maximum depth. In addition, a natural outlet channel to the Lake at 381 m a.s.l. places a maximum possible depth of Lake Sambhar at 21 m above present-day lake bottom. If one were to assume a 2 m rise in the lake bed level since the mid-Holocene, the 6 m difference would imply an 8 m deep paleo-lake with a maximum possible depth of 23 m. From ecological interpretations of pollen stratigraphy, *Singh et al.* (1974) estimate that mid-Holocene precipitation could have been 50% greater than that today. *Swain et al.* (1983) utilized calibration

functions to fine tune these predictions and found that an increase of about 40% more than present-day precipitation at Lake Lunkaransar was more appropriate for that lake, which compares closely to other estimations made using pollen-climate calibration functions by *Bryson and Swain* (1981).

With these various benchmarks in mind, we compare our lake model results to the three main lines of thought described above: (1) How much precipitation would it take to fill Lake Sambhar completely to a height of 381 m a.s.l?; (2) How much precipitation would it take to fill Lake Sambhar to an average annual depth of 8 m as inferred by *Singh et al.* (1974)?; and (3) How deep would Lake Sambhar be if present-day precipitation increased by 40% as estimated from various pollen studies?

According to our results, more than a doubling of present-day precipitation is necessary to fill Lake Sambhar to its maximum depth of 23 m (Figure 5.6a). This seems unlikely, as there is no evidence for such a drastic shift in precipitation regime (discussed in further detail in Section 5.6). Our model calculates that an increase of present-day precipitation by 65% would deepen to 8.1 ± 2.3 m. A 50% increase in precipitation would deepen Lake Sambhar to 5.7 ± 1.7 m, close to a 6 m deep lake assuming no sedimentation. On the lower end, a 40% increase in precipitation, as inferred by pollen reconstructions, would deepen Lake Sambhar to 3.8 ± 1.4 m.

Despite a large discrepancy in estimates of mid-Holocene precipitation depending upon the method used, our calculations suggest that the possible range of increased precipitation is perhaps not so large after all. Specifically, our model results differ from those of *Swain et al.* (1983) who predicted that a 40% increase in precipitation, as inferred from pollen calibrations, would result in a 21-m deep lake, but a 6-m increase in depth would require only a 7% increase in precipitation. Using the Sambhar lake model, both geologic shoreline evidence suggesting a level 6 m above the present-day lake floor and pollen calibration estimates fall within a range of increased precipitation of 40-65% greater than present-day precipitation.

5.5 Role of winter evaporation

As mentioned previously, early- to mid-Holocene insolation calls for greater amounts in summer, with correspondingly smaller amounts in winter, than today. Other studies (**?**) have modeled lake-level changes over monsoonal Asia and found that reduced evaporation during both summer (due to increased cloud cover) and winter (due to the decreased insolation) played a role in sustaining lakes in multiple regions, including Rajasthan, India. Theoretically, reduced winter insolation could reduce winter evaporation and allow the lake, particularly at low levels, to remain full until the following monsoon season. We calculated water depths on May 1st as functions of depths at Lake Sambhar on the previous October 1st and evaporation rates for the Present and early Holocene (8-9 ka), and found no visible difference between spring lake levels, despite the expected reduced evaporation in early Holocene time. We repeated this exercise using data from years where lake depths on October 1 were 2 m or lower, with the thought that perhaps the role of winter evaporation was visible only at very low lake levels. Again, there was no discernible difference between lake levels with present-day insolation and those with early-Holocene insolation. From this we conclude that winter evaporation plays little to no role in sustaining lake levels.

5.6 Lake dynamics

Although the inputs and outputs (precipitation, evaporation, and runoff,) of the lake model affect the volume of water in a lake approximately linearly, the introduction of the non-linearity of the hypsometric relationships introduces interesting lake dynamics. This can be seen in Figure 5.6, where lake level does not increase linearly with precipitation. Instead, for 40% greater precipitation than present-day and higher, lake depth is more sensitive to increased precipitation than it is for smaller precipitation amounts. This non-linear relationship suggests that there are states (or levels) to which the lake tends to be attracted. Hidden Markov (HM) models (*Zucchini and MacDonald*, 2009) are appropriate for model-

ing systems that switch between states, such as precipitation (*Jackson*, 1975; *Zucchini and Guttorp*, 1991) or streamflow (*Bracken et al.*, 2014). An order-m HM model identifies m 'hidden' states, each characterized as a probability distribution function (PDF), and the transition probabilities to move between them for each time step. Thus, the model fitting involves estimating the parameters of the state PDFs and transition probabilities. The best order of the HM model, m, is obtained using objective criteria such as Akaike Information Criteria or Bayesian Information Criteria (*Zucchini and MacDonald*, 2009). For the simulated depth time series of Lake Sambhar from a range of possible precipitation scenarios, we fitted order-3 HM models for each precipitation scenario to capture the low, medium, and high lake levels.

The PDFs of the three states are shown for a range of precipitation increase scenarios in Figure 5.7. Several interesting features are apparent. Currently, Lake Sambhar tends to sustain shallow depths of about 0 - 1.5 m seen by the two dominant PDFs centered around ∼0.5 m and ∼1 m (blue and orange curves, respectively; Figure 5.7a), and infrequently to higher depths of 1.5 - 3 m (as shown by the green curve centered around 2 m; Figure 5.7a). With a 50% increase in precipitation there is a drastic shift in the PDFs. The lower state PDF is centered at ∼3 m, the medium state PDF near ∼5 m, and the high state PDF near ∼8 m. The overall lake level PDF (black curve) indicates that the lake depths range between 4 and 8 m (the middle part of the distribution). For a 75% increase in precipitation the lake tends to be higher than 5 m, and for a 100% increase, the levels are greater than 12 m, suggesting a persistently deeper Lake Sambhar closer to its maximum possible depth of 23 m.

Regarding the formation of shorelines, a consistent depth of the lake is necessary in order to allow waves to carve a shoreline into the surrounding rock. Frequent variation in lake depth would not be conducive to creating shorelines. Therefore, it is possible that although a 40 - 65% increase in precipitation deepened Lake Sambhar, the seasonal variability inhibited its ability to form a clear shoreline. If this were the case, the lack of sharply defined ancient

shoreline at Lake Sambhar would not be surprising. Furthermore, this HM analysis shows that for Lake Sambhar to reach depths close to 21 m, the lake shifts into regimes that are closer together with lower variability. Therefore, if precipitation had exceeded twice its current amount, one would expect to see evidence of shorelines had the lake reached its maximum depth.

5.7 Discussion

We have shown that a relatively straightforward hydrological model captures the seasonal variability of ancient lakes in Rajasthan, India, as well as capturing the historically deep events due to periods of persistent rainfall as recorded in the early 1980s by *IndiaToday* (1999). The only data required to run this model were precipitation, temperature, insolation, soil-type and land-use data, and lake hypsometry. The lack of wind and specific humidity data was avoided using the Priestley-Taylor evaporation method.

Increases in precipitation of 40% or 50%, as hypothesized by pollen reconstructions, would increase Lake Sambhar from an average annual depth of 1.1 ± 0.8 m under present-day rainfall to 3.8 ± 1.4 m or 5.7 ± 1.7 m, respectively. Furthermore, as shown in our Hidden Markov Model analysis, a 50% increase in precipitation not only shifts the PDF of Lake Sambhar depths to greater amounts, but also shows marked variability in depths due to the hypsometry (Figure 5.2), with depths between 4 and 8 m comparably frequent. This marked variability could potentially explain the lack of visibly obvious shorelines today. Finally, we conclude that Lake Sambhar most likely did not fill to 21 m above the present day lake floor during the early- to mid-Holocene, which according to our lake model would require more than twice the current day precipitation. The evidence one would expect from such an event would include, but not be limited to, prominent shorelines and evidence that nearby lakes (i.e. Didwana and Lunkaransar) would have reached extreme depths ($\sim$8 m and $\sim$4 m, respectively). None of this evidence has been found to our knowledge. In summary, we estimate the range of plausible precipitation increases to approximately 40-65% during early-

to mid-Holocene, which is narrower but higher than the range of 7-40% previously reported (*Singh et al.*, 1974; *Bryson and Swain*, 1981; *Swain et al.*, 1983).

Additional considerations favor the lower end of the the 40-65% range. First, differences in mid-Holocene pollen from present-day vegetation imply that vegetation has changed since the mid-Holocene. Under an increased precipitation regime, one would expect: (1) watershed conditions to remain saturated and therefore in AMCIII condition for a higher percentage of the year, (2) vegetation to increase, and (3) soil texture to shift from less sand to more loam. All three of these changes would result in increased runoff. Apart from the uncertainty in the curve number provided in Figure 6, we did not explicitly consider changing vegetation cover or soil in our model. It is possible that the added runoff from increased vegetation would shift the precipitation range to the lower part of 40-65%.

Second, our model does not consider the possibility of smaller interannual variability of mid-Holocene precipitation than that today. As discussed in the Introduction, several paleoceanographic and paleoclimatic studies suggest that the tropical Pacific was in an enhanced La-Niña-like state with reduced ENSO variability during this early- to mid-Holocene. By analogy with ENSO correlations in modern climate, this implies that the monsoon was strong from year to year. In our model, we randomly sample years, including those during both El Niño and La Niña events. We anticipate that if precipitation was preferentially sampled for strong monsoons, during La Niña years, this reduced variability among rainier summers, too, would push the precipitation estimate to the lower part of the 40-65% range.

Third, GCM modeling studies suggest that with higher rainfall and therefore, higher cloud cover, surface temperatures of the mid-Holocene would be lower than those today *Li and Morrill* (2010); *Battisti et al.* (2014), and hence, evaporation would have been lower. As discussed earlier, a 1° decrease in temperature results in small decreases in evaporation. If the monsoon region was several °C cooler during the mid-Holocene, however, the effect of temperature would be more influential, in which case, Lake Sambhar would require less precipitation to sustain the same lake levels.

The question of what climatic forcing led to heavier rainfall in the mid-Holocene than present time remains. The traditional school of thought has been that the primary mechanism creating a strong monsoon during mid-Holocene time is enhanced solar radiation that strengthened the land-ocean temperature gradient, and thus, the pressure gradient, which in turn enhanced moisture transport onto India and enhanced convergence there. As a second mechanism, we know La Niña SST conditions are also particularly conducive to a productive South Asian monsoon. Although increased summer insolation presumably could enhance the land-ocean pressure gradient over the Indian subcontinent, and induce a stronger monsoon, it seems likely that the La Niña-like state of the Pacific contributed to the 40-65% increase in precipitation as well.

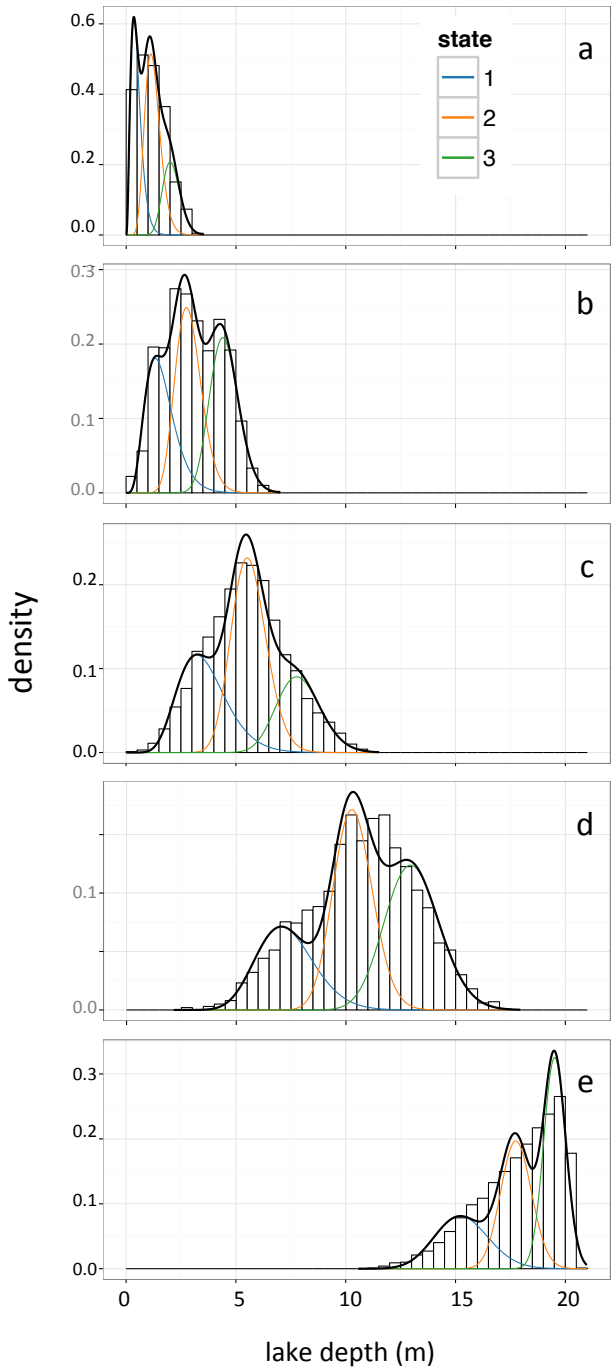

Figure 5.7: Hidden Markov (HM) results for average annual lake depths of Lake Sambhar following runs of the lake model with various precipitation levels: (a) current precipitation, (b) 25% increase, (c) 50% increase, (d) 75% increase and, (e) 100% (doubling) of precipitation. The blue, orange, and green lines correspond to States 1 (low depth), 2 (medium depth), and 3 (high depth), respectively as modeled by the HM analysis.

Chapter 6

Dissertation Conclusions

6.1 Summary

In *Sub-Seasonal Variations in Spatial Signatures of ENSO on the Indian Summer Monsoon* (Chapter 2), correlations of NINO3.4 SST anomalies with seasonal average rainfall anomalies over India reveal a rich teleconnection mosaic across the subcontinent that shifts as the monsoon season progresses through early, middle, and late sub-seasons. As a result, some regions of India are more affected by anomalous SSTs in the Pacific during certain sub-seasons more than others. Specifically, a 1°C cooling of the central equatorial Pacific (i.e. La Niña conditions) can result in: $\sim$ 70-100% increase in precipitation in north-central Indian and the Indo-Gangetic Plains during the early season, $\sim$ 30-80% increase in peak season precipitation in south-central India, and northwestern Rajasthan, and $\sim$ 60-100% increase in late season precipitation in northern, north-western, and central India. Addtionally, we note spatial and temporal asymmetries between the signature of rainfall associated with La Niña versus El Niño conditions. For example, El Niño suppresses peak season rainfall in the south-central and northwestern Rajasthan regions more than La Niña enhances it. In the late-season, however, La Niña writes a stronger signature than El Niño in the northern, northwestern, and central India. Composites of geopotential height and velocity potential suggest anomalous subsidence (ascent) during El Niño (La Niña) seasons with slightly different patterns during the early season as compared to the middle or late season. These patterns are consistent with the hypothesis that local Hadley cell circulation is the primary

mechanism responsible for enhanced or reduced rainfall over India during the early season, but that as the monsoon season progresses, larger scale teleconnections (associated with a shifted Walker circulation) dominate the dynamics. The findings of this study urge that monsoon forecasting efforts incorporate ENSO asymmetries and focus on smaller regions by utlizing high resolution rainfall datasets during sub-seasonal periods.

In *Multi-Proxy Reconstruction of Equatorial Pacific SST and Zonal Wind Fields of the past 10,000 years using Mg/Ca and Alkenone Records* (Chapter 3), Mg/Ca and U_{37}^{k} proxy SST records are used to reconstruct full fields of SST and zonal wind anomalies for 10, 8, 6, 4 and 2 ka. The reconstructions reveal coldest SST anomalies ($\sim$ -1°C) occur in the eastern Pacific at 10 ka. At the same time, the largest zonal wind anomalies ($\sim$ 8 m s^{-1}) occur in the central Pacific, which is indicative of strong easterlies. The largest zonal temperature anomaly differences (average east Pacific SST minus average west Pacific SST) are -0.36°C and -0.33°C, which occur at 6 and 10 ka, respectively. After 10 ka until 2 ka, the eastern Pacific warms, the zonal temperature difference decreases, and the easterlies weaken.

Using a similar methodology to Chapter 3, *Multi-Proxy Reconstruction of Indian Summer Monsoon Winds and Precipitation of the past 10,000 years using Mg/Ca and Alkenone Records* (Chapter 4), Mg/Ca and U_{37}^{k} proxy SST records are used to reconstruct full fields of summer monsoon wind stress curl and Indian rainfall for 10, 8, 6, 4 and 2 ka. Consistent with the Pacific SST reconstructions, strongest wind stress curl and rainfall anomalies over the monsoonal region occur during 10 ka, gradually weakening to present day. Despite large uncertainties, this chapter suggests that telconnections from the Pacific could be responsible for the mid-Holocene wetness as revealed by proxy records scattered across the south Asian summer monsoon region.

In *An Assessment of the Mean Annual Precipitation Needed to Sustain Lake Sambhar in Rajasthan, India during Mid-Holocene Time* (Chapter 5), a simple hydrological model for Lake Sambhar provides tighter bounds on the range of increased precipitation needed to sustain lakes in Rajasthan, India during the early- to mid-Holocene. The lake model

reveals that precipitation during high lake stands was likely 40-65% greater than present day precipitation levels, which would result in a lake depth of $\sim$ 6 to 8 m.

6.2 Discussion

This dissertation presents quantitatively reconstructed Indian monsoon hydroclimate variability over the past 10 ka using contemporary relationships between Pacific SSTs and Indian monsoon rainfall and proxy SST records that span the Holocene time. According to Mg/Ca and U^k_{37} proxy SST records, coldest temperatures and greatest easterlies (i.e. La Niña-like conditions) were strongest at 10 and 6 ka during the early- to mid-Holocene. Additionally, this research tested the plausibility of the hypothesis that ENSO teleconnections could account for the enhanced wetness as implied by early- to mid-Holocene paleo-proxies across the monsoon region. Proxy records suggest a 40% increase in precipitation during the early- to mid-Holocene, which, according to the results of the lake model study, would account for the majority, if not all, of the precipitation needed to sustain Lake Sambhar. We emphasize that this research shows that it is possible that Pacific SSTs were resposible for the early- to mid-Holocene wetness over India.

6.3 Future Work

This work sets the stage for interesting extensions in the fields of monsoon forecasting, climate field prediction, and lake modeling.

The findings of the contemporary analysis provide the basis for creating a sub-seasonal and regional monsoon forecasting tool. Another interesting area to investigate would be trends in the asymmetry between La Niña and El Niño. We found preliminary evidence that although El Niño's have continued to suppress rainfall over India in recent decades, the relationship between La Niña's enhancing rainfall has diminished. This suggests that the overall weakening in the ENSO-monsoon teleconnection that has been documented in recent years is due to the La Niña-side only. It is possible this could be tied to strong warming of

the Indian Ocean, however, more rigorous analysis is needed.

A shortcoming to the reduced dimension reconstruction methodologies is the difficulty to define uncertainties in a CCA-based approach. Bayesian hierarchies offer a tool that can be used to interpret sparse and uncertain data and has been applied to paleo-climate reconstructions . Hierarchical relationships between the desired climate fields are established, and errors are more easily propagated through the reconstruction.

The lake model built for Lake Sambhar provides a tool that could be esily applied to various lake beds throughout the Indian monsoon region. Lake levels have typically been reconstructed by using proxy records, such as pollen. Proxy records, however, can be biased by environmental factors. A hydrological lake model allows one to model lake levels directly using the principals of a watershed balance. If a lake bed has dateable shorelines, assumptions of this methodology are minimal. Application of this simple lake model to scattered lake beds could provide a spatial picture of rainfall levels during early- to mid-Holocene time.

It is likely that a wetter precipitation regime would drastically change vegetation throughout the monsoon region. An increase in vegetation would likely increase runoff, which would potentially make 40-65% an overestimate. A worthy endeavor would involve reconstructing vegetation throughout India to better reconstruct hydrological processes and further tighten the bounds of possible precipitation levels.

Finally, following this research, one might wonder whether the enhanced La Niña-like state was a result of changes in insolation during the early- to mid-Holocene time. This is an entirely different question than those addressed in this dissertation, but an interesting one nonetheless, as it will be important to understand how ENSO might respond to future warming.

Bibliography

Achyuthan, H., J. Quade, L. Roe, and C. Placzek (2007), Stable isotopic composition of pedogenic carbonates from the eastern margin of the thar desert, rajasthan, india, *Quaternary International*, *162*, 50–60.

Aggarwal, S. C. (1951), *The Sambhar lake salt source*, Government of India Press.

Aggarwal, S. C. (1957), *Pachbadra & Didwana salt sources: by SC Aggarwal, Salt Commissioner to the Government of India, Ministry of Production*.

Allan, R. J., J. A. Lindesay, and C. J. Reason (1995), Multidecadal variability in the climate system over the indian ocean region during the austral summer, *Journal of Climate*, *8*(7), 1853–1873.

Anand, P., H. Elderfield, and M. H. Conte (2003), Calibration of mg/ca thermometry in planktonic foraminifera from a sediment trap time series, *Paleoceanography*, *18*(2).

Annamalai, H., and J. Slingo (2001), Active/break cycles: diagnosis of the intraseasonal variability of the asian summer monsoon, *Climate Dynamics*, *18*(1-2), 85–102.

Ashok, K., and N. Saji (2007), On the impacts of enso and indian ocean dipole events on sub-regional indian summer monsoon rainfall, *Natural Hazards*, *42*(2), 273–285.

Ashok, K., and T. Yamagata (2009), Climate change: The el niño with a difference, *Nature*, *461*(7263), 481–484.

Ashok, K., Z. Guan, and T. Yamagata (2001), Impact of the indian ocean dipole on the relationship between the indian monsoon rainfall and enso, *Geophysical Research Letters*, *28*(23), 4499–4502.

Ashok, K., Z. Guan, N. Saji, and T. Yamagata (2004), Individual and combined influences of enso and the indian ocean dipole on the indian summer monsoon, *Journal of Climate*, *17*(16), 3141–3155.

Ashok, K., S. K. Behera, S. A. Rao, H. Weng, and T. Yamagata (2007), El niño modoki and its possible teleconnection, *Journal of Geophysical Research: Oceans (1978–2012)*, *112*(C11).

Bard, E., F. Rostek, and C. Sonzogni (1997), Interhemispheric synchrony of the last deglaciation inferred from alkenone palaeothermometry, *Nature*, *385*(6618), 707–710.

Barnett, T., and R. Preisendorfer (1987), Origins and levels of monthly and seasonal forecast skill for united states surface air temperatures determined by canonical correlation analysis, *Monthly Weather Review*, *115*(9), 1825–1850.

Barnston, A. G. (1994), Linear statistical short-term climate predictive skill in the northern hemisphere, *Journal of Climate*, *7*(10), 1513–1564.

Barnston, A. G., and C. F. Ropelewski (1992), Prediction of enso episodes using canonical correlation analysis, *Journal of climate*, *5*(11), 1316–1345.

Barnston, A. G., and T. M. Smith (1996), Specification and prediction of global surface temperature and precipitation from global sst using cca, *Journal of Climate*, *9*(11), 2660–2697.

Bartlein, P., S. Harrison, S. Brewer, S. Connor, B. Davis, K. Gajewski, J. Guiot, T. Harrison-Prentice, A. Henderson, O. Peyron, et al. (2011), Pollen-based continental climate reconstructions at 6 and 21 ka: a global synthesis, *Climate Dynamics*, *37*(3-4), 775–802.

Battisti, D., Q. Ding, and G. Roe (2014), Coherent pan-asian climatic and isotopic response to orbital forcing of tropical insolation, *Journal of Geophysical Research: Atmospheres*, *119*(21), 11–997.

Beaufort, L., S. Kaars, F. Bassinot, and V. Moron (2010), Past dynamics of the australian monsoon: precession, phase and links to the global monsoon concept, *Climate of the Past*, *6*(5), 695–706.

Bemis, E., H. J. Spero, J. Bijma, and D. W. Lea (1998), Reevaluation of the oxygen isotopic composition of planktonic foraminifera: Experimental results and revised paleotemperature equations, *Paleoceanography*, *13*(2), 150–160.

Benway, H. M., A. C. Mix, B. A. Haley, and G. P. Klinkhammer (2006), Eastern pacific warm pool paleosalinity and climate variability: 0–30 kyr, *Paleoceanography*, *21*(3).

Berger, A. (1992), Orbital variations and insolation database, *IGBP PAGES/World Data Center-A for Paleoclimatology Data Contribution Series*, *92*(007).

Berger, A., and M.-F. Loutre (1991), Insolation values for the climate of the last 10 million years, *Quaternary Science Reviews*, *10*(4), 297–317.

Berliand, M., and T. Berliand (1952), Measurement of the effective radiation of the earth with varying cloud amounts, *Izv. Akad. Nauk SSSR Ser. Geofiz*, *1*, 64–78.

Bhaskaran, B., and J. Mitchell (1998), Simulated changes in southeast asian monsoon precipitation resulting from anthropogenic emissions, *International Journal of Climatology*, *18*(13), 1455–1462.

Bolliet, T., A. Holbourn, W. Kuhnt, C. Laj, C. Kissel, L. Beaufort, M. Kienast, N. Andersen, and D. Garbe-Schönberg (2011), Mindanao dome variability over the last 160 kyr: Episodic glacial cooling of the west pacific warm pool, *Paleoceanography*, *26*(1).

Boos, W. R., and K. A. Emanuel (2009), Annual intensification of the somali jet in a quasi-equilibrium framework: Observational composites, *Quarterly Journal of the Royal Meteorological Society*, *135*(639), 319–335.

Boos, W. R., and Z. Kuang (2010), Dominant control of the south asian monsoon by orographic insulation versus plateau heating, *Nature*, *463*(7278), 218–222.

Bracken, C., B. Rajagopalan, and E. Zagona (2014), A hidden markov model combined with climate indices for multidecadal streamflow simulation, *Water Resources Research*, *50*(10), 7836–7846.

Brassell, S., G. Eglinton, I. Marlowe, U. Pflaumann, and M. Sarnthein (1986), Molecular stratigraphy: a new tool for climatic assessment, *Nature*, *320*, 129–133.

Bretherton, C. S., C. Smith, and J. M. Wallace (1992), An intercomparison of methods for finding coupled patterns in climate data, *Journal of climate*, *5*(6), 541–560.

Bryson, R. A., and A. Swain (1981), Holocene variations of monsoon rainfall in rajasthan, *Quaternary Research*, *16*(2), 135–145.

Budyko, M. (1974), *Climate and Life (International Geophysics)*, New York: Academic Press.

Cane, M. A., A. C. Clement, A. Kaplan, Y. Kushnir, D. Pozdnyakov, R. Seager, S. E. Zebiak, and R. Murtugudde (1997), Twentieth-century sea surface temperature trends, *Science*, *275*(5302), 957–960.

Carré, M., J. P. Sachs, S. Purca, A. J. Schauer, P. Braconnot, R. A. Falcón, M. Julien, and D. Lavallée (2014), Holocene history of enso variance and asymmetry in the eastern tropical pacific, *Science*, *345*(6200), 1045–1048.

Cash, B. A., J. L. Kinter III, J. Adams, E. Altshuler, B. Huang, E. K. Jin, J. Manganello, L. Marx, and T. Jung (2015), Regional structure of the indian summer monsoon in observations, reanalysis, and simulation, *Journal of Climate*, *28*, 1824–1841.

Central Water Commission, G. o. I. (2006), Evaporation control in reservoirs.

Chazen, C. R., M. A. Altabet, and T. D. Herbert (2009), Abrupt mid-holocene onset of centennial-scale climate variability on the peru-chile margin, *Geophysical Research Letters*, *36*(18).

Cherry, S. (1996), Singular value decomposition analysis and canonical correlation analysis, *Journal of Climate*, *9*(9), 2003–2009.

Clement, A., R. Seager, and M. Cane (1999), Orbital controls on the el niño/southern oscillation and the tropical climate, *Paleoceanography*, *14*(4), 441–456.

Clement, A. C., R. Seager, M. A. Cane, and S. E. Zebiak (1996), An ocean dynamical thermostat, *Journal of Climate*, *9*(9), 2190–2196.

Clement, A. C., R. Seager, and M. A. Cane (2000), Suppression of el niño during the mid-holocene by changes in the earth's orbit, *Paleoceanography*, *15*(6), 731–737.

Cobb, K. M., N. Westphal, H. R. Sayani, J. T. Watson, E. Di Lorenzo, H. Cheng, R. Edwards, and C. D. Charles (2013), Highly variable el niño–southern oscillation throughout the holocene, *Science*, *339*(6115), 67–70.

Conroy, J. L., J. T. Overpeck, J. E. Cole, T. M. Shanahan, and M. Steinitz-Kannan (2008), Holocene changes in eastern tropical pacific climate inferred from a galápagos lake sediment record, *Quaternary Science Reviews*, *27*(11), 1166–1180.

Conte, M. H., M.-A. Sicre, C. Rühlemann, J. C. Weber, S. Schulte, D. Schulz-Bull, and T. Blanz (2006), Global temperature calibration of the alkenone unsaturation index (ukâĂš 37) in surface waters and comparison with surface sediments, *Geochemistry, Geophysics, Geosystems*, *7*(2).

Cook, E. R., D. M. Meko, D. W. Stahle, and M. K. Cleaveland (1999), Drought reconstructions for the continental united states*, *Journal of Climate*, *12*(4), 1145–1162.

Curry, W., D. Ostermann, M. Guptha, and V. Ittekkot (1992), Foraminiferal production and monsoonal upwelling in the arabian sea: evidence from sediment traps, *Geological Society, London, Special Publications*, *64*(1), 93–106.

de Garidel-Thoron, T., Y. Rosenthal, F. Bassinot, and L. Beaufort (2005), Stable sea surface temperatures in the western pacific warm pool over the past 1.75 million years, *Nature*, *433*(7023), 294–298.

de Garidel-Thoron, T., Y. Rosenthal, L. Beaufort, E. Bard, C. Sonzogni, and A. C. Mix (2007), A multiproxy assessment of the western equatorial pacific hydrography during the last 30 kyr, *Paleoceanography*, *22*(3).

Deb, S. (1952), Occurrence of natural salts and selenite gypsum in the neighbourhood of lunkaransar tal, north of bikaner, western rajputana, *Bulletin of the National Institute of Sciences of India*, *1*, 94–99.

Dekens, P. S., D. W. Lea, D. K. Pak, and H. J. Spero (2002), Core top calibration of mg/ca in tropical foraminifera: Refining paleotemperature estimation, *Geochemistry, Geophysics, Geosystems*, *3*(4), 1–29.

Deotare, B., M. Kajale, S. Rajaguru, S. Kusumgar, A. Jull, and J. Donahue (2004), Palaeoenvironmental history of bap-malar and kanod playas of western rajasthan, thar desert, *Journal of Earth System Science*, *113*(3), 403–425.

Department of Agriculture, G. o. I. (2014), Contingency plan.

Doose-Rolinski, H., U. Rogalla, G. Scheeder, A. Lückge, and U. Rad (2001), High-resolution temperature and evaporation changes during the late holocene in the northeastern arabian sea, *Paleoceanography*, *16*(4), 358–367.

Durbude, D. G., B. Purandara, and A. Sharma (2001), Estimation of surface runoff potential of a watershed in semi-arid environmentâĂŤa case study, *Journal of the Indian Society of Remote Sensing*, *29*(1-2), 47–58.

Emile-Geay, J., M. Cane, R. Seager, A. Kaplan, and P. Almasi (2007), El niño as a mediator of the solar influence on climate, *Paleoceanography*, *22*(3).

Enzel, Y., L. Ely, S. Mishra, R. Ramesh, R. Amit, B. Lazar, S. Rajaguru, V. Baker, and A. Sandler (1999), High-resolution holocene environmental changes in the thar desert, northwestern india, *Science*, *284*(5411), 125–128.

Evans, M. N., A. Kaplan, and M. A. Cane (2002), Pacific sea surface temperature field reconstruction from coral δ18o data using reduced space objective analysis, *Paleoceanography*, *17*(1), 7–1.

Fleitmann, D., S. J. Burns, M. Mudelsee, U. Neff, J. Kramers, A. Mangini, and A. Matter (2003), Holocene forcing of the indian monsoon recorded in a stalagmite from southern oman, *Science*, *300*(5626), 1737–1739.

Fleitmann, D., S. J. Burns, A. Mangini, M. Mudelsee, J. Kramers, I. Villa, U. Neff, A. A. Al-Subbary, A. Buettner, D. Hippler, et al. (2007), Holocene itcz and indian monsoon dynamics recorded in stalagmites from oman and yemen (socotra), *Quaternary Science Reviews*, *26*(1), 170–188.

Flohn, H. (1957), Large-scale aspects of the" summer monsoon" in south and east asia, *J. Meteor. Soc. Japan*, *75*, 180–186.

Flohn, H. (1968), *Contributions to a meteorology of the Tibetan Highlands*, 130, Department of Atmospheric Science, Colorado State University Fort Collins, Colorado.

Gajbhiye, S., S. Mishra, and A. Pandey (2014), Relationship between scs-cn and sediment yield, *Applied Water Science*, pp. 1–8.

Gill, E., B. Rajagopalan, and P. Molnar (2015), Subseasonal variations in spatial signatures of enso on the indian summer monsoon from 1901 to 2009, *Journal of Geophysical Research, Atmospheres*.

Godbole, N. (1952), The salinity of sambhar lake, in *Proceedings of symposium on Rajputana Desert, Bull Nat Inst Sci India*, vol. 1, pp. 89–93.

Goodbred, S. L., and S. A. Kuehl (2000), Enormous ganges-brahmaputra sediment discharge during strengthened early holocene monsoon, *Geology*, *28*(12), 1083–1086.

Goswami, B. (1998), Interannual variations of indian summer monsoon in a gcm: External conditions versus internal feedbacks, *Journal of Climate*, *11*(4), 501–522.

Govil, P., and P. D. Naidu (2010), Evaporation-precipitation changes in the eastern arabian sea for the last 68 ka: Implications on monsoon variability, *Paleoceanography*, *25*(1).

Guhathakurta, P., and M. Rajeevan (2008), Trends in the rainfall pattern over india, *International Journal of Climatology*, *28*(11), 1453–1469.

Gupta, A. K., D. M. Anderson, and J. T. Overpeck (2003), Abrupt changes in the asian southwest monsoon during the holocene and their links to the north atlantic ocean, *Nature*, *421*(6921), 354–357.

Hastings, D., M. Kienast, S. Steinke, and A. Whitko (2001), A comparison of three independent paleotemperature estimates from a high resolution record of deglacial sst records in the tropical south china sea, in *AGU Fall Meeting Abstracts*, vol. 1, p. 10.

Herbert, T. (2003), Alkenone paleotemperature determinations, Elsevier.

Hsu, P.-c., T. Li, H. Murakami, and A. Kitoh (2013), Future change of the global monsoon revealed from 19 cmip5 models, *Journal of Geophysical Research: Atmospheres*, *118*(3), 1247–1260.

Hu, Z.-Z., M. Latif, E. Roeckner, and L. Bengtsson (2000), Intensified asian summer monsoon and its variability in a coupled model forced by increasing greenhouse gas concentrations, *Geophysical Research Letters*, *27*(17), 2681–2684.

Ihara, C., Y. Kushnir, and M. A. Cane (2008a), July droughts over homogeneous indian monsoon region and indian ocean dipole during el niño events, *International Journal of Climatology*, *28*(13), 1799–1805.

Ihara, C., Y. Kushnir, and M. A. Cane (2008b), Warming trend of the indian ocean sst and indian ocean dipole from 1880 to 2004*, *Journal of Climate*, *21*(10), 2035–2046.

Ihara, C., Y. Kushnir, M. A. Cane, and A. Kaplan (2008c), Timing of el nino-related warming and indian summer monsoon rainfall, *Journal of Climate*, *21*(11), 2711–2719.

IndiaToday (1999), Sambhar lake: India's largest inland source of salt being killed slowly.

Islam, S., Y. Tang, and P. L. Jackson (2013), Asian monsoon simulations by community climate models cam4 and ccsm4, *Climate dynamics*, *41*(9-10), 2617–2642.

Ivanochko, T. S., R. S. Ganeshram, G.-J. A. Brummer, G. Ganssen, S. J. Jung, S. G. Moreton, and D. Kroon (2005), Variations in tropical convection as an amplifier of global climate change at the millennial scale, *Earth and Planetary Science Letters*, *235*(1), 302–314.

Jackson, B. B. (1975), Markov mixture models for drought lengths, *Water resources research*, *11*(1), 64–74.

Joseph, P. (2012), Synoptic systems during monsoon seasons, *Monsoon Monographs*, *2*, 1–34.

Jourdain, N. C., A. S. Gupta, A. S. Taschetto, C. C. Ummenhofer, A. F. Moise, and K. Ashok (2013), The indo-australian monsoon and its relationship to enso and iod in reanalysis data and the cmip3/cmip5 simulations, *Climate dynamics*, *41*(11-12), 3073–3102.

Ju, J., and J. Slingo (1995), The asian summer monsoon and enso, *Quarterly Journal of the Royal Meteorological Society*, *121*(525), 1133–1168.

Kajale, M., and B. Deotare (1997), Late quaternary environmental studies on salt lakes in western rajasthan, india: a summarised view, *Journal of Quaternary Science*, *12*(5), 405–412.

Kalnay, E., M. Kanamitsu, R. Kistler, W. Collins, D. Deaven, L. Gandin, M. Iredell, S. Saha, G. White, J. Woollen, et al. (1996), The ncep/ncar 40-year reanalysis project, *Bulletin of the American meteorological Society*, *77*(3), 437–471.

Kane, R. (2000), Enso relationship with indian rainfall in different months, *International journal of climatology*, *20*(7), 783–792.

Kaplan, A., M. A. Cane, Y. Kushnir, A. C. Clement, M. B. Blumenthal, and B. Rajagopalan (1998), Analyses of global sea surface temperature 1856–1991, *Journal of Geophysical Research: Oceans (1978–2012)*, *103*(C9), 18,567–18,589.

Kaufman, D. S., D. P. Schneider, N. P. McKay, C. M. Ammann, R. S. Bradley, K. R. Briffa, G. H. Miller, B. L. Otto-Bliesner, J. T. Overpeck, B. M. Vinther, et al. (2009), Recent warming reverses long-term arctic cooling, *Science*, *325*(5945), 1236–1239.

Keshavamurty, R. (1982), Response of the atmosphere to sea surface temperature anomalies over the equatorial pacific and the teleconnections of the southern oscillation, *Journal of the Atmospheric Sciences*, *39*(6), 1241–1259.

Kienast, M., S. Steinke, K. Stattegger, and S. Calvert (2001), Synchronous tropical south china sea sst change and greenland warming during deglaciation, *Science*, *291*(5511), 2132–2134.

Kienast, M., S. S. Kienast, S. E. Calvert, T. I. Eglinton, G. Mollenhauer, R. François, and A. C. Mix (2006), Eastern pacific cooling and atlantic overturning circulation during the last deglaciation, *Nature*, *443*(7113), 846–849.

Kim, J.-H., N. Rimbu, S. J. Lorenz, G. Lohmann, S.-I. Nam, S. Schouten, C. Rühlemann, and R. R. Schneider (2004), North pacific and north atlantic sea-surface temperature variability during the holocene, *Quaternary Science Reviews*, *23*(20), 2141–2154.

Kitoh, A., S. Yukimoto, A. Noda, and T. Motoi (1997), Simulated changes in the asian summer monsoon at times of increased atmospheric co2, *Journal of the Meteorological Society of Japan*, *75*(6), 1019–1031.

Koutavas, A., and J. P. Sachs (2008), Northern timing of deglaciation in the eastern equatorial pacific from alkenone paleothermometry, *Paleoceanography*, *23*(4).

Koutavas, A., J. Lynch-Stieglitz, T. M. Marchitto, and J. P. Sachs (2002), El nino-like pattern in ice age tropical pacific sea surface temperature, *Science*, *297*(5579), 226–230.

Koutavas, A., G. C. Olive, J. Lynch-Stieglitz, et al. (2006), Mid-holocene el niño–southern oscillation (enso) attenuation revealed by individual foraminifera in eastern tropical pacific sediments, *Geology*, *34*(12), 993–996.

Krishna Kumar, K., M. Soman, and K. R. Kumar (1995), Seasonal forecasting of indian summer monsoon rainfall: a review, *Weather*, *50*(12), 449–467.

Krishna Kumar, K., B. Rajagopalan, and M. A. Cane (1999), On the weakening relationship between the indian monsoon and enso, *Science*, *284*(5423), 2156–2159.

Krishna Kumar, K., B. Rajagopalan, M. Hoerling, G. Bates, and M. Cane (2006), Unraveling the mystery of indian monsoon failure during el nino, *Science*, *314*(5796), 115–119.

Krishna Kumar, K., K. Kamala, B. Rajagopalan, M. P. Hoerling, J. K. Eischeid, S. Patwardhan, G. Srinivasan, B. Goswami, and R. Nemani (2011), The once and future pulse of indian monsoonal climate, *Climate dynamics*, *36*(11-12), 2159–2170.

Krishnamurthy, V., and B. P. Kirtman (2003), Variability of the indian ocean: Relation to monsoon and enso, *Quarterly Journal of the Royal Meteorological Society*, *129*(590), 1623–1646.

Krishnamurthy, V., and J. Shukla (2000), Intraseasonal and interannual variability of rainfall over india, *Journal of Climate*, *13*(24), 4366–4377.

Krishnamurthy, V., and J. Shukla (2007), Intraseasonal and seasonally persisting patterns of indian monsoon rainfall, *Journal of climate*, *20*(1), 3–20.

Krishnan, R., T. Sabin, D. Ayantika, A. Kitoh, M. Sugi, H. Murakami, A. Turner, J. Slingo, and K. Rajendran (2013), Will the south asian monsoon overturning circulation stabilize any further?, *Climate dynamics*, *40*(1-2), 187–211.

Krishnaswamy, J., S. Vaidyanathan, B. Rajagopalan, M. Bonell, M. Sankaran, R. Bhalla, and S. Badiger (2014), Non-stationary and non-linear influence of enso and indian ocean dipole on the variability of indian monsoon rainfall and extreme rain events, *Climate Dynamics*, pp. 1–10.

Kudrass, H., A. Hofmann, H. Doose, K. Emeis, and H. Erlenkeuser (2001), Modulation and amplification of climatic changes in the northern hemisphere by the indian summer monsoon during the past 80 ky, *Geology*, *29*(1), 63–66.

Kutzbach, J., and B. Otto-Bliesner (1982), The sensitivity of the african-asian monsoonal climate to orbital parameter changes for 9000 years bp in a low-resolution general circulation model, *Journal of the Atmospheric Sciences*, *39*(6), 1177–1188.

Kutzbach, J. E. (1981), Monsoon climate of the early holocene: climate experiment with the earthâĂŹs orbital parameters for 9000 years ago, *Science*, *214*(4516), 59–61.

Lal, M., U. Cubasch, R. Voss, and J. Waszkewitz (1995), Effect of transient increase in greenhouse gases, *Current Science*, *69*(9), 752–763.

Lau, K., and H. Wu (2001), Principal modes of rainfall-sst variability of the asian summer monsoon: A reassessment of the monsoon-enso relationship, *Journal of Climate*, *14*(13), 2880–2895.

Lea, D. W., and P. A. Martin (1996), A rapid mass spectrometric method for the simultaneous analysis of barium, cadmium, and strontium in foraminifera shells, *Geochimica et Cosmochimica Acta*, *60*(16), 3143–3149.

Lea, D. W., T. A. Mashiotta, and H. J. Spero (1999), Controls on magnesium and strontium uptake in planktonic foraminifera determined by live culturing, *Geochimica et Cosmochimica Acta*, *63*(16), 2369–2379.

Lea, D. W., D. K. Pak, and H. J. Spero (2000), Climate impact of late quaternary equatorial pacific sea surface temperature variations, *Science*, *289*(5485), 1719–1724.

Lea, D. W., D. K. Pak, C. L. Belanger, H. J. Spero, M. A. Hall, and N. J. Shackleton (2006), Paleoclimate history of galapagos surface waters over the last 135,000 yr, *Quaternary Science Reviews*, *25*(11), 1152–1167.

Leduc, G., L. Vidal, K. Tachikawa, F. Rostek, C. Sonzogni, L. Beaufort, and E. Bard (2007), Moisture transport across central america as a positive feedback on abrupt climatic changes, *Nature*, *445*(7130), 908–911.

Leduc, G., R. Schneider, J.-H. Kim, and G. Lohmann (2010), Holocene and eemian sea surface temperature trends as revealed by alkenone and mg/ca paleothermometry, *Quaternary Science Reviews*, *29*(7), 989–1004.

Lee, T. C., F. W. Zwiers, and M. Tsao (2008), Evaluation of proxy-based millennial reconstruction methods, *Climate Dynamics*, *31*(2-3), 263–281.

Levi, C., L. Labeyrie, F. Bassinot, F. Guichard, E. Cortijo, C. Waelbroeck, N. Caillon, J. Duprat, T. de Garidel-Thoron, and H. Elderfield (2007), Low-latitude hydrological cycle and rapid climate changes during the last deglaciation, *Geochemistry, Geophysics, Geosystems*, *8*(5).

Li, B., D. W. Nychka, and C. M. Ammann (2010), The value of multiproxy reconstruction of past climate, *Journal of the American Statistical Association*, *105*(491), 883–895.

Li, C., and M. Yanai (1996), The onset and interannual variability of the asian summer monsoon in relation to land-sea thermal contrast, *Journal of Climate*, *9*(2), 358–375.

Li, Y., and C. Morrill (2010), Multiple factors causing holocene lake-level change in monsoonal and arid central asia as identified by model experiments, *Climate dynamics*, *35*(6), 1119–1132.

Liu, Z., J. Kutzbach, and L. Wu (2000), Modeling climate shift of el nino variability in the holocene, *Geophysical Research Letters*, *27*(15), 2265–2268.

Liu, Z., B. Otto-Bliesner, J. Kutzbach, L. Li, and C. Shields (2003), Coupled climate simulation of the evolution of global monsoons in the holocene*, *Journal of Climate*, *16*(15), 2472–2490.

Loader, C. (1999), *Local regression and likelihood*, vol. 47, springer New York.

Loader, C. R., et al. (1996), Local likelihood density estimation, *The Annals of Statistics*, *24*(4), 1602–1618.

Luan, Y., P. Braconnot, Y. Yu, W. Zheng, and O. Marti (2012), Early and mid-holocene climate in the tropical pacific: seasonal cycle and interannual variability induced by insolation changes, *Climate of the Past*, *8*(3), 1093–1108.

Lückge, A., M. Mohtadi, C. Rühlemann, G. Scheeder, A. Vink, L. Reinhardt, and M. Wiedicke (2009), Monsoon versus ocean circulation controls on paleoenvironmental conditions off southern sumatra during the past 300,000 years, *Paleoceanography*, *24*(1).

Luterbacher, J., E. Xoplaki, D. Dietrich, R. Rickli, J. Jacobeit, C. Beck, D. Gyalistras, C. Schmutz, and H. Wanner (2002), Reconstruction of sea level pressure fields over the eastern north atlantic and europe back to 1500, *Climate Dynamics*, *18*(7), 545–561.

Luterbacher, J., D. Dietrich, E. Xoplaki, M. Grosjean, and H. Wanner (2004), European seasonal and annual temperature variability, trends, and extremes since 1500, *Science*, *303*(5663), 1499–1503.

Maidment, D. R., et al. (1992), *Handbook of hydrology.*, McGraw-Hill Inc.

Mann, M. E., R. S. Bradley, and M. K. Hughes (1998), Global-scale temperature patterns and climate forcing over the past six centuries, *Nature*, *392*(6678), 779–787.

Mann, M. E., Z. Zhang, M. K. Hughes, R. S. Bradley, S. K. Miller, S. Rutherford, and F. Ni (2008), Proxy-based reconstructions of hemispheric and global surface temperature variations over the past two millennia, *Proceedings of the National Academy of Sciences*, *105*(36), 13,252–13,257.

Marchitto, T. M., R. Muscheler, J. D. Ortiz, J. D. Carriquiry, and A. van Geen (2010), Dynamical response of the tropical pacific ocean to solar forcing during the early holocene, *Science*, *330*(6009), 1378–1381.

Mays, L. W. (2011), *Ground and surface water hydrology*, Wiley, New Jersey.

McGregor, H., M. Fischer, M. Gagan, D. Fink, S. Phipps, H. Wong, and C. Woodroffe (2013), A weak el niño/southern oscillation with delayed seasonal growth around 4,300 years ago, *Nature Geoscience*, *6*(11), 949–953.

Meehl, G. A., and W. M. Washington (1993), South asian summer monsoon variability in a model with doubled atmospheric carbon dioxide concentration, *Science*, *260*(5111), 1101–1104.

Menon, A., A. Levermann, and J. Schewe (2013), Enhanced future variability during india's rainy season, *Geophysical Research Letters*, *40*(12), 3242–3247.

Mishra, S., J. Tyagi, V. Singh, and R. Singh (2006), Scs-cn-based modeling of sediment yield, *Journal of Hydrology*, *324*(1), 301–322.

Mo, K. C. (2003), Ensemble canonical correlation prediction of surface temperature over the united states, *Journal of climate*, *16*(11), 1665–1683.

Moberg, A., D. M. Sonechkin, K. Holmgren, N. M. Datsenko, and W. Karlén (2005), Highly variable northern hemisphere temperatures reconstructed from low-and high-resolution proxy data, *Nature*, *433*(7026), 613–617.

Mockus, V., and A. T. Hjelmfelt (2004), National Resources Conservation Service, US Department of Agriculture, Washington, DC.

Mohtadi, M., S. Steinke, A. Lückge, J. Groeneveld, and E. C. Hathorne (2010), Glacial to holocene surface hydrography of the tropical eastern indian ocean, *Earth and Planetary Science Letters*, *292*(1), 89–97.

Molnar, P., and M. A. Cane (2002), El niño's tropical climate and teleconnections as a blueprint for pre-ice age climates, *Paleoceanography*, *17*(2), 11–1.

Molnar, P., and M. A. Cane (2007), Early pliocene (pre–ice age) el niño–like global climate: Which el niño?, *Geosphere*, *3*(5), 337–365.

Moy, C. M., G. O. Seltzer, D. T. Rodbell, and D. M. Anderson (2002), Variability of el niño/southern oscillation activity at millennial timescales during the holocene epoch, *Nature*, *420*(6912), 162–165.

Müller, P. J., G. Kirst, G. Ruhland, I. von Storch, and A. Rosell-Melé (1998), Calibration of the alkenone paleotemperature index u 37 kâĂš based on core-tops from the eastern south atlantic and the global ocean (60 n-60 s), *Geochimica et Cosmochimica Acta*, *62*(10), 1757–1772.

Neff, U., S. Burns, A. Mangini, M. Mudelsee, D. Fleitmann, and A. Matter (2001), Strong coherence between solar variability and the monsoon in oman between 9 and 6 kyr ago, *Nature*, *411*(6835), 290–293.

Nürnberg, D., J. Bijma, and C. Hemleben (1996), Assessing the reliability of magnesium in foraminiferal calcite as a proxy for water mass temperatures, *Geochimica et Cosmochimica Acta*, *60*(5), 803–814.

Otto-Bliesner, B. L., E. C. Brady, S.-I. Shin, Z. Liu, and C. Shields (2003), Modeling el niño and its tropical teleconnections during the last glacial-interglacial cycle, *Geophysical Research Letters*, *30*(23).

Pahnke, K., J. P. Sachs, L. Keigwin, A. Timmermann, and S.-P. Xie (2007), Eastern tropical pacific hydrologic changes during the past 27,000 years from d/h ratios in alkenones, *Paleoceanography*, *22*(4).

Palmer, T., Č. Brankovic, P. Viterbo, and M. Miller (1992), Modeling interannual variations of summer monsoons, *Journal of climate*, *5*(5), 399–417.

Parthasarathy, B., and G. Pant (1985), Seasonal relationships between indian summer monsoon rainfall and the southern oscillation, *Journal of climatology*, *5*(4), 369–378.

Parthasarathy, B., A. Munot, and D. Kothawale (1994), All-india monthly and seasonal rainfall series: 1871–1993, *Theoretical and Applied Climatology*, *49*(4), 217–224.

Parthasarathy, B., K. Rupa Kumar, and A. Munot (1996), *Homogeneous regional summer monsoon rainfall over India: interannual variability and teleconnections*, Indian Institute of Tropical Meteorology.

Pattanaik, D. (2012), Indian monsoon variability, *Monsoon Monographs*, *2*, 35–77.

Pelejero, C., and J. O. Grimalt (1997), The correlation between the uk'37 index and sea surface temperatures in the warm boundary: The south china sea, *Geochimica et Cosmochimica Acta*, *61*(22), 4789–4797.

Pelejero, C., J. O. Grimalt, S. Heilig, M. Kienast, L. Wang, et al. (1999), High-resolution uk37 temperature reconstructions in the south china sea over the past 220 kyr, *Paleoceanography*, *14*(2), 224–231.

Pena, L., I. Cacho, P. Ferretti, and M. Hall (2008), El niño–southern oscillation–like variability during glacial terminations and interlatitudinal teleconnections, *Paleoceanography*, *23*(3).

Penman, H. L. (1948), Natural evaporation from open water, bare soil and grass, *Proceedings of the Royal Society of London. Series A. Mathematical and Physical Sciences*, *193*(1032), 120–145.

Ponton, C., L. Giosan, T. I. Eglinton, D. Q. Fuller, J. E. Johnson, P. Kumar, and T. S. Collett (2012), Holocene aridification of india, *Geophysical Research Letters*, *39*(3).

Prahl, F. G., L. A. Muehlhausen, and D. L. Zahnle (1988), Further evaluation of long-chain alkenones as indicators of paleoceanographic conditions, *Geochimica et Cosmochimica Acta*, *52*(9), 2303–2310.

Prasad, S., S. Kusumgar, and S. Gupta (1997), A midâĂŞlate holocene record of palaeoclimatic changes from nal sarovarâĂŤa palaeodesert margin lake in western india, *Journal of Quaternary Science*, *12*, 153–159.

Prell, W., and W. Curry (1981), Faunal and isotopic indices of monsoonal upwelling-western arabian sea, *Oceanologica Acta*, *4*(1), 91–98.

Priestley, C., and R. Taylor (1972), On the assessment of surface heat flux and evaporation using large-scale parameters, *Monthly weather review*, *100*(2), 81–92.

Rajagopalan, B., and P. Molnar (2012), Pacific ocean sea-surface temperature variability and predictability of rainfall in the early and late parts of the indian summer monsoon season, *Climate dynamics*, *39*(6), 1543–1557.

Rajagopalan, B., and P. Molnar (2013), Signatures of tibetan plateau heating on indian summer monsoon rainfall variability, *Journal of Geophysical Research: Atmospheres*, *118*(3), 1170–1178.

Rajagopalan, B., and P. Molnar (2014), Combining regional moist static energy and enso for forecasting of early and late season indian monsoon rainfall and its extremes, *Geophysical Research Letters*, *41*(12), 4323–4331.

Rajeevan, M., J. Bhate, J. Kale, and B. Lal (2006), High resolution daily gridded rainfall data for the indian region: Analysis of break and active monsoon spells., *Current Science (00113891)*, *91*(3).

Ratnam, J. V., S. K. Behera, Y. Masumoto, K. Takahashi, and T. Yamagata (2010), Pacific ocean origin for the 2009 indian summer monsoon failure, *Geophysical Research Letters*, *37*(7).

Rein, B., A. Lückge, L. Reinhardt, F. Sirocko, A. Wolf, and W.-C. Dullo (2005), El niño variability off peru during the last 20,000 years, *Paleoceanography*, *20*(4).

Riedinger, M. A., M. Steinitz-Kannan, W. M. Last, and M. Brenner (2002), A 6100 14 c yr record of el niño activity from the galápagos islands, *Journal of Paleolimnology*, *27*(1), 1–7.

Rodbell, D. T., G. O. Seltzer, D. M. Anderson, M. B. Abbott, D. B. Enfield, and J. H. Newman (1999), An˜ 15,000-year record of el niño-driven alluviation in southwestern ecuador, *Science*, *283*(5401), 516–520.

Rosenthal, Y., and G. P. Lohmann (2002), Accurate estimation of sea surface temperatures using dissolution-corrected calibrations for mg/ca paleothermometry, *Paleoceanography*, *17*(3), 16–1.

Rosenthal, Y., D. W. Oppo, and B. K. Linsley (2003), The amplitude and phasing of climate change during the last deglaciation in the sulu sea, western equatorial pacific, *Geophysical Research Letters*, *30*(8).

Rostek, F., G. Ruhland, F. Bassinot, P. Müller, L. Labeyrie, Y. Lancelot, and E. Bard (1993), Reconstructing sea surface temperature and salinity using¿ lso and alkenone records, *Nature*, *364*, 319–321.

Rostek, F., E. Bard, L. Beaufort, C. Sonzogni, and G. Ganssen (1997), Sea surface temperature and productivity records for the past 240 kyr in the arabian sea, *Deep Sea Research Part II: Topical Studies in Oceanography*, *44*(6), 1461–1480.

Roxy, M. K., K. Ritika, P. Terray, and S. Masson (2014), The curious case of indian ocean warming, *Journal of Climate*, (2014).

Rutherford, S., M. Mann, T. Osborn, K. Briffa, P. D. Jones, R. Bradley, and M. Hughes (2005), Proxy-based northern hemisphere surface temperature reconstructions: sensitivity to method, predictor network, target season, and target domain, *Journal of Climate*, *18*(13), 2308–2329.

Saji, N., B. N. Goswami, P. Vinayachandran, and T. Yamagata (1999), A dipole mode in the tropical indian ocean, *Nature*, *401*(6751), 360–363.

Salas, J. D., C. Fu, and B. Rajagopalan (2010), Long-range forecasting of colorado streamflows based on hydrologic, atmospheric, and oceanic data, *Journal of Hydrologic Engineering*.

Sandweiss, D. H., J. B. Richardson, E. J. Reitz, H. B. Rollins, and K. A. Maasch (1996), Geoarchaeological evidence from peru for a 5000 years b.p. onset of el niÃśo, *Science*, *273*(5281), 1531–1533.

Sandweiss, D. H., K. A. Maasch, R. L. Burger, J. B. Richardson, H. B. Rollins, and A. Clement (2001), Variation in holocene el niño frequencies: Climate records and cultural consequences in ancient peru, *Geology*, *29*(7), 603–606.

Sangha, H. (2008), The birds of sambhar lake and its environs, *Indian Birds*, *4*(82), e97.

Saraswat, R., R. Nigam, S. Weldeab, A. Mackensen, and P. Naidu (2005), A first look at past sea surface temperatures in the equatorial indian ocean from mg/ca in foraminifera, *Geophysical research letters*, *32*(24).

Saraswat, R., D. W. Lea, R. Nigam, A. Mackensen, and D. K. Naik (2013), Deglaciation in the tropical indian ocean driven by interplay between the regional monsoon and global teleconnections, *Earth and Planetary Science Letters*, *375*, 166–175.

Sarkar, A., R. Ramesh, B. Somayajulu, R. Agnihotri, A. Jull, and G. Burr (2000), High resolution holocene monsoon record from the eastern arabian sea, *Earth and Planetary Science Letters*, *177*(3), 209–218.

Schulte, S., and P. J. Müller (2001), Variations of sea surface temperature and primary productivity during heinrich and dansgaard-oeschger events in the northeastern arabian sea, *Geo-Marine Letters*, *21*(3), 168–175.

Schulz, H., K.-C. Emeis, H. Erlenkeuser, U. von Rad, and C. Rolf (2002), The toba volcanic event and interstadial/stadial climates at the marine isotopic stage 5 to 4 transition in the northern indian ocean, *Quaternary Research*, *57*(1), 22–31.

Shanahan, T. M., J. T. Overpeck, W. Sharp, C. A. Scholz, and J. A. Arko (2007), Simulating the response of a closed-basin lake to recent climate changes in tropical west africa (lake bosumtwi, ghana), *Hydrological processes*, *21*(13), 1678–1691.

Shukla, J. (1987), Interannual variability of monsoons, in *Monsoons*, edited by J. S. Fein and P. L. Stephens, pp. 399–464, John Wiley and Sons.

Shukla, J., and D. Mooley (1987), Empirical prediction of the summer monsoon rainfall over india, *Monthly Weather Review*, *115*(3), 695–704.

Shukla, J., and D. A. Paolino (1983), The southern oscillation and long-range forecasting of the summer monsoon rainfall over india, *Monthly Weather Review*, *111*(9), 1830–1837.

Shukla, J., and J. Wallace (1983), Numerical simulation of the atmospheric response to equatorial pacific sea surface temperature anomalies, *Journal of the Atmospheric Sciences*, *40*(7), 1613–1630.

Shulmeister, J., and B. G. Lees (1995), Pollen evidence from tropical australia for the onset of an enso-dominated climate at c. 4000 bp, *The Holocene*, *5*(1), 10–18.

Shuttleworth, W. J. (2012), *Terrestrial hydrometeorology*, John Wiley & Sons.

Singh, G., R. D. Joshi, and A. Singh (1972), Stratigraphic and radiocarbon evidence for the age and development of three salt lake deposits in rajasthan, india, *Quaternary Research*, *2*(4), 496–505.

Singh, G., S. Chopra, and A. Singh (1973), Pollen-rain from the vegetation of north-west india, *New Phytologist*, *72*(1), 191–206.

Singh, G., R. Joshi, S. Chopra, and A. Singh (1974), Late quaternary history of vegetation and climate of the rajasthan desert, india, *Philosophical Transactions of the Royal Society of London. B, Biological Sciences*, *267*(889), 467–501.

Singh, G., R. Wasson, and D. Agrawal (1990), Vegetational and seasonal climatic changes since the last full glacial in the thar desert, northwestern india, *Review of Palaeobotany and Palynology*, *64*(1), 351–358.

Singh, O. (2001), Multivariate enso index and indian monsoon rainfall: relationships on monthly and subdivisional scales, *Meteorology and Atmospheric physics*, *78*(1-2), 1–9.

Singh, P., V. Vasudevan, J. Chowdary, and C. Gnanaseelan (2014), Subseasonal variations of indian summer monsoon with special emphasis on drought and excess rainfall years, *International Journal of Climatology*.

Sinha, R., D. Stueben, and Z. Berner (2004), Palaeohydrology of the sambhar playa, thar desert, india, using geomorphological and sedimentological evidences, *JOURNAL-GEOLOGICAL SOCIETY OF INDIA*, *64*(4), 419–430.

Slingo, J., and H. Annamalai (2000), 1997: The el niño of the century and the response of the indian summer monsoon, *Monthly Weather Review*, *128*(6), 1778–1797.

Smith, T. M., R. W. Reynolds, T. C. Peterson, and J. Lawrimore (2008), Improvements to noaa's historical merged land-ocean surface temperature analysis (1880-2006), *Journal of Climate*, *21*(10), 2283–2296.

Soman, M., and J. Slingo (1997), Sensitivity of the asian summer monsoon to aspects of sea-surface-temperature anomalies in the tropical pacific ocean, *Quarterly Journal of the Royal Meteorological Society*, *123*(538), 309–336.

Sontakke, N., G. Pant, and N. Singh (1993), Construction of all-india summer monsoon rainfall series for the period 1844-1991, *Journal of Climate*, *6*(9), 1807–1811.

Sonzogni, C., E. Bard, F. Rostek, R. Lafont, A. Rosell-Mele, and G. Eglinton (1997), Core-top calibration of the alkenone index vs sea surface temperature in the indian ocean, *Deep Sea Research Part II: Topical Studies in Oceanography*, *44*(6), 1445–1460.

Sonzogni, C., E. Bard, and F. Rostek (1998), Tropical sea-surface temperatures during the last glacial period: a view based on alkenones in indian ocean sediments, *Quaternary Science Reviews*, *17*(12), 1185–1201.

Sperber, K. R., H. Annamalai, I.-S. Kang, A. Kitoh, A. Moise, A. Turner, B. Wang, and T. Zhou (2013), The asian summer monsoon: an intercomparison of cmip5 vs. cmip3 simulations of the late 20th century, *Climate dynamics*, *41*(9-10), 2711–2744.

Sprent, P., and G. R. Dolby (1980), Query: the geometric mean functional relationship, *Biometrics*, pp. 547–550.

Srivastava, A., M. Rajeevan, and S. Kshirsagar (2009), Development of a high resolution daily gridded temperature data set (1969–2005) for the indian region, *Atmospheric Science Letters*, *10*(4), 249–254.

Staubwasser, M., F. Sirocko, P. Grootes, and M. Segl (2003), Climate change at the 4.2 ka bp termination of the indus valley civilization and holocene south asian monsoon variability, *Geophysical Research Letters*, *30*(8).

Steinke, S., M. Kienast, J. Groeneveld, L.-C. Lin, M.-T. Chen, and R. Rendle-Bühring (2008), Proxy dependence of the temporal pattern of deglacial warming in the tropical south china sea: toward resolving seasonality, *Quaternary Science Reviews*, *27*(7), 688–700.

Stott, L., C. Poulsen, S. Lund, and R. Thunell (2002), Super enso and global climate oscillations at millennial time scales, *Science*, *297*(5579), 222–226.

Stott, L., K. Cannariato, R. Thunell, G. H. Haug, A. Koutavas, and S. Lund (2004), Decline of surface temperature and salinity in the western tropical pacific ocean in the holocene epoch, *Nature*, *431*(7004), 56–59.

Sukumar, R., R. RamoshâĂŹr, R. Panti, and G. Rajagopalani (1993), A 5130 record of late, *Nature*, *364*, 19.

Swain, A., J. Kutzbach, and S. Hastenrath (1983), Estimates of holocene precipitation for rajasthan, india, based on pollen and lake-level data, *Quaternary Research*, *19*(1), 1–17.

Terray, P., and S. Dominiak (2005), Indian ocean sea surface temperature and el nino-southern oscillation: A new perspective, *Journal of Climate*, *18*(9), 1351–1368.

Timmermann, A., Y. Okumura, S.-I. An, A. Clement, B. Dong, E. Guilyardi, A. Hu, J. Jungclaus, M. Renold, T. Stocker, et al. (2007), The influence of a weakening of the atlantic meridional overturning circulation on enso, *Journal of Climate*, *20*(19), 4899–4919.

Tingley, M. P., and P. Huybers (2010), A bayesian algorithm for reconstructing climate anomalies in space and time. part i: Development and applications to paleoclimate reconstruction problems, *Journal of Climate*, *23*(10), 2759–2781.

Tudhope, A. W., C. P. Chilcott, M. T. McCulloch, E. R. Cook, J. Chappell, R. M. Ellam, D. W. Lea, J. M. Lough, and G. B. Shimmield (2001), Variability in the el niño-southern oscillation through a glacial-interglacial cycle, *Science*, *291*(5508), 1511–1517.

Vecchi, G. A., and D. Harrison (2004), Interannual indian rainfall variability and indian ocean sea surface temperature anomalies, *Earth's Climate*, pp. 247–259.

Vecchi, G. A., B. J. Soden, A. T. Wittenberg, I. M. Held, A. Leetmaa, and M. J. Harrison (2006), Weakening of tropical pacific atmospheric circulation due to anthropogenic forcing, *Nature*, *441*(7089), 73–76.

Visser, K., R. Thunell, and L. Stott (2003), Magnitude and timing of temperature change in the indo-pacific warm pool during deglaciation, *Nature*, *421*(6919), 152–155.

von Rad, U., M. Schaaf, K. H. Michels, H. Schulz, W. H. Berger, and F. Sirocko (1999), A 5000-yr record of climate change in varved sediments from the oxygen minimum zone off pakistan, northeastern arabian sea, *Quaternary Research*, *51*(1), 39–53.

Von Storch, H., and F. W. Zwiers (2001), *Statistical analysis in climate research*, Cambridge university press.

Walker, G. (1924), Correlations in seasonal variations of weather. mem. 24, indian meteorol, *Dep., New Delhi*, pp. 275–332.

Walker, G. (1928), World weather, *Quarterly Journal of the Royal Meteorological Society*, *54*(226), 79–87.

Wasson, R., G. Smith, and D. Agrawal (1984), Late quaternary sediments, minerals, and inferred geochemical history of didwana lake, thar desert, india, *Palaeogeography, Palaeoclimatology, Palaeoecology*, *46*(4), 345–372.

Webster, P. (1987), The elementary monsoon, in *Monsoons*, edited by J. S. Fein and P. L. Stephens, John Wiley and Sons.

Webster, P. J., V. O. Magana, T. Palmer, J. Shukla, R. Tomas, M. u. Yanai, and T. Yasunari (1998), Monsoons: Processes, predictability, and the prospects for prediction, *Journal of Geophysical Research: Oceans (1978–2012)*, *103*(C7), 14,451–14,510.

Weng, H., K. Ashok, S. K. Behera, S. A. Rao, and T. Yamagata (2007), Impacts of recent el niño modoki on dry/wet conditions in the pacific rim during boreal summer, *Climate Dynamics*, *29*(2-3), 113–129.

Wu, G., Y. Liu, Q. Zhang, A. Duan, T. Wang, R. Wan, X. Liu, W. Li, Z. Wang, and X. Liang (2007), The influence of mechanical and thermal forcing by the tibetan plateau on asian climate, *Journal of Hydrometeorology*, *8*(4), 770–789.

Xu, H., Y. Hong, and B. Hong (2012), Decreasing asian summer monsoon intensity after 1860 ad in the global warming epoch, *Climate dynamics*, *39*(7-8), 2079–2088.

Yanai, M., and G.-X. Wu (2006), Effects of the tibetan plateau, in *The Asian Monsoon*, pp. 513–549, Springer.

Yanai, M., C. Li, and Z. Song (1992), Seasonal heating of the tibetan plateau and its effects on the evolution of the asian summer monsoon, *Journal of the Meteorological Society of Japan*, *70*(1B), 319–351.

Yang, S., and K.-M. Lau (1998), Influences of sea surface temperature and ground wetness on asian summer monsoon., *Journal of climate*, *11*(12).

Yatagai, A., K. Kamiguchi, O. Arakawa, A. Hamada, N. Yasutomi, and A. Kitoh (2012), Aphrodite: Constructing a long-term daily gridded precipitation dataset for asia based on a dense network of rain gauges, *Bulletin of the American Meteorological Society*, *93*(9), 1401–1415.

Zhang, Z., M. E. Mann, and E. R. Cook (2004), Alternative methods of proxy-based climate field reconstruction: application to summer drought over the conterminous united states back to ad 1700 from tree-ring data, *The Holocene*, *14*(4), 502–516.

Zhao, M., C.-Y. Huang, C.-C. Wang, and G. Wei (2006), A millennial-scale u 37 kâĂš sea-surface temperature record from the south china sea (8 n) over the last 150 kyr: Monsoon and sea-level influence, *Palaeogeography, Palaeoclimatology, Palaeoecology*, *236*(1), 39–55.

Zheng, W., P. Braconnot, E. Guilyardi, U. Merkel, and Y. Yu (2008), Enso at 6ka and 21ka from ocean–atmosphere coupled model simulations, *Climate Dynamics*, *30*(7-8), 745–762.

Zhou, T., B. Wu, A. Scaife, S. Brönnimann, A. Cherchi, D. Fereday, A. Fischer, C. Folland, K. Jin, J. Kinter, et al. (2009), The clivar c20c project: which components of the asian–australian monsoon circulation variations are forced and reproducible?, *Climate dynamics*, *33*(7-8), 1051–1068.

Zucchini, W., and P. Guttorp (1991), A hidden markov model for space-time precipitation, *Water Resources Research*, *27*(8), 1917–1923.

Zucchini, W., and I. L. MacDonald (2009), *Hidden Markov models for time series: an introduction using R*, CRC Press.

Appendix A

Appendix A: Sub-Seasonal Variations in Spatial Signatures of ENSO on the Indian Summer Monsoon from 1901-2009

Signatures of NINO4 and NINO3 Indices on Indian Monsoon Rainfall. This appendix contains figures that show the signature of SSTs from the NINO4 and NINO3 regions on seasonal monsoon rainfall over India. Specifically shown are the results of an SMA regression analysis of daily monsoon rainfall with the NINO4 (Figure A.1) and NINO3 (Figure A.2) indices.

Influence of Indian Ocean Dipole (IOD) on Indian Monsoon Rainfall Some studies have suggested that Indian summer monsoon rainfall is tied to the Indian Ocean Dipole (IOD) (e.g. *Ashok et al.*, 2001, 2004; *Saji et al.*, 1999) and that while the ENSO-monsoon relationship has weakened in recent times, the IOD-monsoon relationship has strengthened (*Ashok et al.*, 2001, 2004; *Ashok and Saji*, 2007; *Ihara et al.*, 2008b; *Krishnaswamy et al.*, 2014). To investigate the importance of considering IOD in our analysis, we scatterplot AISMR seasonal rainfall versus seasonal IOD SST anomalies and provide correlations (in red) between the two time series (Figure A.3). The IOD indices were computed using the Japan Agency for Marine-Earth Science and Technology (JAMSTEC) definition of eastern Indian Ocean SSTs (averaged over the region of 90°E - 110°E and 10°S - 0°) subtracted from western Indian Ocean SSTs (averaged over the region of 50°E - 70°E and 10°S - 10°N). SST anomalies used in calculation of the IOD index were obtained from *Kaplan et al.* (1998). As seen in Figure A.3, all correlations are negative, but weak. The strongest of the

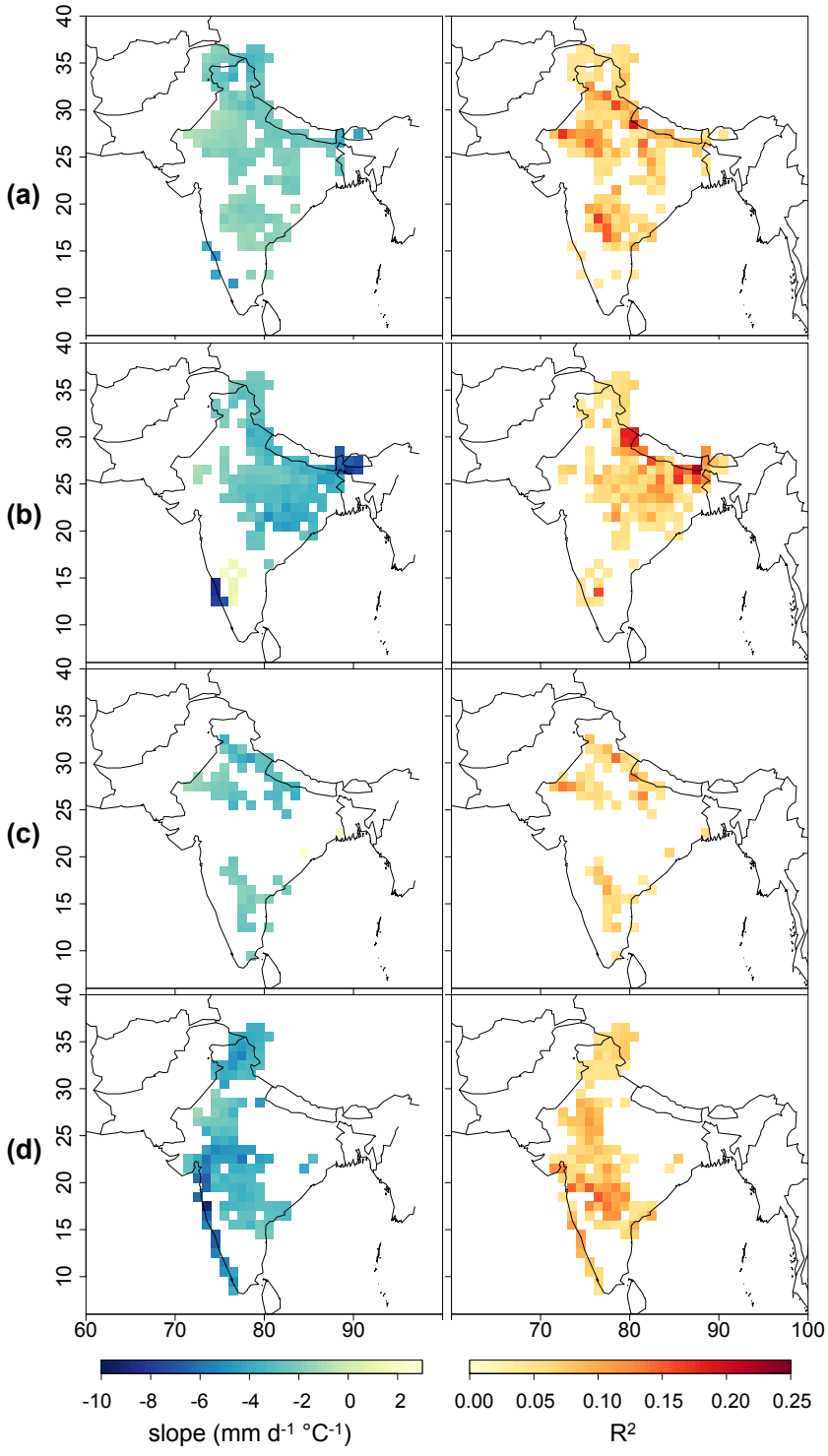

Figure A.1: Same as Figure 2.3 but using the NINO4 index.

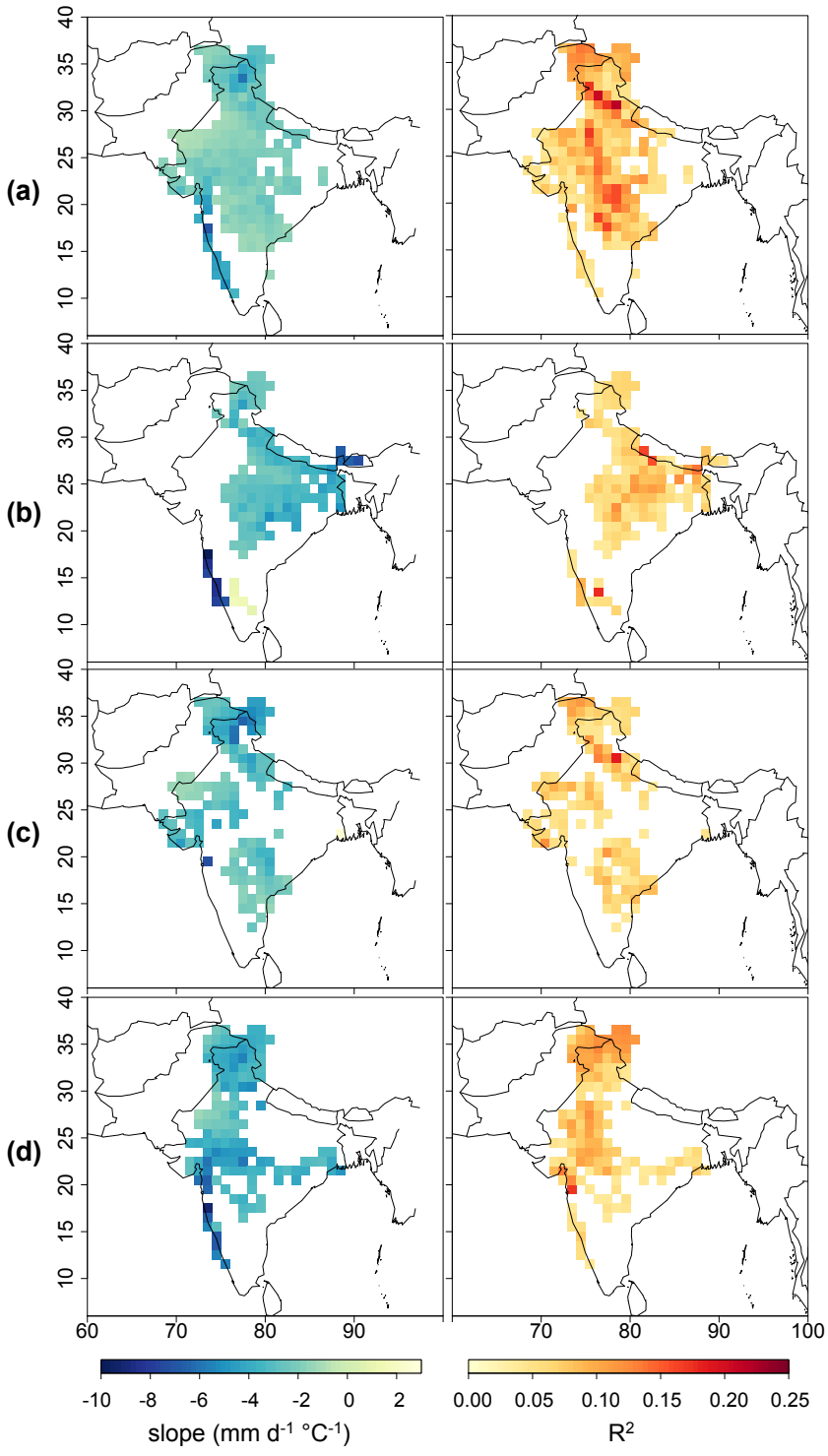

Figure A.2: Same as Figure 2.3 but using the NINO3 index.

four is during the late season, but it is still only -0.25. To look at this relationship spatially, we plot the slopes and R^2 values from the SMA regression between IOD and *Rajeevan et al.* (2006) gridded rainfall (Figure A.4). Due to weak correlations and sparse spatial signatures throughout most of the monsoon season, we proceed with the analysis without distinguishing between positive and negative IOD years.

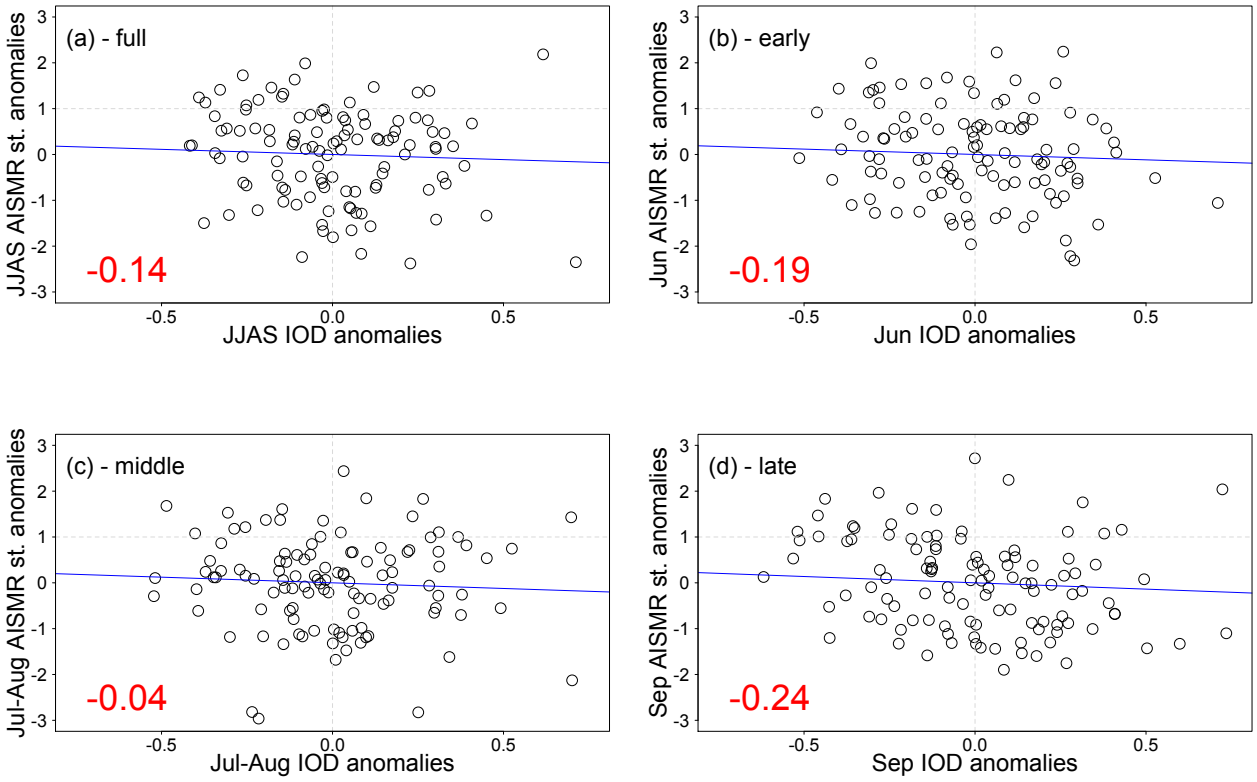

Figure A.3: Scatterplot of IOD anomalies with AISMR standardized total rainfall anomalies or the (a) full, (b) early, (c) middle and (d) late seasons. The blue line plots the SMA regression trend through the points. The correlation between the two time series is displayed in red in the lower left corner of each plot. The IOD indices were computed using the Japan Agency for Marine-Earth Science and Technology (JAMSTEC) definition of eastern Indian Ocean SSTs (averaged over the region of 90°E - 110°E and 10°S - 0°) subtracted from western Indian Ocean SSTs (averaged over the region of 50°E - 70°E and 10°S - 10°N). SST anomalies used in calculation of the IOD index were obtained from (*Kaplan et al.*, 1998).

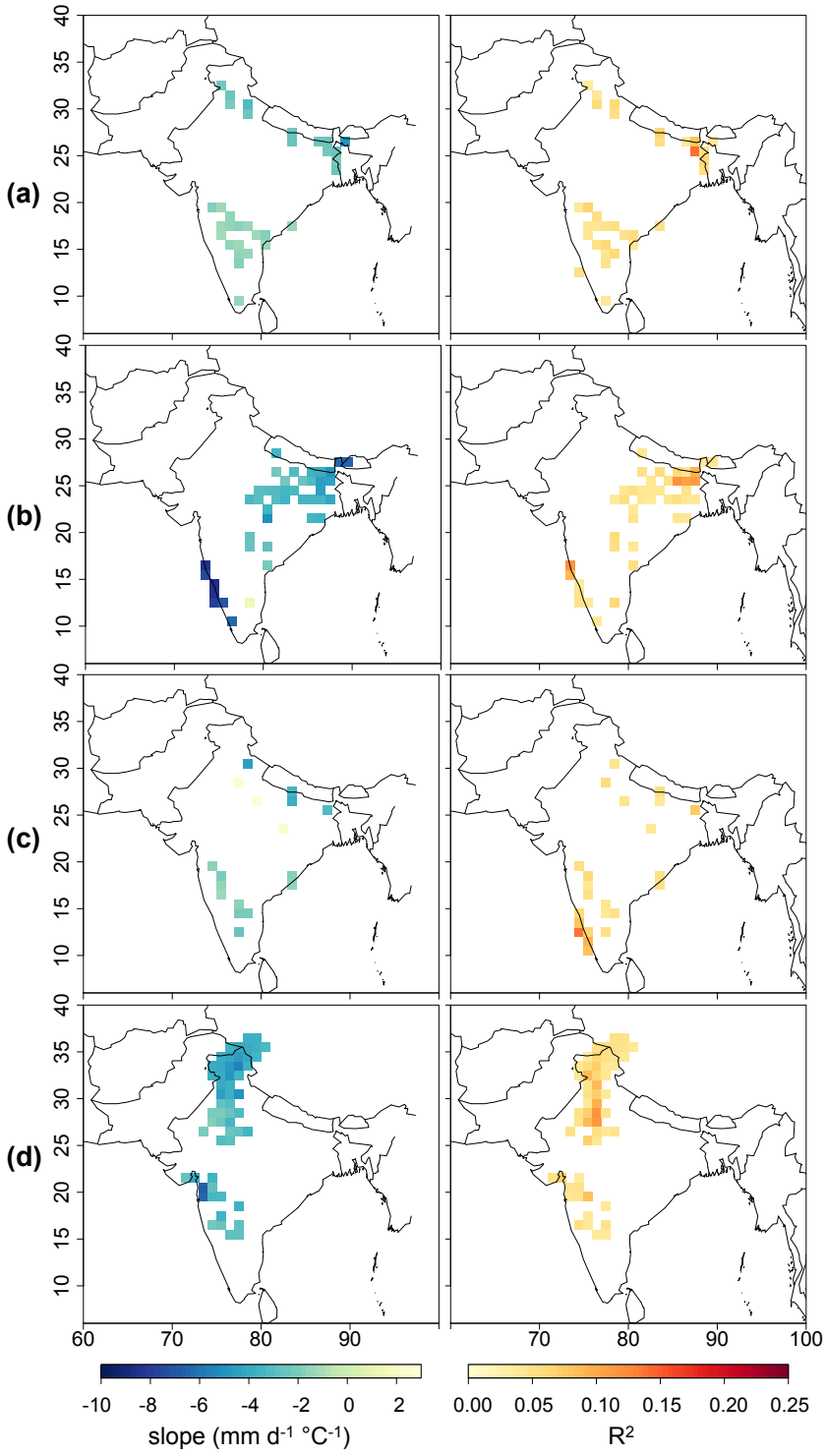

Figure A.4: Slopes of SMA regression between average daily rainfall (*Rajeevan et al.*, 2006) and NINO3 SSTs from 1901-2009 (*Kaplan et al.*, 1998) for the full (a - June to September), early (b - June), middle (c - July and August), and late (d - September) seasons. The first and second columns show the slopes (mm d^{-1} $^{\circ}C^{-1}$) and R^2 values of the SMA regressions, respectively. Colored regions show values at least 95% significant.